Master's thesis

NTNU
Norwegian University of Science and Technology
Faculty of Engineering
Department of Marine Technology

Petter Grudt Hals

Numerical & Experimental Studies on the Hydrodynamic Loads on Square-Shaped and Diamond-Shaped Cylinders in Close Proximity Exposed to a Forced Oscillatory Fluid Flow

Master's thesis in Marine Technology
Supervisor: Professor Trygve Kristiansen
June 2023

NTNU
Norwegian University of
Science and Technology

Petter Grudt Hals

Numerical & Experimental Studies on the Hydrodynamic Loads on Square-Shaped and Diamond-Shaped Cylinders in Close Proximity Exposed to a Forced Oscillatory Fluid Flow

Master's thesis in Marine Technology
Supervisor: Professor Trygve Kristiansen
June 2023

Norwegian University of Science and Technology
Faculty of Engineering
Department of Marine Technology

NTNU
Norwegian University of
Science and Technology

Department of Marine Technology

Master's Thesis

Numerical & Experimental Studies on the Hydrodynamic Loads on Square-Shaped and Diamond-Shaped Cylinders in Close Proximity Exposed to a Forced Oscillatory Fluid Flow

Author:
Petter Grudt Hals

June, 2023

Preface

This thesis is the culmination of my five-year Master of Science degree in Marine Hydrodynamics in Marine Technology at the Department of Marine Technology (IMT) at the Norwegian University of Science and Technology (NTNU).

The thesis examines the hydrodynamic interaction between square and diamond-shaped cylinders in close proximity to each other in a forced oscillatory flow. It is highly applicable to both industry and research to study these effects due to the existing studies and literature on the topic being sparse. The studies being conducted for the thesis are relevant to multiple types of floating modular structures but especially toward the multi-modular floating solar island concept developed by Moss Maritime and Equinor. This is due to the prevalence of hydrodynamic loads and wake interaction between the pontoons supporting the modules when exposed to waves. The importance of these studies is to produce data on the expected loads on the pontoons from the hydrodynamic interaction, which is essential for the development and longevity of the concept. Offshore solar energy has the potential to utilize great areas without interfering with nature and infrastructure and is therefore a crucial part of the world's transition to greener energy.

This thesis and its studies are continuations of the work of several previous master's students. Additionally, some of the studies are done in collaboration with other master's students. The reader should have prior knowledge of hydrodynamics and general fluid mechanics, as well as signal processing and data post-processing.

Petter Grudt Hals, Trondheim, June 11^{th}, 2023

Acknowledgements

Of the many people without whom the completion of this thesis would not have been possible I would first like to express my gratitude to my supervisor Professor Trygve Kristiansen. His devotion, experience, and expertise in the field of hydrodynamics have been essential to the culmination of the thesis. Thank you for your support and for all our interesting conversations. I also wish to express my gratitude to Senior Research Scientist Senthuran Ravinthrakumar who greatly helped me with my OpenFOAM analyses. Without his help, the numerical data for this thesis would not have been possible to procure.

My thanks also go to Terje Rosten and Robert Opland for their help in setting up the experimental studies produced for this thesis and for their continuous support during the tests. I wish to thank my fellow master's student Carlos Santamaria Izquierdo, who had previously used the experimental set-up for his thesis, for his help in getting the tests running, and for helping us with the script used to control the test rig. Additionally, I would like to thank my lab partners and fellow master's students Kristian Mikkelsen and Vilde Solberg for sharing the load of the tests making it possible for us to procure the amount of data that was needed, for their help during the post-processing and presentation of the data, and for their invaluable support throughout the year. I would also like to thank my good friends and office partners Sander Nesse-Hansen and Håkon Mørkeseth for their moral support during the thesis.

And finally, to my dearest fiancee and best friend Sofie. Thank you for all your support and help throughout these years, thank you for always being there to give me advice and make me laugh. Without you, none of this would have been possible, and I am forever grateful.

Abstract

The present work studies the hydrodynamic loads and wake interaction experienced by two or more cylinders in close proximity to each other exposed to a forced harmonically oscillating flow. This has been achieved primarily through two-dimensional numerical simulations, but also through preliminary three-dimensional experimental tests using three different cylinder sizes. The numerical and experimental analyses are based on a tandem configuration of two cylinders, which has been expanded on by changing the spacing between the cylinders, the cylinder shape, the number of cylinders, and the inflow angle which corresponds to the direction of the oscillation motion.

One of the key motivations behind the thesis work is the impact it can have on the development of structures related to green energy. Also, there is a limited amount of existing literature on the topic and few studies on closely placed cylinders in an oscillating flow have been carried out. A literature review has been performed on the existing literature, and an extensive theory chapter has been created to give the reader as much knowledge on the topic as possible.

The preliminary experimental tests were performed at Ladertanken at the Marine Technology Center at Tyholt in Trondheim. The tank is a relatively small wave flume and the experiments were performed by attaching crafted cylinders to actuator plates fastened to a rig in the middle of the tank. The cylinders were then oscillated up and down. A total of seven test configurations were tested experimentally for a range of KC numbers. As expected, there were large forces from the rig itself which introduced uncertainties to the measured data that had to be filtered out in the post-processing stages through thorough synchronization of the case data and the data from an empty rig test.

The numerical analyses in this thesis were all performed using the `pvcFoam` solver in OpenFOAM. The first simulations recreated the preliminary experiments as a base of comparison, but since the numerical tests were two-dimensional and the experiments were three-dimensional the comparisons are not fully fledged. After the initial cases had been modeled, two of the cases were modeled further with inflow angles ranging from $\theta = 0°$ to 90° with 5-degree increments. This was done to investigate how sensitive the hydrodynamic interaction was to the inflow angle. One case was further tested at an inflow angle of $\theta = 90°$, first with slight horizontal offsets of one cylinder and then with a number of different distances, or spacings, between the cylinders. When all of the numerical results had been gathered, they were compared to both three-dimensional and two-dimensional experimental results on the same cases to study if the effects were based on the dimensions or if they were purely numerical. Finally, a sensitivity analysis with regard to the mesh size, time step, and some case-specific parameters was performed.

These analyses showed a clear hydrodynamic dependence on the cylinder shape, KC number, inflow angle, and the spacing between the cylinders. They also show large nonlinear contributions to the forces, especially from the 2ω harmonic force amplitude. The models are able to capture these higher-order effects well in two dimensions and have a tendency to overpredict them in comparison with three-dimensional results. The existing load formulation from Morison's equation is not able to fully account for all these nonlinear components at the same time, and thus a key recommendation for further work on the topic is to develop and implement a more complete load formulation. Additional experimental and numerical tests should also be performed to further study the topic.

Sammendrag

Denne oppgaven studerer de hydrodynamiske belastningene og kjølvannsinteraksjonen som oppleves av to eller flere sylindre i umiddelbar nærhet av hverandre utsatt for en tvunget harmonisk oscillerende strøm. Dette er først og fremst oppnådd gjennom todimensjonale numeriske simuleringer, men også gjennom innledende tredimensjonale eksperimentelle tester med tre forskjellige sylinderstørrelser. De numeriske og eksperimentelle analysene er basert på en tandemkonfigurasjon av to sylindre, som har blitt utvidet ved å endre avstanden mellom sylindrene, sylinderformen, antall sylindre og innstrømningsvinkelen som tilsvarer retningen til oscillasjonsbevegelsen.

En av hovedmotivasjonene bak oppgaven er påvirkningen den kan ha på utviklingen av strukturer knyttet til grønn energi. Det er også en begrenset mengde eksisterende litteratur om emnet, og få studier på tett plasserte sylindre i en oscillerende strøm er gjennomført. Det er utført en litteraturstudie på eksisterende litteratur, og det er laget et omfattende teorikapittel for å gi leseren mest mulig kunnskap om temaet.

De innledende eksperimentelle testene ble utført i Ladertanken ved Marinteknologisenteret på Tyholt i Trondheim. Tanken er en relativt liten bølgesjakt og forsøkene ble utført ved å feste spesiallagde sylindre til aktuatorplater festet til en rigg i midten av tanken. Sylindrene ble så oscillert opp og ned. Totalt syv testkonfigurasjoner ble testet eksperimentelt for en rekke KC-tall. Som forventet var det store krefter fra selve riggen som introduserte usikkerheter til de målte dataene som måtte filtreres ut i postprosesseringen gjennom grundig synkronisering av testdata og data fra en tom riggtest.

De numeriske analysene i denne oppgaven ble alle utført ved hjelp av `pvcFoam`-løseren i OpenFOAM. De første simuleringene gjenskapte de innledende eksperimentene som et sammenligningsgrunnlag, men siden de numeriske testene var todimensjonale og eksperimentene var tredimensjonale, er ikke sammenligningene fullstendige. Etter at de første testkonfigurasjonene var modellert, ble to av konfigurasjonene modellert videre med innstrømningsvinkler fra $\theta = 0°$ til $90°$ med 5-graders inkrementer. Dette ble gjort for å undersøke hvor følsom den hydrodynamiske interaksjonen var for innstrømningsvinkelen. En konfigurasjon ble videre testet ved en innstrømningsvinkel på $\theta = 90°$, først med små horisontale forskyvninger av en sylinder og deretter med en rekke forskjellige distanser, eller avstander, mellom sylindrene. Når alle de numeriske resultatene var samlet, ble de sammenlignet med både tredimensjonale og todimensjonale eksperimentelle resultater på de samme konfigurasjonene for å studere om effektene var basert på dimensjonene eller om de var rent numeriske. Til slutt ble det utført en sensitivitetsanalyse med hensyn til maske-størrelse, tidstrinn og noen konfigurasjons-spesifikke parametere.

Disse analysene viste en klar hydrodynamisk avhengighet av sylinderformen, KC-tall, innstrømningsvinkel og avstanden mellom sylindrene. De viser også store ikke-lineære bidrag til kreftene, spesielt fra den harmoniske 2ω kraftamplituden. Modellene er i stand til å fange disse høyere ordens effektene godt i to dimensjoner og har en tendens til å overpredikere dem sammenlignet med tredimensjonale resultater. Den eksisterende lastformuleringen fra Morisons ligning er ikke i stand til å redegjøre fullt ut for alle disse ikke-lineære komponentene samtidig, og derfor er en sentral anbefaling for videre arbeid med temaet å utvikle og implementere en mer komplett lastformulering. Ytterligere eksperimentelle og numeriske tester bør også utføres for å studere emnet videre.

Table of Contents

Nomenclature

List of Abbreviations

PV	Photovoltaic
CFD	Computational Fluid Dynamics
SOF	Sinusoidally Oscillating Flow
$RANS$	Reynolds-Averaged Navier-Stokes
LES	Large Eddy Simulation
$2D$	Two-dimensional
$3D$	Three-dimensional

List of Symbols

KC $[-]$	Keulegan-Carpenter number
Re $[-]$	Reynolds number
C_D $[-]$	Drag coefficient
C_M $[-]$	Mass coefficient
C_A $[-]$	Added mass coefficient
C_B $[-]$	Damping coefficient
C_F $[-]$	Froude-Kriloff coefficient
η $[m]$	Motion of oscillation
$\dot{\eta}$ $[m/s]$	Velocity of oscillation
$\ddot{\eta}$ $[m/s^2]$	Acceleration of oscillation
ϕ $[m^2/s]$	Velocity potential
u $[m/s]$	Body velocity in the x-direction
$\dot{u}$ $[m/s^2]$	Body acceleration in the x-direction
ζ_a $[m]$	Incident wave amplitude
ω $[rad/s]$	Wave frequency
k $[rad/m]$	Wave number
λ $[m]$	Wave length
h $[m]$	Water depth
ρ $[kg/m^3]$	Water density
θ $[\,^\circ\,]$	Inflow angle
D $[m]$	Cylinder diameter
L $[m]$	Cylinder length
s $[m]$	Cylinder spacing
T $[s]$	Oscillation period
F_D $[N]$	In-line force, referred to as drag force
F_L $[N]$	Cross-flow force, referred to as lift force
CFL $[-]$	Courant–Friedrichs–Lewy number

Chapter 1

Introduction

1.1 Background & motivation

By 2050 the world's electricity demand will have doubled in size compared to what it is today. Despite this, the use of coal as an energy source is expected to drop by almost 70 %, the use of oil will drop by 45 %, and natural gas usage will drop by about 10 %. This raises the question of how the world's energy needs will be met when three of its largest energy contributors are in rapid decline, and the answer lies in the use and development of renewable energy resources. In 2022, DNV's energy transition forecast has for the first time ever found that by 2050 non-fossil energy will contribute to more than 50 % of the world's primary energy sources. They have also found that solar photovoltaic (PV) energy and wind energy will increase massively as shown in Figure 1.1 from [DNV 2022].

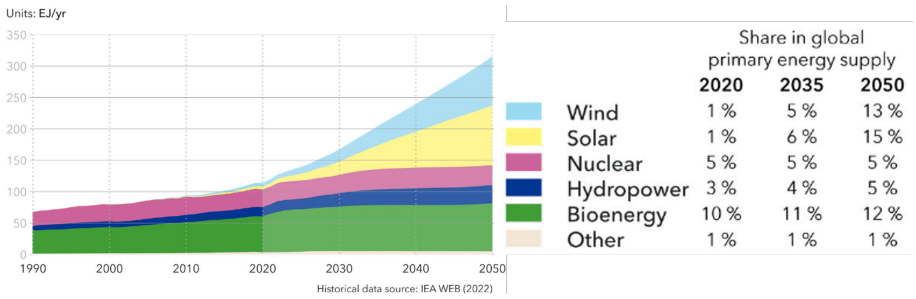

Figure 1.1: The world's grid-connected electricity generation by power station type.

With the rise of solar PV power and wind energy in the global energy industry, there will be a great increase in technology development both now and in the years to come. Many new and exciting concepts will be introduced around the world, one of these concepts being the multi-modular floating solar island that has been developed by Moss Maritime and Equinor to gather PV energy in the Norwegian Sea. Since the installation will be located offshore, it is of vital importance that it can withstand the large hydrodynamic forces and environmental loads that will be prevalent. The concept has been tested both experimentally and numerically for several years to improve its design toward better efficiency, productivity, and longevity. The basis of the concept consists of modular platforms housing the solar PV panels and being linked together in a grid by hinges. Each platform will be kept afloat by four pontoon legs, one in each corner, while the whole grid is kept in

place by mooring lines. A CGI render of the concept is shown in Figure 1.2. Due to the nature of the grid, it will tend to follow the wave elevation. Each platform will be able to move on its own, but since they are all hinged together every motion of one platform will be transferred to its neighbors. Moreover, the entire grid is also able to move with global motions due to the stiffness of the hinges connecting the grid together.

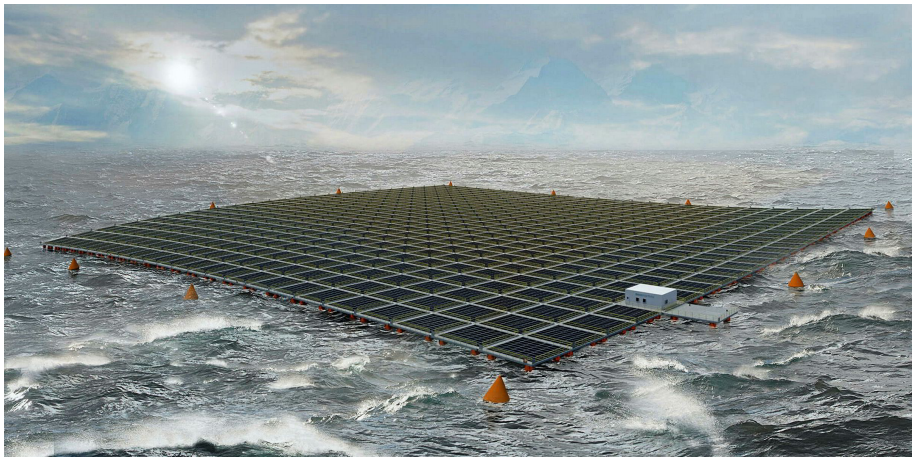

Figure 1.2: A CGI render of the multi-modular floating solar island concept developed by Moss Maritime and Equinor [SAIPEM 2020].

Each pontoon is a cylinder whose shape is one of the aspects being studied in this thesis. They have a diameter, $D = 2R$, that is relatively small compared to the wavelength, $\lambda \gg D$, meaning that the cylinders can be assumed slender and that flow separation will dominate the wave and current loads for each platform. However, at the junctions between the modules, pontoons from different modules will be in close proximity to each other resulting in wake interaction which will result in an alteration of the stress in the hinges, which is already high, and other loads on the pontoons. Therefore, the forces acting on the pontoons will be studied and compared to find the force difference caused by hydrodynamic interaction. A sketch of the platforms is shown in Figure 1.3, where pontoons A and B represent a junction where the forces must be studied.

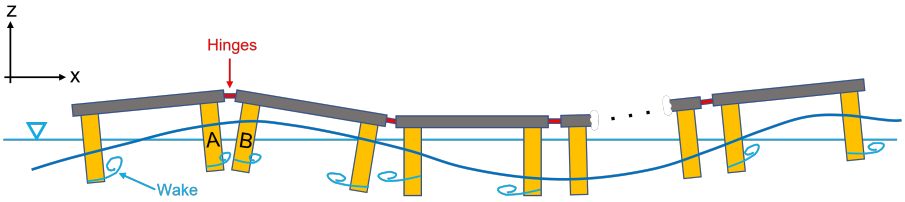

Figure 1.3: Side-view of the modules of the floating solar island concept. A junction, where hydrodynamic interaction must be studied, is represented by pontoons A and B.

The floating solar island concept has been studied previously by other master students. [Onsrud 2019] studied the wake interaction between the pontoons and the wave-induced vertical responses through model tests, while [Reiten 2022] looked into the hydrodynamic forces and wake interaction between the pontoons both numerically and experimentally while focusing on the two-dimensional effects. In addition to this several other students are currently working on the concept resulting in collaboration and information sharing between students studying different aspects of the floating solar island.

When the platform modules are floating and following the wave elevation, they will experience a horizontally oscillating flow due to the motion of the waves. The effects of a steady flow on both a single cylinder body and several cylinder bodies have been studied before, but few have been done for harmonically oscillating flows. A single pontoon in an oscillating flow is not hard to study as one can assume infinite fluid and thus no wake interaction, but when the other pontoons are added they will all experience hydrodynamic loads and wake interaction from each other resulting in a much more complex system. Most studies focus on circular cylinders, while in this thesis the geometries in question are square and diamond-shaped cylinders. This thesis is a part of SFI BLUES which is a research program studying floating structures [BLUES 2022].

1.2 Literature review

There are a lot of excellent resources when it comes to the research of wake interaction on cylindrical bodies, solar PV power plants, hydrodynamic loads and flows around different geometries, and marine hydrodynamics in general. Combined, these sources will provide an excellent foundation for understanding the system in question and how to approach and modify the studies to account for a harmonically oscillating flow.

In his review, [Zdravkovich 1977] studied the flow interference between two circular cylinders in various arrangements. He asserts that of the infinite arrangements of two parallel cylinders positioned in an incoming flow all but two configurations, cylinders in tandem and cylinders side-by-side, are just staggered arrangements of each other. The tandem arrangement, where the cylinders are positioned one behind the other in the direction of the incoming flow, has been studied experimentally from the early days of aeronautical engineering where the forces on tandem circular wires with different distances between them were measured. [Pannell et al. 1915] found that when the two wires were touching the combined drag force of the wires was 40 % of that of a singular wire, due to an improvement in the streamlining. They also found that when increasing the distance between the wires with increments of one diameter at a time, the wires would have to be more than six times the diameter apart to achieve a combined drag force equal to that of two wires, and that is with a 20° angle of stagger. Moreover, the increments of the drag force would decrease as more distance was added. The authors added another intermediate spacing of 3.5 times the diameter due to the very large increment between the spacing of three and four diameters. The results can be found in Figure A.1 in Appendix A.

[Biermann and Herrnstein 1933] conducted further investigations into the effect of the drag by extending the distance range between the wires to nine times the diameter. They measured the drag force on each wire separately and introduced an interference drag coefficient defined as the difference in the drag coefficients of one of the tandem wires and a single wire at the same Reynolds number. The combined interference drag coefficient was then found by adding the two interference coefficients of the two tandem wires. When they graphed their results as functions of the longitudinal spacing ratio, $^{L}/_{D}\,[-]$, they found that the drag interference coefficient of the upstream cylinder was close to zero for all tested Reynolds numbers. For the downstream cylinder, it was much larger in a negative sense. Both curves corresponded with a "kink" at approximately $^{L}/_{D} = 3$. To try and locate the position of minimal interference, the bottom of the "kink", they introduced several intermediate points between $^{L}/_{D} = 2.5$ and $^{L}/_{D} = 4$. Their results indicate a substantial hydrodynamic interaction between the wires when they are close enough together. The results can be found in Figure A.2 in Appendix A.

[Hori 1959] was the first to measure the pressure distributions around tandem circular cylinders. He measured the pressure for three spacings: 1.2, 2, and 3 times the diameter. The pressure distributions he found are shown in Figure A.3 in Appendix A. He found that the pressure on the front of the upstream cylinder was not affected by the presence of the downstream cylinder. Also, the base pressure coefficient increased with increasing spacing, and the interference drag coefficient described by [Biermann and Herrnstein 1933] decreases due to the base pressure only, which might explain the "kink" in Figure A.2. Furthermore, when he studied the pressure distribution around the downstream cylinder he found that the negative pressure on the inner side was very low, almost equal to the base pressure of the upstream cylinder indicating a stagnant flow between the cylinders. Moreover, the base pressure coefficient on the outer side of the downstream cylinder was even lower, meaning that the downstream cylinder experienced a negative drag force.

[Zdravkovich and Stanhope 1972] had previously measured the pressure distribution around the downstream cylinder for higher Reynolds numbers. From their findings, shown in Figure A.4 in Appendix A, they proposed two types of pressure distributions around the downstream cylinder:

(i) For small spacings (up to the kink) there are two symmetric peaks, presumably corresponding to the reattachment points.

(ii) For greater spacings (beyond the kink) there is a single peak corresponding to the stagnation point.

When investigating further they measured three velocity profiles in the area between the two cylinders in addition to one velocity profile across the wake behind the downstream cylinder. For a distance of less than 3.5 times the diameter the velocity profiles showed a very small velocity between the cylinders, confirming the finding of an almost stagnant flow, while the wake profile was significantly larger due to the streamlines from around the cylinders. Beyond this distance, all four velocity profiles became more similar as there was no longer any stagnation between the cylinders. This change between the flow patterns is due to the change from pressure distribution (i) to (ii) and is expected to happen gradually as the distance increases, however, from their experiments they found that it happens instantaneously. The change also induces vortex shedding behind both cylinders, while before the change it was only prevalent behind the downstream cylinder.

The side-by-side cylinder arrangement was also studied by [Biermann and Herrnstein 1933], and they presented their results through the interference drag coefficient shown in Figure A.5 in Appendix A. What they found was that for smaller distances, $^{L}/_{D} < 2$, there were quite strange changes in the interference drag. From these results, they proclaimed that the type of flow, with regard to positive or negative interference drag, changes rapidly as the distance decreases, and that it may even change while the distance is kept constant. These proclamations were the first indications of the bistable nature of the two different flow patterns at the tested distances.

[Zdravkovich 1977] uses these results to classify five different regions of flow regimes depending on whether the drag force is greater or less than for a single cylinder, and whether the lift force is positive, negative, or negligible. First, the upstream cylinder can be situated in three regions:

1. Reduced drag force and negligible lift force. Here, the distance between the cylinders

is very small meaning that the flow separates at the upstream cylinder and passes by the downstream cylinder.

2. Reduced drag force and a small repulsive lift force. Here, the distance is large enough so that the flow reattaches on the downstream cylinder after separating on the upstream cylinder. Vortex shedding from the downstream cylinder is induced.

3. Increased drag force and a repulsive lift force. This regime occurs when the flow experiences non-periodic reattachment resulting in irregular loads and vortex shedding.

Secondly, the downstream cylinder can, in addition to the first three regions, be situated in two other regions:

4. Increased drag force and negligible lift force. This region is quite small and there is no interference beyond it. For this regime to happen the distance must be just large enough for the downstream cylinder to be hit by the recirculation of the wake from the upstream cylinder, and the vortex shedding behind both cylinders is synchronized.

5. Decreased drag force and a negative lift force. This region is dominant for the downstream cylinder and occurs when the distance is so large that the vortex shedding behind the cylinders is no longer synchronized.

[Sarpkaya 2010] studied experimentally the correlation between the drag coefficient and the KC number on cylinders in a sinusoidally oscillating flow, SOF, for different Reynolds numbers. From his experiments, he found that there was a remarkable correlation between the force coefficients, the Reynolds number, and the KC number. In the inertia-dominated regime, $\mathrm{KC} < 5$, he found that the extraction of the drag coefficient became difficult and that this was especially the case for the experiments with the smallest cylinders. His data for the drag coefficient and the inertia coefficient are shown in Figure A.6 and Figure A.7 in Appendix A, and it shows that for an increasing Reynolds number the drag coefficient decreases to about 0.5 (depending on the KC number) and that it afterward gradually rises to a constant, post-supercritical value. The inertia coefficient will however increase with an increasing Reynolds number and gradually approach a constant value of 1.85.

These results were in opposition to the drag and inertia coefficients made by [Keulegan and Carpenter 1958] through measurements on submerged horizontal cylinders and plates placed in the node of a standing wave and applying theoretically derived values for the velocities and accelerations. [Sarpkaya 2010] believes that their data for the drag coefficient are not reliable for $\mathrm{KC} > 15$ since the drag coefficient of a cylinder in SOF is not always larger than for steady flow at the same Reynolds number. It will in fact be smaller for a large range of Reynolds numbers where drag coefficients for $\mathrm{KC} > 15$ dominate, which according to Figure A.6 in Appendix A happens for a range of Reynolds numbers between approximately 60 000 and 400 000.

[Kristiansen 2021] states in his report that the pontoons supporting the modules of the multi-modular floating solar island are categorized as small-volume structures since the horizontal dimension of the pontoons is much smaller than the dominant wavelengths at the exposed locations. This means that $\lambda \gg D$, and that the free-surface diffraction is negligible according to potential flow theory. However, the typical wave heights are large relative to the horizontal dimensions, resulting in the viscous effects due to flow separation

being dominant. He asserts that the Morison equation with KC-dependent hydrodynamic coefficients found for a single cylinder in infinite fluid may be attempted in an analysis of the pontoons, but that due to the expected wake interaction, these coefficients will be inaccurate or wrong. Also, the three-dimensional effects on the pontoons will matter, especially for the pontoons with a low draft.

He then describes the importance of studying the wake interaction between two pontoons as the downstream pontoon is in the wake of the upstream pontoon and may therefore experience an oppositely directed horizontal force relative to the upstream pontoon. The dimensions of the system are also addressed in this thesis. Because of practical limitations with regard to installation and maintenance, he considers that each floating solar island may be limited to a size of 10 x 10 modules, with each module being of the order $10\,m$ x $10\,m$, implying that the island is in the order of $100\,m$ x $100\,m$. Additionally, he states that the diameter of each pontoon being in the range of 0.5 - $2\,m$ is a reasonable estimate and that the resonance periods for the vertical motions of the modules are in the order of 2 - $3\,s$. This means that the vertical motions will be in the quasi-static frequency regime and that the modules will follow the waves vertically.

The significance of flow separation can be evaluated based on the KC number, which he shows can be quite high for these pontoons. For KC > 6 the potential flow assumption is violated and linear potential flow theory is no longer a valid model of reality. This is due to the flow separation which alters the flow and is therefore a dominant effect of the hydrodynamic load. Due to the high KC numbers, one should also expect wake interaction between the pontoons.

In their report [Dadmarzi et al. 2022] conducts a preliminary literature study on the modeling of large modular floating structures, of which the multi-modular floating solar island is an example. Their work is a part of SFI BLUES. On the concept of modular floating PV structures, they state that these concepts are receiving increased attention because of an increasing need for green energy, but that the literature on the hydrodynamic analysis of the concepts is sparse. They go on to describe several concepts for modular floating concepts, among them the concept by Moss Maritime and Equinor used in this thesis. Of this concept, they state that the conventional Morison's equation and strip theory may be a good first solution for analyses, but that a number of other effects might be important to include in an analysis such as the wave interaction and interference of the pontoons, three-dimensional effects due to the finite length of the pontoons, and the interaction between the free surface and the generated wake of each pontoon. Therefore, the report expresses the importance of model testing and CFD analysis of the hydrodynamic loads and viscous effects to highlight the important physical effects that occur for these types of multi-modular systems.

1.3 Project work fall 2022

This thesis has been done as a continuation of the work done during the specialization project performed in the fall of 2022 [Hals 2022]. The project was done as an introduction to the main thesis, and parts of the project thesis, such as the literature review, have been reused here. The specialization project focused mainly on building a substantial theoretical foundation while also generating preliminary experimental data that will be presented and discussed in this thesis and seen in comparison with new numerical results.

1.4 Scope of work

The main objective of this thesis is to study the presence of hydrodynamic loads between cylinders in close proximity to each other that are exposed to a forced harmonically oscillating flow and understand how these loads are affected by case-specific parameters such as cylinder shape, inflow angle, the distance between the cylinders, and several other parameters. These results will then be presented and analyzed to determine which parameters should be subjected to further testing. The results that will be presented are primarily gathered from numerical simulations created for the thesis, but some preliminary experimental results and experimental results from previous theses are used to compare and validate the numerical models.

As a way of achieving this, a set of objectives have been laid out to portray the scope of work for the thesis:

- Create a solid foundation of understanding regarding the hydrodynamics involved in the thesis through an extensive literature review and theory chapter.
- Use the preliminary data gathered from the experiments to investigate which configurations and case-specific parameters could be interesting to further analyze, and which parameters can be disregarded.
- Numerically simulate a number of case configurations and examine the hydrodynamic loads acting on and between the cylinders.
- Perform sensitivity analyses regarding the mesh, time step, and other case-specific parameters to validate results and create guidelines for further work.
- Investigate the usage of the model parameters used in the numerical models and find out if other models should have been used or if some model parameters should have been adjusted.
- Look into the harmonic force contributions of the forces experienced by the cylinders and examine how existing load formulations are able to capture all of the effects.
- Compare numerical and experimental results to validate numerical simulations and find model parameters that should be exchanged.
- Use the findings of the thesis to provide a basis for further investigations on the subject of hydrodynamic loads between closely spaced cylinders in a forced oscillatory flow.

Chapter 2

Theory

This chapter will cover the general and relevant theories, governing equations, and assumptions that are currently used in the study of hydrodynamic loads and wake interactions, and in the field of multi-modular floating solar islands. Parts of this chapter have been gathered from the specialization project [Hals 2022].

2.1 Potential flow theory

Many numerical solvers such as OpenFOAM [OpenCFD 2004], with for instance the `potentialFoam` solver, and WAMIT [Lee and Newman 1999] are based on potential flow theory to solve hydrodynamic problems. It can describe the interaction between bodies and waves based on several assumptions. The three most important ones are that the fluid must be *incompressible* and *inviscid* and that the flow is *irrotational*. With these assumptions, the boundary value problem, BVP, can be linearized in order to procure the first-order solution for potential flow theory, which is the velocity potential, ϕ, and is expressed by [Faltinsen 1993] for finite water depth as

$$\phi(x, y, z, t) = \frac{g\zeta_a}{\omega} \frac{\cosh(k[z+h])}{\cosh(kh)} \cos(\omega t - kx), \tag{2.1}$$

and for infinite water depth as

$$\phi(x, y, z, t) = \frac{g\zeta_a}{\omega} e^{kz} \cos(\omega t - kx), \tag{2.2}$$

where g is the gravitational constant, ζ_a is the wave amplitude, ω is the wave frequency, $k = \frac{2\pi}{\lambda}$ is the wave number where λ is the wavelength, h is the water depth, t is the time, x is the x-coordinate, and z is the z-coordinate. The transition from finite to infinite water depth is defined by [Kristiansen et al. 2021] as when $kh \to \infty$, but more commonly the condition is seen as infinite, or deep when $\frac{h}{\lambda} \geq 0.5$ since there is hardly any water particle motion at that depth due to the rapid exponential decay of ϕ in Equation 2.2.

The velocity potential is useful for finding the response of the body exposed to linear waves, and since the potential, pressure, and loads all oscillate with ω, the steady-state

response of each frequency can be solved to find the response amplitude operators, RAOs, for each rigid body mode. Additionally, the potential flow theory gives the linear dispersion relation which provides the relation between ω and k and is equal to

$$\omega^2 = gk\tanh(kh) \qquad \text{and} \qquad \omega^2 = gk \tag{2.3}$$

for finite and infinite water depth respectively. The velocity potential is further used by [Faltinsen 1993] to describe the fluid velocity vector $\boldsymbol{u}(x, y, z, t) = (u, v, \omega)$ at a time t at the point $\boldsymbol{x} = (x, y, z)$, meaning that

$$\boldsymbol{u} = \nabla\phi \equiv \boldsymbol{i}\frac{\partial\phi}{\partial x} + \boldsymbol{j}\frac{\partial\phi}{\partial y} + \boldsymbol{k}\frac{\partial\phi}{\partial z}. \tag{2.4}$$

To account for the assumption that the fluid flow is irrotational, the vorticity vector

$$\boldsymbol{\omega} = \boldsymbol{\nabla} \times \boldsymbol{u} \tag{2.5}$$

is set equal to zero everywhere in the fluid. The incompressibility assumption is met by the fluid having zero divergence, meaning that

$$\boldsymbol{\nabla} \cdot \boldsymbol{u} = 0. \tag{2.6}$$

From Equation 2.6 it follows that throughout the fluid ϕ must satisfy the Laplace equation

$$\nabla^2\phi = \frac{\partial^2\phi}{\partial x^2} + \frac{\partial^2\phi}{\partial y^2} + \frac{\partial^2\phi}{\partial z^2} = 0. \tag{2.7}$$

2.2 Navier-stokes equations

The Navier-Stokes equations were formulated by Navier and Stokes around 1850 and consist of four equations in three dimensions; three for the dimensional axes, x, y, and z, called the momentum equations, and one called the continuity equation. The Navier-Stokes equations are also referred to as the governing equations for fluid motion and adhere to the universal laws of conservation of mass, momentum, and energy. Conservation of energy is the basis of heat transfer and is therefore not covered in this thesis. [Kristiansen et al. 2021] states that the Navier-Stokes equations are based on the fluid being divided into numerous small fluid elements, which move together in a fluid continuum, where each element is given pressure, density, and viscosity properties that are used by the Navier-Stokes equations.

2.2.1 The momentum equations

The conservation of momentum is the basis of the three momentum equations through Newton's second law of motion

$$\Sigma F = m\boldsymbol{a} \quad \Rightarrow \quad \boldsymbol{F_p} + \boldsymbol{F_\tau} + \boldsymbol{F_g} = \Delta m \frac{D\boldsymbol{u}}{Dt}, \tag{2.8}$$

where $\boldsymbol{a}$ and $\boldsymbol{u} = [u, v, w]$ are the acceleration and velocity of the fluid, while F_p, F_τ, and F_g are the pressure, shear, and gravity forces acting on the fluid element. The gravity force acts through the center of gravity of the elements, while the pressure and shear forces are external forces acting on the element boundaries. The pressure forces act normally on the boundaries, while the shear forces act tangentially. When the pressure forces are integrated along the boundaries, a pressure gradient appears due to opposite forces on opposite boundaries. This also applies to the shear forces. The substantial derivative of the fluid velocity in Equation 2.8 can be expanded to

$$\frac{D\boldsymbol{u}}{Dt} = \frac{\partial \boldsymbol{u}}{\partial t} + \boldsymbol{u} \cdot \boldsymbol{\nabla} \boldsymbol{u} \tag{2.9}$$

and the element mass can be expressed as

$$\Delta m = \rho \Delta \boldsymbol{u}. \tag{2.10}$$

Using the gradients found in the above paragraph together with Equations 2.8, 2.9, and 2.10, the momentum equations become

$$\frac{\partial \boldsymbol{u}}{\partial t} + \boldsymbol{u} \cdot \boldsymbol{\nabla} \boldsymbol{u} = -\frac{1}{\rho} \nabla p + \boldsymbol{g} + \nu \nabla^2 \boldsymbol{u}, \tag{2.11}$$

where the kinematic viscosity, ν, is equal to the dynamic viscosity, μ, divided by the density, ρ.

2.2.2 The continuity equation

The fluid velocity in Equation 2.11 has three unknown variables, and the pressure is also unknown. This leads to the need for a fourth equation; the continuity equation, which is based on the conservation of mass and states that

$$\nabla \boldsymbol{u} = \frac{\partial u}{\partial x} + \frac{\partial v}{\partial y} + \frac{\partial w}{\partial z} = 0, \tag{2.12}$$

meaning that the mass that goes into a fluid element must also go out keeping the mass in the element constant. This is only valid for a fluid assumed to be incompressible, which is the case for potential flow theory as shown in Equation 2.6.

2.2.3 Simplifying the Navier-Stokes equations

In many cases, the Navier-Stokes equations can be heavily simplified by eliminating terms. An example of this is the case of a sinusoidally oscillating fluid flow where the flow oscillates along the x-axis, with no fluid flow along the other axes [Kristiansen 2023]. This will occur when a moored body, such as a floating solar island module, is floating in regular waves.

In this case, the continuity equation becomes

$$\nabla \boldsymbol{u} = \frac{\partial u}{\partial x} + \cancelto{0}{\frac{\partial v}{\partial y}} + \cancelto{0}{\frac{\partial w}{\partial z}} = \frac{\partial u}{\partial x} = 0. \tag{2.13}$$

Now, using the assumption of inviscid fluid from potential theory together with Equation 2.13, the momentum equations can be simplified. If this case only the momentum equation in the x-direction is needed, meaning that the gravity term disappears, and the pressure gradient is only calculated in the x-direction. The momentum equation then becomes

$$\frac{\partial u}{\partial t} + \boldsymbol{u} \cdot \boldsymbol{\nabla} u = \frac{\partial u}{\partial t} + u\cancelto{0}{\frac{\partial u}{\partial x}} + v\cancelto{0}{\frac{\partial u}{\partial y}} + w\cancelto{0}{\frac{\partial u}{\partial z}} = -\frac{1}{\rho}\frac{\partial p}{\partial x} + \nu\cancelto{0}{\nabla^2 u}$$

$$\Rightarrow \quad \frac{\partial u}{\partial t} = -\frac{1}{\rho}\frac{\partial p}{\partial x} \quad \Rightarrow \quad \frac{\partial p}{\partial x} = -\rho\frac{\partial u}{\partial t}, \tag{2.14}$$

which then can be used to define the pressure boundary conditions of the fluid domain of the case. If this example case domain has a length C in the x-direction, the pressure at each end of the domain will, due to anti-symmetry, be equal and opposite, meaning that

$$p\left(-\frac{C}{2}\right) = -p\left(\frac{C}{2}\right). \tag{2.15}$$

To find the pressure difference one can then integrate the pressure gradient found in Equation 2.14 over the length of the domain, and by using Equation 2.15 the pressure at the end boundaries of the domain becomes

$$p\left(\frac{C}{2}\right) - p\left(-\frac{C}{2}\right) = \int_{-C/2}^{C/2} \frac{\partial p}{\partial x} dx = -\rho \int_{-C/2}^{C/2} \frac{\partial u}{\partial t} dx = -\rho C \frac{\partial u}{\partial t}$$

$$\Rightarrow \quad p\left(\frac{C}{2}\right) = p\left(-\frac{C}{2}\right) = -\frac{1}{2}\rho C \frac{\partial u}{\partial t}. \tag{2.16}$$

2.3 Boundary value problem

When a body is placed in a fluid flow, such as for instance a floating solar island in current and waves, there must exist a boundary condition on the body that hinders any fluid from passing through the body surface. The boundary value problem is used by many numerical solvers to simulate the flow around bodies and the free surface conditions, and while it is not used directly in the numerical simulations in this thesis it is still important to be aware of it due to the free surface interaction that will most probably occur in the preliminary experiments. The boundary condition is defined as

$$\frac{\partial \phi}{\partial n} = 0, \tag{2.17}$$

where n is the normal of the body surface where the positive normal direction is defined as into the fluid. This boundary condition can also be used to express the impermeability of the seabed by using the z-normal for $z = -h$, where h is the depth of the fluid. Equation 2.17 can be generalized if the body has a velocity $\boldsymbol{U}$ to

$$\frac{\partial \phi}{\partial n} = \boldsymbol{U} \cdot \boldsymbol{n}. \tag{2.18}$$

2.3.1 Kinematic boundary condition

The substantial derivative of a function $F(x, y, z, t)$ expresses the rate of change with time for the function of a fluid particle moving through space and is defined in the same way as Equation 2.9 as

$$\frac{DF}{Dt} = \frac{\partial F}{\partial t} + \boldsymbol{u} \cdot \boldsymbol{\nabla} F. \tag{2.19}$$

The function F for a free surface $z = \zeta(x, y, t)$ can be established as

$$F(x, y, z, t) = z - \zeta(x, y, t) = 0. \tag{2.20}$$

[Faltinsen 1993] assumes that a fluid particle on the free surface will stay on the free surface, meaning that the Equation 2.19 is equal to zero. Combining this with Equation 2.4 the kinematic boundary condition on the free surface is found as

$$\frac{\partial}{\partial t}(z - \zeta(x, y, t)) + \boldsymbol{\nabla}\phi \cdot \boldsymbol{\nabla}(z - \zeta(x, y, t)) = 0, \tag{2.21}$$

which can be expressed as

$$\frac{\partial \zeta}{\partial t} + \frac{\partial \phi}{\partial x}\frac{\partial \zeta}{\partial x} + \frac{\partial \phi}{\partial y}\frac{\partial \zeta}{\partial y} - \frac{\partial \phi}{\partial z} = 0 \quad \text{on} \quad z = \zeta(x, y, t). \tag{2.22}$$

2.3.2 Dynamic free surface condition

In addition to the kinematic boundary condition, there is also a need for a dynamic free surface condition. This boundary condition is defined by the water pressure, p, being equal to the ambient pressure, p_0, on the free surface. The water pressure is defined by Bernoulli's equation when the z-axis is assumed vertical and positive upwards as

$$p + \rho g z + \rho \frac{\partial \phi}{\partial t} + \frac{\rho}{2}\boldsymbol{u} \cdot \boldsymbol{u} = C, \tag{2.23}$$

where the arbitrary function of time C is a constant as its time dependence is captured by

ϕ. When C is chosen as p_0/ρ, Equation 2.23 can be expressed as the dynamic free surface condition

$$g\zeta + \frac{\partial \phi}{\partial t} + \frac{1}{2}\left[\left(\frac{\partial \phi}{\partial x}\right)^2 + \left(\frac{\partial \phi}{\partial y}\right)^2 + \left(\frac{\partial \phi}{\partial z}\right)^2\right] = 0. \tag{2.24}$$

2.3.3 Linearizing and combining the boundary conditions

Both the conditions shown in Equations 2.22 and 2.24 are non-linear, and thus the location of the free surface is unknown prior to the equations being solved. By linearizing the equations the problem can be simplified, and is known as linear wave theory, or Airy wave theory [Faltinsen 1993]. If the wave amplitude is small relative to the wavelengths and body dimensions, linear theory can be applied which means that the velocity potential is proportional to the wave amplitude. The free surface conditions can then be transferred from the free surface to the mean free surface where $z = 0$ by Taylor expansions. The final linearized terms are then equal to

$$\frac{\partial \zeta}{\partial t} = \frac{\partial \phi}{\partial z} \quad \text{on} \quad z = 0 \tag{2.25}$$

$$g\zeta + \frac{\partial \phi}{\partial t} = 0 \quad \text{on} \quad z = 0 \tag{2.26}$$

for the kinematic and dynamic conditions respectively. The linearized conditions can now be united into the combined free surface condition

$$\frac{\partial^2 \phi}{\partial t^2} + g\frac{\partial \phi}{\partial z} = 0 \quad \text{on} \quad z = 0, \tag{2.27}$$

which for a harmonically oscillating velocity potential with frequency ω becomes

$$-\omega^2 \phi + g\frac{\partial \phi}{\partial z} = 0 \quad \text{on} \quad z = 0. \tag{2.28}$$

2.4 The equations of motions

To adequately describe the rigid body motions of a floating structure in a steady state SOF, the equations of motions are needed. They are defined by [Faltinsen 1993] as

$$\sum_{k=1}^{6} = \left[\left(M_{jk} + A_{jk}\right)\ddot{\eta}_k + B_{jk}\dot{\eta}_k + C_{jk}\eta_k\right] = F_j e^{-i\omega t}, \qquad j = 1, ..., 6 \tag{2.29}$$

where M_{jk} represents the components of the mass matrix of the structure, A_{jk} is the added mass coefficients, B_{jk} is the damping coefficients, C_{jk} is the restoring coefficients, and F_j represents the excitation forces. Here, η_k, is defined as

$$\eta_k = \mathfrak{Re}\left\{\eta_{ka} e^{i\omega t}\right\}, \tag{2.30}$$

where η_{ka} is the oscillation amplitude in the k-th degree of freedom. The motion of any point on the body can be written as

$$\boldsymbol{s} = \eta_1 \boldsymbol{i} + \eta_2 \boldsymbol{j} + \eta_3 \boldsymbol{k} + \boldsymbol{\omega} \times \boldsymbol{r}, \tag{2.31}$$

where

$$\boldsymbol{\omega} = \eta_4 \boldsymbol{i} + \eta_5 \boldsymbol{j} + \eta_6 \boldsymbol{k}, \quad \boldsymbol{r} = x\boldsymbol{i} + y\boldsymbol{j} + z\boldsymbol{k} \tag{2.32}$$

This means that the motion of any point can be rewritten using Equation 2.31 and 2.32 into

$$\boldsymbol{s} = (\eta_1 + z\eta_5 - y\eta_6)\boldsymbol{i} + (\eta_2 - z\eta_4 + x\eta_6)\boldsymbol{j} + (\eta_3 + y\eta_4 - x\eta_5)\boldsymbol{k} \tag{2.33}$$

2.5 Wave-body interaction

The wave-body interaction problem in hydrodynamics of a moored floating body is described by [Greco 2019] as consisting of two sub-problems called the radiation problem and the diffraction problem. This problem can be directly related to floating solar islands and is applicable both for experimental tests as performed by [Onsrud 2019], and numerical simulations exposing the body to waves instead of a forced oscillatory flow, and can thus be used in further numerical investigations.

2.5.1 Radiation problem

The radiation problem is defined as the body being forced to oscillate in its six degrees of freedom in the fluid without incident waves

$$\eta_j(t) = \eta_{ja}\cos(\omega t) = \mathfrak{Re}\left\{\eta_{ja} e^{i\omega t}\right\}, \tag{2.34}$$

with j corresponding to each of the six degrees of freedom, η being the oscillation motion of the body, η_a being the motion amplitude, and ω being the oscillation frequency. The oscillations cause waves to be radiated away from the body with velocity potentials

$$\phi_R(x, y, z, t) = \mathfrak{Re}\left\{\sum_{j=1}^{6} \dot{\eta_j}\phi_j\right\}, \tag{2.35}$$

where $\dot{\eta_j}$ is the velocity for mode j. ϕ_j is the potential per unit velocity, and is unknown, meaning it must satisfy the body-boundary condition

$$\frac{\partial \phi_j}{\partial n} = n_j \tag{2.36}$$

for all points on the wetted body surface, meaning that the fluid must move with the body along its wetted surface. Additionally, the disturbance on the fluid from the body must die down as the depth decreases, i.e. $z \to -\infty$, and far from the body the radiation condition is needed to ensure physical waves. Due to the oscillation of the body, it will be exposed to hydrodynamic loads consisting of added mass, damping, and restoring terms. The added mass and damping terms are connected to the dynamic pressure that is caused by the body's motions, and it can be shown that

$$F_{rad,k}(t) = -\int\limits_{S_{0B}} \rho \frac{\partial \phi_R}{\partial t} n_k dS = \sum_{j=1}^{6} \{-A_{kj}\ddot{\eta}_j - B_{kj}\dot{\eta}_j\} \quad \text{for} \quad k = 1...6, \tag{2.37}$$

where S_{0B} is the wetted surface of the body, and the added mass and damping coefficients are

$$A_{kj}(\omega) = \mathfrak{Re}\left\{\rho \int\limits_{S_{0B}} \phi_j n_k dS\right\} \quad \text{and} \quad B_{kj}(\omega) = -\omega \mathfrak{Im}\left\{\rho \int\limits_{S_{0B}} \phi_j n_k dS\right\}. \tag{2.38}$$

The restoring term is connected to the hydrostatic pressure and is caused by the changes in the buoyancy of the body on account of the rigid body motions. The generalized restoring loads can be shown to be

$$F_{hydr,k}(t) = -\sum_{j=1}^{6} C_{kj}\eta_j \quad \text{for} \quad k = 1...6. \tag{2.39}$$

The restoring coefficient, C_{kj} can then be found by estimating the variations of buoyancy.

2.5.2 Diffraction problem

The second sub-problem of wave-body interaction, the diffraction or excitation problem, is solved by keeping the body still in the fluid and exposing it to incident waves. The spatial velocity potential will then be the sum of the potentials for the incident waves, ϕ_0, and the diffracted waves, ϕ_D,

$$\phi(x, y, z, t) = \phi_0(x, y, z, t) + \phi_D(x, y, z, t). \tag{2.40}$$

The potential follows the impermeability condition

$$\frac{\partial \phi}{\partial n} = \frac{\partial \phi_0 + \phi_D}{\partial n} = 0 \tag{2.41}$$

for all points on the wetted surface of the body, which splits the problem into two potential problems. The first potential problem regards the incident wave potential and states that the flow due to the incident waves will penetrate the body as if it was not there, which causes hydrodynamic loads acting on the body called Froude-Kriloff forces [Faltinsen 1993]. To counter the penetrating flow and restore the impermeability of the body, the presence

of the body will cause a flow, which again generates diffraction waves. This impermeability condition comes from Equation 2.41 and diffracted flow is the equal and opposite of the incident flow

$$\frac{\partial \phi_D}{\partial n} = -\frac{\partial \phi_0}{\partial n}. \tag{2.42}$$

From potential theory, the excitation force is found by integrating the pressure over the wetted surface of the body

$$F_{exc,k}(t) = \int\limits_{S_{0B}} p n_k dS \quad \text{where} \quad p = -\rho \frac{\partial \phi}{\partial t} - \rho g z. \tag{2.43}$$

When Equations 2.40 and 2.43 are combined, it can be shown that

$$F_{exc,k}(t) = -\int\limits_{S_{0B}} \rho \frac{\partial \phi_0}{\partial t} n_k dS - \int\limits_{S_{0B}} \rho \frac{\partial \phi_D}{\partial t} n_k dS = \mathfrak{Re}\left\{ \int\limits_{S_{0B}} -i\omega e^{i\omega t} \rho(\phi_0 + \phi_D) n_k dS \right\}. \tag{2.44}$$

Moreover, it can be shown that

$$F_{exc,k} = \zeta_a \mathfrak{Re}\left\{ e^{i\omega t} X_k(\omega\beta) \right\} \quad \text{for} \quad k = 1...6, \tag{2.45}$$

where the complex variable $X_k(\omega, \beta)$ is the transfer function for $F_{exc,k}$ where ω is the wave frequency and β is the direction. It can give the load amplitude per wave amplitude

$$|X_k(\omega, \beta)| = \frac{|F_{exc,k}|}{\zeta_a} \tag{2.46}$$

as well as the phase, α of the excitation loads.

2.5.3 Haskind relation

Together the radiation and diffraction problems can be conjoined through the Haskind relation [Greco 2019]

$$\int\limits_{S_{0B}} \phi_D \frac{\partial \phi_k}{\partial n} dS = \int\limits_{S_{0B}} \phi_k \frac{\partial \phi_D}{\partial n} dS \quad \text{where} \quad \frac{\partial \phi_k}{\partial n} = n_k \quad \text{and} \quad \frac{\partial \phi_D}{\partial n} = -\frac{\partial \phi_0}{\partial n}. \tag{2.47}$$

The Haskind relation can then be used together with Equation 2.44 to form

$$F_{exc,k}(t) = \mathfrak{Re}\left\{ \int\limits_{S_{0B}} -i\omega e^{i\omega t} \rho(\phi_0 \frac{\partial \phi_k}{\partial n} - \phi_k \frac{\partial \phi_0}{\partial n}) dS \right\}, \tag{2.48}$$

which is a useful formula for cases where the diffraction velocity potentials are difficult to acquire.

2.6 Morison's equation

Morison's equation is a semi-empirical method of calculating the in-line wave loads on cylindrical members of offshore structures where viscous forces are important. The equation consists of two parts; an inertia force that is in phase with the acceleration of the flow and a drag force that is proportional to the square of the instantaneous fluid velocity. For a differential strip section of length dz on a rigid vertical cylinder, it is defined by [Morison et al. 1950] as

$$dF = \left[\rho\frac{\pi}{4}D^2C_M\frac{\partial u}{\partial t} + \frac{1}{2}\rho C_D D|u|u\right]dz, \tag{2.49}$$

where ρ is the density of the water, D is the diameter of the cylinder, C_M is the mass coefficient, C_D is the drag coefficient, and u and $\frac{\partial u}{\partial t}$ are the undisturbed fluid velocity and acceleration at the mid-point of the strip. Morison's equation can also be used to describe the forces on a moving body as

$$F_m(t) = \rho\frac{\pi}{4}D^2C_A\dot{u}(t) + \frac{1}{2}\rho C_D D|u(t)|u(t), \tag{2.50}$$

where $u(t)$ and $\dot{u}(t)$ are the velocity and acceleration of the body and $C_A = C_M - C_F$ is the added mass coefficient, where C_F is the Froude-Kriloff coefficient which more often than not is set equal to one. Here, F_m is the total Morison forces found by integrating Equation 2.49 over the wet area of the cylinder.

2.7 Hydrodynamic parameters

[Reynolds 1883] found from his experiments that an important ratio in fluid mechanics is the ratio between the inertial forces and the viscous forces. The ratio was later dubbed the Reynolds number and is defined as

$$\mathrm{Re} = \frac{UD}{\nu}, \tag{2.51}$$

where U is the mean inflow velocity, D is the characteristic length of the body, and ν is the kinematic viscosity coefficient of the fluid. The Reynolds number, along with the relative surface roughness are crucial in locating unknown flow separation points.

[Keulegan and Carpenter 1958] found that the coefficients on bodies in oscillating flow were functions of a ratio of the oscillation velocity amplitude, U, oscillation period, T, and characteristic length, D. The ratio became known as the Keulegan-Carpenter, KC, number and is defined as

$$\mathrm{KC} = \frac{UT}{D} \tag{2.52}$$

If the body is oscillating harmonically [Molin 2023] shows that the ratio can be rewritten as

$$\mathrm{KC} = 2\pi\frac{A}{D}, \tag{2.53}$$

where $A = \eta_a$ is the motion amplitude of the oscillation. This is true because the velocity, U, can also be described as the amplitude of a water particle when the body is subjected to waves. Due to this fact, it can also be rewritten based on the wave amplitude, ζ_a, as

$$\mathrm{KC} = \frac{2\pi\zeta_a}{D}. \tag{2.54}$$

2.8 Hydrodynamic forces & coefficients

When analyzing a structure in incident regular sinusoidal waves of small wave steepness, the hydrodynamic problem can be solved in two parts; the diffraction problem and the radiation problem, as described in Section 2.5. For the latter case, the hydrodynamic force becomes a sum of an inertial term and a damping term and can be expressed as

$$F = -A\ddot{\eta} - B\dot{\eta}, \tag{2.55}$$

where A and B are the added mass and damping forces, while $\ddot{\eta}$ and $\dot{\eta}$ are the acceleration and velocity of the body. They are derived from the oscillation motion of the body which can be defined as

$$\eta = \eta_a \cos(\omega t), \tag{2.56}$$

which ultimately results in

$$\dot{\eta} = -\eta_a\omega\sin(\omega t) \qquad \text{and} \qquad \ddot{\eta} = -\eta_a\omega^2\cos(\omega t). \tag{2.57}$$

Now, using Fourier averaging, A can be found. This method is done by multiplying each side of Equation 2.55 by the acceleration and integrating all terms over n periods, where n is an integer. This results in

$$\int_{nT} F\ddot{\eta}dt = -\int_{nT} A\ddot{\eta}\ddot{\eta}dt - \cancelto{0}{\int_{nT} B\dot{\eta}\ddot{\eta}dt}, \tag{2.58}$$

where the last term is 0 because the acceleration, which is a cosine expression, is multiplied by the velocity, which is a sine expression, and integrated over n whole periods, resulting in orthogonality over the interval. The same process is done to find B, but now Equation 2.55 is multiplied by the velocity before being integrated, resulting in the added mass term becoming zero. Now, A and B can be found as

$$A = -\frac{\int_{nT} F\ddot{\eta}dt}{\int_{nT} \ddot{\eta}\ddot{\eta}dt} \qquad \text{and} \qquad B = -\frac{\int_{nT} F\dot{\eta}dt}{\int_{nT} \dot{\eta}\dot{\eta}dt}. \tag{2.59}$$

Finally, the non-dimensional force can be expressed as

$$\frac{F}{\omega^2 \eta_a A_0} = \frac{A}{A_0}\cos(\omega t) + \frac{B}{A_0}\sin(\omega t) = \sqrt{\left(\frac{A}{A_0}\right)^2 + \left(\frac{B}{A_0}\right)^2}\sin(\omega t + \theta), \tag{2.60}$$

where θ is the phase difference between the force and the velocity, and A_0 is the reference added mass. The force amplitude can be expressed as

$$\frac{F_a}{\omega^2 \eta_a A_0} = \sqrt{\left(\frac{A}{A_0}\right)^2 + \left(\frac{B}{A_0}\right)^2} = \sqrt{C_A^2 + C_B^2}, \tag{2.61}$$

where C_A and C_B are the normalized added mass and damping coefficients. The reference added masses for a circular cylinder and a square cylinder are defined by [Pettersen 2007] as

$$A_0 = \rho\frac{\pi}{4}D^2 L \qquad \text{and} \qquad A_0^S = 1.51\rho\frac{\pi}{4}D^2 L, \tag{2.62}$$

where ρ is the fluid density, D is the characteristic length, and L is the length into the plane. From here, the normalized added mass and damping coefficients can be found as

$$C_A = \frac{A}{A_0} \quad \text{and} \quad C_B = \frac{B}{\omega A_0}, \tag{2.63}$$

where A_0 is the circular reference added mass even though the cylinders are square-shaped. This is done so that the coefficients can easily be related back to the coefficients of a circular cylinder, which is used as a base case in most areas of hydrodynamics. The ratio between the added mass and damping coefficients can give an indication of the contribution of each coefficient relative to the other. The ratio is defined as

$$\frac{C_B}{C_A} = \frac{\frac{B}{\omega A_0}}{\frac{A}{A_0}} = \frac{B}{\omega A}, \tag{2.64}$$

where a value greater than one indicates a greater damping contribution than added mass contribution, and vice versa. Furthermore, the amount of contribution each coefficient has on the force amplitude can be found as

$$\frac{C_A}{\sqrt{C_A^2 + C_B^2}} = \frac{\frac{B}{\omega A}}{\sqrt{1 + \left(\frac{B}{\omega A}\right)^2}} \tag{2.65}$$

for the damping, and likewise for the added mass. By relating the drag term from Morison's equation in Equation 2.50 with the damping term in Equation 2.55, the drag coefficient can be found as a function of the damping. However, the damping of a harmonically

oscillating system is not only linear, but it has contributions from both linear and non-linear sources. A quadratic damping term can be added to the linear damping term to account for the largest contributor to the non-linearity. [Kristiansen et al. 2021] states that this is done by equivalent linearization, and the damping term in Equation 2.55 now becomes

$$B^{(eqv.)}\dot{\eta} = B^{(1)}\dot{\eta} + B^{(2)}\dot{\eta}|\dot{\eta}|, \tag{2.66}$$

where $B^{(1)}$ is the linear damping and $B^{(2)}$ is the quadratic damping. Now, after discussions with [Kristiansen 2023] the linearized drag term in Equation 2.50 is

$$F_D^{lin} = \frac{1}{2}\rho C_D D L \eta_a \omega \frac{8}{3\pi} u = \frac{2}{3\pi^2}\rho C_D D^2 L \omega \mathrm{KC} u, \tag{2.67}$$

where the velocity u is the equivalent of the velocity $\dot{\eta}$. Finally, the drag coefficient can be found by equalling the linear damping term and the linearized drag term and solving for C_D. The expression becomes

$$C_D = \frac{B\dot{\eta}}{\frac{2}{3\pi^2}\rho D^2 L \omega \mathrm{KC} u} = \frac{\omega \rho \frac{\pi}{4} D^2 L C_B \dot{\eta}}{\frac{2}{3\pi^2}\rho D^2 L \omega \mathrm{KC} u} = \frac{3\pi^3}{8\mathrm{KC}} C_B, \tag{2.68}$$

where the drag coefficient is only dependent on the KC number and the damping coefficient.

2.9 Velocity & acceleration amplitudes based on the KC number

By rewriting Equation 2.53 with regards to the motion amplitude and inserting it into Equation 2.57 with the fact that $\omega = {}^{2\pi}/_{T}$, new expressions for the velocity and acceleration can be found, and are defined as

$$\dot{\eta} = -\left(\frac{\mathrm{KC}\, D}{2\pi}\right)\left(\frac{2\pi}{T}\right)\sin(\omega t) = -\frac{\mathrm{KC}\, D}{T}\sin(\omega t) \tag{2.69}$$

$$\ddot{\eta} = -\left(\frac{\mathrm{KC}\, D}{2\pi}\right)\left(\frac{2\pi}{T}\right)^2\cos(\omega t) = -\frac{2\pi\, \mathrm{KC}\, D}{T^2}\cos(\omega t). \tag{2.70}$$

This leads to the velocity and acceleration amplitudes being defined as

$$\dot{\eta}_a = \frac{\mathrm{KC}\, D}{T} \quad \text{and} \quad \ddot{\eta}_a = \frac{2\pi\, \mathrm{KC}\, D}{T^2} \tag{2.71}$$

From these expressions, specific KC numbers can be applied to a system with known values for T and D by applying specific velocity or acceleration amplitudes. Since the amplitudes are proportional to the KC number, higher amplitudes result in a higher KC number.

2.10 The Courant–Friedrichs–Lewy number

In a numerical solver, the Courant–Friedrichs–Lewy (CFL) number [Courant et al. 1928], sometimes referred to as simply the Courant number, is a dimensionless constant dictating the maximum allowed time step so that there is no information loss in the system. If a particle can travel more than the length of a cell in the mesh during each time step there will be cells that do not output any information about the flow. This flaw in the solver is negated by the CFL number, which is expressed by [Roache 1998] as

$$\mathrm{CFL} = u\frac{\Delta t}{\Delta x}, \tag{2.72}$$

where u is the flow velocity, Δt is the time step, and Δx is the length of the cell in the flow direction. By limiting the CFL number to always be less than one, the maximum allowed time step which does not allow the information to travel further than one cell length can be found by rearranging Equation 2.72. This is done automatically in many numerical solvers where the CFL number is checked for each cell in the meshed domain, and the time step can even be non-uniform over the domain to maximize the efficiency of the solver.

Chapter 3

Forced motion studies of 3D experiments

The main part of the experimental tests was performed in September 2022 in collaboration with master student Kristian Mikkelsen [Mikkelsen 2023], and parts of this chapter are gathered from the specialization project [Hals 2022]. The experimental tests presented in this chapter were performed at Ladertanken, or the Lader tank, at the Marine Technology Center at Tyholt in Trondheim. The tests were conducted prior to any numerical simulations to gain an extensive amount of data to form a basis for what results were to be expected from later studies and simulations. Based on the works of previous master's students [Reiten 2022] and [Onsrud 2019] it is clear that experimental data is important for validation and verification of numerical data, and that performing experiments generates experience and understanding regarding both the test cases and the hydrodynamic phenomena affecting them.

3.1 Experimental setup

Ladertanken is a relatively small wave flume and is mainly used by students doing research for their Master's thesis or Ph.D., or by lecturers during classes. It has a total length of $13.5\,m$, a breadth of $0.60\,m$, and an adjustable water depth, which during these tests was kept constant at $1\,m$ to ensure stability in the test results. A sketch of the tank characteristics is shown in Figure 3.1. The tank can be used for several different types of experiments and can support many types of sensors and machinery. The equipment used in this case is an actuator that can accelerate the test setup vertically to simulate the structure in an oscillating flow. The real oscillating flow is horizontal so this vertical setup may induce small sources of error due to the gravity forces, but since there is no free fluid surface directly interacting with the cylinders these forces are not induced and the errors become negligible. To measure the output data from the test rig the data program Catman Easy from HBM was used [HBM 2022]. The program records the time series of a specified number of channels, each either connected to a sensor or calculating results based on another channel.

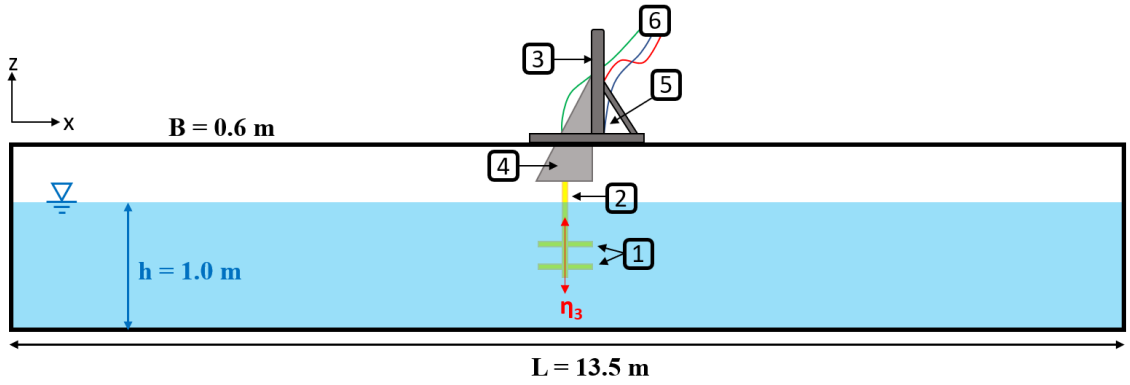

Figure 3.1: A simple sketch depicting the experimental test setup at Ladertanken, and some of the dimensions of the tank.

The numbered labels in Figure 3.1 indicate the following equipment that is attached to the test rig:

1. The cylinder model that is tested in each specific case, where three cylinder pairs with different lengths were used.
2. The actuator plates that the cylinders are attached to, one inner plate attached to the top cylinder(s) and an outer plate attached to the bottom cylinder(s).
3. The actuator that moves the test setup vertically exposing the cylinders to a forced oscillatory motion.
4. The rigid frame connecting the plate to the actuator.
5. The actuator rig that holds the actuator in place and holds most of the sensor equipment.
6. Cables carrying the information to and from the vertical actuator and its sensors.

The test rig is located at the midpoint of the tank to simulate infinite fluid and to ensure the least amount of effect from the ends of the tank. There are also parabolic beaches installed at each end of the tank to dampen the radiated waves. The vertical actuator can operate at a range of $\pm 20\,cm$. The base plate that the cylinders are attached to consists of two parts; an inner and an outer plate each connected to an array of sensors measuring the forces and acceleration of their particular plate, meaning that the plates are independent. This can be seen in Figure 3.2a where gaps are shown between the plates on both sides as well as between the cylinders to get independent measurements. The inner and outer plates are however not fully rigid which may lead to movements causing measuring errors. This will later be studied numerically in Section 4.1.3.

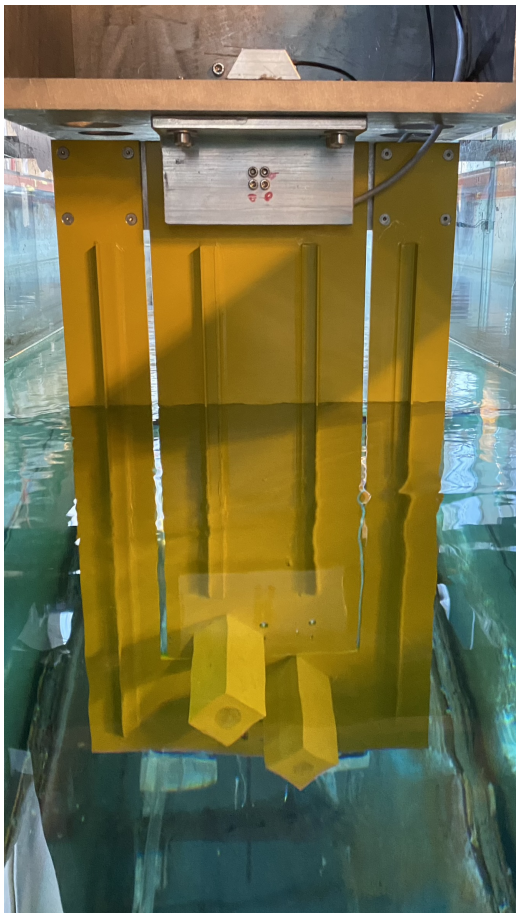

(a) The actuator plate where the gaps between the inner and outer plate are shown. Here, Case 4 with $^{L}/_{D} = 2$ is installed.

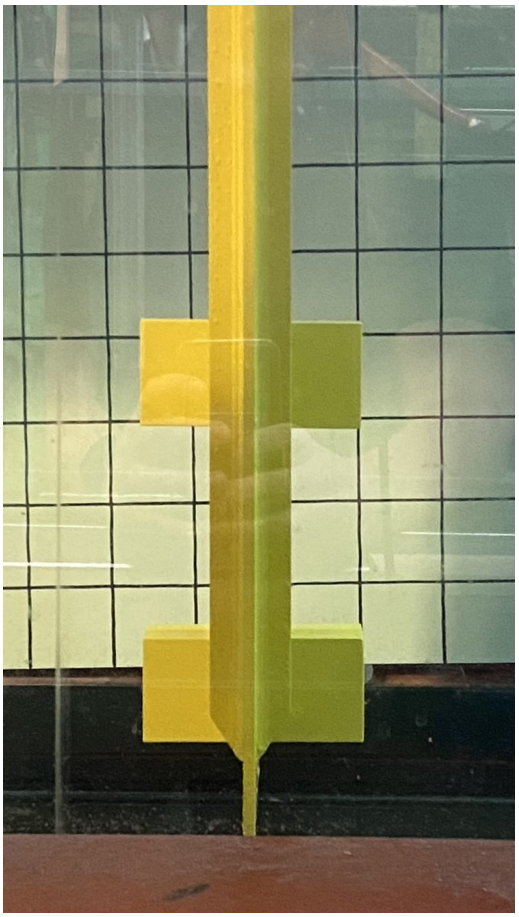

(b) A side-view of Case 2 with $^{L}/_{D} = 1$ installed on the actuator plate prior to a run, with the configuration shown in Figure 3.3.

Figure 3.2: Cases 4 and 2 installed on the actuator plate where the gaps between the inner and outer plate and the case configurations of the installed cases are shown.

There are several sensors attached to the test rig. On top of the actuator, a position sensor is attached that can continuously measure the position of the frame and thus the actuator plate. This data is mainly used for post-processing calibration since it is the data with the least amount of interference, meaning that it can be used to synchronize the data sets of the cases with the data from a test with an empty rig, which is done to remove forces induced by the actuator plates. Inside the actuator frame, there are two types of sensors; accelerometers and force transducers, one for each of the plates. The accelerometers measure the acceleration of each plate which is needed during post-processing to account for the force contributions of the mass of the cylinders. The force transducers measure the forces in the x-, y- and z-directions of each plate. The force output of these transducers can be used to study the interaction between the cylinders. In addition to these sensors, there were also two wave probes located in front and behind the test rig to measure the waves created by the actuator, but the data from these probes were not used in this project as the cylinders had no direct interaction with the free surface of the fluid.

All of the sensors were calibrated prior to the experiments, and due to the relatively short total test duration, it was not deemed necessary to re-calibrate the sensors during the testing period. This may have led to measuring errors in the sensors, but they were most

likely negligible. The first sensor to be calibrated was the position sensor. It was laid flat on a table and the cord was extended in intervals of 10 cm while recording the sensor output. This was done to find the calibration factor which shows how much measuring error there is in the sensor with regards to known data, which in this case was the known increments on the table. The calibration factor is found by curve fitting the plot points from Catman Easy in Excel and then implementing it into Catman Easy to ensure correct measurement data. Similarly, the force transducers were calibrated by applying known forces in the x-, y-, and z-directions, capturing the calibration factors, and implementing them in Catman Easy. The accelerometers are calibrated somewhat differently as the only known acceleration that is easy to apply is the acceleration of gravity. They are calibrated by turning them to positions where the outputs are only based on the acceleration of gravity, measuring the output, finding the calibration factor, and implementing it into Catman Easy. The wave probes were calibrated by incrementally lowering them into the water and recording the output, similar to the calibration of the position sensor.

In addition to these calibrations a hammer test, or decay test, should be performed to identify the eigenfrequencies of the components in the test rig, and thus find the frequency ranges where noise pollution on the signals due to vibration can be expected. The hammer test was not performed before the experiments during the specialization project but was later performed by master student Kristian Mikkelsen when he conducted new experiments for his Master's thesis. The results from this hammer test were that some higher-order frequencies could be polluted by noise, but that it did not affect the frequencies used in this thesis.

3.2 Test cases

There are two main objectives of the tests, one being to achieve a basis for the force responses that will later be validated and verified with the help of numerical tests, and the other being to identify and investigate potentially new hydrodynamic phenomena. In Figure 3.3 the seven cases that were tested experimentally are shown. Some of these cases were also later tested numerically as described in Section 4.1.1. The cases consist of a combination of square- and diamond-shaped cylinders in configurations of either two or four cylinders with varying distances. Cases 1 - 3 correspond with cases 11 - 13 with regard to the number of cylinders, but they have different geometries. Additionally, the distances between the midpoints of the cylinders are kept the same from cases 1 - 3 to 11 - 13, but the distances between the cylinders themselves are shorter for cases 11 - 13. This will in addition to the geometry lead to different flows in the cases. Case 4 is a stand-alone case with two square-shaped cylinders being exposed to an angled inflow of 45 degrees, and is the same as rotating Case 1 by 45 degrees. Due to the chosen geometry of the cylinders, there was only a need for one set of cylinders as they could be used for all cases.

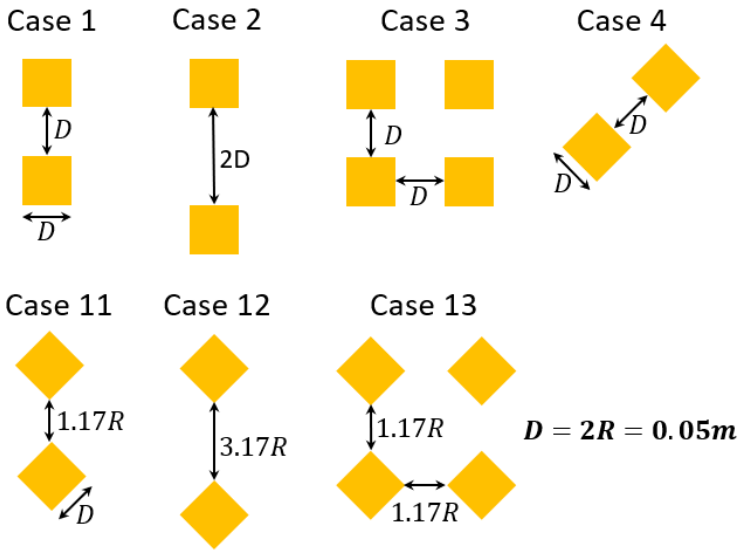

Figure 3.3: The seven cases that were tested using the experimental setup at Ladertanken during the specialization project.

Similar tests have been run by previous master students. Those tests were done to study for instance two-dimensional effects as done by [Reiten 2022]. The tests in this thesis are done to study the three-dimensional effects, and as such, it is of interest to test different length-to-diameter ratios, $^{L}/_{D}$. Three ratios were chosen and tested for each test. The ratios are shown in Figure 3.4. Each cylinder consists of two identical pieces fastened on each side of the actuator plates with a rod through both pieces securing them to the plates and a guidance pin ensuring correct orientation. The $^{L}/_{D}$ ratios are only based on one piece since each case will be mirrored around the plates. Due to the different ratios, the cylinder masses are different as shown in Table 3.1.

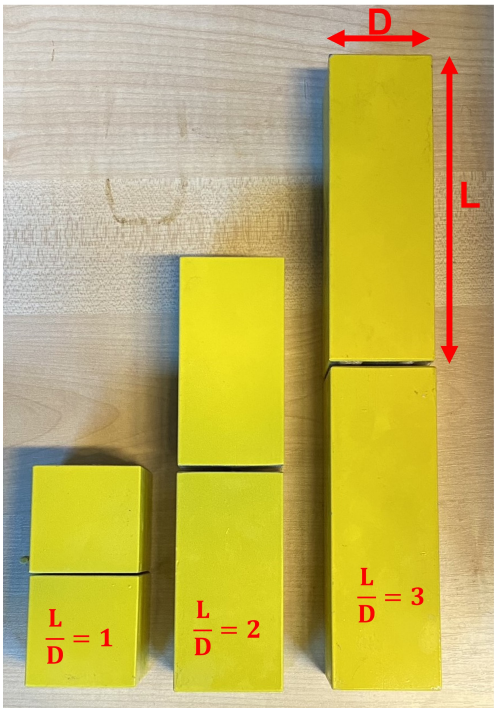

Figure 3.4: The three different length-to-diameter ratios used in the experimental tests.

Table 3.1: The mass of each cylinder size including the mass of the bolt and the putty used to cover the gaps around the bolt to ensure smooth surfaces. The masses are measured in air and have a $\pm 10\,g$ margin of error. For easier identification, the cylinder sizes were nick-named "Small", "Medium", and "Large".

Name	$^{L}/_{D}\,[-]$	$m\,[kg]$
Small	1	0.69
Medium	2	1.39
Large	3	2.08

3.3 Test procedure

Each of the seven test cases from Figure 3.3 was run for a range of KC numbers from 1 to 21.5 with an increment of $\Delta\text{KC} = 0.5$. The formulation of the KC number is shown in Equation 2.53 in Section 2.7. To achieve a steady state for the measured data each step of each run had an oscillation duration of 30 oscillation periods with four oscillation periods of ramping before and after the oscillations. Additionally, a 30-second pause was added between the runs to ensure that there was no disturbance in the water from the previous measurement when a new one began. Each KC increment step was tested for two oscillation periods of $1\,s$, and $1.5\,s$ to ensure a wider spectrum of results.

Using the maximum actuator motion amplitude of $\eta_a = 0.2\,m$ and the diameter of the cylinders which is $D = 0.05\,m$ the maximum KC number is found to be $\text{KC} = 25$. However, to account for inaccuracies in the actuator the maximum KC number was chosen to be $\text{KC} = 21.5$ giving the actuator a motion amplitude of $0.17\,m$. This ensures a large enough margin of error so that the actuator will not be accidentally strained and damaged during the tests. Later, when reviewing the position data of the actuator, the maximum motion amplitude of the actuator was found to be over $0.19\,m$ meaning that it would have surpassed its threshold had a higher KC number been used. This could also mean that the actual KC numbers were larger, which could lead to some discrepancies later on, but this was deemed negligible at the time.

By using the range of KC numbers and two oscillation periods for the case configurations, it resulted in a total of 84 oscillation steps for each case. Accounting for the downtime the total duration for each test was around $6\,500\,s$. For all 22 test runs, one empty rig to account for unwanted measurements from the actuator plate itself, and three different cylinder sizes for each of the seven cases, this accounted for a total of 143 000 seconds or 40 hours of runtime.

The reconfiguration process between each case was quite cumbersome as it required the water level to be lowered by roughly $0.5\,m$ to access the cylinders. Each cylinder was fastened tightly with a bolt and the bolt ends on each side were covered with putty to smooth the edges and get the correct end effect measurements. The emptying and re-filling of the tank took about 20 minutes, and the reconfiguration could take anywhere between 5 and 15 minutes to achieve due to the different configurations. In total, roughly 10 hours were used for the reconfiguration in between runs.

3.4 Post-processing

After the data had been obtained they were first post-processed in Matlab to extract some preliminary results, and later on in Python. An existing code for reading the binary data files was used for the output before it was further processed. The read function gathers all the channels from the binary files, and the channels useful for the thesis were stored. These channels were the time, position, acceleration, and forces acting on the top and bottom cylinders. These channels are first gathered for the empty rig case and used in the other cases to account for the effects of the actuator plate itself.

Since there is no way to accurately start the actuator at an exact time after the recording of the channels has begun, the first post-processing step is to synchronize the data from each case with the empty rig so that its contributions can be correctly accounted for. This is done by a process called the L_2-norm [Shkoller 2009] where two signals are synchronized together by holding the first signal, f_1, in place and moving the other signal, f_2, n increments in each direction along the shared axis. For each increment, the area between the signal curves is measured by the expression

$$L_2 = \left[\int_0^t (f_1 - f_2)^2\right]^{1/2}, \tag{3.1}$$

which is the second stage of the more general expression for the L_p-norm

$$L_p = \left[\int_0^t (f_1 - f_2)^p\right]^{1/p} \qquad \text{where} \qquad L_\infty = \max(f_1,\, f_2) \tag{3.2}$$

Now, the f_2 signal is phase-shifted by the amount required to reach the location with the least area between the signals, which is where the peaks of the signals line up. The signals before and after this process are shown in Figure 3.5.

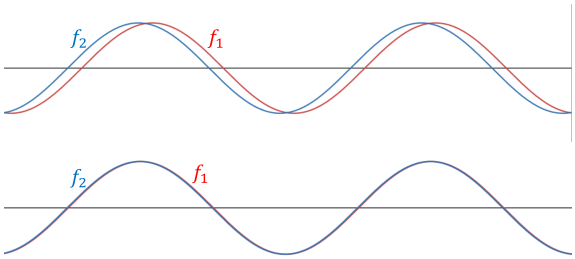

Figure 3.5: Two example signals before and after the L_2-norm synchronization.

When the signal for the active case is synchronized with the empty rig signal, the force contributions from the rig can be subtracted from the forces for the case to get the force output from just the cylinders. In addition to this, the mass forces from the cylinders must be added to the forces in the z-direction to only keep the hydrodynamic forces. The acceleration has the opposite sign of the force, and therefore the mass forces must be added to the total force to remove their contributions. This process is done for the in-line forces that are present in the same direction as the oscillation motion, which is the z-direction, of the top cylinder as follows

$$F_{z,top} = F_{z,top,measured} - F_{z,top,emptyRig} + m \cdot a_{measured}, \tag{3.3}$$

where $F_{z,top,measured}$ is the data from the case, $F_{z,top,emptyRig}$ is the data from the empty rig case, and $a_{measured}$ is the measured acceleration for the case. It is then repeated for the forces in the z-direction for the bottom cylinder. The mass, m, depends on both the cylinder size, as shown in Table 3.1, and on the number of cylinders.

After this has been done for all the necessary parameters, new parameters can be made based on them. The difference in the force on the top and bottom cylinders is interesting to study. It is defined for the z-direction as

$$\Delta F_z = F_{z,top} - F_{z,bottom}, \tag{3.4}$$

and gives an indication of the forces acting between the cylinders. If $\Delta F_z > 0$ there is an attractive force acting between them since the bottom cylinder is less affected by the flow and has force contributions pushing it towards the top cylinder, and likewise if $\Delta F_z < 0$ the force is repulsive since the bottom cylinder is pushed away from the top cylinder. Similarly, the total force, $F_{z,Total}$, is found by adding together the contributions and is a useful indicator of the amount of force acting on the system as a whole.

The force data can now be plotted as functions of time to visualize the results. However, they must be filtered to remove noise pollution to get readable results. This is done by using the bandpass filter `bpass2.m` provided by Prof. Trygve Kristiansen. This is a function that takes a piece of the data series, one steady state run, as an input, as well as the time step and the cutoff frequencies, and outputs a clean time series. The low cutoff frequency has in this case been set to $^{0.8}/_{T}$ and the high cutoff frequency to $^{10}/_{T}$ where T is the period of oscillation for the given run. The time step, dt, is set equal to $^{1}/_{Fs}$, where $Fs = 200\,Hz$ is the sampling frequency used by the Catman Easy program. The cutoff frequencies were chosen based on input from Prof. Trygve Kristiansen.

In Figure 3.6 a comparison between the measured and filtered data for the force in the z-direction for the top cylinder is shown. The force difference between the two cylinders is also shown. This figure shows that the readability of the data increases drastically when it is filtered.

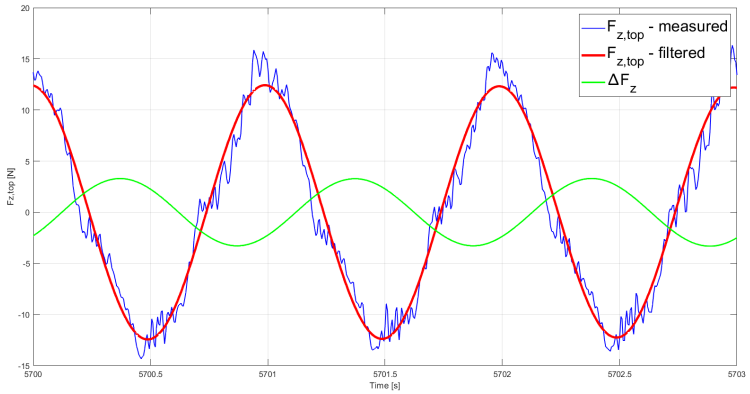

Figure 3.6: The measured force in the z-direction vs. the filtered force in the z-direction for the top cylinder. A filtered ΔF_z is also shown.

After the data is filtered, everything can be plotted to visualize the results. In Figure 3.6 the data is shown with values measured directly from Catman Easy, but at later stages, the results will be non-dimensionalized on account of the geometry of the cylinders to be able to easily compare them to other studies. Additional plots can also be created to give a better understanding of the system. For instance, the higher-order harmonic contributions of the force data can be extracted and plotted as functions of the KC number to show which frequency amplitudes dominate the cases. This is done by Fourier transforming the data and extracting the frequency and amplitude values. This is later shown in chapter 5.

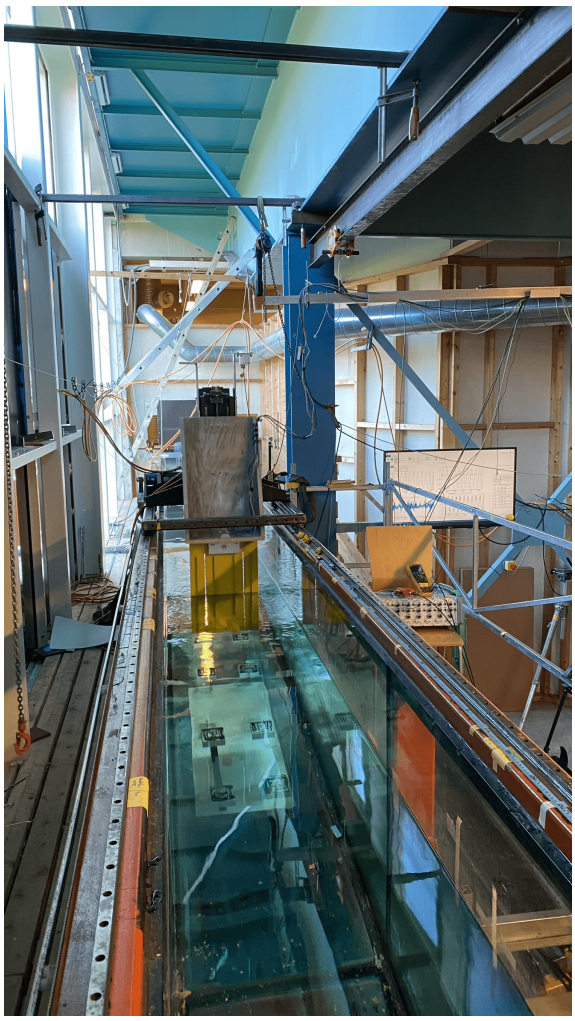

Figure 3.7: A view of Ladertanken showing the wave flume, the test rig, and much of the equipment used for the experiments.

Chapter 4

Numerical studies of 2D CFD simulations

[Roache 1998] states that computational fluid dynamics (CFD) is its own branch within fluid dynamics in between the theoretical and experimental branches, containing aspects of both branches and supplementing them. He further discusses that CFD can be considered closer to the experimental branch than a pure theoretical branch since it relies heavily on heuristic reasoning, physical intuition, experience, and trial-and-error procedures, along with rigorous mathematical analysis of simpler, linearized, and more or less related problems to the problem of interest. He then compares CFD simulations to physical experiments in that an analyst will "turn on" the equations and see what happens, much in the same way that a physical experimenter does with their devices, and that actual discovery of physical phenomena is possible using only numerical experiments, but that experimental validation is necessary. If a numerical model is created and validated through experimental results, it can be expanded and used for similar systems and methods with expected outcomes with high validity. CFD also has advantages through complete control over the fluid properties, enormous flexibility in the choices of fluid parameters, arbitrary selections of boundary layer properties that would be impossible in physical experiments, and the possibility of running true two-dimensional cases, something that cannot be fully replicated in a lab environment.

4.1 Numerical model configurations

In this section, all the cases that were modeled numerically for this thesis are presented, as well as the reasoning behind choosing these specific cases. The first step of the modeling process is to create the three-dimensional files called `.stl`-files of the geometries of each case that were to be inserted in OpenFOAM. These `.stl`-files were made in Python using a script with the `stl` library [Atkins 2015]. When the script had been run with the characteristic parameters for each case, the geometries were exported as three-dimensional objects that could be imported into OpenFOAM.

4.1.1 Modeling the experimental cases

The first cases that were interesting to model numerically were the same cases that had been tested experimentally during the specialization project, presented in Figure 3.3, both

to possibly validate the experimental results and to get more familiar with OpenFOAM through known cases. Case 4 was the only case not modeled during this phase as it would be modeled at a later stage. The script used for creating these geometries, as well as the base geometries of later cases can be found in Appendix F. After importing the `.stl`-files into OpenFOAM, each of the cylinders in the cases were defined and labeled so that the forces of each of them could be extracted. In Figure 4.1 the geometries for the models of the experimental cases are shown after being imported into OpenFOAM and meshed, which will later be described in Section 4.2.1.

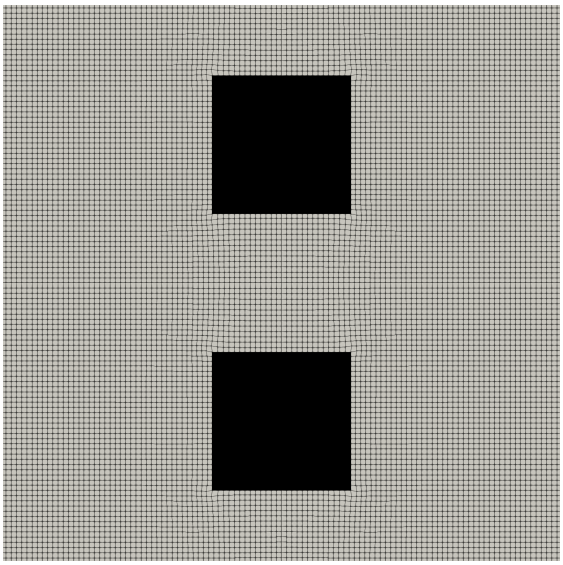

(a) The geometries of Case 1 with two square-shaped cylinders.

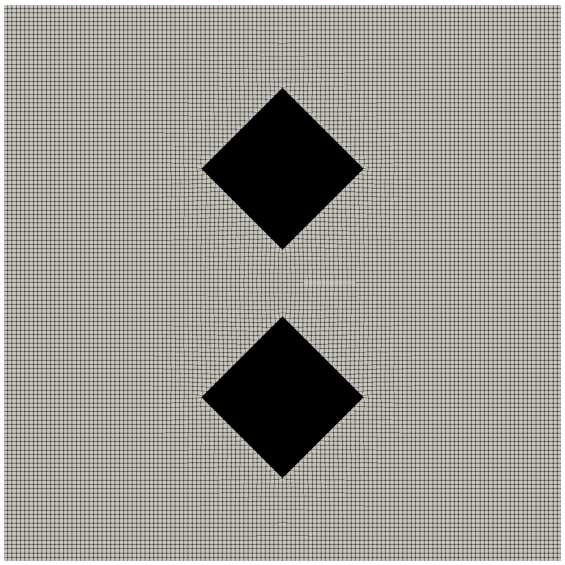

(b) The geometries of Case 11 with two diamond-shaped cylinders.

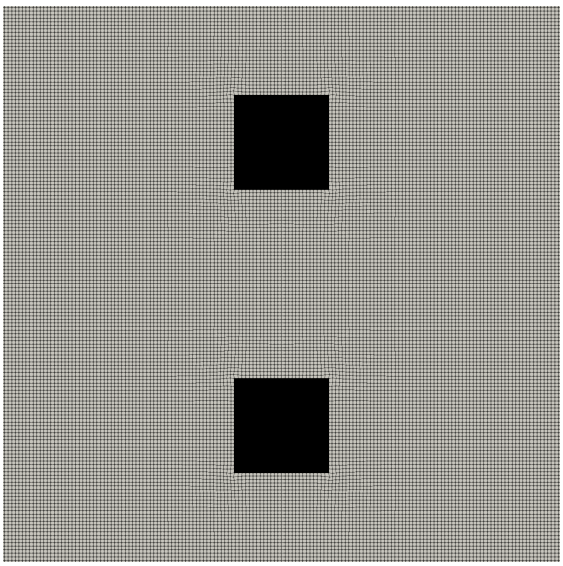

(c) The geometries of Case 2 with two square-shaped cylinders.

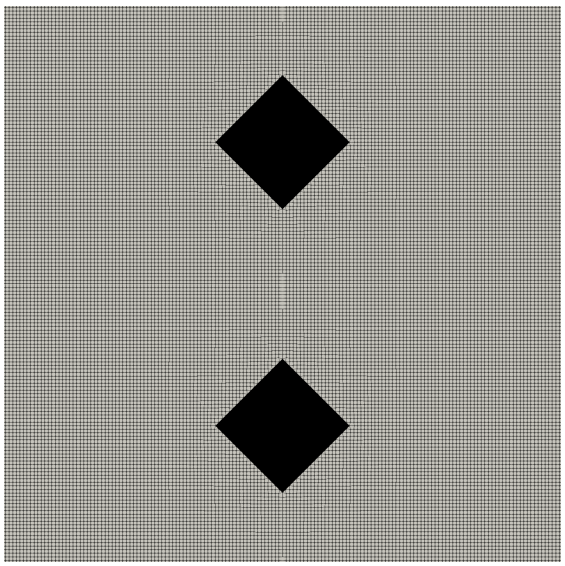

(d) The geometries of Case 12 with two diamond-shaped cylinders.

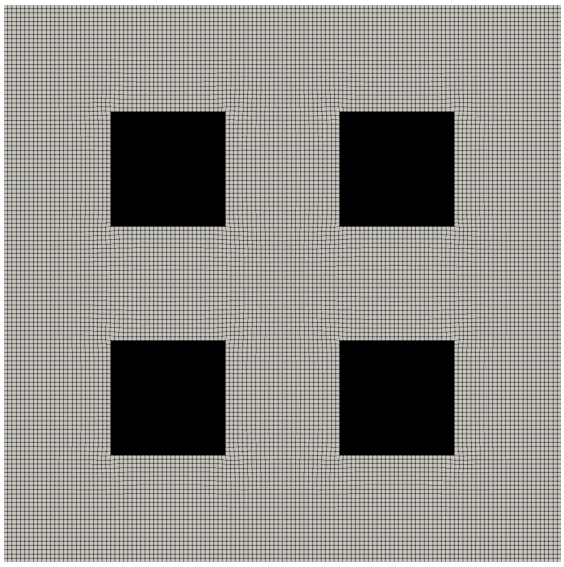

(e) The geometries of Case 3 with four square-shaped cylinders.

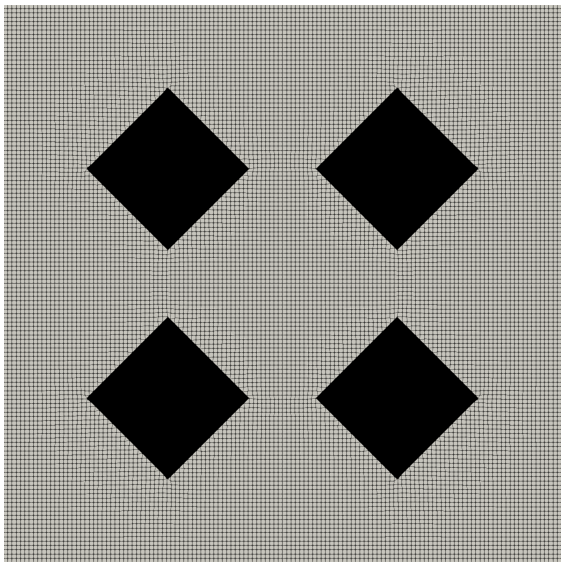

(f) The geometries of Case 13 with four diamond-shaped cylinders.

Figure 4.1: The geometries in the numerical models of the experimental cases described in Section 3.2 after being imported and meshed in OpenFOAM.

In the experiments these numerical models are based on, each case was run for a range of KC numbers from 1 to 21.5 with an increment of 0.5, where each run oscillated for 30 seconds. To be as consistent with the experiments as possible the numerical models were run for the same KC number range, but it was only deemed necessary that each run would oscillate for 20 seconds. Additionally, each experimental case was tested for two oscillation periods of 1 and 1.5 seconds, while the numerical models only use a period of 1 second. These differences from the experimental cases were measures taken to limit the needed computational time and power, while still maintaining the quality of the data.

4.1.2 Varying the inflow angle

After the experimental cases had been modeled numerically, it was interesting to look at the effect of changing the inflow angle. This had also been tested experimentally to a small degree in Case 4, which is the same as Case 1 with an inflow angle of $\theta = 45°$. At this point, it was decided to not pursue the diamond-shaped cylinders and focus only on the square-shaped ones. Also, Case 3 was not pursued further so that the focus could be on the differences between cases 1 and 2, as in the spacing between the cylinders. Thus, it was only deemed necessary to use cases 1 and 2 for the varying inflow angle study. The cases had been modeled such that the oscillation occurred in the z-direction, meaning that from the perspective of a neutral axis along the x-axis, cases 1 and 2 were in a 90-degree configuration. Importantly, the x-axis in the numerical models corresponds to the y-axis in the physical model, while the z-axis remains the same. The configuration in cases 1 and 2 is referred to as the tandem configuration by [Zdravkovich 1977]. He also uses the term staggered configuration for the case when two cylinders are side-by-side, which would mean a 0-degree configuration for these cases. Therefore it was decided to model cases 1 and 2 from a staggered configuration to a tandem configuration varying the inflow angle by 5 degrees for each case iteration. This resulted in 19 runs for each case. All cases were performed at KC = 16 with a duration of 20 seconds and an oscillation period of 1 second.

A selection of geometries for Case 1 is shown in Figure 4.2.

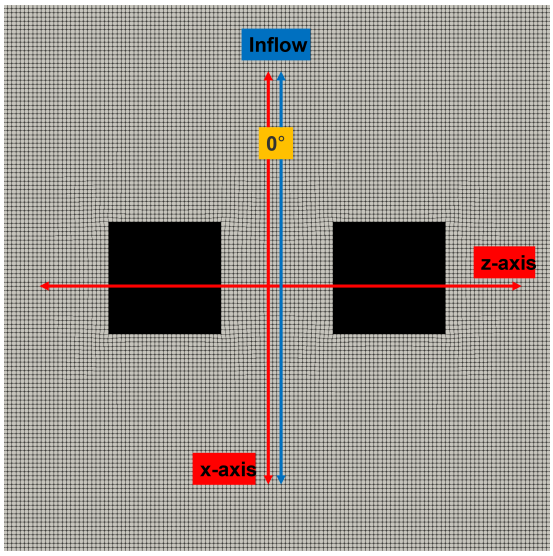

(a) Case 1 with an inflow angle of $\theta = 0°$.

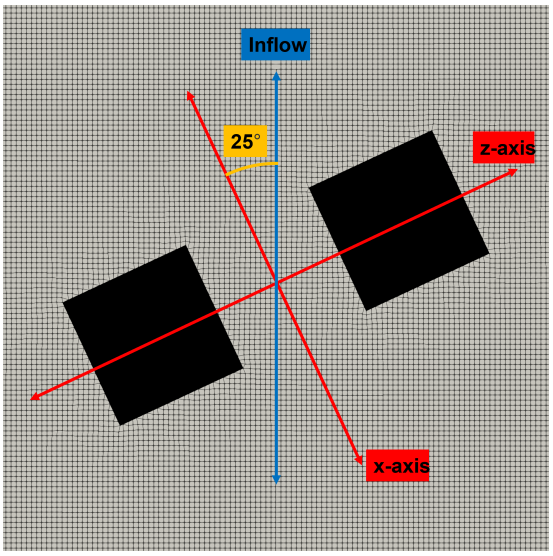

(b) Case 1 with an inflow angle of $\theta = 25°$.

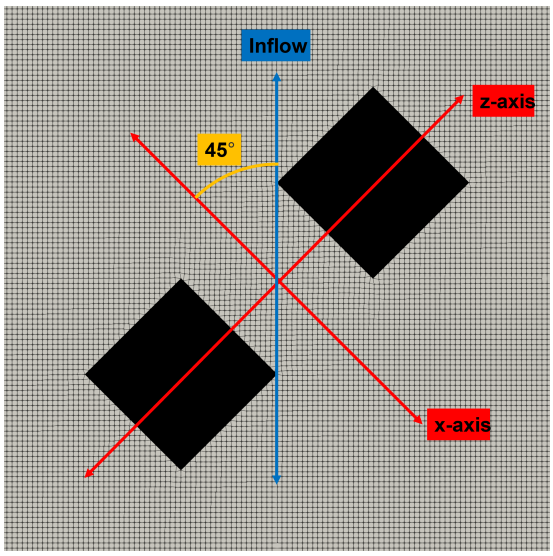

(c) Case 1 with an inflow angle of $\theta = 45°$, same as Case 4 from Figure 3.3.

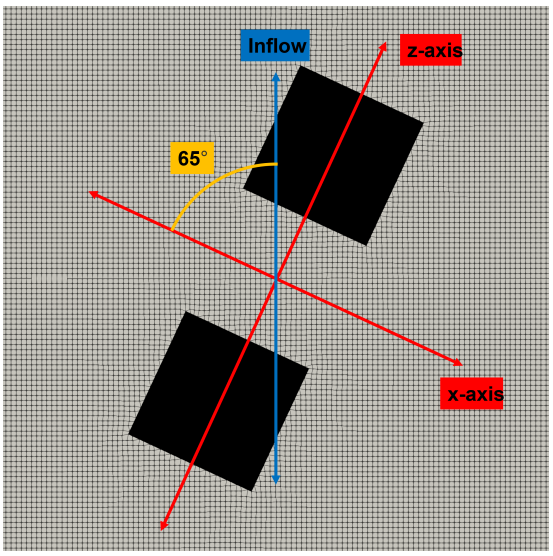

(d) Case 1 with an inflow angle of $\theta = 65°$.

Figure 4.2: The geometries in Case 1 with a varying inflow angle after being imported and meshed in OpenFOAM, with added lines indicating the inflow angle. The oscillation occurs along the inflow axis.

4.1.3 Horizontal misalignment of the cylinders

As described in Section 3.1 the cylinders in the experimental cases were attached to an inner and an outer actuator plate which were not fastened to each other so that the forces on each plate could be measured independently. This did however lead to some independent movement as well, especially in the y-direction of the tank. These movements could lead to the cylinders not being exactly in line with each other, which could cause

some unwanted noise that polluted the results. It was therefore a good idea to also model this numerically to see if the imperfection in alignment had an undesirable effect on the numerical results.

Three new cases were created from the base of Case 2 with an increasing horizontal misalignment. Only Case 2 was used for these new cases as it was deemed unnecessary to use both cases and that Case 2 could possibly have more fluctuations as the cylinders are further apart than in Case 1. Each of these three new cases was also exposed to a varying inflow angle in the same way as in Section 4.1.2 so that the data could be compared to that of Case 2 with zero imperfections. The horizontal misalignments of the cylinders were chosen to be 3, 5, and 10 percent of the width of one cylinder, meaning a relative misalignment of 1.5, 2.5, and 5 mm since the width of one cylinder is 5 cm. In the same way as the previous cases, these cases were also run for 20 seconds at KC = 16 with an oscillation period of 1 second.

A similar study has previously been performed by [Reiten 2022]. His study used Case 1 in its normal 90-degree configuration for an increasing range of KC numbers. He also used three cases with misalignments of 0, 2, and 5 cell sizes which in his case is closely equal to 0, 4, and 10 mm, but due to a stretching of the cells close to the geometries, it is hard to exactly determine the actual misalignment. The results of his study indicate that for the larger KC numbers the misalignments have some effect. To get a wider base understanding of the misalignment effect it was decided that for this thesis the study should be dependent on the inflow angle and not the KC number.

The geometries and meshing for these cases were done in the same way as for previously described cases, and below in Figure 4.3 the geometries for each of the misalignments are shown for an inflow angle of $\theta = 90°$.

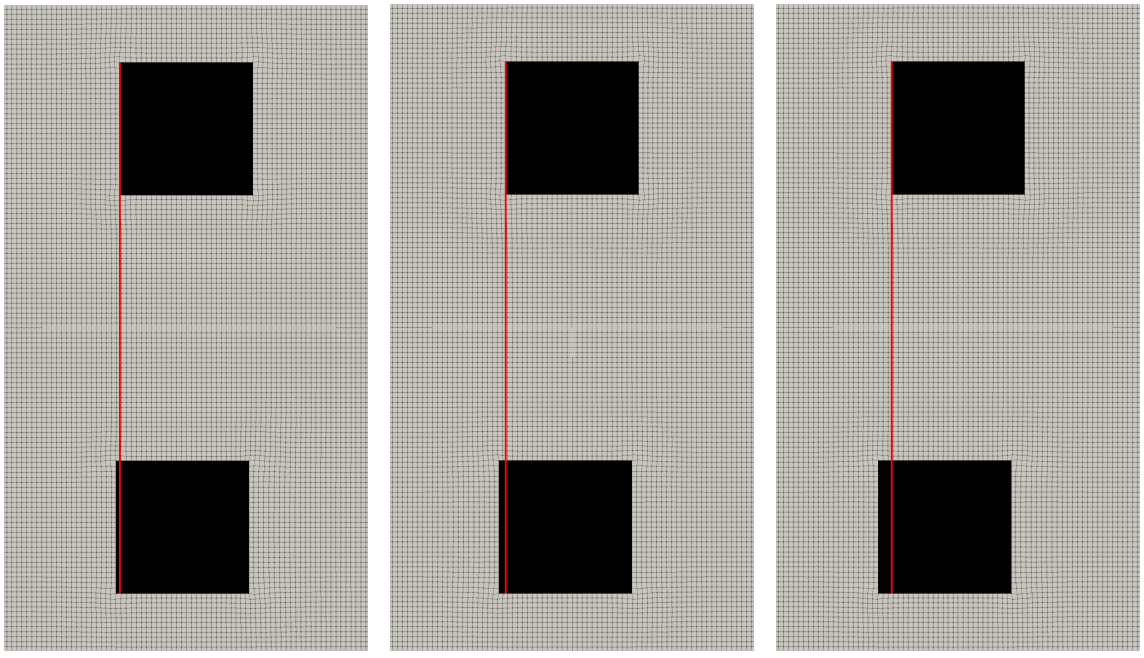

(a) Case 2 with a horizontal misalignment of 1.5 mm.

(b) Case 2 with a horizontal misalignment of 2.5 mm.

(c) Case 2 with a horizontal misalignment of 5 mm.

Figure 4.3: The geometries in Case 2 with an increasing horizontal misalignment after being imported and meshed in OpenFOAM. The red line is added to indicate the misalignment.

4.1.4 The effect of the spacing between the cylinders

Since cases 1 and 2 have been modeled and tested in many configurations it was compelling to perform a study into the main difference between the cases which is the spacing between the two cylinders. If the width of one cylinder is defined as $D = 5\,cm$, and the distance between the cylinders is denoted as s, the ratio s/D will equal the number of cylinders that could fit between the cylinders in the cases. This means that the s/D ratio for cases 1 and 2 equals exactly 1 and 2. A total of 17 cases were created with a s/D ratio ranging from 0.2 to 5. From 0.2 to 2.2 the spacing increased by 0.2 for each case, and after 2.2 the cases had ratios of 2.5, 3, 3.5, 4, 4.5, and 5.

The smaller ratio increases for the lower ratios were done to have a better data resolution since it is somewhere in these ranges that [Zdravkovich 1977] found the flow regimes of the cylinders to change. This also meant that another interesting part of this study in addition to the study of the non-linear hydrodynamic effects, was the study of the change in the coefficients of the cylinders which would indicate flow regime changes. These coefficients can be exported directly from OpenFOAM as explained in Section 4.2.2.

These cases were also run for 20 seconds each with an oscillation period of 1 second and with KC = 16. All numerical models except the experimental models have used this value for its KC number. This was intentionally done so that the data could easily be compared across cases if needed. This value was chosen because it is not so small that there is not much happening around the geometries, there will be fluctuations at this level of oscillation, and at the same time, it is not so large that the flow is at risk of entering a quasi-steady state.

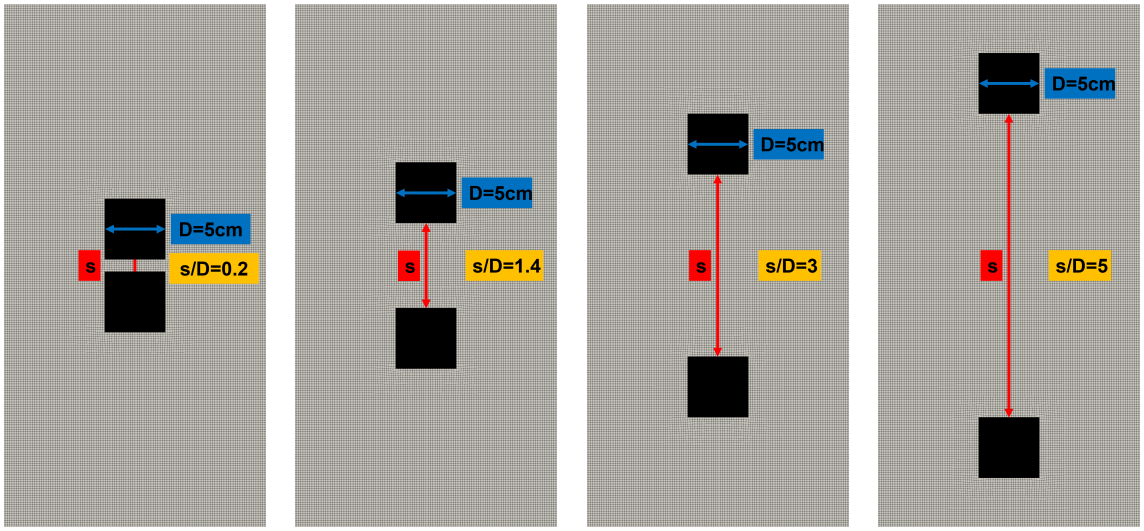

(a) Tandem cylinders with $s/D = 0.2$.

(b) Tandem cylinders with $s/D = 1.4$.

(c) Tandem cylinders with $s/D = 3$.

(d) Tandem cylinders with $s/D = 5$.

Figure 4.4: The geometries of two tandem cylinders with an increasing s/D ratio after being imported and meshed in OpenFOAM.

4.2 OpenFOAM

In this thesis, all numerical cases have been created, tested, and executed using OpenFOAM version 6 on a Ubuntu 18.04 system [Canonical 2018] with the solver `pvcFoam` developed by [Senthuran Ravinthrakumar 2023], which makes it possible to operate with an oscillating flow. The cases have mostly been tested using an 8-core laptop, and run in parallel on an 80-core computer nicknamed Schlichting after the German fluid dynamics engineer Hermann Schlichting.

4.2.1 Case creation and meshing

To successfully run a numerical model in OpenFOAM, the case domain and geometry must first be created and meshed. This is done using a series of commands in a step-by-step process that activates a multitude of dictionaries in a nested folder structure within the case. Firstly, the case domain is created using the command `blockMesh`, where the size of the domain and the boundary characteristics are determined by its corresponding dictionary. Secondly, the case geometry must be imported into the domain which is done by the command `surfaceFeatures`. The case geometry is created prior to the case creation where each geometry in the case is defined by a three-dimensional file. These files are created using a Python script that exports them directly into the case folder.

After defining the case domain and geometry, the case must be meshed. Traditionally, and as done in the specialization project before this thesis, it is done manually by utilizing the program `gmsh` [Geuzaine and Remacle 2009]. However, for these cases, the meshing is done automatically using the command `snappyHexMesh` which is a part of the `pvcFoam` solver, as well as other similar solvers. The dictionary used by this command subdivides the domain into regions in a stacked box configuration, where the mesh becomes finer as one gets closer to the case geometry with transitioning cells around each box as seen in Figure 4.5. This meshing technique allows the details of the flow around the geometry to be excellently captured, while the less interesting parts of the domain can be more coarsely meshed to save computational time. Even though the fluid flow details in the outermost boxes are not interesting for the cases, it is still vital to keep the domain at a certain size to minimize the data pollution from the boundaries.

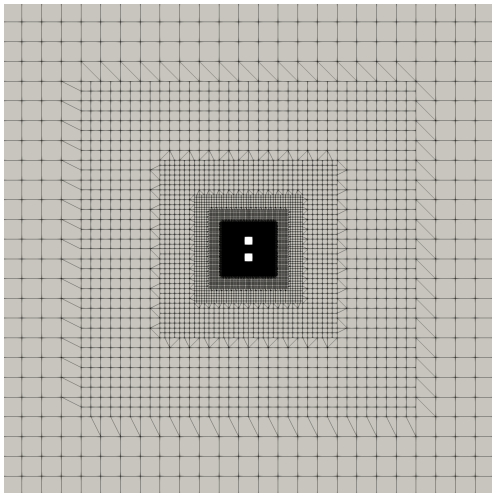

Figure 4.5: The meshing strategy on Case 1 on the full domain. The details around the geometries are visible in Figure 4.1a.

After the meshing is completed it is extruded into three dimensions by applying a depth to the domain. This will allow for the fluid to flow through the domain and is a necessary step even for two-dimensional cases. This new dimension will however not be meshed, and OpenFOAM will then treat it as two-dimensional. The extrusion is done by the command `extrudeMesh`, which is the final command in the case creation process. There are more commands used for saving the mesh and creating patches, but these will not be discussed in this thesis.

4.2.2 Running the cases

After the cases have been created and meshed, they are ready to run. This is done by initiating the OpenFOAM solver command, in this case, `pvcFoam`, which initiates the run. The solver is operated by the `controlDict` dictionary which specifies parameters such as duration, time step, and maximum allowed CFL number as presented in Section 2.10. Functions can also be established in the `controlDict` dictionary to calculate for instance the drag and lift coefficients on a body in the flow domain throughout the time-domain analysis. The solver also needs initial values for parameters such as velocity and pressure to initialize the simulation. This is done in the `0`-folder which represents the initial time step where the time is equal to zero. In the dictionary initializing the velocity, a constant velocity can be applied to the domain for cases that have a uniform flow, but since the cases in this thesis are exposed to a forced oscillatory flow, the velocity is initialized as zero in all directions. To achieve an oscillatory flow in the `pvcFoam` solver a dictionary called `movingCoordinateSystemProperties` is used. In this dictionary, the acceleration amplitude is defined which determines which KC number is applied to the case, as shown in Section 2.9. Additionally, the type of oscillation is defined, as well as its period, phase, and ramp-up segment. Examples of this dictionary and the `controlDict` dictionary can be found in Appendix B.

After a case is finished running the calculated values at each time step from the functions specified in the `controlDict` are stored in output files which can be extracted and used for post-processing. The parameters initialized in the `0`-folder can be viewed using a visualization program called ParaView [Kitware 2002]. Paraview is also useful for viewing and inspecting the mesh prior to the run, such as in Figure 4.5. In this thesis, all numerical post-processing has been done using Python scripts.

4.2.3 Previous numerical studies in OpenFOAM

During the specialization project in the fall of 2022 [Hals 2022], some numerical studies were modeled in OpenFOAM to achieve an understanding of the program and to get into the meshing techniques. The modeled cases were the same as the ones tested experimentally, and they were only modeled for 10-second runs in a uniform flow. The `pvcFoam` solver was not yet available, so the standard `icoFoam` solver was used. These models were not useful with regards to the results and in the validation of the experiments, but rather as a way of learning about the functionality of OpenFOAM in preparation for the work done in this thesis. In Figure 4.6 the velocity streamlines for cases 11 and 12 are shown. The results gathered from these models are not further presented as they are irrelevant to the purpose of the thesis.

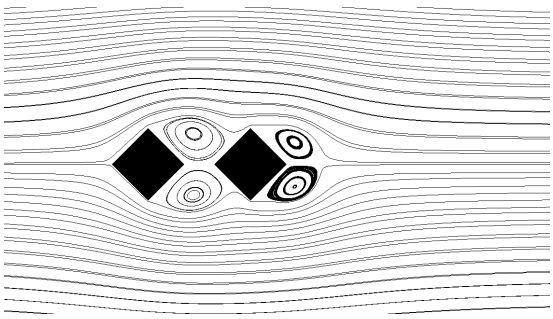

(a) The velocity streamlines surrounding the bodies in Case 11 in a uniform flow after 10 seconds.

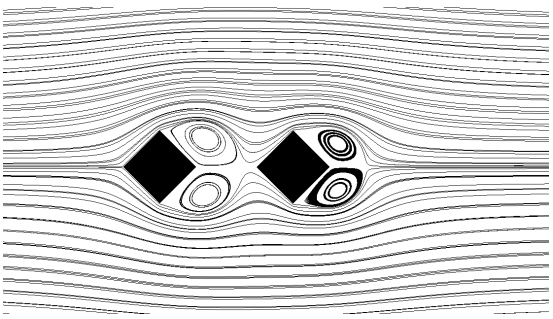

(b) The velocity streamlines surrounding the bodies in Case 12 in a uniform flow after 10 seconds.

Figure 4.6: The velocity streamlines in cases 11 & 12 in a uniform flow after 10 seconds.

4.2.4 Turbulence model in OpenFOAM

The turbulence model used in OpenFOAM for this thesis is the Reynolds Averaged Simulation (RAS) model with input parameters from the k-ε model. This turbulence model was used in the example that came with the `pvcFoam` solver, and it was therefore chosen for these numerical models as well. In [OpenCFD 2020] it is stated that a property of the k-ε model is that it uses a two transport-equation linear-eddy-viscosity turbulence closure model with a turbulent kinetic energy, k, and a turbulent kinetic energy dissipation rate, ε. The turbulent kinetic energy equation is defined as

$$\frac{\partial}{\partial t} + \nabla \cdot (\alpha\rho\mathbf{u}k) - \nabla^2(\alpha\rho D_k k) = \alpha\rho G - \left(\frac{2}{3}\alpha\rho\nabla\cdot\mathbf{u}k\right) - \left(\alpha\rho\frac{\varepsilon}{k}k\right) + S_k + S_{fvOptions}, \quad (4.1)$$

and the turbulent kinetic energy dissipation rate equation is defined as

$$\frac{\partial}{\partial t} + \nabla \cdot (\alpha\rho\mathbf{u}\varepsilon) - \nabla^2(\alpha\rho D_\varepsilon \varepsilon) = C_1\alpha\rho G\frac{\varepsilon}{k} - \left(\left(\frac{2}{3}C_1 - C_{3,RDT}\right)\alpha\rho\nabla\cdot\mathbf{u}\varepsilon\right)$$

$$- \left(C_2\alpha\rho\frac{\varepsilon}{k}\varepsilon\right) + S_\varepsilon + S_{fvOptions}. \quad (4.2)$$

An additional equation that is used in this model is the turbulent viscosity equation which is defined as

$$\nu_t = C_\mu\frac{k^2}{\varepsilon}. \quad (4.3)$$

The parameters of Equations 4.1, 4.2, and 4.3, their definitions, and their default values, if they exist, are shown in Table 4.1.

Table 4.1: The parameters from the turbulence equations, their descriptions, and their default values used in OpenFOAM if they are defined.

Parameter	Description	Default Value
$\alpha\,[-]$	Phase fraction of the given phase	-
$\rho\,[kgm^{-3}]$	Density of the fluid	-
$G\,[m^2s^{-3}]$	Turbulent kinetic energy production rate	-
$D_\varepsilon\,[-]$	Effective diffusivity for ε	-
$C_\mu\,[-]$	Model coefficient for the turbulent viscosity	0.09
$C_1\,[s]$	Model coefficient	1.44
$C_2\,[-]$	Model coefficient	1.92
$C_3\,[-]$	Compression term coefficient	-
$C_{3,RDT}\,[-]$	Rapid-distortion theory compression term coefficient	0.0
S_ε	Internal source term for ε	-
S_k	Internal source term for k	-
$S_{fvOptions}$	Source terms introduced by the `fvOptions` dictionary for k & ε	-
$\sigma_k\,[-]$	Data fitting model constant for k	1.0
$\sigma_\varepsilon\,[-]$	Data fitting model constant for ε	1.3

The downside of using this turbulence model for the numerical models in this thesis is that OpenFOAM uses the default values. These values are mainly valid for a uniform flow, while the values for an oscillating flow are unknown. The effect this has on the models is uncertain and could lead to discrepancies with experimental results. Another possible model that could have been used is the Large Eddy Simulation (LES) model, but it is however optimized in OpenFOAM for three-dimensional cases and is not appropriate for reduced-dimension cases [OpenCFD 2016]. Despite the uncertainties, the RAS turbulence model with the k-ε model parameters is still one of the best options that can be used without extensive research and data fitting for these specific cases, and it is quite safe to assume that the results will still be valid, even if they are somewhat tainted by numerical uncertainties.

Chapter 5

Results and discussions

In this chapter, the results that have been obtained from the experimental and numerical tests will be presented and discussed. The results are presented in chronological order after when they were gathered. The preliminary experimental results were obtained during the specialization project, and parts of this chapter are gathered directly from the project report. Some newer results developed by master student Kristian Mikkelsen [Mikkelsen 2023] will be used as a comparison with similar numerical results in Section 5.3, as his experiments were done more efficiently and with a larger focus on removing error sources such as the noise pollution from the lab-environment into the frequencies of the cases. The preliminary results will be directly compared to the numerical results in Section 5.2.1. The numerical results are all from this thesis and will be presented as stand-alone results, while some will be compared with experimental results. A sensitivity analysis has also been performed and will be presented in this chapter, along with some summarizing comments on the thesis results.

It is important to note that in this chapter, the in-line force that is present in the same direction as the oscillation motion, the z-direction in both the experiments and CFD, is referred to as the drag force even though it consists of both a pressure force and a viscous force. This has been done because the only cross-flow force that is present, which is in the y-direction for the experiments and the x-direction for the CFD, is the lift force. This works out as an easier comparison and a way of avoiding misconceptions when comparing the in-line and cross-flow forces.

5.1 Experimental results of 3D cylinders

This section contains the preliminary results gathered from the experimental tests runs during the specialization project, and parts of the section are gathered directly from the project report. All figures in this section are created using a Matlab script that was developed in collaboration with master student Kristian Mikkelsen. Additional experimental tests were as mentioned performed by him, but the results from his tests will not be introduced in this section.

The preliminary results are from the cases discussed in Section 3.2, and are focusing on three KC numbers from each test. These three numbers were chosen to be 8, 16, and 21.5 to give a large spread of results, while also avoiding using the lowest KC numbers for which

the results were somewhat indistinct due to the small oscillations. The selected oscillation period of the presented tests was chosen to be $T = 1$ second rather than $T = 1.5$ seconds, as the smaller period allowed for a greater force output which increases the readability of the data and because all numerical tests and later experimental tests only used a one-second oscillation.

Unfortunately, during the experimental tests for the medium and large cylinders in Case 2, an unknown source corrupted the data making it unreadable in the case of the large cylinders, and implausible for the medium cylinders. Since the data for the small cylinders survived, there can be some focus on the spacing between the cylinders in this section, but the main significance of the experimental tests will be the differences between the square and diamond-shaped cylinders.

5.1.1 Case 1, square cylinders

This section contains some of the results from Case 1 with a focus on the tests which utilized the length-to-diameter ratio $^L/_D = 1$ since the smallest cylinders had the largest disparity between the two cylinders making the readability of the figures increase. The end effects, which are phenomena that occur in these three-dimensional tests since the fluid flow can also flow around the ends of the cylinders, could also be more prominent for this cylinder length. The rest of the sections focusing on the preliminary results also use the same ratio for comparison's sake. The remaining figures for Case 1 are presented in Appendix C.1 and C.2.

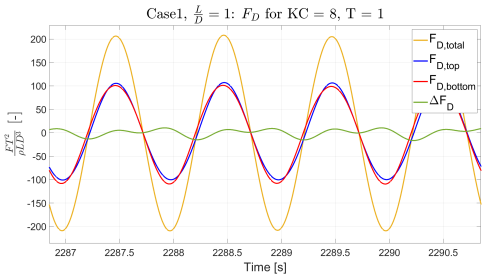

(a) The forces acting on the system for KC = 8 for cylinders with $^L/_D = 1$ in Case 1.

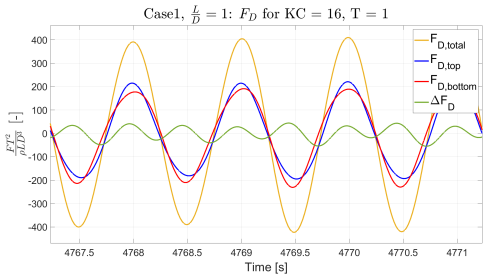

(b) The forces acting on the system for KC = 16 for cylinders with $^L/_D = 1$ in Case 1.

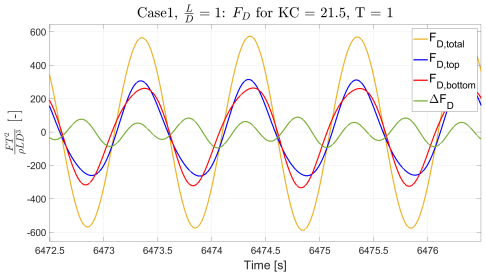

(c) The forces acting on the system for KC = 21.5 for $^L/_D = 1$ in Case 1.

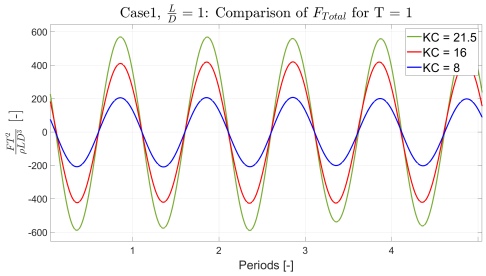

(d) A comparison of the total force for KC = 8, 16, and 21.5 for cylinders with $^L/_D = 1$ in Case 1.

Figure 5.1: The forces acting on the system with $^L/_D = 1$ in Case 1, as well as a comparison of the total forces.

Figure 5.1 makes it clear that for the whole range of KC numbers, one cylinder experiences a larger force at the peaks, and that which cylinder experiences more force switches

between the top and bottom cylinder based on if the rig is moving in a positive or negative z-direction. This is also evident from the ΔF_D curve having half the oscillation period of the other curves. Moreover, the ΔF_D curve seems to become more intense as the KC number increases. This implies that the interaction between the cylinders increases with an increasing KC number. Also, from Figure 5.1d it is evident that the force amplitudes increase with an increasing KC number, and it seems as if the increase is almost linear since a doubling of the KC number from 8 to 16 doubles the total force amplitude. However, the increase in the total force amplitude from KC = 16 to KC = 21.5 is around 45 % while a linear increase would be 34.4 %, meaning that at least for higher KC numbers the total force amplitudes will not increase linearly.

Another observation is that for a higher KC numbers the downstream cylinder i.e., the bottom cylinder when the rig is moving up and vice versa, will have a broader force curve than the upstream cylinder. The reason for this may be a greater influence from higher-order frequencies due to a more prominent wake interaction between the cylinders, and also possibly due to the end effects. To further analyze this, the force curves will undergo a Fourier transformation to identify the frequencies and frequency amplitudes of the signal. This has been done for all KC numbers in all cases, but only the analysis for KC = 21.5 for Case 1 with $^L/_D = 1$ will be shown and discussed due to the process being similar for all cases. The force curve for the top cylinder for KC = 21.5 and its Fourier transformation are shown in Figure 5.2.

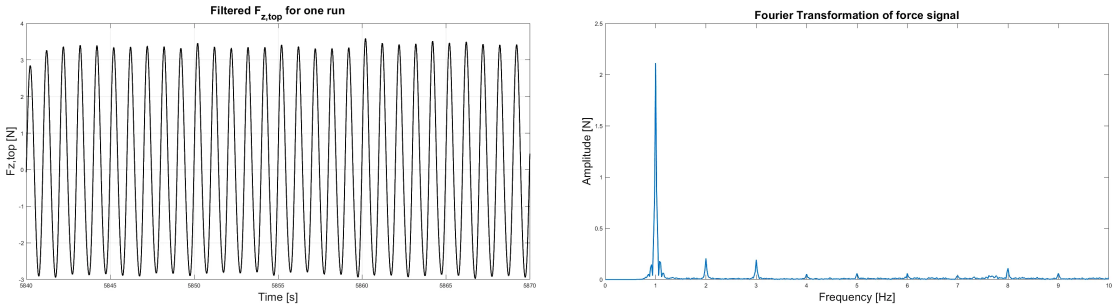

(a) The filtered force curve for the top cylinder in the z-direction for one entire steady state run.

(b) The Fourier transformation of the force time-series in Figure 5.2a

Figure 5.2: The force curve and Fourier transformation for the top cylinder for Case 1 with $^L/_D = 1$ at KC = 21.5.

After the Fourier analysis is completed, the frequencies and frequency amplitudes are stored for further use. A study comparing the effect of the frequency amplitudes of all KC numbers for the first four frequencies, 1ω, 2ω, 3ω, and 4ω, and the mean force difference, $\overline{\Delta F_D}$, has been done for all cases. The study has only been done for $F_{D,top}$ and ΔF_D to be compared with the observations from Figure 5.1. The study was deemed unnecessary for $F_{D,bottom}$ as it was too similar to the study for $F_{D,top}$, and for $F_{D,Total}$ due to it not showing signs of higher-order contributions due to cancellations between the cylinder forces when they are added together. In Figure 5.3 the study for $^L/_D = 1$ for Case 1 is shown for $F_{D,top}$ and for ΔF_D. The frequency amplitude has been non-dimensionalized to increase the comparability of the study.

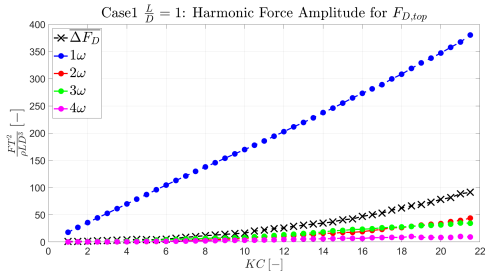

(a) The harmonic force amplitudes for $F_{D,top}$ and the mean force difference for Case 1 with $\frac{L}{D} = 1$.

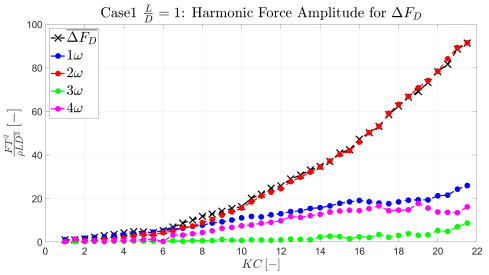

(b) The harmonic force amplitudes for ΔF_D and the mean force difference for Case 1 with $\frac{L}{D} = 1$.

Figure 5.3: The harmonic force amplitudes for $F_{D,top}$ and ΔF_D and the mean force difference for Case 1 with $\frac{L}{D} = 1$.

Figure 5.3a shows that for the top cylinder it is the 1ω force amplitude that dominates the drag force. It is as good as linear for all KC numbers, and the other frequencies contribute almost nothing until about KC = 10. Even after that, the higher-order frequencies only account for roughly 10 % of the 1ω force contribution each. Of the other frequencies, 2ω and 3ω develop the most for higher KC numbers. $\overline{\Delta F_D}$ becomes larger for an increasing KC number and has about twice the contribution as 2ω. The linearity of the 1ω force component can be traced back to Figure 5.1, where the shapes of the curves closely resemble sinusoidal waves, which themselves are linear. This means that for the forces on each cylinder, the higher-order frequencies have little effect, and the forces are almost linear.

The results from Figure 5.3b show a very different aspect of the force contributions when looking at the force difference between the top and bottom cylinder. Here, it is the 2ω force amplitude that dominates after approximately KC = 8 and develops almost exponentially following $\overline{\Delta F_D}$. This shows that the mean force difference is almost entirely made up of the 2ω force amplitude. There is not much happening with the force contributions for the lower KC values, which might be due to the same reasons why [Sarpkaya 2010] found it difficult to extract the drag coefficient at these KC numbers, and also due to that fact that the lower range of KC numbers has a lower actuator velocity meaning that the force amplitudes are in general smaller. In addition to this, the 4ω force amplitude develops almost identically to the 1ω force amplitude, with the exception of the highest KC numbers. This shows that both the 2ω and 4ω force amplitudes have very large contributions to the force difference when comparing them to the 1ω and 3ω force amplitudes, which is due to the cancellation of the amplitudes from subtracting the force of the bottom cylinder from the top cylinder.

An interesting observation is that the drag force term from Morison's equation in Equation 2.50 only predicts the 1ω and 3ω force amplitudes, and all other odd-numbered frequency components, from its Fourier series, meaning that large parts of the harmonic force amplitudes are not predicted by Morison's equation alone both when dealing with a single cylinder and when studying the force difference of two cylinders. [Sævik 2015] shows the Fourier series of the drag term in Morison's equation as

$$F(t) = F_0 \left[\frac{8}{3\pi} \sin \omega t - \frac{8}{15\pi} \sin 3\omega t - \frac{8}{105\pi} \sin 5\omega t + ... \right], \tag{5.1}$$

where it can be noted that the linear term is the same term used in the linearization of the

drag term in Equation 2.67. He then explains that the even frequency components will be present in the case of current in combination with waves, but for cases such as the ones in this thesis, a current is not relevant and a better load model than Morison's equation should be developed and utilized.

The results presented in this section are fairly similar to the ones presented by [Reiten 2022], at least with regard to the 2ω domination for ΔF_D and the development of $\overline{\Delta F_D}$. The main difference from his results is a much larger contribution from 1ω for ΔF_D, which in his case was almost zero for all KC numbers, but is significantly higher in Figure 5.3b. He also argues that the minimal contribution from 1ω comes from the cancellation effects in the calculation of ΔF_D, but these effects may not be as prevalent here due to inaccuracies in the synchronization and phase-shifting, or due to three-dimensional effects that were not included in his two-dimensional experimental investigations.

5.1.2 Case 2, square cylinders

This section presents the preliminary results for Case 2 with $\frac{L}{D} = 1$, and as previously mentioned, the tests for Case 2 were not entirely successful, and the data for $\frac{L}{D} = 2$ and $\frac{L}{D} = 3$ are unusable. Therefore, there are no figures for Case 2 in the appendix, everything is presented here in Figures 5.4 and 5.5. Also, the results for Case 2 that are presented here are most likely incorrect, and should only be seen in comparison with other cases, such as from [Mikkelsen 2023].

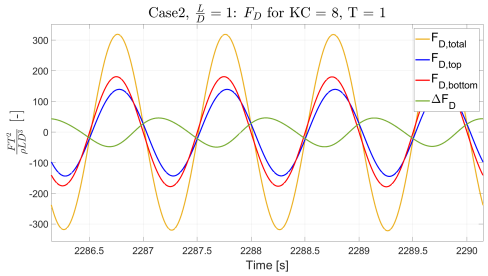

(a) The forces acting on the system for KC = 8 for cylinders with $L/D = 1$ in Case 2.

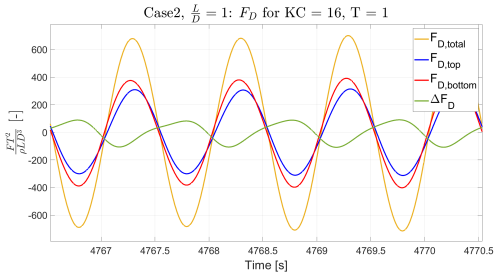

(b) The forces acting on the system for KC = 16 for cylinders with $L/D = 1$ in Case 2.

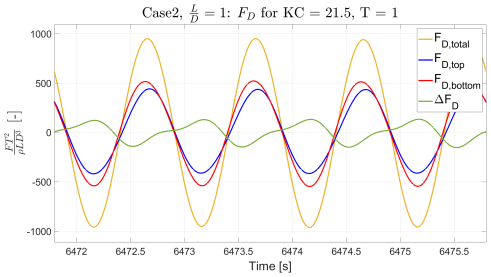

(c) The forces acting on the system for KC = 21.5 for cylinders with $L/D = 1$ in Case 2.

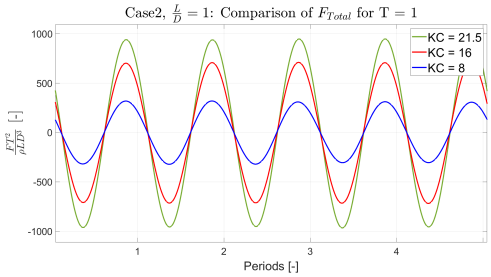

(d) A comparison of the total force for KC = 8, 16, and 21.5 for $L/D = 1$ in Case 2.

Figure 5.4: The forces acting on the system with $L/D = 1$ in Case 2, as well as a comparison of the total forces.

The first element to note is that for all three KC numbers Case 2 experiences much larger drag forces than Case 1 with a factor of roughly 60 %. The only change between the test setups is the spacing between the top and bottom cylinder, and it must thus be the spacing that induces the increase. This is explained by the theories of [Zdravkovich 1977]

in that for this spacing the two cylinders are in different flow regimes and the wakes of the upstream cylinder directly hits the downstream cylinder increasing the forces on it, while for the spacing in Case 1, they are in the same flow regime and the downstream cylinder is much less affected.

Another element worth noting is that the bottom cylinder consistently experiences a larger force amplitude than the top cylinder. This is not a real hydrodynamic phenomenon as it doesn't occur for any other case or cylinder size, but rather a large source of error caused by disturbances in the lab environment. It is possible that the same error source that corrupted the larger cylinders also affected the smallest cylinders but to a lesser extent. The results presented in this section should therefore not be fully trusted.

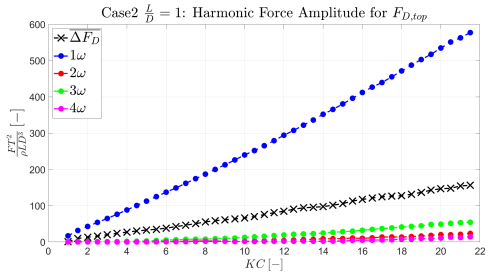

(a) The harmonic force amplitudes for $F_{D,top}$ and the mean force difference for Case 2 with $\frac{L}{D} = 1$.

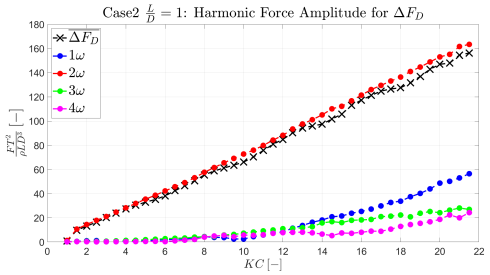

(b) The harmonic force amplitudes for ΔF_D and the mean force difference for Case 2 with $\frac{L}{D} = 1$.

Figure 5.5: The harmonic force amplitudes for $F_{D,top}$ and ΔF_D and the mean force difference for Case 2 with $\frac{L}{D} = 1$.

Figure 5.5 shows many of the same results for Case 2 as Case 1, that the 1ω force amplitude increases linearly with the KC number and dominates the drag force for the top cylinder, and that the 2ω force amplitude follows the mean force difference closely and dominates the experienced force difference between the cylinders. One of the results that are different in Case 2 than in Case 1 is that the 2ω force amplitude and mean force difference are close to linear, and not exponential. Again, this can be due to the change in spacing between the cylinders. For later analyses, the linearity in the 2ω force amplitude disappears, either meaning that the connection of the spacing and cylinder shape in Case 2 creates the linearity, or that it is another byproduct of the error source. Either way, the amplitudes increase by between 50 % and 70 % from Case 1 to Case 2 which corresponds well with the general force increase of about 60 %.

5.1.3 Case 3, square cylinders

In this section, the results from Case 3 with $\frac{L}{D} = 1$ are presented and discussed. The results for the rest of the Case 3 tests are presented in Appendix C.1 and C.2.

As expected, in Figure 5.6 the force magnitudes are quite close to the force magnitudes in Figure 5.1 for Case 1, since it is in many ways the same case, but with twice as many cylinders. To get an estimate of the forces for the top and bottom cylinders when there are four cylinders, the measured forces of the inner and outer actuator plates were divided by two, and the mass forces were multiplied by two.

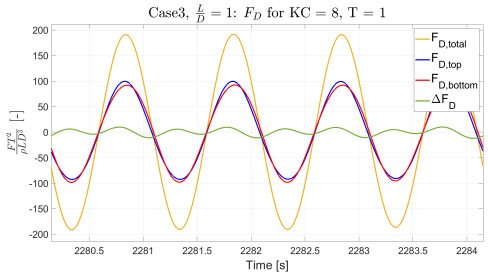

(a) The forces acting on the system for KC = 8 for cylinders with $^L/_D = 1$ in Case 3.

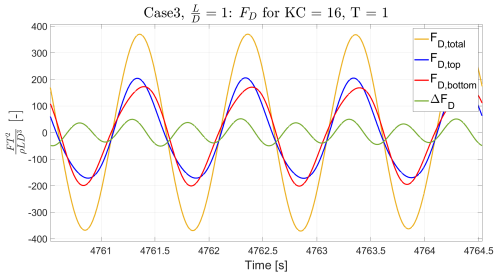

(b) The forces acting on the system for KC = 16 for cylinders with $^L/_D = 1$ in Case 3.

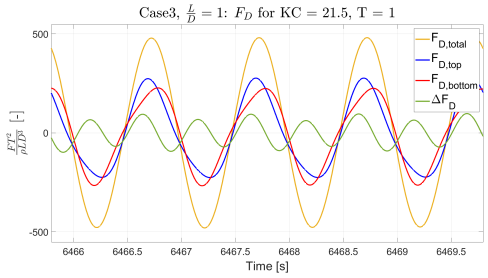

(c) The forces acting on the system for KC = 21.5 for cylinders with $^L/_D = 1$ in Case 3.

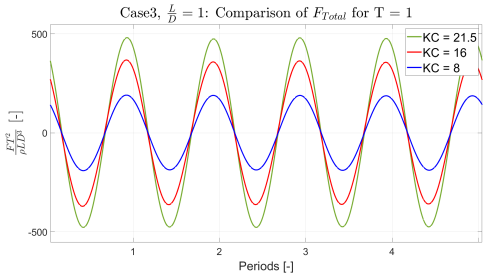

(d) A comparison of the total force for KC = 8, 16, and 21.5 for $^L/_D = 1$ in Case 3.

Figure 5.6: The forces acting on the system with $^L/_D = 1$ in Case 3, as well as a comparison of the total forces.

The resulting force magnitudes are lower than for Case 1, which intuitively may seem odd since the flow is more complex as it is forced to move faster past the insides of the cylinders than on the outsides, but this will create a pressure gradient on the cylinders and disperse some of the forces in the y-direction of the tank. Additionally, some of the fluid that is forced past the insides will be pushed out between the top and bottom cylinders. In total this means that the experienced drag forces on the top and bottom row of cylinders are lower for each cylinder than if they were in the Case 1 configuration.

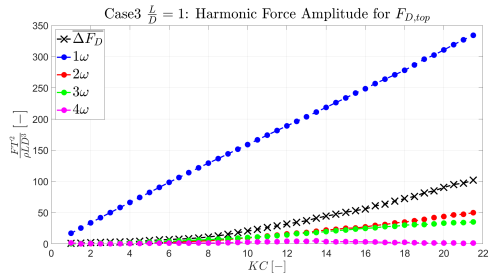

(a) The harmonic force amplitudes for $F_{D,top}$ and the mean force difference for Case 3 with $\frac{L}{D} = 1$.

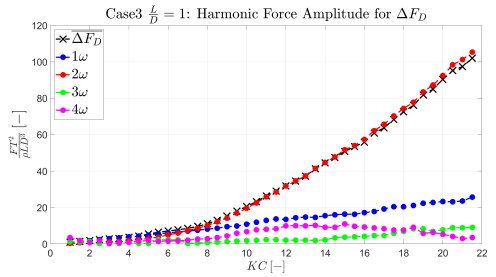

(b) The harmonic force amplitudes for ΔF_D and the mean force difference for Case 3 with $\frac{L}{D} = 1$.

Figure 5.7: The harmonic force amplitudes for $F_{D,top}$ and ΔF_D and the mean force difference for Case 3 with $\frac{L}{D} = 1$.

The findings from Figure 5.6 continue through to Figure 5.7a where the magnitude of the harmonic force amplitudes are a bit lower than for Case 1, but the same linearity and dominance of the 1ω force amplitude is present. Counterintuitively though, the findings do not translate well to Figure 5.7b where the 2ω force amplitude is about 13 % larger than for Case 1. This is probably because of the complexity of the flow due to the increase in the

number of cylinders making the forces more influenced by higher-order force amplitudes.

As a final remark on this case, finding the forces on the cylinders by dividing the total forces from the actuator plates in two may not be without uncertainties. Some false data can be procured from this method if the test setup is not fully symmetrical, which can happen for physical experiments, and since the setup is not actually in infinite fluid the effects of both the free surface and walls may affect the system by causing the fluid to not affect each of the top and bottom cylinders equally. But, since there was no other way of testing four cylinders in the lab, this method provides the most accurate representation of the forces.

5.1.4 Case 4, square cylinders

This section focuses on the preliminary results of Case 4, which is the same as Case 1 with an inflow angle of $\theta = 45°$, with $\frac{L}{D} = 1$. Additional figures for Case 4 with $\frac{L}{D} = 2$ and $\frac{L}{D} = 3$ can be found in Appendix C.1 and C.2.

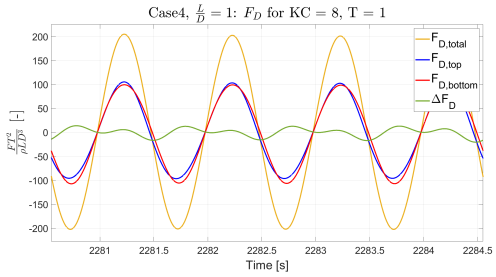

(a) The forces acting on the system for KC = 8 for cylinders with $^L/_D = 1$ in Case 4.

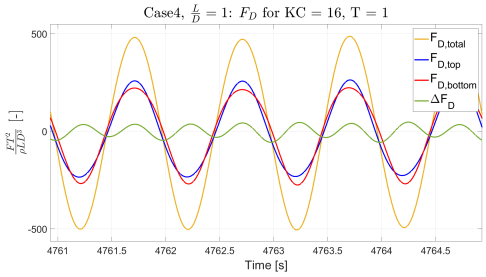

(b) The forces acting on the system for KC = 16 for cylinders with $^L/_D = 1$ in Case 4.

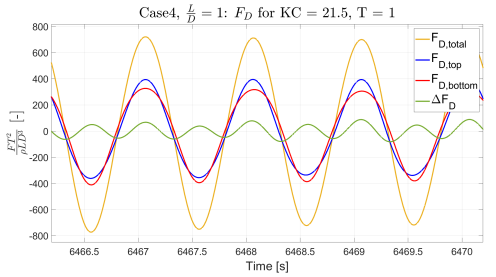

(c) The forces acting on the system for KC = 21.5 for cylinders with $^L/_D = 1$ in Case 4.

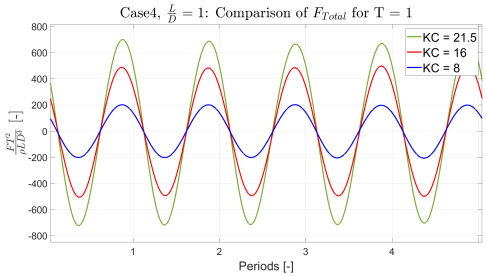

(d) A comparison of the total force for KC = 8, 16, and 21.5 for $^L/_D = 1$ in Case 4.

Figure 5.8: The forces acting on the system with $^L/_D = 1$ in Case 4, as well as a comparison of the total forces.

The forces from Case 4 are shown in Figure 5.8. An interesting remark when comparing these results with Figure 5.1 is that the figure for KC = 8 is almost identical for the two cases with the same force amplitudes and the same behavior of the ΔF_D curve. This trend does however not continue on to the higher KC numbers as Case 4 experiences an increase of about 25 % for KC = 16 and KC = 21.5. The reason for this property change is most likely that for KC = 8 the flow is calm enough that cylinders still remain in basically the same flow regime, while for the higher KC numbers the wake from the upstream cylinder will be intense enough to affect the downstream cylinder, even though they remain in the same regime.

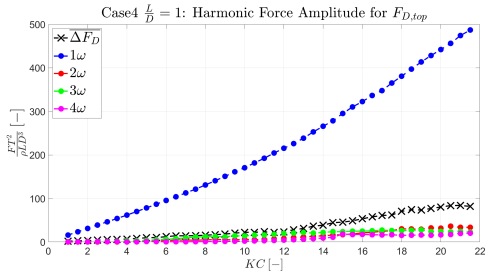

(a) The harmonic force amplitudes for $F_{D,top}$ and the mean force difference for Case 4 with $\frac{L}{D} = 1$.

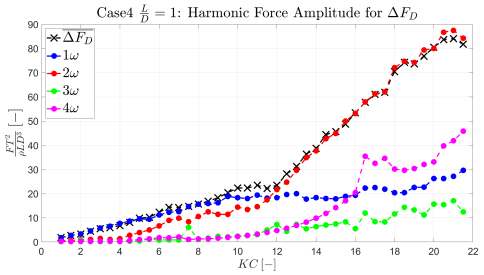

(b) The harmonic force amplitudes for ΔF_D and the mean force difference for Case 4 with $\frac{L}{D} = 1$.

Figure 5.9: The harmonic force amplitudes for $F_{D,top}$ and ΔF_D and the mean force difference for Case 4 with $\frac{L}{D} = 1$.

Figure 5.9a has many of the same properties as the harmonic force amplitudes for $F_{D,top}$ for Case 1, but the 1ω force amplitude is much less linear in this case as it grows linearly up until about KC = 10, and grows much faster after that. This confirms the difference in force amplitudes seen in Figure 5.8 as the values for 1ω are the same for the low KC numbers and different for the higher ones. If it had grown linearly with the same rate as before KC = 10, it would be very close to the 1ω force amplitude from Case 1.

The behavior of the harmonic force amplitudes for the force difference is however very different in Case 4 than in Case 1. It is much more dominated by the 1ω amplitude for the lower KC numbers, and the 2ω amplitude is a lot more chaotic for the higher values in this case. It does still follow the mean force difference, but only after about KC = 12. Additionally, the 4ω amplitude is a lot more prominent than in Case 1, and even the 3ω amplitude behaves differently.

All of the differences between Case 4 and Case 1 are consequences of the inflow angle as it is the only factor that has been altered. This causes the flow to be much more turbulent and chaotic which causes the experienced forces to be much more influenced by higher-order frequencies. To get the full picture of how the force amplitudes are affected by the inflow angle a much wider study with many more inflow angles should be carried out. This was done during the spring of 2023 by master student Kristian Mikkelsen, but by varying the inflow angle of Case 2 instead of Case 1 since the spacing in Case 1 made the rotated tests difficult to execute in practice. His findings will not be discussed here but rather used as a comparison later on. The comparison, as well as the effects found in this section, will be discussed numerically in Section 5.2.2.

5.1.5 Cases 11, 12, and 13, diamond cylinders

As previously stated, cases 11, 12, and 13 are direct copies of cases 1, 2, and 3, but with diamond-shaped cylinders instead of square-shaped cylinders, and all the diamond cases will therefore be presented together in this section. Since the effects of changing the spacing and number of cylinders already have been discussed for cases 1, 2, and 3, the main focus of this chapter will be how the diamond cylinder shape affects the cases, and how the results behave compared to the results from the square cases. To avoid any repetitiveness in the discussions only the cases using $\frac{L}{D} = 1$ at KC = 16 will be discussed in this section. The remaining figures for cases 11, 12, and 13 can be found in Appendix C.1 and C.2.

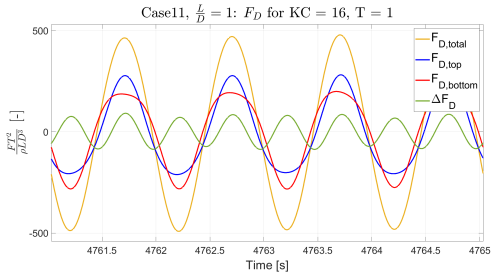

(a) The forces acting on the system for KC = 16 for cylinders with $^L/_D = 1$ in Case 11.

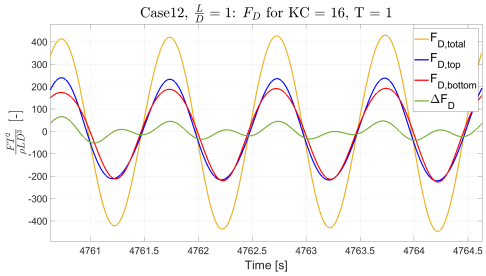

(b) The forces acting on the system for KC = 16 for cylinders with $^L/_D = 1$ in Case 12.

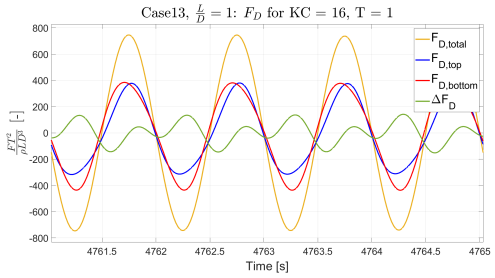

(c) The forces acting on the system for KC = 16 for cylinders with $^L/_D = 1$ in Case 13.

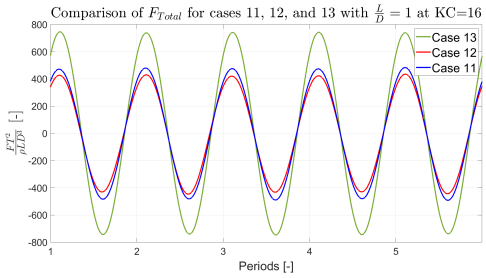

(d) A comparison of the total force for KC = 16 for $^L/_D = 1$ in cases 11, 12, and 13.

Figure 5.10: The forces acting on the system in cases 11, 12, and 13 with $^L/_D = 1$ and KC = 16, as well as a comparison of the total forces.

In Figure 5.10 the forces in cases 11, 12, and 13 for $\frac{L}{D} = 1$ at KC = 16, as well as a comparison plot of the total force of the cases, are shown. The first thing to note is that the total forces in Figure 5.10d seem to behave quite differently than for the square cases. Here, Case 12 which has the largest spacing between the cylinders has the lowest total force, while the opposite is true for Case 2, and Case 13, which has four cylinders has the largest total force, while Case 3 had the lowest. Case 11 and Case 1 seem to correspond well with each other, with Case 11 having around 13 % higher total force. These behavioral differences can be caused by two factors; the cylinder shape or false data caused by noise pollution in the lab environment. The latter factor is the less likely one, but should still be considered when viewing the results.

When comparing the force curves for cases 1 and 11 in Figures 5.1b and 5.10a it can be seen that the ΔF_D curve has a much larger amplitude relative to $F_{D,top}$ for Case 11 than for Case 1, indicating that there may be more prominent effects from the higher-order harmonic force amplitudes for the diamond shaped cylinders. This is also apparent from the widening of the force curves of the downstream cylinder, which means that they are further from a linear sinusoidal wave function than in Case 1.

The comparison of cases 2 and 12 is difficult as much of the data from Case 2 is unusable, but for $\frac{L}{D} = 1$ at KC = 16 in Figures 5.4b and 5.10b it is clear that Case 12 experiences lower force amplitudes than Case 2 resulting in a much lower total force. Also, Case 12 has a more regular hydrodynamic relation between the cylinders where it is the upstream cylinder that experiences the highest forces, instead of the false hydrodynamic phenomena in Case 2 where the bottom cylinder always experienced the highest force amplitudes regardless of whether it was upstream or downstream. Unfortunately, this further implies that all of Case 2 may be corrupted, not just for $\frac{L}{D} = 2$ and $\frac{L}{D} = 3$, and that further analyses into the effects of spacing on the hydrodynamic relation between the cylinders should be conducted, which for this thesis have been done numerically as later presented

in Section 5.2.4.

The difference in the force amplitude behavior from Case 3 to Case 13 is very interesting to study. Firstly, the magnitudes of the forces are much higher in Case 13 than in Case 3, even though both cases are practically the same except for the cylinder shape. A probable reason for this is that the diamond-shaped cylinders allow for more of the flow to be forced past both the insides and outsides of the cylinders than the square-shaped ones meaning that less of the flow passes over the ends of the cylinders and more fluid can directly interact with the sides of the cylinders causing a larger experienced drag force. Secondly, while Case 3 had a pretty uniform ΔF_D curve, the curve for Case 13 is much more harmonically affected by the higher-order frequency amplitudes. This can also induce larger drag forces since the amplitudes of the nonlinear terms of the forces increase, which in turn increases their influence on the force amplitudes. This means that while Case 1 and Case 3 had semi-similar force contributions, Case 11 and Case 13 have vastly different ones, which again is caused by the differences in the cylinder shape where the diamond-shaped cylinders allow more of the flow to pass through the system.

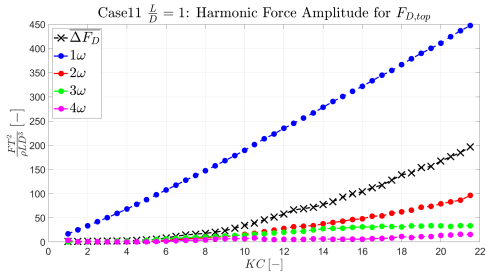

(a) The harmonic force amplitudes for $F_{D,top}$ and the mean force difference for Case 11 with $\frac{L}{D} = 1$.

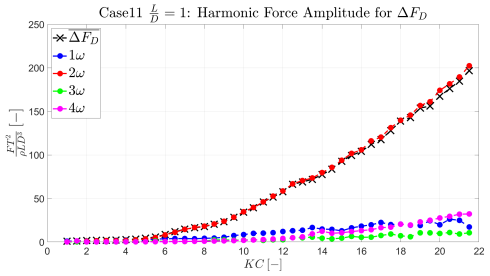

(b) The harmonic force amplitudes for ΔF_D and the mean force difference for Case 11 with $\frac{L}{D} = 1$.

Figure 5.11: The harmonic force amplitudes for $F_{D,top}$ and ΔF_D and the mean force difference for Case 11 with $\frac{L}{D} = 1$.

Figure 5.11a shows that the 1ω harmonic force amplitude evolves linearly as a function of the KC number in the same way as for Case 1 in Figure 5.3a, and that the amplitude values correspond well with the values for the experienced forces. There is however a much larger presence of the higher-order amplitudes for $F_{D,top}$ for Case 13 than for Case 3, which again implies that the diamond-shaped cases have more nonlinearity in their experienced forces than Case 3. The values for both the 2ω force amplitude and the mean force difference for $F_{D,top}$ are about twice as high for Case 13 as for Case 3, but the 3ω and 4ω force amplitudes have around the same values in both cases. This is further shown in Figure 5.11b where the 2ω force amplitude for Case 13 follows the mean force difference almost exponentially, but with twice as high values as for Case 3. Case 13 does actually show less influence by the 4ω force amplitude on the ΔF_D force than in Case 3, but the values are too small to be certain of the cause of the 4ω amplitude in the first place. It could be heavily influenced by noise pollution from the surrounding environment of the test setup.

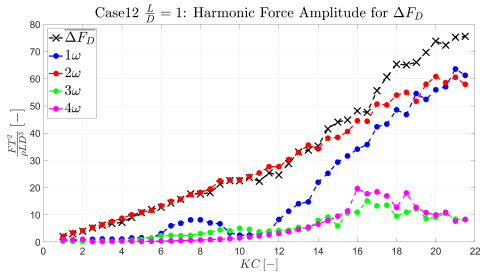

(a) The harmonic force amplitudes for ΔF_D and the mean force difference for Case 12 with $\frac{L}{D} = 1$.

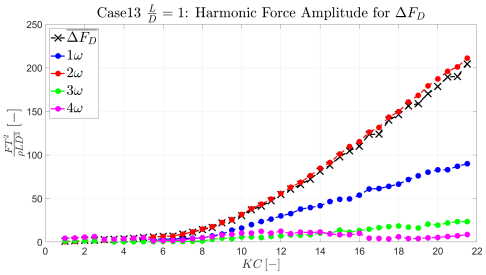

(b) The harmonic force amplitudes for ΔF_D and the mean force difference for Case 13 with $\frac{L}{D} = 1$.

Figure 5.12: The harmonic force amplitudes for ΔF_D and the mean force difference for cases 12 and 13 with $\frac{L}{D} = 1$.

The harmonic force amplitudes of $F_{D,top}$ for cases 12 and 13 behave very similarly to Case 11 and are therefore only shown in Appendix C.2. The harmonic force amplitudes of ΔF_D shown in Figure 5.12 do however behave in a very different manner for cases 12 and 13 than for cases 2 and 3, and must be discussed. The harmonic force amplitudes for Case 12 seem very chaotic and at times incoherent. It is heavily influenced by its 1ω amplitude, which is not the case for any of the other cases, and it even surpasses the 2ω amplitude at the highest KC numbers. One of the reasons for this 1ω dominance may be that the force difference is very linear. This does not mean that Case 12 has much less nonlinearity, but it may imply that the cancellation effects from subtracting the bottom cylinder force from the top cylinder are much more prominent in this case. This will also explain the very low values for both the 2ω force amplitude and the mean force difference as they are both around only 40 % as high as the corresponding values for Case 2, while the 1ω amplitudes have roughly the same values in cases 2 and 12.

The harmonic force amplitudes for the ΔF_D force for Case 13 shown in Figure 5.12b behave almost similarly as in Case 3, but all of the values are larger. The 2ω, 3ω, and 4ω force amplitudes are about twice as large for Case 13 as for Case 3, which corresponds well with the results of the total forces in the two cases. The main difference between the cases is the 1ω force amplitude which is four times larger for Case 13 than for Case 3. This does reflect some of the findings from Case 12 with the force difference being more linear, and that the cancellation effects may be more eminent for diamond-shaped cylinders than for square-shaped cylinders.

The results found for cases 11, 12, and 13 substantiate what will be the main takeaway from the experimental cases; the differences between the square-shaped and diamond-shaped cylinders are crucial when designing structures that will be subjugated to a harmonically oscillating flow. Even though more tests should be performed to further analyze the effects of the cylinder shape, these preliminary results show that the diamond-shaped cylinders experience more nonlinearity, and may in general experience higher forces which will make them the less desirable choice for designing floating structures.

5.2 Numerical results of 2D cylinders

All results from the numerical models will be presented and discussed in this section in the same order as they were introduced in Section 4.1.1. As previously mentioned, the results are all gathered from simulations run in OpenFOAM using the `pvcFoam` solver based on an example from [Senthuran Ravinthrakumar 2023], and post-processed in Python using self-made scripts. All of the numerical analyses were done for two-dimensional cases to minimize the necessary computing time and power. All of the cases were run for a harmonically oscillating flow with a period of $T = 1$ second, as this period was found to give more readable results than $T = 1.5$ seconds.

5.2.1 Modeling the experimental cases

The results from the numerical models of the physical experiments will be presented in this section. The model simulations for the experimental cases were based on the same case configurations as the physical experimental cases shown in Figure 3.3, and discussed in Section 5.1, with the exception of Case 4 as this case would be incorporated into the study with a varying inflow angle shown in Section 5.2.2. Here, the cases were configured as two-dimensional and tested for a range of KC numbers from 1 to 21 with a step size of $\Delta\text{KC} = 0.5$, which is the same range as for the physical cases. The numerical results will also be discussed in the same way as the experimental cases, focusing on $\text{KC} = 8, 16$, and 21.5, and presenting a comparison of the total forces of the three KC numbers, in addition to the harmonic force component figures for the top cylinder forces and force difference between the cylinders.

Even though the cases were tested in two dimensions, they needed to be defined in three dimensions so that the fluid flow could pass through the system in OpenFOAM, before being spliced through the middle reducing the dimensions of the cases. The length-to-diameter ratio was chosen to be $\frac{L}{D} = 2$ meaning that $L = 0.1\,m$ was used in the non-dimensionalizing of the cases, but other than that the length into the plane would not matter.

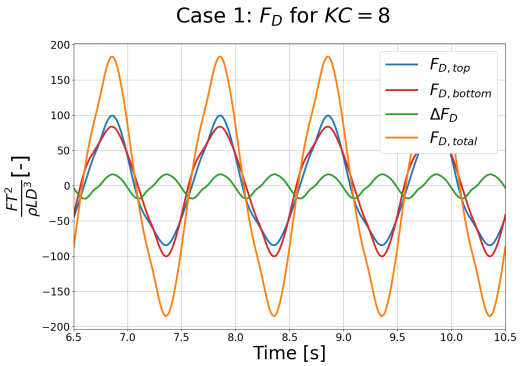

(a) The forces acting on the numerically simulated system for KC = 8 in Case 1.

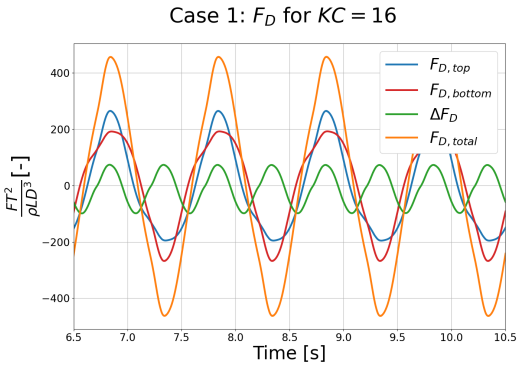

(b) The forces acting on the numerically simulated system for KC = 16 in Case 1.

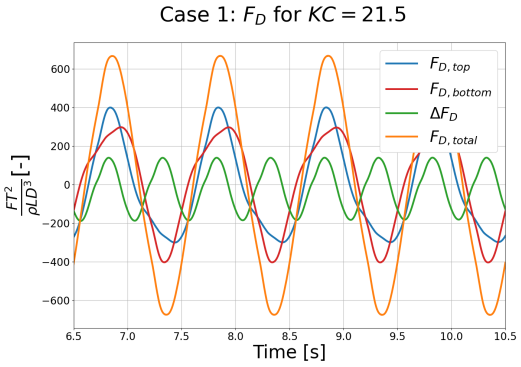

(c) The forces acting on the numerically simulated system for KC = 21.5 in Case 1.

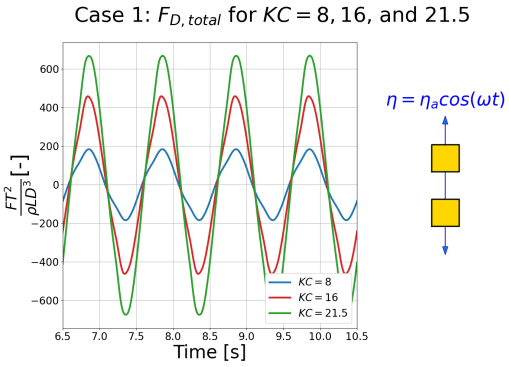

(d) A comparison of the total force for KC = 8, 16, and 21.5 in Case 1.

Figure 5.13: The numerical force amplitudes and a comparison of the total forces acting on the system in Case 1.

The first simulation that was tested was the numerical model for Case 1, and its results are shown in Figure 5.13. In the same way as the results from the experimental Case 1, the upstream cylinder clearly experiences more drag force than the downstream cylinder, with the force difference becoming clearer as the KC number increases, and with the ΔF_D curve having half the oscillation period of the other force curves. This does imply that the hydrodynamic interaction between the cylinders increases for higher KC numbers, which is also the case for the experimental tests. The broadening of the force amplitude curve of the downstream cylinder for higher KC numbers is also present in the numerical results. This indicates that also the numerical simulations are influenced by higher-order harmonic force amplitudes.

The numerical force amplitudes are quite consistent with the experimental ones, even though they operate in a different number of dimensions. This could be a coincidental result, but it can also mean that the most important parameters that influence the force amplitudes are not dependent on the third dimension, or that OpenFOAM manages to capture these effects and relay them into two dimensions. Since the magnitudes of the force amplitudes for Case 1 are similar for both the experimental and numerical analyses, the total force amplitude comparison in Figure 5.13d shows roughly the same relations between the three curves, and that the total force amplitude experienced by the system increases almost linearly with the KC number.

A remark on the shapes of the force amplitude curves is that the numerical curves seem less linear and more affected by higher-order harmonic force amplitudes as they are less rounded towards the peaks and look more uneven than the experimental curves. This, in addition to the broadening of the downstream force amplitude curve and the behavior of the ΔF_D curve, means that the numerical analyses may overpredict the influence of nonlinear force terms, at least with regard to three-dimensional cases.

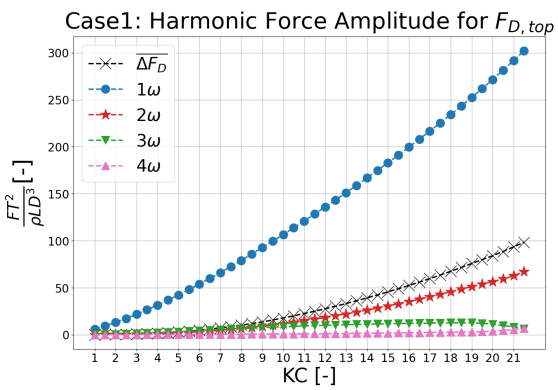

(a) The numerical harmonic force amplitudes for $F_{D,top}$ and the mean force difference in Case 1.

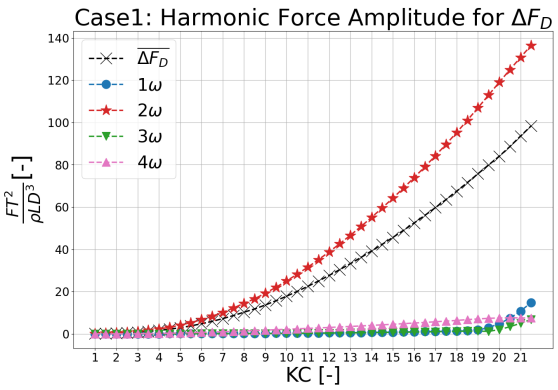

(b) The numerical harmonic force amplitudes for ΔF_D and the mean force difference in Case 1.

Figure 5.14: The numerical harmonic force amplitudes for $F_{D,top}$ and ΔF_D and the mean force difference in Case 1.

The harmonic force amplitudes in Figure 5.14 show that the higher-order harmonic force amplitudes are in fact much more prominent for the numerical case than in the experimental one. The harmonic force amplitudes of the top cylinder shows that the 1ω force amplitude has about 75 % as high values as the experimental case meaning that the influence of the linear force amplitude is not quite the same numerically as experimentally for Case 1. It also shows that the 2ω amplitude is a bit more prominent numerically. The harmonic force amplitudes for the force difference do however show that the 2ω amplitude is around 40 % higher numerically, and with lower contributions from the other harmonic amplitudes. This does mean that in total the numerical model estimates that the 2ω force amplitude for the force difference will be equal to about 47 % of the 1ω force amplitude for the top cylinder, while for the experimental test, it is equal to only about 23 % of the 1ω force amplitude. In addition to this, it would seem that the mean force difference, $\overline{F_D}$, is numerically estimated to be about the same as for the experimental case. But, while the 2ω force amplitude for ΔF_D closely follows the mean force difference for the experimental case, it overshoots it numerically by about 40 % for the highest KC values. This further backs up the theory that the numerical model overestimated the nonlinear influence of the force amplitudes in the system.

Moving on to the next case which is the numerical model of Case 2, the first thing to notice for the force amplitudes presented in Figure 5.15 is the exceptionally small force difference, especially for KC = 8. This is a good example of how Case 2 positions the cylinders in different flow regimes as discussed by [Zdravkovich 1977], since for the lowest KC numbers it is almost as if they are single cylinders in infinite fluid, and they experience almost no hydrodynamic interaction with each other. This was not the case for the experimental test, but again the credibility of that specific test is not to be fully trusted. Some information about the flow may be lost numerically since the cases are two-dimensional, and there may be more hydrodynamic interaction than what is simulated.

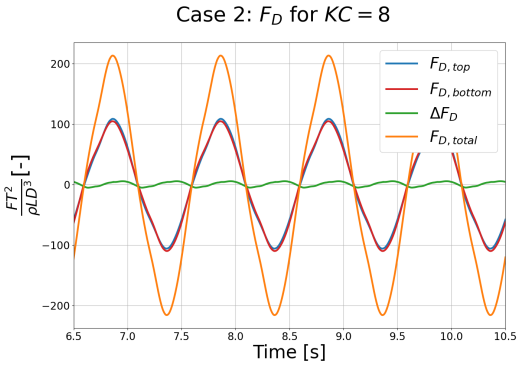

(a) The forces acting on the numerically simulated system for KC = 8 in Case 2.

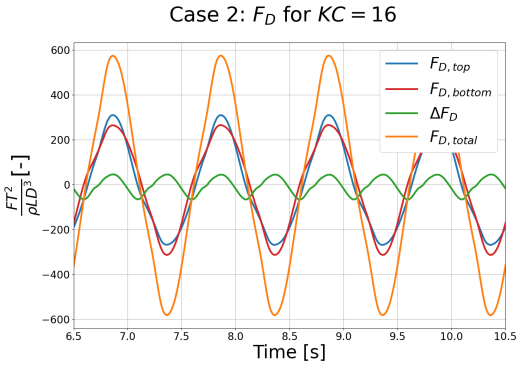

(b) The forces acting on the numerically simulated system for KC = 16 in Case 2.

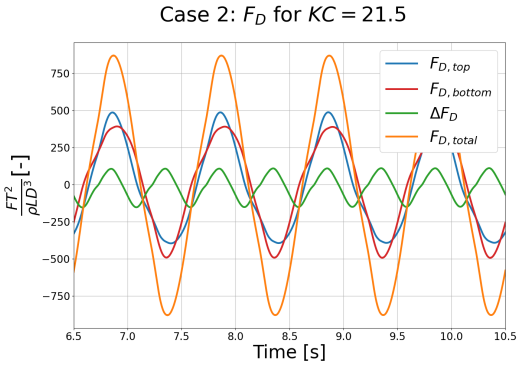

(c) The forces acting on the numerically simulated system for KC = 21.5 in Case 2.

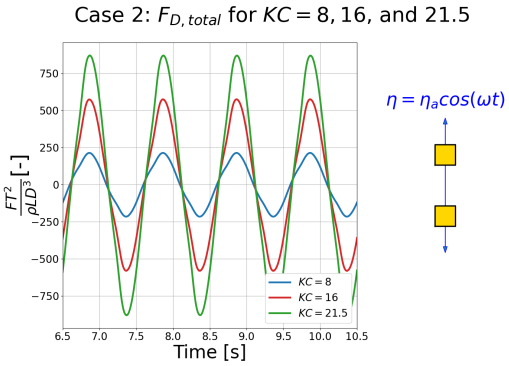

(d) A comparison of the total force for KC = 8, 16, and 21.5 in Case 2.

Figure 5.15: The numerical force amplitudes and a comparison of the total forces acting on the system in Case 2.

For higher KC numbers there are more hydrodynamic interactions between the cylinders since the force difference curve has a higher amplitude, and since the force curve of the downstream cylinder is more rounded. Still, there is not as much hydrodynamic interaction as in Case 1, which is as expected since the cylinders are further apart, but it does give validation to the numerical model simulations. The force curves for Case 2 are also more rounded toward the peaks, and look more even than the corresponding curves for Case 1, indicating that there is a lesser influence of the nonlinear force terms. This can also be seen in Figure 5.16 where the harmonic force amplitudes for $F_{D,top}$ and ΔF_D are shown.

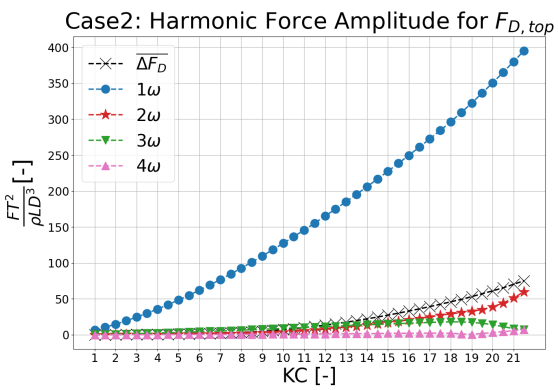

(a) The numerical harmonic force amplitudes for $F_{D,top}$ and the mean force difference in Case 2.

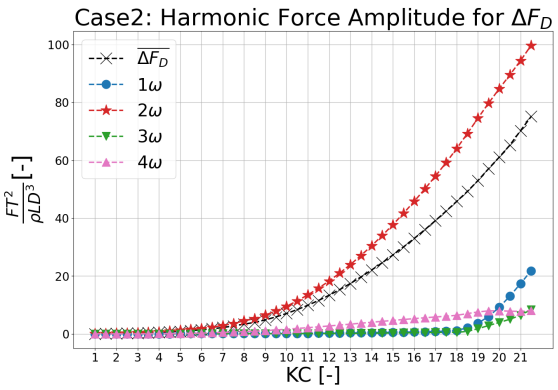

(b) The numerical harmonic force amplitudes for ΔF_D and the mean force difference in Case 2.

Figure 5.16: The numerical harmonic force amplitudes for $F_{D,top}$ and ΔF_D and the mean force difference in Case 2.

Compared to the experimental case the harmonic force amplitude results look nothing alike with a less linear 1ω force amplitude in Figure 5.16a and a nonlinear 2ω force amplitude in Figure 5.16b, both with generally lower values. However, the results do compare well with the same results from the numerical model of Case 1, with a similar, but larger 1ω amplitude for the top cylinder and smaller 2ω curve for the force difference, which can be linked directly to the earlier findings of less nonlinear contribution to the force and less hydrodynamic interaction between the cylinders for Case 2 than for Case 1. The 2ω force amplitude for the top cylinder is also smaller compared to the 1ω amplitude in this case which further validates the findings. The differences between the $\overline{\Delta F_D}$ and 2ω curves also seem consistent between the cases.

Case 3 is the next numerical model that will be discussed, and its force curves are shown in Figure 5.17. When compared to the same results for the experimental test, it can be seen that the numerical simulation overestimates the experienced drag force on the cylinders. For KC = 8 the differences in force amplitudes are small, only about 10 %, but for the higher KC values the differences are more substantial with a 22 % difference for KC = 16 and a 65 % difference for KC = 21.5. These differences could be due to the reduced dimensions of the model leaving out the end effects, or due to the turbulence model used in the project not calculating the forces correctly as explained in Section 4.2.4. Either way, the numerical model for Case 3 does output results that are coherent with Case 1, and that could be expected from doubling the number of cylinders in the system.

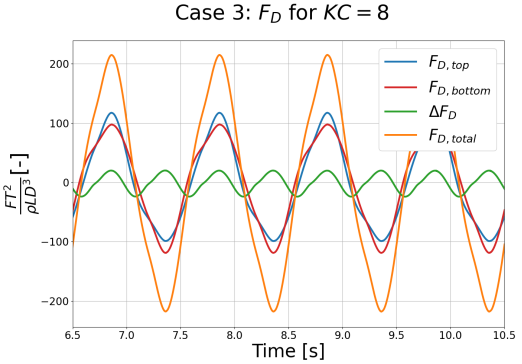

(a) The forces acting on the numerically simulated system for KC = 8 in Case 3.

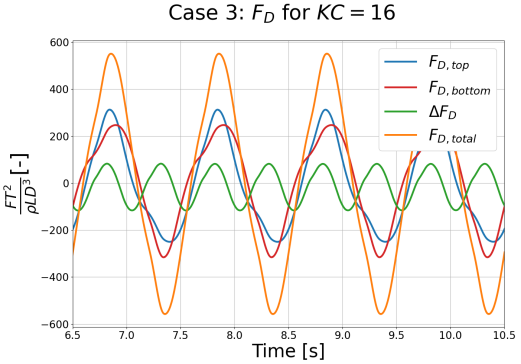

(b) The forces acting on the numerically simulated system for KC = 16 in Case 3.

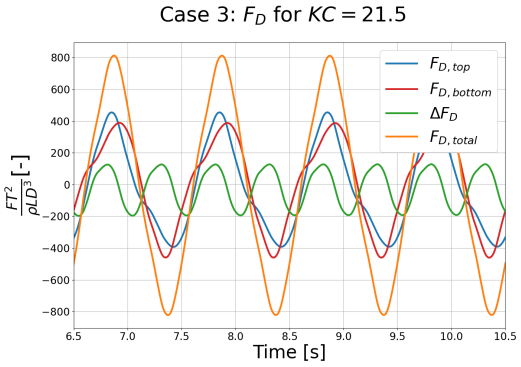

(c) The forces acting on the numerically simulated system for KC = 21.5 in Case 3.

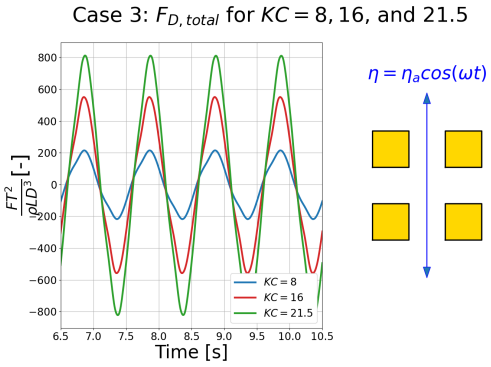

(d) A comparison of the total force for KC = 8, 16, and 21.5 in Case 3.

Figure 5.17: The numerical force amplitudes and a comparison of the total forces acting on the system in Case 3.

In the same manner as the other numerical models, the force amplitude curves for Case 3 are also more pointed toward the peaks and are less even than their experimental equivalent. The force difference curve is also a lot more prominent numerically with a more established oscillation than the experimental force difference, especially for KC = 8, and with more prominent peaks. Similar to cases 1 and 2 this implies a stronger contribution from nonlinear force terms meaning larger higher-order frequency amplitudes.

The harmonic force amplitudes for $F_{D,top}$ and ΔF_D are shown in Figure 5.18. When compared to the experimental force amplitudes, it can be seen that they are quite similar in both linearity and amplitudes. The 1ω force amplitude for the top cylinder is slightly less linear than its experimental counterpart, which is probably due to the numerical 2ω force amplitude for the top cylinder being twice as high as the experimental amplitude for large KC numbers. Other than that, the 1ω amplitude barely overestimates the force amplitude with only about 5 %, and is about 20 % higher than for the numerical model of Case 1. The 2ω force amplitude of ΔF_D does overestimate the experimental results by roughly 30 %, but the numerical mean force difference curve is almost identical to the experimental one, which means that Case 3 has the same 2ω overprediction as cases 1 and 2.

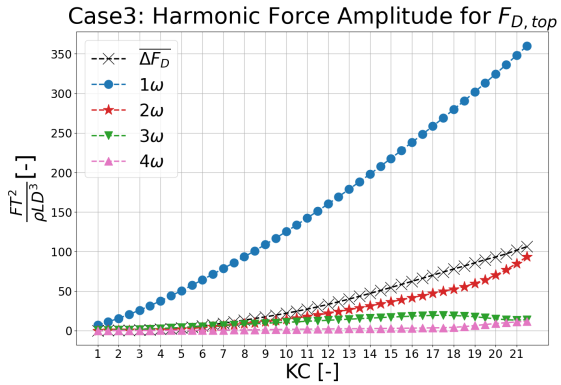

(a) The numerical harmonic force amplitudes for $F_{D,top}$ and the mean force difference in Case 3.

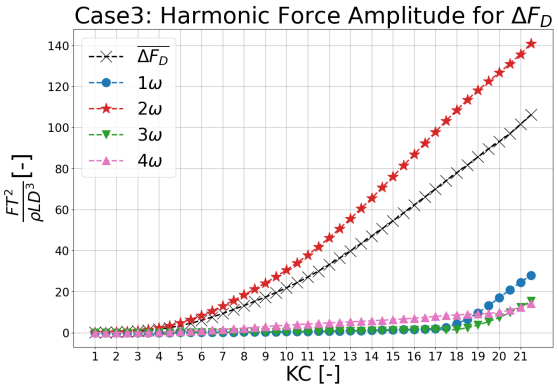

(b) The numerical harmonic force amplitudes for ΔF_D and the mean force difference in Case 3.

Figure 5.18: The numerical harmonic force amplitudes for $F_{D,top}$ and ΔF_D and the mean force difference in Case 3.

Since Case 4 was not modeled numerically as a stand-alone case, the next simulations that will be presented are cases 11, 12, and 13, and they will be presented together in the same manner as the experimental cases. The results from the three cases are presented for KC = 16, with a total force comparison figure comparing the three cases to each other in Figure 5.19. The figures showing the rest of the force amplitudes and comparison plots can be located in Appendix C.1.

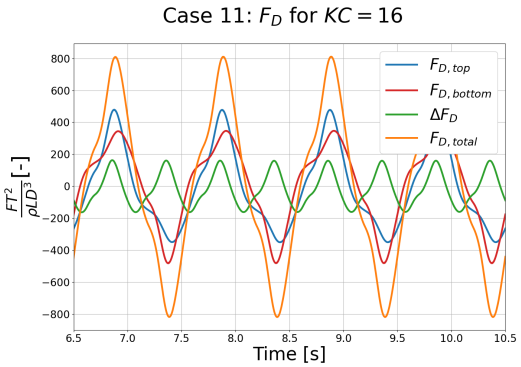

(a) The forces acting on the numerically simulated system for KC = 16 in Case 11.

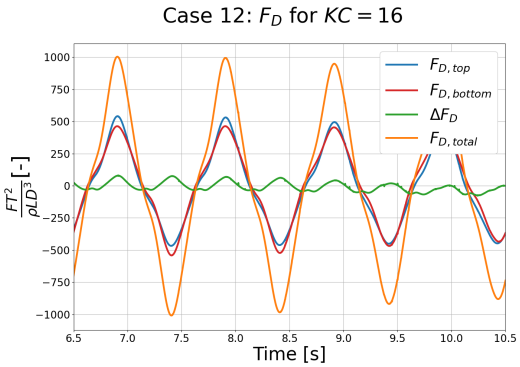

(b) The forces acting on the numerically simulated system for KC = 16 in Case 12.

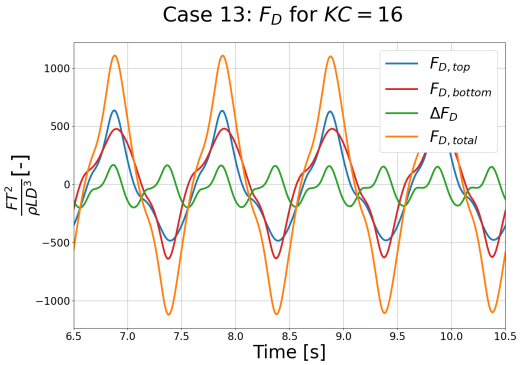

(c) The forces acting on the numerically simulated system for KC = 16 in Case 13.

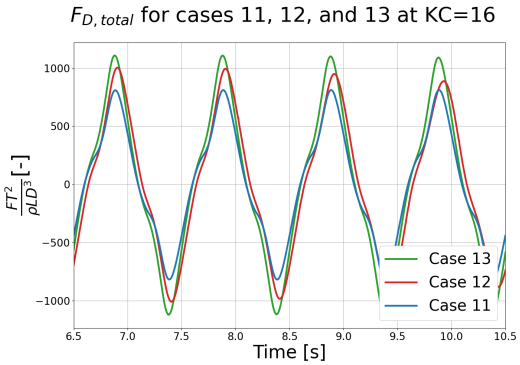

(d) A comparison of the total force for KC = 16 in cases 11, 12, and 13.

Figure 5.19: The numerical force amplitudes and a comparison of the total forces acting on the cylinders in KC = 16 in cases 11, 12, and 13.

The first thing to notice about these force amplitudes is that they are significantly less linear than the corresponding experimental force amplitudes and that their peak values are much larger. This does again mean a significant nonlinear contribution to the force amplitudes, and to an even greater extent than for the square-shaped numerical force amplitudes which are much more rounded and linearly oscillating. The larger numerical impact on the force of the higher-order harmonic force amplitudes does once again show that the diamond-shaped cylinders are probably less desirable when designing floating structures that will be exposed to harmonically oscillating flows.

Another element that is important to study is the numerical relation between the total force curves in comparison with the experimental relation of cases 11, 12, and 13. For both types of cases, it is Case 13 that has the highest peak values of F_{Total} for KC = 16, but numerically it is Case 11 that has the lowest values, and experimentally the lowest values belong to Case 12. Also, the peak values for Case 13 are much higher experimentally in comparison with the other two cases, while numerically they are only slightly larger. The

takeaway from these findings is that the numerical models overestimate the influence of the nonlinear force terms, which is probably both due to the solver not capturing all of the data of the flow due to the implemented turbulence model. It is also probably due to the reduced dimension of the numerical simulations not taking into account the fluid that escapes past the ends of the cylinders, as it is an inherently three-dimensional effect.

The numerical nonlinearity of cases 11, 12, and 13 can be further seen in the harmonic force amplitudes for $F_{D,top}$ and ΔF_D in the same manner as in cases 1, 2, and 3. Figure 5.20a shows that the 1ω amplitude is very similar for Case 11 numerically as it was experimentally, with a close to linear curve in both cases and with almost identical values. The nonlinearity of the force amplitudes of the top cylinder does therefore stem from the higher-order force amplitudes, which behave differently for the numerical case than the experimental case. The numerical 2ω amplitude follows the mean force difference curve much closer than the experimental amplitude, especially for the highest KC values, and both the 3ω and 4ω amplitudes are a lot more substantial in the numerical figure, even though both these amplitudes are lowered towards the highest KC numbers.

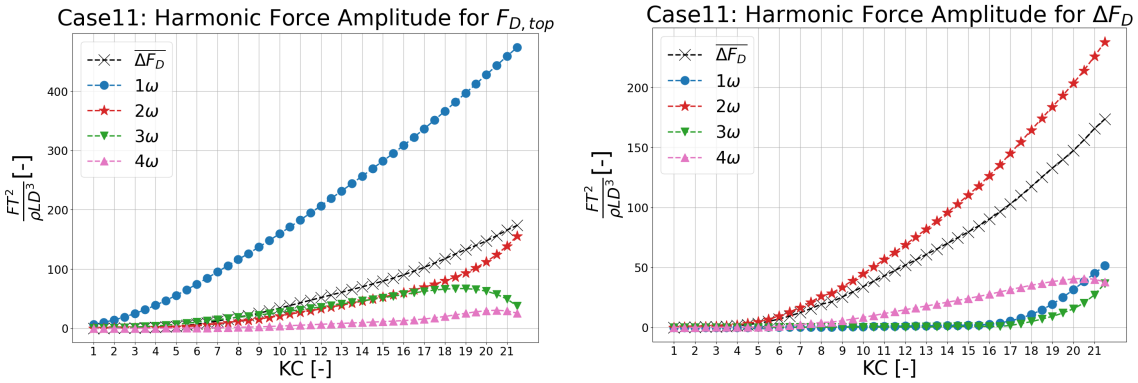

(a) The numerical harmonic force amplitudes for $F_{D,top}$ and the mean force difference in Case 11.

(b) The numerical harmonic force amplitudes for ΔF_D and the mean force difference in Case 11.

Figure 5.20: The numerical harmonic force amplitudes for $F_{D,top}$ and ΔF_D and the mean force difference in Case 11.

For cases 12 and 13 only the harmonic force amplitudes of the force difference will be presented since for the top cylinder the harmonic amplitudes behaved similarly to the ones in Case 11. They can still be found in Appendix C.2. A first remark on the harmonic amplitudes of Case 12 in Figure 5.21a is that the almost chaotic state of the same results for the experimental test is not replicated numerically. This is an indication of the turbulence model implemented in the simulations not being able to catch the irregularities of the flow, while still maintaining the most vital information needed to understand the behavior of the model. The numerical 2ω harmonic force amplitude for Case 11 is also a lot closer to the $\overline{\Delta F_D}$ curve than any of the other 2ω amplitudes from the rest of the numerical cases, and the 4ω curve is much more prominent. This could be because of the lower values for the 1ω and 3ω amplitudes.

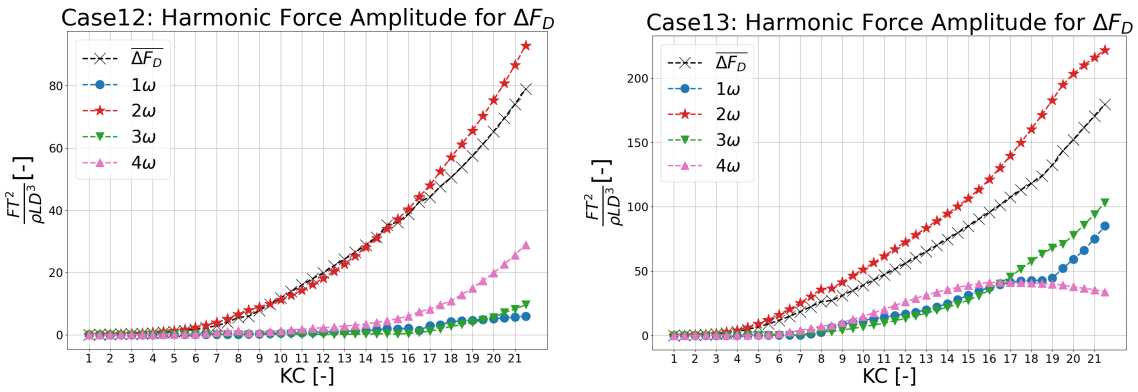

(a) The numerical harmonic force amplitudes for ΔF_D and the mean force difference in Case 12.

(b) The numerical harmonic force amplitudes for ΔF_D and the mean force difference in Case 13.

Figure 5.21: The numerical harmonic force amplitudes for ΔF_D and the mean force difference in cases 12 and 13.

The harmonic amplitudes for Case 13 are shown in Figure 5.21b, and are quite different from their experimental counterparts. The mean force difference is closely numerically estimated to the experimental curve, and the 2ω force amplitude overestimates the experimental values in the same way as for most of the other numerical cases. What is different about Case 13 is the other higher-order amplitudes which are much more prominent than in the rest of the cases, where for the highest KC numbers the 1ω and 3ω amplitude values are almost equivalent to half of the 2ω amplitude. The 4ω amplitude is also very prominent in this case. These facts all contribute to the increase in the nonlinearity of the experienced forces of the numerical simulation of Case 13 compared to the experimental case.

The numerical models of the experimental cases did a good job of estimating the cases' experienced forces and harmonic force amplitudes and validated many of the experimental results. This validation also means that the numerical solver will most likely predict decent results for the other case configurations presented later in this chapter. A general rule of these numerical simulations is that they will overestimate the nonlinear force contributions, especially the 2ω force amplitude, but will relay most of the flow information correctly, and can therefore be used to gather data for modeling new cases as well as being used on existing and tested cases.

A final analysis of the numerical models of the experimental cases is to study the added mass, damping, and drag coefficients and has been done for cases 1 and 2. The coefficients have been calculated based on the force outputs from OpenFOAM, the coefficient equations from Section 2.8, and the constructed acceleration and velocity data from Section 2.9. The three coefficients for the top and bottom cylinders, as well as the mean drag coefficient of both cylinders, are presented in Figure 5.22.

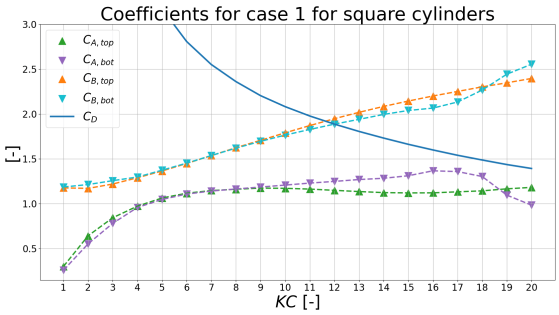

(a) The added mass, damping, and drag coefficients of Case 1.

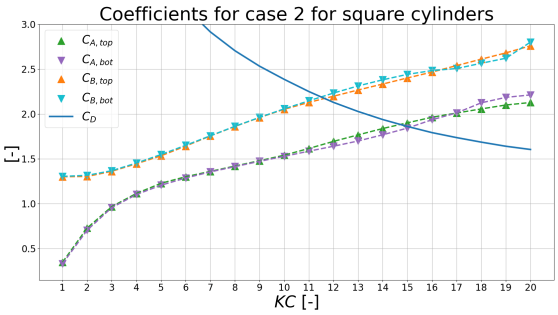

(b) The added mass, damping, and drag coefficients of Case 2.

Figure 5.22: The added mass, damping, and drag coefficients of cases 1 and 2.

It immediately becomes clear from the drag coefficient curve that the drag coefficient model created in Section 2.8 is not applicable for small KC numbers. Since the only variables that affect the drag coefficient in this model are the KC number and the damping coefficients, the drag coefficient will blow up for small KC values if the damping coefficient is not sufficiently low, which is the case in these figures. It does seem to stabilize for higher KC values, but should still not be completely trusted. Another problem is that the damping coefficients in both cases seem unnaturally high and have tendencies of running almost parallel to the added mass coefficients while never being lower at any point. This should not happen for the lowest KC numbers where the oscillation is minimal, and there should be only a tiny amount of damping. The most probable reason for these strange damping coefficients is that the RANS turbulence model smears a lot of the flow field data when averaging causing it to record falsely high values of damping in the forces. The added mass coefficients do however seem less strange, especially for Case 1 where it seems to stabilize at around $C_A = 1.2$. For Case 2 it steadily grows for all KC numbers, but the growth seems to let off towards the end where the added mass coefficient is around $C_A = 2.2$. The expected value for the added mass coefficient is around 1.51, as shown earlier in Equation 2.62, for a single square cylinder in an infinite fluid. This value may not be comparable at all to cases 1 and 2 since they consist of two cylinders in close proximity, but the fact that the added mass coefficients in the two cases are close to the reference value with Case 1 being lower and Case 2 being higher shows that the coefficient model is not entirely false. Later in this chapter, it can be seen that for a constant KC value, the model manages to give a very good estimation of the drag coefficients of two cylinders that moves away from each other.

5.2.2 Varying the inflow angle

The experimental results for cases 1 and 4 presented in Section 3.2 made it clear that the experienced forces on the cylinders are dependent on the inflow angle, and that a cylinder configuration resulting in an inflow angle that is not directly in line with the configuration may lead to higher forces and higher nonlinear contributions. However, there were not enough data from these two experimental cases alone to establish a full picture of the inflow angle dependency and how sensitive the cylinder configuration is to small adjustments in the inflow angle. It was therefore decided to further test the inflow angle dependency of cases 1 and 2 numerically by rotating them from their tandem configurations in the experiments, which has an inflow angle defined as $\theta = 90°$, to a side-by-side configuration with an inflow angle of $\theta = 0°$, with 5-degree increments. It was decided to test cases 1 and

2 since these cases could also show if the two spacing configurations had different effects from the inflow angle variation. Case 3 was not tested as it was deemed unnecessary mostly on account of the double-axis symmetry of the case making the full rotation obsolete. Cases 11, 12, and 13 were also not tested as the experimental tests and the previous numerical models indicated that diamond-shaped cylinders were less favorable than square-shaped cylinders, and would therefore not be further used in the simulations.

As a first study of the inflow angle effects on the systems, the general time series of the drag forces will be compared for a selection of inflow angles which are $\theta = 0°$, $25°$, $45°$ and $75°$. This can also be compared to the 90-degree configurations of cases 1 and 2 from the numerical simulations of the experiments. All the simulations that are presented in this section have been performed at KC = 16 with an oscillation period of $T = 1\,s$.

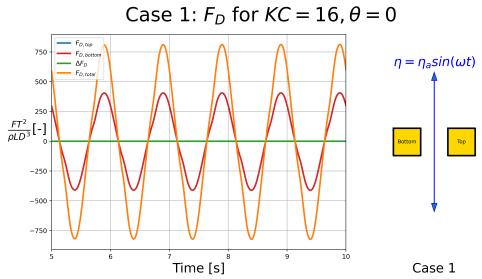

(a) The forces acting on the numerically simulated system for KC = 16 in Case 1 with an inflow angle of $\theta = 0°$.

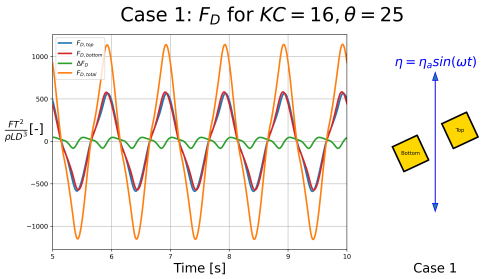

(b) The forces acting on the numerically simulated system for KC = 16 in Case 1 with an inflow angle of $\theta = 25°$.

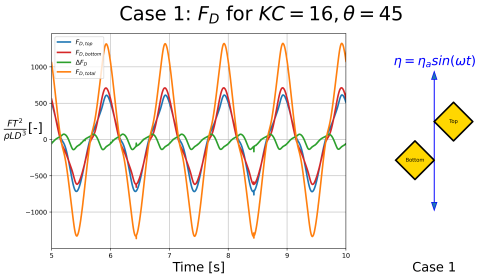

(c) The forces acting on the numerically simulated system for KC = 16 in Case 1 with an inflow angle of $\theta = 45°$.

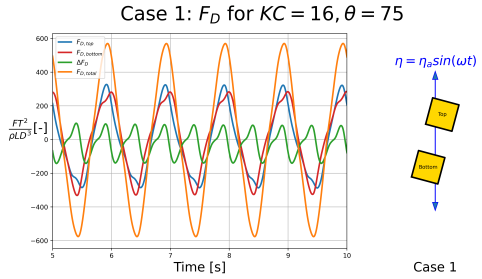

(d) The forces acting on the numerically simulated system for KC = 16 in Case 1 with an inflow angle of $\theta = 75°$.

Figure 5.23: The forces acting on the numerically simulated system for KC = 16 in Case 1 with a range of inflow angles.

The drag force time series for Case 1 at the four inflow angles are shown in Figure 5.23. As expected, for an inflow angle of $\theta = 0°$ the experienced drag forces of each of the cylinders are equal and there is thus no force difference since the cylinders are side-by-side with regards to the inflow angle, which is the same as the direction of oscillation. This means that there is no noticeable hydrodynamic interaction between the cylinders. However, this side-by-side cylinder configuration will be subjected to a minuscule amount of the effects experienced by a perforated plate exposed to the same conditions, where the fluid velocity in the gaps of the plate will be larger than the general fluid velocity generating pockets of lower moving or still fluid directly behind the solid portions of the plate.

Cases 1 and 2 are not perforated plates since [Mentzoni 2020] found that at least nine bodies in side-by-side configurations would be needed for the same effects. Still, the fluid velocity in between the cylinders is larger than the fluid velocities on the outsides of the

cylinders mimicking the perforation effects. This can be seen in Figure 5.24 where the velocity in the z-direction of the case is shown as both streamlines, which are continuous lines through the data set, and glyphs, which are rendered geometries at certain data points showing the direction and intensity of the flow. A red-to-blue scale has been used to indicate the fluid velocity, where a dark red color indicates a high velocity downwards, a dark blue color indicates a high velocity upwards, and a lighter blue color indicates very slow-moving fluid. From the figures, it can be seen that there is a darker shade of red or a larger glyph concentration between the cylinders than elsewhere.

This small amount of perforation effect can lead to an overall larger experienced drag force than for instance the same case with an inflow angle of $\theta = 90°$. This will be further shown and discussed in a study later in this section.

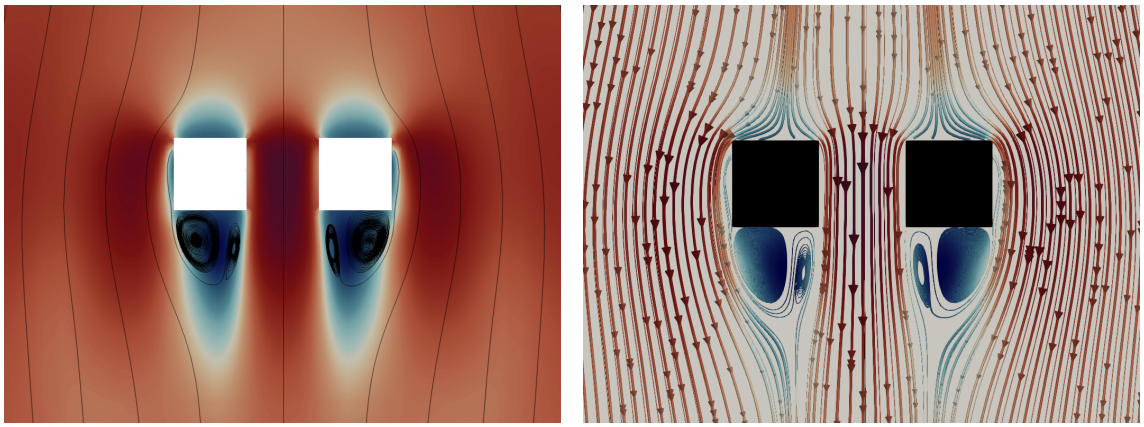

(a) The velocity streamlines in the z-direction of Case 1 at KC = 16 with $\theta = 0°$.

(b) The velocity glyphs in the z-direction of Case 1 at KC = 16 with $\theta = 0°$.

Figure 5.24: The velocity streamlines and glyphs for Case 1 at KC = 16 with $\theta = 0°$. Both subfigures use the red-to-blue color scale for the fluid velocity.

For the force time series of Case 1 with an inflow angle of $\theta = 25°$ from Figure 5.23b, there are some noticeable changes from the smaller inflow angle. Firstly, the total force amplitude, and thus the force amplitudes for both cylinders, has increased by around a third of the same amplitude for $\theta = 0°$ meaning that this configuration experiences larger forces. Secondly, the force difference is no longer zero as there is some hydrodynamic interaction between the cylinders. This is because this inflow angle has an upstream and a downstream cylinder where the upstream cylinder will somewhat disturb the flow experienced by the downstream cylinder. The hydrodynamic interaction is still quite small, but it shows that even cylinders that are nearly side-by-side will affect each other.

The numerical equivalent to Case 4, which is Case 1 with an inflow angle of $\theta = 45°$, is shown in Figure 5.23c, and the results show an overestimation of the force amplitudes when compared to the experimental case. As previously seen in Section 5.2.1, the numerical simulations will overestimate the nonlinear force contributions for cases with an inflow angle of $\theta = 90°$, and for other inflow angles this overestimation can be even more drastic. Compared to the smaller inflow angles, the difference between the experienced forces of the upstream and downstream cylinders is larger and more nonlinear. This is both due to the general nonlinear overestimation from the numerical solver and the flow becoming much more turbulent causing a larger hydrodynamic interaction between the cylinders.

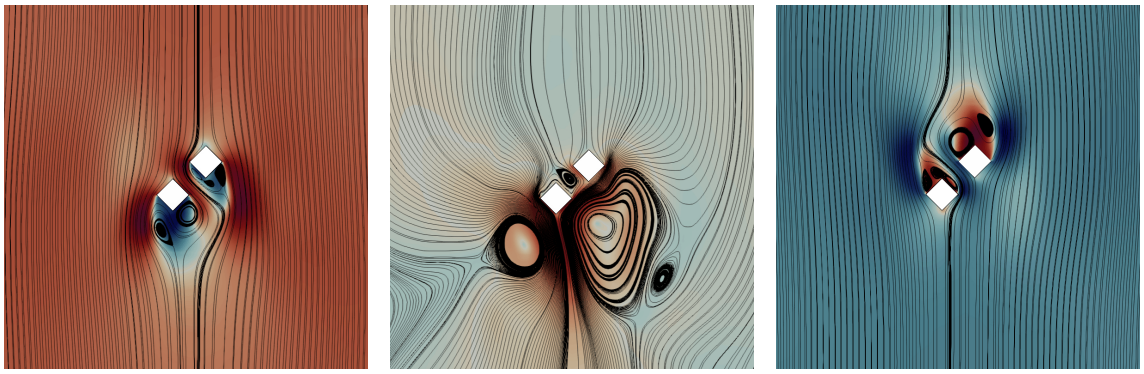

(a) The velocity streamlines of Case 1 with an inflow angle of $\theta = 45°$ at KC $= 16$ at $T = 10\,s$.

(b) The velocity streamlines of Case 1 with an inflow angle of $\theta = 45°$ at KC $= 16$ at $T = 10.25\,s$.

(c) The velocity streamlines of Case 1 with an inflow angle of $\theta = 45°$ at KC $= 16$ at $T = 10.5\,s$.

Figure 5.25: The velocity streamlines of Case 1 with an inflow angle of $\theta = 45°$ at KC $= 16$ at $T = 10$, 10.25, and 10.5 seconds.

In figure Figure 5.25 the streamlines of Case 1 with an inflow angle of $\theta = 45°$ at KC $= 16$ are shown at three different times during an oscillation period. The first image shows the streamlines at $T = 10\,s$ which corresponds to a point where the fluid velocity is at its peak, and the fluid acceleration is equal to zero. At this point, the wakes are fully formed underneath each cylinder. The second figure shows the streamlines a quarter period later at $T = 10.25\,s$ which is the turning point of the flow meaning that the fluid velocity is close to zero in most of the domain and the wakes below the cylinders begin to shift around to the top. The third figure shows the streamlines at $T = 10.5\,s$ which is the exact opposite of the first figure, meaning that the fluid velocity is at a negative peak, the acceleration is zero, and the wakes are fully formed on the top of the cylinders.

Together these three figures show half an oscillation period of the flow. They show that the wakes are at their largest just as the oscillation movement turns when the fluid velocity is zero, but that they at the same time are less intense. The fully formed wakes in the first and third figures are the ones that will cause the most hydrodynamic interaction between the cylinders, and the interaction can be seen in these figures from the way the streamlines are bent through the system creating irregularities in the fluid flow and causing the wakes to not be directly in line with the oscillation motion, but fluctuating outwards. The streamline plots for Case 1 at inflow angles of $\theta = 0°$, $65°$, and $90°$ are shown in Appendix D. The cases with inflow angles of $\theta = 25°$ and $75°$ were not simulated in ways that allowed for these streamline plots to be created, and are therefore not included.

Finally, in Figure 5.23d the forces for Case 1 with an inflow angle of $\theta = 75°$ are shown. Here, the total force amplitude is lower than for the two previous inflow angles, but at the same time, there are a lot more nonlinear force contributions. At this point, most of the area of the downstream cylinder in the z-direction is directly covered by the area of the upstream cylinder, which causes the flow to be much more disrupted before reaching the downstream cylinder, and more turbulent. This will increase the nonlinear contributions to the forces. Also, for inflow angles of $\theta = 25°$ and $45°$, the downstream cylinder experienced higher drag forces than the upstream cylinder, while here it is the opposite. This happens since the flow that was impacting the upstream cylinder at the smaller inflow angles was pushed to the side and was also impacting the downstream cylinder. This can be seen in Figure 5.25a where the region just above the top right of the downstream cylinder has

a darker color than the same region for the upstream cylinder. For an inflow angle of $\theta = 75°$ the same effect is not present as the fluid being pushed to the side will overshoot the downstream cylinder causing it to experience less force. The switch in which of the cylinders experiences more force means that for a specific inflow angle, the experienced drag force will be equal for both cylinders and there will be no force difference. This effect will also be discussed in a later study in this section.

Now that the effects of changing the inflow angle in Case 1 have been discussed, it is time to do the same for Case 2. This is also the case that was tested experimentally by master student Kristian Mikkelsen, and it is the results found in this section that will be compared to his experimental results in Section 5.3. The force time series for Case 2 at KC = 16 for inflow angles of $\theta = 0°$, $25°$, $45°$ and $75°$ are shown in Figure 5.26.

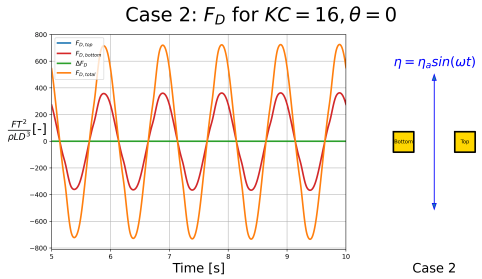

(a) The forces acting on the numerically simulated system for KC = 16 in Case 2 with an inflow angle of $\theta = 0°$.

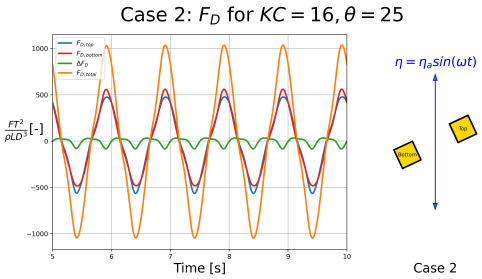

(b) The forces acting on the numerically simulated system for KC = 16 in Case 2 with an inflow angle of $\theta = 25°$.

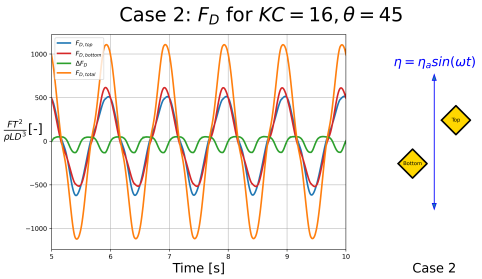

(c) The forces acting on the numerically simulated system for KC = 16 in Case 2 with an inflow angle of $\theta = 45°$.

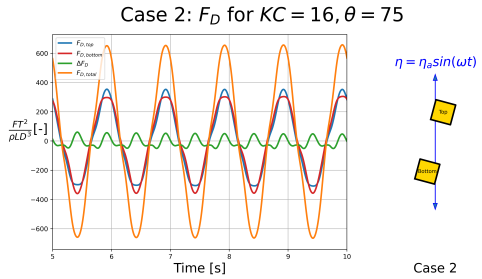

(d) The forces acting on the numerically simulated system for KC = 16 in Case 2 with an inflow angle of $\theta = 75°$.

Figure 5.26: The forces acting on the numerically simulated system for KC = 16 in Case 2 with a range of inflow angles.

In the same way as Case 1, the experienced forces on the cylinders for an inflow angle of $\theta = 0°$ are equal, and there is no force difference between the cylinders meaning no hydrodynamic interaction. The perforation effect from Case 1 is much smaller for Case 2 as the spacing between the cylinders has doubled, meaning that the fluid flow is not moving as fast between the cylinders. This can be seen in Figure 5.27 where the velocity streamlines and glyphs for Case 2 with an inflow angle of $\theta = 0°$ are shown. It can be seen in the first figure that the area between the cylinders is not as dark in color as it was in the same figure for Case 1, and in the second figure, the glyph concentration between the cylinders is less prominent than for Case 1. This means that the cylinders in Case 2 at this inflow angle experience slightly less drag force than in Case 1. This perforation effect is a hydrodynamic effect caused by the cylinders being in close proximity to each other meaning that even at an inflow angle of $\theta = 0°$ there exists some degree of hydrodynamic interaction between the cylinders for both Case 1 and Case 2, but not in the same way as

the nonlinear hydrodynamic effects of the other inflow angles.

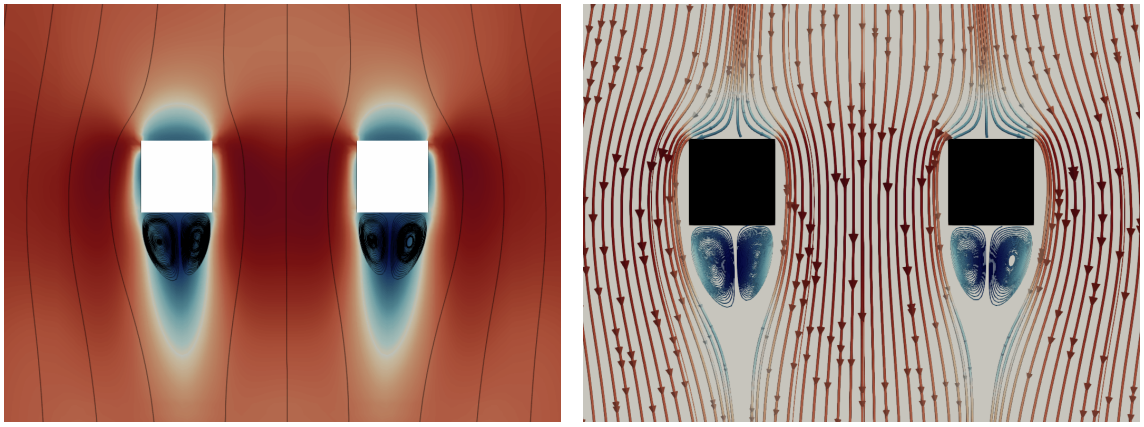

(a) The velocity streamlines in the z-direction of Case 2 at KC = 16 with $\theta = 0°$.

(b) The velocity glyphs in the z-direction of Case 2 at KC = 16 with $\theta = 0°$.

Figure 5.27: The velocity streamlines and glyphs for Case 2 at KC = 16 with $\theta = 0°$. Both subfigures use the red-to-blue color scale for the fluid velocity.

For an inflow angle of $\theta = 25°$ the force amplitudes in Case 2 are slightly lower than in Case 1, which is as expected since the cylinders are further apart and less of the fluid being pushed to the side of the upstream cylinder will impact the downstream cylinder. However, the force difference between the cylinders is larger for Case 2 than for Case 1, where the downstream cylinder experiences significantly more force than the upstream cylinder. Additionally, the downstream force seems to be almost equal in both cases, and it is the upstream force that is much smaller in this case meaning that the flow that is pushed to the side of the upstream cylinder in Case 1 tends to be pushed between the cylinders at a much higher velocity than in Case 2, since the spacing has doubled, leading to more force on the upstream cylinder in Case 1. This is also due to the small amount of perforation effect that affects the system, which clearly is not only present at $\theta = 0°$. Another detail about this inflow angle is that the force curves are still affected by nonlinear contributions in Case 2 but to a somewhat lesser degree than in Case 1 as the curves are slightly more rounded at the peaks. This is also due to the increased spacing which causes less wake interaction and irregularities between the cylinders.

When it comes to the inflow angle of $\theta = 45°$ the force amplitudes are overall slightly lower for Case 2 than in Case 1, which is probably due to the same reasons as for $\theta = 25°$ where the increased spacing affects the impact of the downstream cylinder from the flow of the upstream cylinder. In Case 1, at this inflow angle, the inner vertex of the two cylinders lined up exactly at the center of the system, while in Case 2 this does not happen, which means that more fluid is allowed to move between the cylinders causing less interference and hydrodynamic interaction between the cylinders. This is also reflected by the force curve shapes for Case 2 which are much less nonlinear than for Case 1. This can be especially seen when comparing the force difference curves.

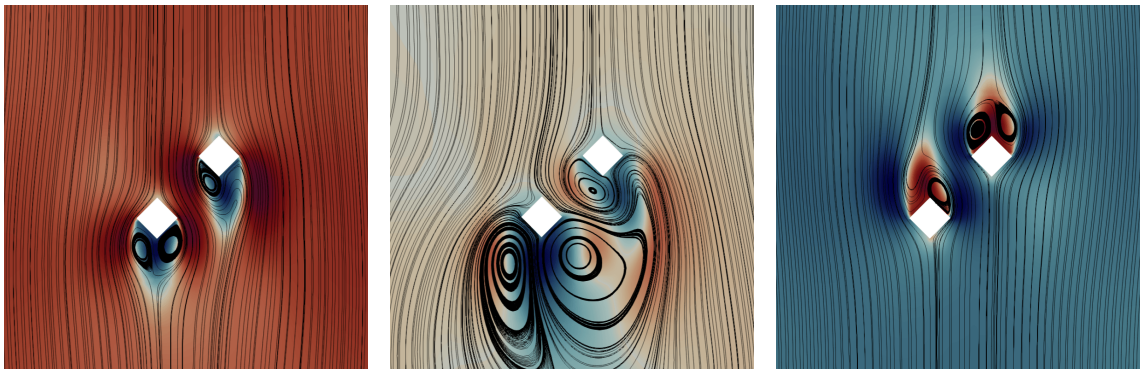

(a) The velocity streamlines of Case 2 with an inflow angle of $\theta = 45°$ at KC $= 16$ at $T = 10\,s$.

(b) The velocity streamlines of Case 2 with an inflow angle of $\theta = 45°$ at KC $= 16$ at $T = 10.25\,s$.

(c) The velocity streamlines of Case 2 with an inflow angle of $\theta = 45°$ at KC $= 16$ at $T = 10.5\,s$.

Figure 5.28: The velocity streamlines of Case 2 with an inflow angle of $\theta = 45°$ at KC $= 16$ at $T = 10$, 10.25, and 10.5 seconds.

In the same way as Case 1, the velocity streamlines of Case 2 with an inflow angle of $\theta = 45°$ at KC $= 16$ are shown in Figure 5.28, with the three figures showing the development of the flow at $T = 10$, 10.25, and 10.5 seconds. The streamline plots for Case 2 at inflow angles of $\theta = 0°$, 65°, and 90° are shown in Appendix D. In the first figure, it can be seen that at the point of maximum downward fluid velocity, the wakes are fully formed below the cylinders. In the second figure, the fluid velocity is equal to zero and the oscillation is at a turning point, which means that the wakes are much larger and less intense than in the first figure as they are transitioning to the top of the cylinders. Finally, in the third figure, the wakes are fully formed on top of the cylinders, and the fluid has reached a maximum upwards velocity. The wakes themselves are very similar in all three figures for cases 1 and 2, but the flow moving between the cylinders is much less intense in this case, which reflects many of the findings discussed in the previous paragraph.

The largest differences between cases 1 and 2 can be found for an inflow angle of $\theta = 75°$. Unlike the previously discussed inflow angles, it is Case 2 that experiences the largest forces in this case. This is most probably due to how the cylinders align in this case compared to Case 1. Here, the inner vertex of the upstream cylinder aligns almost exactly with the midpoint of the top inner face of the downstream cylinder, meaning that the wake of the upstream cylinder will impact the downstream cylinder head-on. This does not happen in Case 1 since the inner vertex of the upstream cylinder aligns with a point much further out on the downstream cylinder allowing much more of the flow to pass it by. Case 2 is also a lot less nonlinear than Case 1, and has a much less irregular force difference. This is also due to the alignment of the cylinders, and since the spacing has doubled the wake from the upstream cylinder is allowed to form a lot more before impacting the downstream cylinder meaning that the hydrodynamic interaction between them becomes much less dependent on higher-order harmonic force amplitudes.

The effects the inflow angle has on the nonlinearity and amplitude of the experienced forces in the system are quite interesting to study. The experimental data and the data from the previous numerical simulations only give results that are valid at an inflow angle of $\theta = 90°$, and the results are far from conservative in comparison to the results from a number of other inflow angles. This means that finding the results for a specific inflow angle is not enough to understand the entirety of the hydrodynamic interactions between the cylinders

and a full analysis of the system should be performed to understand and implement these effects correctly. The outward bending of the flow as seen in the streamline plots is another interesting effect related to the inflow angle that can cause large lift forces on the cylinders, which in these cases means forces acting orthogonal to the oscillation direction. Together, these effects show that a harmonic analysis of the force components at all inflow angles between $\theta = 0°$ and $\theta = 90°$ is necessary. This has been done in the same manner as for the numerical models of the experimental cases in Section 5.2.1 where it was done for each KC number, and the results are presented in polar plots relating the non-dimensional harmonic force amplitudes to the inflow angles. All polar plots presented in this section were created based on the results for KC = 16.

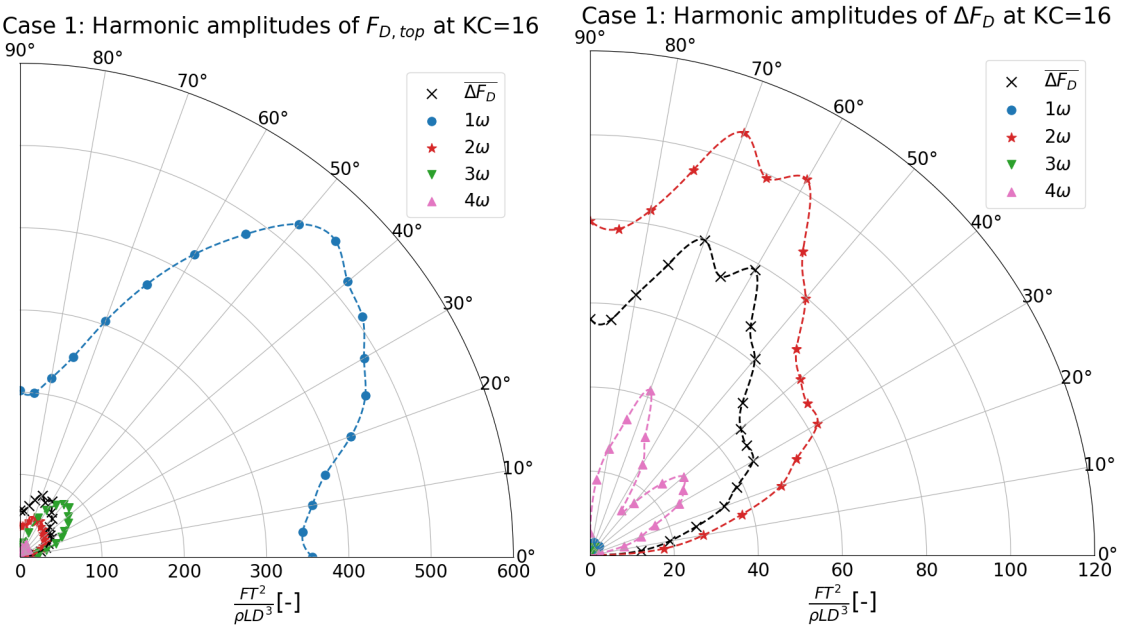

(a) A polar plot showing the harmonic force amplitudes of $F_{D,top}$ for Case 1 at KC = 16 for all inflow angles.

(b) A polar plot showing the harmonic force amplitudes of ΔF_D for Case 1 at KC = 16 for all inflow angles.

Figure 5.29: Polar plots showing the harmonic force amplitudes of $F_{D,top}$ and ΔF_D for Case 1 at KC = 16 for all inflow angles.

Figure 5.29 shows the polar plots for the harmonic force contributions for $F_{D,top}$ and ΔF_D for Case 1 at KC = 16. In the first figure, it can be seen that the experienced drag force of the top cylinder has almost no higher-order harmonic force contributions, and is almost entirely linear. The plot shows that the 1ω force amplitude increases drastically for inflow angles around $\theta = 45°$, which reflects the amplitudes of the force curves from Figure 5.23. The amplitude is almost three times as large for $\theta = 45°$ as for $\theta = 90°$, which again shows that results from modeling only the tandem configuration of the cylinders can not be relied on to reflect the actual forces experienced by the system in all conditions. Also, for the smaller inflow angles, it can be seen that the 1ω amplitude slightly increases. This is due to the perforation effect discussed earlier in this section which induces a higher experienced drag force on the cylinders. This also shows that the 1ω amplitude for $\theta = 0°$ is actually much larger than for $\theta = 90°$, meaning that the negative drag induced on the cylinders in the tandem configuration amount to a lot. It is also worth mentioning that of the higher-order contributions it is the 3ω harmonic amplitude that has the highest amplitude values.

The second figure shows the harmonic force contributions of the drag force difference between the cylinders. As for the standard cases presented earlier, there is next to no contribution from the 1ω and 3ω amplitudes as they are canceled out when subtracting the bottom force from the top force. The force difference is therefore heavily influenced by the 2ω force amplitude, and in the same way as the other numerical cases, the 2ω amplitude is overestimated since it overshoots the mean force difference while their shapes coincide. The 4ω contribution is also present but to a much smaller degree. It is worth noting that the non-dimensional force axes of the two figures are not equal, and that in total the higher-order contributions of ΔF_D are much smaller than the linear contribution to $F_{D,top}$, which again reflects the results from the previous numerical cases well.

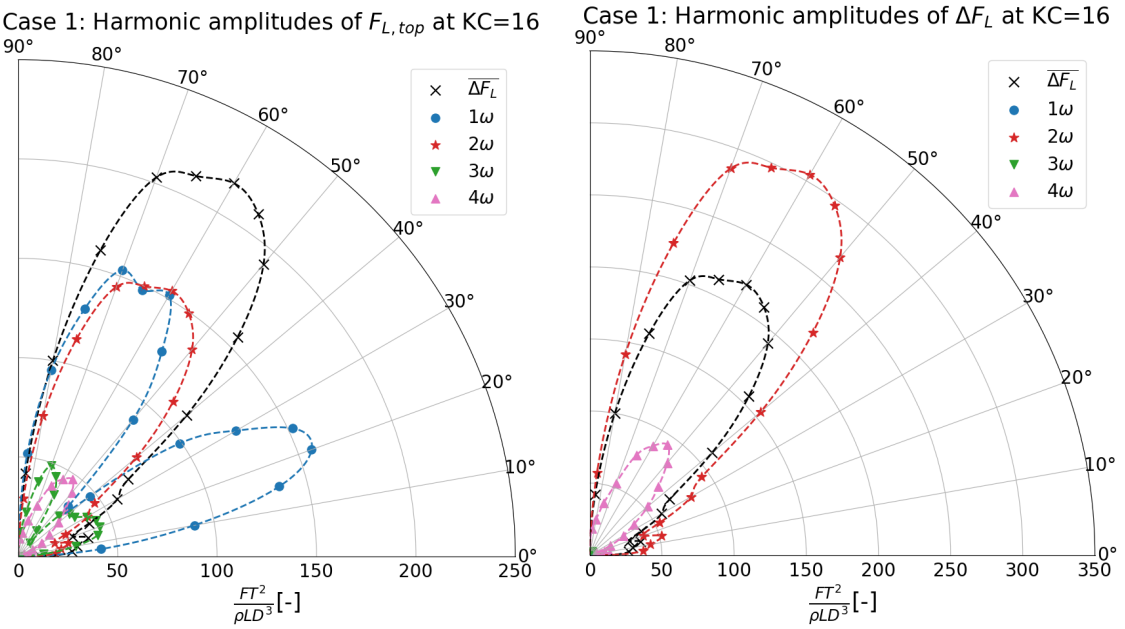

(a) A polar plot showing the harmonic force amplitudes of $F_{L,top}$ for Case 1 at KC = 16 for all inflow angles.

(b) A polar plot showing the harmonic force amplitudes of ΔF_L for Case 1 at KC = 16 for all inflow angles.

Figure 5.30: Polar plots showing the harmonic force amplitudes of $F_{L,top}$ and ΔF_L for Case 1 at KC = 16 for all inflow angles.

The polar plots in Figure 5.30 show the harmonic force contributions for the lift force experienced by the top cylinder, and the lift force difference between the cylinders. As previously mentioned, for many of the inflow angles the lift force may be substantial, and as seen in the first figure the harmonic contributions of $F_{L,top}$ are heavily present for a large range of inflow angles except towards the tandem and side-by-side configurations. The experimental cases and first numerical cases were done for an inflow angle of $\theta = 90°$ and the lift forces were found to be negligible, which coincides with the polar plots where the values at the highest inflow angles go to zero very quickly. An interesting observation on the harmonic amplitudes in the first figure is that in opposition to the drag force for the top cylinder, the lift force is heavily influenced by higher-order harmonic force amplitudes for most of the inflow angles. An exception is for the lowest inflow angles where only the 1ω amplitude is present. Also, for an inflow angle of $\theta = 45°$ the 1ω component races towards zero creating two large regions of the 1ω force amplitude. A theory behind why this has happened is that at this exact inflow angle, the inner vertexes of the cylinders line up exactly in the direction of the oscillation which may cause the 1ω amplitude to

decrease drastically as the flow around the cylinder becomes entirely nonlinear. This may be an entirely numerical phenomenon as the RANS turbulence model used in these simulations does not capture the wake correctly, which may lead to inaccurate results. Another observation of the harmonic amplitudes is that while the 1ω amplitude for $F_{L,top}$ is much lower than for $F_{D,top}$, the 2ω amplitude is actually much larger, meaning that the lift force has much more higher-order harmonic force contributions than the drag force and that it is much more nonlinear.

In the second figure the harmonic force amplitudes of ΔF_L show similar properties to the amplitudes of ΔF_D with some major differences. Firstly, the values of the 2ω and 4ω amplitudes are a lot larger for the lift force difference, and the mean force difference also has much higher values. This again shows how the lift force has way more nonlinear contributions than the drag force. Secondly, the values close to inflow angles of $\theta = 0°$ and $90°$ go rapidly towards zero, explaining the lack of lift forces in the tandem cases. The 1ω and 3ω harmonic force amplitudes are in the same way as for ΔF_D negligible and show that the force difference between the cylinders is completely nonlinear for both the drag and the lift forces. The largest amplitudes in both figures are occurring at an inflow angle of around $\theta = 60°$, with the exception of the 1ω amplitude for $F_{L,top}$ which has an additional peak at $\theta = 20°$. The main peak is located at around the same inflow angle as where the upstream and downstream cylinders switch between who experiences the largest drag force, as explained earlier in this section. This may be coincidental, but it may also show a coupling between the drag and lift forces at these inflow angles, as it is also in the same area where the largest amplitudes for ΔF_D are found.

One important aspect to note when comparing Figure 5.30a with Figure 5.30b is that the 2ω force amplitude curves have close to identical shapes, and the curve in the second figure has around twice as high amplitudes as the one in the first figure. This can be seen by the non-dimensional axes of the figures, as well as by comparing the 2ω amplitude curves with the mean force difference curves which are the exact same curve in the two figures. This phenomenon comes from the creation of the lift force difference where the lift force of one cylinder is subtracted from the other and shows that the 2ω force amplitudes are $180°$ out of phase with each other. This leads to them not canceling out, but being added together due to their phases. These same properties can also be found for the 4ω amplitudes, which also have the same shapes in both figures and twice as high amplitudes in the second figure. The 1ω and 3ω amplitudes do however have the same phase leading to them canceling each other out in the creation of the lift force difference. This phenomenon does not only occur for the lift forces but also the drag forces. It is much harder to see in Figure 5.29, but the 2ω and 4ω force amplitudes do have the same shapes in both figures and twice as high amplitudes in the second figure in the same way as for the lift force.

What this phenomenon means for the system is that while the odd-numbered harmonic force amplitudes will mostly interact with each cylinder on their own, the even-numbered amplitudes will dominate the hydrodynamic loads between them. This could be problematic to model theoretically due to the nature of Morison's equation. When looking at the Fourier series of the drag term of Morison's equation in Equation 5.1, it becomes apparent that only the odd-numbered terms are included in this load formulation, and an improved load formulation should be created to better capture the effects of the even-numbered harmonic force amplitudes.

The polar plots of the harmonic force amplitudes of $F_{D,top}$ and ΔF_D for Case 2 are presented in Figure 5.31 in the same manner as for Case 1. The non-dimensionalized axes have been scaled to the same values as in Figure 5.29 to better show the differences

in the amplitudes between the cases. Figure 5.31a shows that the 1ω force amplitude dominates the drag force of the top cylinder and that the higher-order contributions are a lot smaller, which is the same as for Case 1. Also, all of the harmonic amplitudes for $F_{D,top}$ have lower values for most of the inflow angles than for Case 1, with the exception of inflow angles larger than $\theta = 65°$. This means that the findings from Section 5.2.1 where Case 2 was found to have larger harmonic contributions than Case 1 are not valid for all inflow angles, and that for most inflow angles it is Case 1 that experiences larger forces. This does make sense from a geometry perspective when the increased spacing is considered. The upstream cylinder will cover the downstream cylinder for fewer inflow angles in Case 2 than in Case 1 since the rotation will reveal the downstream cylinder to the flow earlier when the distance between them is greater, and the hydrodynamic interaction between the cylinders will decrease. The fact that the switch between which case experiences higher amplitudes happens at around the same inflow angle as where the upstream and downstream cylinders in both Case 1 and Case 2 switch between who experiences the largest drag force may again be purely coincidental, but it is still worth having in mind.

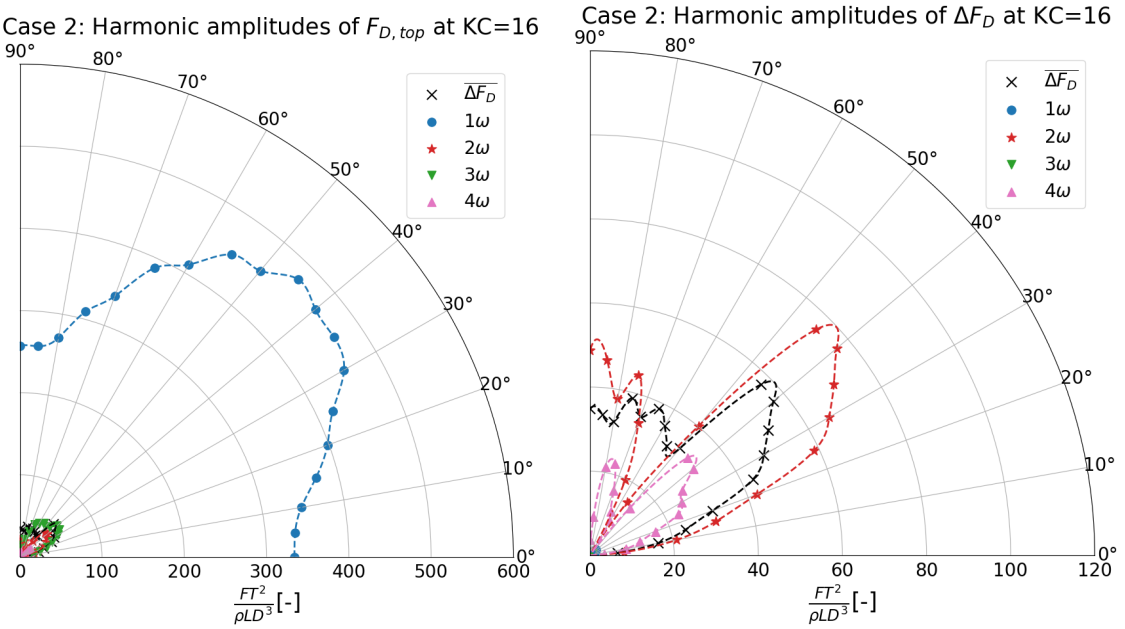

(a) A polar plot showing the harmonic force amplitudes of $F_{D,top}$ for Case 2 at KC = 16 for all inflow angles.

(b) A polar plot showing the harmonic force amplitudes of ΔF_D for Case 2 at KC = 16 for all inflow angles.

Figure 5.31: Polar plots showing the harmonic force amplitudes of $F_{D,top}$ and ΔF_D for Case 2 at KC = 16 for all inflow angles.

Figure 5.29b shows that the harmonic force contributions for ΔF_D behave quite differently in cases 1 and 2. The inflow angles which had the highest 2ω amplitudes in Case 1 have the lowest in Case 2. This can, however, be explained by the same phenomenon found earlier that there exists an inflow angle where the upstream and downstream experience the exact same drag force, which means that the force difference becomes zero at that inflow angle. This will of course mean that there are also no harmonic force contributions as there is nothing to contribute to. This does also happen in Case 1, but very differently since the 2ω amplitude does not go to zero, it only goes a bit down at $\theta = 65°$, and the 4ω goes to a lower value, but at a different inflow angle of $\theta = 50°$. These observations for cases 1

and 2 may lead to the conclusion that this phenomenon is heavily influenced by numerical effects, such as the RANS model, and that in experimental tests, the complexity of the flow would not lead to zero force difference for any inflow angles resulting in more continuous amplitude curves. Even though there are significant differences in how the harmonic force contributions for ΔF_D behave in Case 1 and 2, the same fact still remains that the amplitudes for the higher-order force difference contributions are dominant resulting in an almost strictly nonlinear force difference, while the linear force contribution dominates the force of the top cylinder making $F_{D,top}$ almost linear.

The harmonic force contributions of $F_{L,top}$ and ΔF_L for Case 2 are shown in Figure 5.32. Much in the same way as $F_{D,top}$ the harmonic force contributions for $F_{L,top}$ are very similar in cases 1 and 2, but with slightly lower amplitudes in Case 2. The 2ω amplitude is almost equally dominant as the 1ω amplitude for most inflow angles, with the exception of angles lower than $\theta = 35°$ where the 1ω amplitude has a second peak which dominates the force. The same trend of the 1ω amplitude going towards zero for an inflow angle of $\theta = 45°$ is found in both cases. This was explained in Case 1 as being due to the inner vertexes of the cylinders lining up with the oscillation motion axis making the force entirely nonlinear, but this does not happen in Case 2 since the spacing between the cylinders is increased. It is however at $\theta = 45°$ that the cylinders are exactly diamond-shaped which means that the upstream cylinder should in theory split the flow equally to either side. It is probably this property that creates the nonlinearity in both cases, but the explanation in Case 1 may still be valid for that particular case. Another aspect of the first figure is that at the second peak of the 1ω amplitude, there is also a small 3ω peak. This peak exists for both cases, but it is the only amplitude peak that is larger in Case 2 than in Case 1. This may be traced back to Case 2 being, in general, more influenced by the nonlinear contributions since the wakes have more space to form between the cylinders.

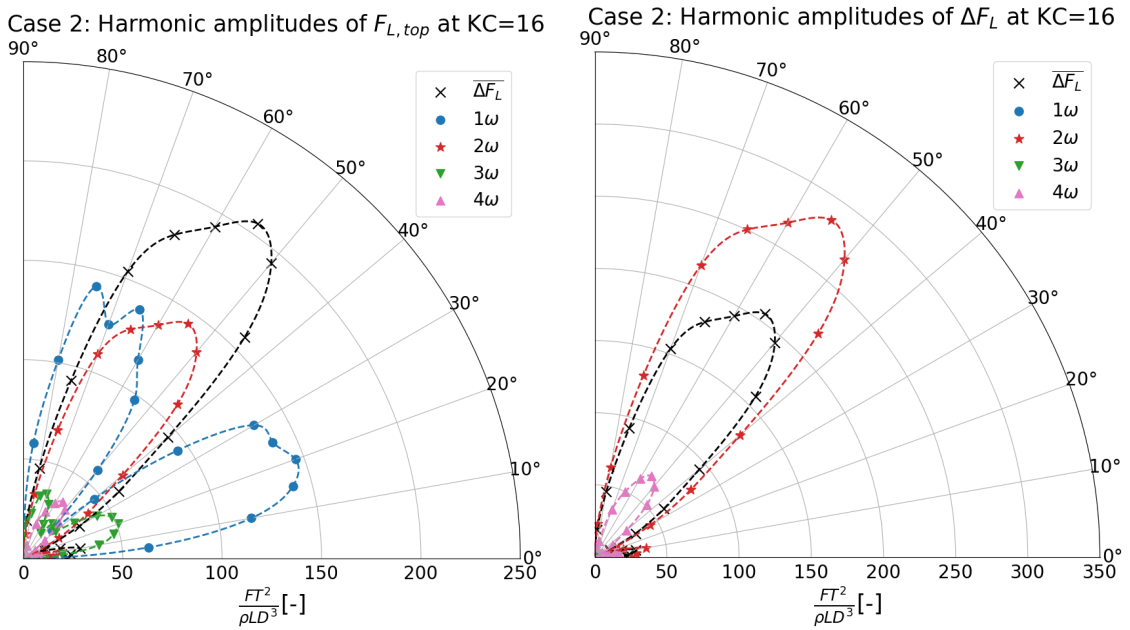

(a) A polar plot showing the harmonic force amplitudes of $F_{L,top}$ for Case 2 at KC = 16 for all inflow angles.

(b) A polar plot showing the harmonic force amplitudes of ΔF_L for Case 2 at KC = 16 for all inflow angles.

Figure 5.32: Polar plots showing the harmonic force amplitudes of $F_{L,top}$ and ΔF_L for Case 2 at KC = 16 for all inflow angles.

The harmonic amplitudes for ΔF_L for Case 2 in Figure 5.32b show similar properties to the same amplitudes in Case 1, but the values are somewhat lower. This indicates that the increased spacing between the cylinders affects the lift force since the fluid flow is impacting the inner faces of the cylinders with less intensity, as the flow is moving slower between the cylinders in Case 2 than in Case 1. The amplitude peaks are less rounded in Case 2 than in Case 1 which means that Case 2 has lift contributions on a smaller range of inflow angles than Case 1. Also, the location of the peak has moved to $\theta = 55°$ which is a lower inflow angle than in Case 1 where the peak was located at $\theta = 60°$. This shift also happened for the main peaks for $F_{L,top}$. In the same way as for Case 1 the 2ω and 4ω amplitudes are 180° out of phase for the top and bottom cylinders and are therefore added together when creating ΔF_L, while the 1ω and 3ω amplitudes are in phase and are canceled out. This again leads to the 2ω and 4ω amplitudes having the same shapes in both figures, but twice the amplitude in the second figure, which once more shows that an improved load formulation than the existing Morison's equation is needed to fully capture the hydrodynamic loads of the system. Polar plots directly comparing the different harmonic force amplitudes of both the drag and lift forces of Case 1 and 2 can be found in Appendix E.

The last part of this study is to look briefly into the vorticity of Case 1 and Case 2 at a selection of inflow angles which is $\theta = 0°$, 45°, 65°, and 90°. The vorticity describes the spinning motion of the fluid, meaning that it describes the wakes, and since these cases are two-dimensional in the xz-plane, the vorticity has no y-component but runs in parallel to the y-axis. The 2D vorticity in the xz-plane is expressed by [Faltinsen 1993] as

$$\omega_y = \frac{\partial u}{\partial z} - \frac{\partial w}{\partial x}, \tag{5.2}$$

where u and w are the fluid velocities in the x and z directions. Since the RANS model is being used to model the turbulence in these cases much of the vorticity is smeared out due to the averaging, and the vorticity of Case 1 and Case 2 is therefore not completely accurate but can be used to get the general idea of how the wakes are formed in these cases. The vorticity for the range of inflow angles is shown in Figure 5.33 for both cases. In these figures, a red color indicates vortexes that spin counter-clockwise, while a blue color indicates a clockwise spin. The vorticity images were all created from the tests with the maximum amount of wakes, which was for KC = 21.5 at points of maximum oscillation velocity.

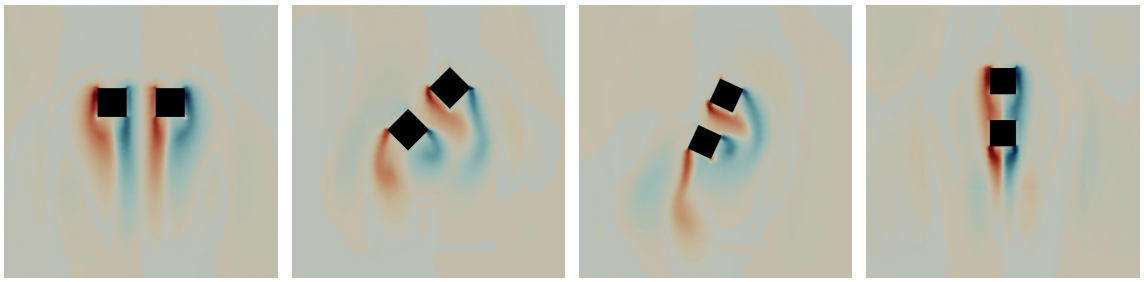

(a) The vorticity of Case 1 at KC = 21.5 for an inflow angle of $\theta = 0°$.

(b) The vorticity of Case 1 at KC = 21.5 for an inflow angle of $\theta = 45°$.

(c) The vorticity of Case 1 at KC = 21.5 for an inflow angle of $\theta = 65°$.

(d) The vorticity of Case 1 at KC = 21.5 for an inflow angle of $\theta = 90°$.

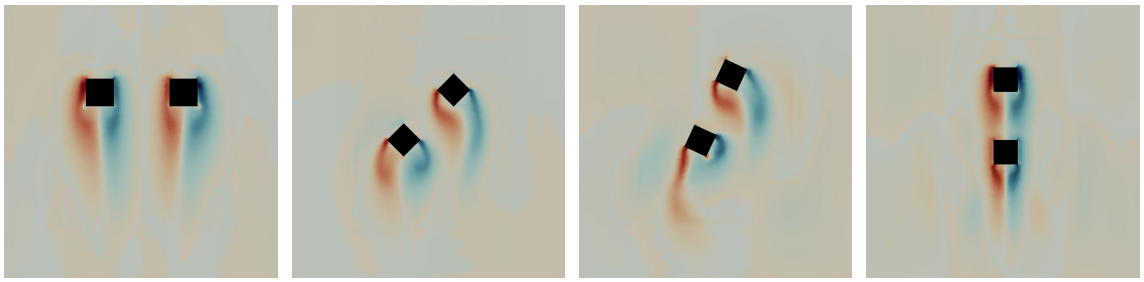

(e) The vorticity of Case 2 at KC = 21.5 for an inflow angle of $\theta = 0°$.

(f) The vorticity of Case 2 at KC = 21.5 for an inflow angle of $\theta = 45°$.

(g) The vorticity of Case 2 at KC = 21.5 for an inflow angle of $\theta = 65°$.

(h) The vorticity of Case 2 at KC = 21.5 for an inflow angle of $\theta = 90°$.

Figure 5.33: The vorticity of Case 1 and Case 2 at KC = 21.5 for inflow angles of $\theta = 0°$, 45°, 65°, and 90°.

For an inflow angle of $\theta = 0°$ the vorticity coming from the inner faces of the cylinders has a darker color in Case 1 than in Case 2, which is because the tighter spacing in Case 1 moves the fluid faster through the system. This does also back the idea that Case 1 experiences some degree of perforation effect, while the effect is much less prevalent in Case 2. The vorticity for an inflow angle of $\theta = 45°$ shows that the inner vorticity of the upstream cylinder is thoroughly forced through the middle of the cylinders in Case 1, and while this also happens in Case 2, it is allowed to move further away from the body. This may lead to the upstream cylinder being exposed to less force than in Case 1. Additionally, the vorticity of the downstream cylinder is very different on the inside and outside of the cylinder in Case 1, while in Case 2 they are much more equal. This is most likely due to more fluid being allowed to pass through the middle of the cylinders inducing a larger vortex shedding off of the inner vertex of the downstream cylinder in Case 2 than in Case 1. The first finding from $\theta = 45°$ is also found for $\theta = 65°$ where the inner vorticity of the upstream cylinder can move more freely away from the body while still being pushed between the cylinders. The inner vorticity of the downstream cylinder seems to be more intense also for this inflow angle, but not so much that it equals the outer vorticity. The final inflow angle of $\theta = 90°$ shows that the vorticity of the upstream cylinder in Case 1 heavily impacts the downstream cylinder, while for Case 2 the vorticity dies out to a certain degree before impacting the downstream cylinder. This is again due to the cylinders going from being in the same flow regime in Case 1 to being in different regimes in Case 2, as proposed by [Zdravkovich 1977]. Other than that, the vorticity behaves similarly in both cases.

A better turbulence model than RANS would have shown more of the vortex shedding

and would have done a better job of showcasing the general vorticity in these images, but as previously mentioned it was the optimal model for these two-dimensional cases. Also, the vorticity of especially $\theta = 0°$ and $90°$ seems to be very symmetrical, and a numerical perturbation should be added to the flow field to encourage more vortex shedding and more fluctuation in the flow. However, some wakes can be seen despite the drawbacks of the turbulence model. For instance, at an inflow angle of $\theta = 65°$, the slightly blue area to the left of the downstream cylinder in both cases is a vortex spinning in a clockwise motion. Similar vortexes can be seen for $\theta = 90°$ where small red and blue areas are present on either side of the vorticity of the downstream cylinder in both cases. These areas are two vortexes that have opposite spinning motions and were shed by the downstream cylinder around half a second earlier when the system was moving with a maximum velocity in the opposite direction. These vortexes, and many more that are blended out by the averaging in these cases, would have been shown much more clearly if a better turbulence model was used.

5.2.3 Horizontal misalignment of the cylinders

These results are gathered from the three cases created with Case 2 as a base, where the downstream cylinder is shifted 3, 5, and 10 percent of the cylinder diameter as described in Section 4.1.3. The cases were tested for a range of inflow angles from $\theta = 0°$ to $90°$, with a 5-degree step size, which is the same range as the one used in Section 5.2.2. The results will be presented from their harmonic force amplitudes in polar plots where the three cases will be presented alongside a reference case with no shift of the downstream cylinder. All of the tests were performed for KC = 16, and with an oscillation period of $T = 1\,s$. Many of the same properties were seen for these cases as for the cases in the last section, and therefore not all harmonic force amplitudes will be shown, as many of them were negligible. Also, the hydrodynamic phenomena seen in the plots will not be discussed in this section as they have been covered in previous sections. Only the effect the cylinder shifting has on the phenomena will be studied. The effects on the drag and lift forces will be presented separately as the combination of the two would make the plots difficult to read both due to the number of curves and also due to the difference in amplitude.

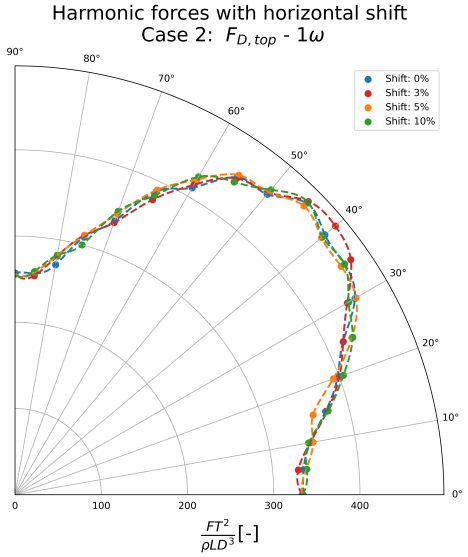

(a) A polar plot showing the 1ω harmonic force amplitude of $F_{D,top}$ for Case 2 at KC = 16 for different cylinder misalignments.

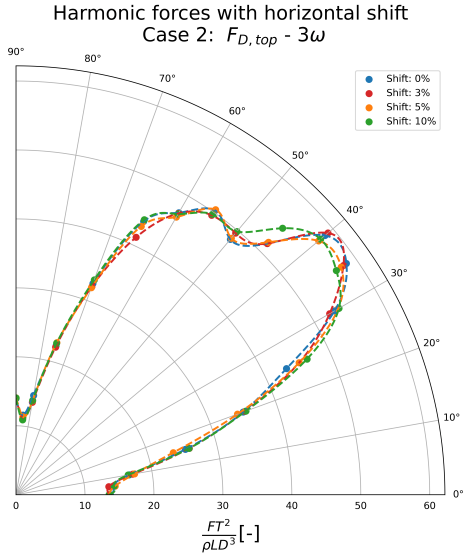

(b) A polar plot showing the 3ω harmonic force amplitude of $F_{D,top}$ for Case 2 at KC = 16 for different cylinder misalignments.

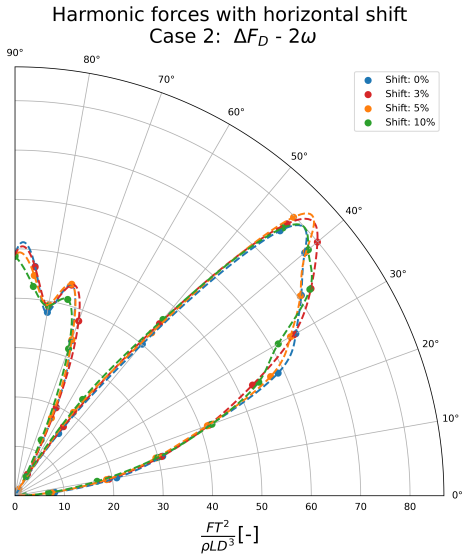

(c) A polar plot showing the 2ω harmonic force amplitude of ΔF_D for Case 2 at KC = 16 for different cylinder misalignments.

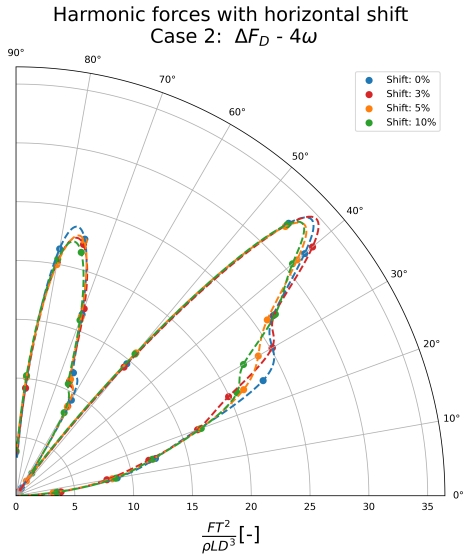

(d) A polar plot showing the 4ω harmonic force amplitude of ΔF_D for Case 2 at KC = 16 for different cylinder misalignments.

Figure 5.34: Polar plots showing the 2ω and 4ω harmonic force amplitudes of ΔF_D for Case 2 at KC = 16 for a cylinder shift of 0 %, 3 %, 5 %, and 10 % of the cylinder diameter.

Figure 5.34 shows the results of the 1ω and 3ω harmonic force amplitudes for $F_{D,top}$ and the 2ω and 4ω harmonic force amplitudes for ΔF_D in Case 2 at KC = 16 for the four different cylinder misalignments. In general, the figures show that the misalignments do not affect the harmonic amplitudes in any significant manner, or in any special pattern. Which case results in the highest amplitudes varies between all three of the new misalignment cases, but they all have generally larger amplitudes for the drag force of the top cylinder than the case with zero misalignments for most inflow angles, even though the amplitude differences are not significant. The force difference seems less negatively affected by the misalignments for the 4ω amplitude where it is the case with zero misalignments that has the largest amplitudes for most inflow angles, while the 2ω amplitude behaves more similarly to the amplitudes of the drag force.

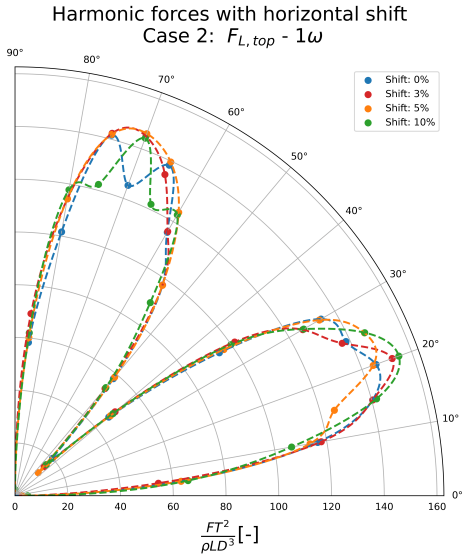

(a) A polar plot showing the 1ω harmonic force amplitude of $F_{L,top}$ for Case 2 at KC = 16 for different cylinder misalignments.

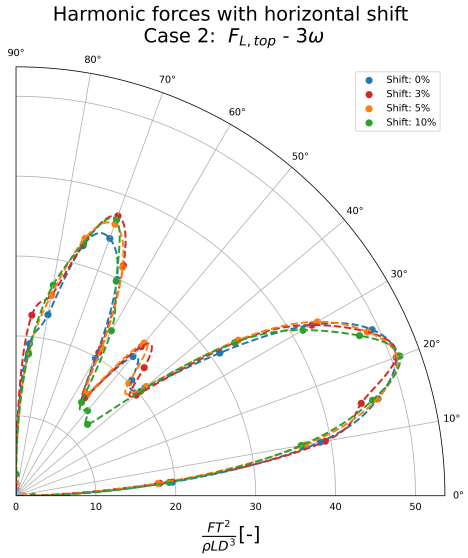

(b) A polar plot showing the 3ω harmonic force amplitude of $F_{L,top}$ for Case 2 at KC = 16 for different cylinder misalignments.

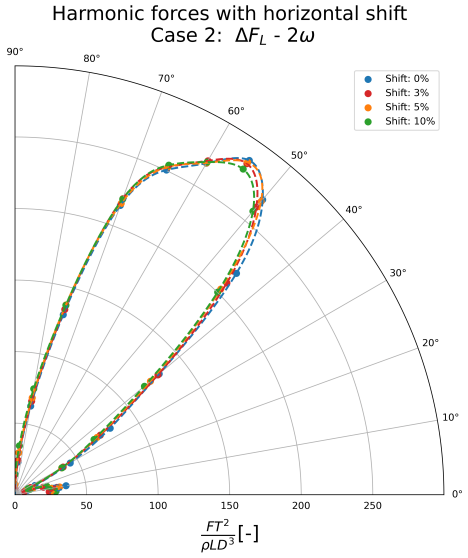

(c) A polar plot showing the 2ω harmonic force amplitude of ΔF_L for Case 2 at KC = 16 for different cylinder misalignments.

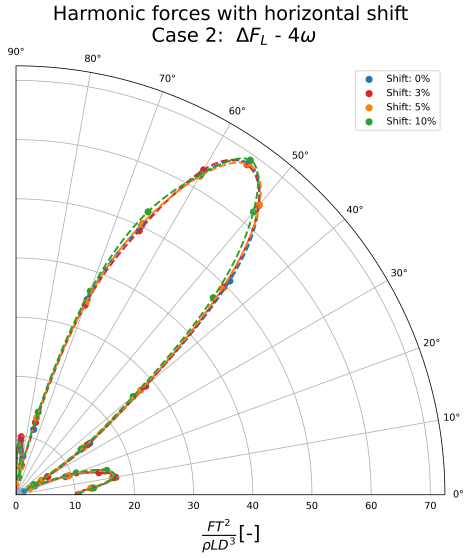

(d) A polar plot showing the 4ω harmonic force amplitude of ΔF_L for Case 2 at KC = 16 for different cylinder misalignments.

Figure 5.35: Polar plots showing the 2ω and 4ω harmonic force amplitudes of ΔF_L for Case 2 at KC = 16 for a cylinder shift of 0 %, 3 %, 5 %, and 10 % of the cylinder diameter.

Much of the same can be seen in Figure 5.35 which shows the results of the harmonic force amplitudes for $F_{L,top}$ and ΔF_L in Case 2 at KC = 16 for the four different cylinder misalignments. Many of the same trends can be seen in the first two figures for the lift force amplitudes of the top cylinder as for the drag force amplitudes, where the misaligned cases in general have higher amplitudes than the reference case. Also, the first of the two peaks for the 1ω amplitude show that of the four cases, the reference case and the case with a 10 % misalignment both experience some anomalies for inflow angles between $\theta = 60°$ and 80°. These anomalies are not present in the 3ω amplitude, which means that there may be much numerical uncertainty and instability interfering with some of the results as a consequence of either the turbulence model, the mesh, the time step, or other factors. The

force difference amplitudes in the last two figures are much more smooth for all four cases and show a smaller level of uncertainty than the drag amplitudes, which is probably not due to higher stability in the system, but rather a poor refinement of the higher harmonic lift force amplitudes due to the turbulence model.

One effect that may be surprising is that the results coincide at $\theta = 90°$ in all of the figures, while at lower inflow angles there are more disparities. This makes perfect sense for the figures where the amplitude values at this point are zero, but for the figures where they are not, it may seem unnatural since the misalignments mean that a portion of the downstream cylinder is directly hit by the fluid flow and that the vorticity of the upstream cylinder impacts it unevenly. This should mean that the results differed more than they do, but this is not the case. This is because the magnitudes of the misalignments are very small in the cases even though they should be significant, but due to the size of the mesh that has been used the misalignments do not account for that much. The mesh that was used in the cases is Mesh 2 from Table 5.1 that is shown later in Section 5.4. The reasons for using this mesh will be explained in that section. With a general cell length of $\Delta x = 0.001667\,m$, and a cylinder diameter of $D = 0.05\,m$, the actual size of the misalignments becomes apparent. This means that a 3 % shift equals less than one cell, a 5 % shift equals one and a half cells, and a 10 % shift equals three cells. When this is combined with the fact that the RANS turbulence model does not simulate the wakes well enough it becomes obvious that most of the effects are averaged and smeared, and that both a finer mesh and a better turbulence model should have been used for this analysis so that the finer details of the flow and thus the small effects of the misalignments would be captured.

In spite of this, the study did procure relevant results and indications which show that the misalignment caused by independent movements of experimental test rigs can pollute the test data and that one should be cautious of these issues, since the amplitudes may become larger or smaller at seemingly random places. It does, however, seem likely that the bandpass filtering used for the experimental cases as explained in Section 3.4 will filter out most of the pollution caused by these movements. Numerically, the independent movement is of course not a problem as the only misalignments that should be possible to create are made on purpose, as has been done in this analysis. This can also be done to find uncertainty levels that can be applied to the numerical data to better mimic experimental data, or it can be done as a way of refining experimental data by tuning it using the misalignment uncertainty results to get rid of any pollution that is left after filtering the data.

5.2.4 The effect of the spacing between the cylinders

In this section, the results from the numerical models of two square cylinders with increasing spacing between them are shown. These tests were done to thoroughly study the effects of the spacing between the cylinders, and what would happen to the harmonic force components when the cylinders were moved away from each other. The chosen spacings for the models started at $s/D = 0.2$, where s is the distance between the cylinders and D is the cylinder diameter. The next ten cases were then created at intervals of 0.2 until $s/D = 2.2$ before creating six cases with $s/D = 2.5, ...5.0$ with intervals of 0.5. A larger interval was chosen for the larger spacings as the dependency on the distance was expected to drop as the distance increased. The creation of the cases is also discussed earlier in Section 4.1.4. The effect the spacing between the cylinders has on the added mass, damping, and drag coefficients of the two cylinders will also be covered in this section. The same coefficient

model that was used to calculate the coefficients for cases 1 and 2 in Section 5.2.1 is also implemented for these cases.

All of the cases presented in this section were performed using the same parameters as previous numerical tests, with KC=16 and an oscillation period of $T = 1\,s$, again for better correspondence with the other cases so that they can more easily be compared. The most interesting part of these models are the harmonic force amplitudes and coefficients, and therefore the standard force curve figures for the cases will not be presented here.

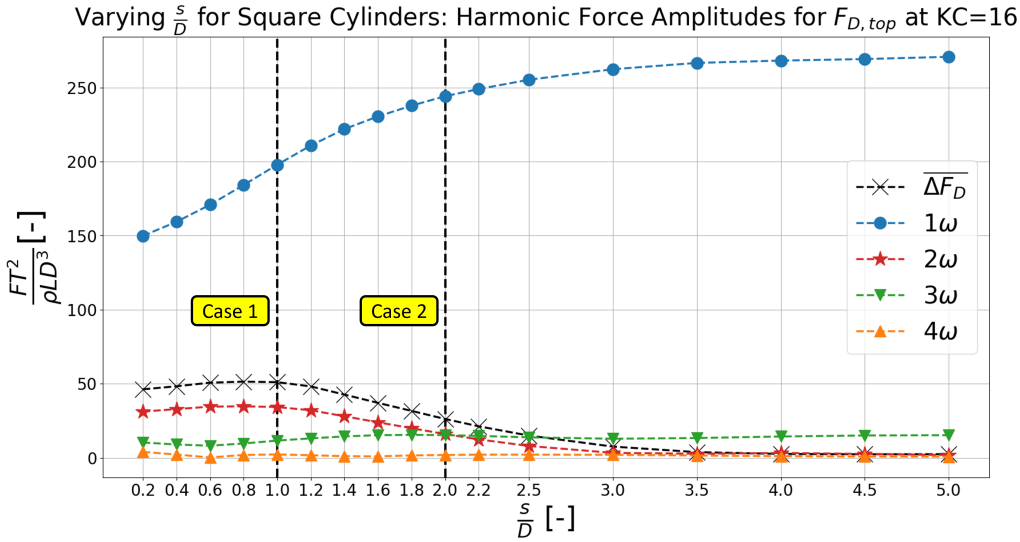

Figure 5.36: The harmonic force amplitudes of $F_{D,top}$ for the square cylinder cases with a varying s/D at KC = 16.

In Figure 5.36 the harmonic force amplitudes of $F_{D,top}$ for the cases with varying s/D at KC=16 are shown. In the same way as in previous numerical models, the results of the top and bottom cylinders are too close to necessitate individual presentations, and thus the findings from this figure are also valid for the drag force of the bottom cylinder. Two vertical lines have also been plotted and labeled in the figure to better show exactly which s/D values correspond with cases 1 and 2. From this figure, the dependency of the distance between the cylinders on the harmonic drag force amplitudes, and thus the drag force, is obvious. The 1ω force amplitude is rapidly increasing with increasing spacing, before evening out after around $s/D = 3.0$, which corresponds to a case with three times the cylinder spacing as Case 1. The value that it seems the 1ω amplitude converges towards is roughly 80 % larger than its initial value at $s/D = 0.2$. This convergence implies that the effect the spacing has on the force results will diminish with an increased s/D, and after a certain distance between the cylinders each cylinder will behave as a single cylinder in infinite fluid, and the hydrodynamic interaction between the cylinders is gone.

The statement that Case 1 has both cylinders in the same flow regime and Case 2 has each cylinder in a different flow regime, is not reflected that well from the 1ω amplitude. It is however clear from the 2ω amplitude and to a lesser degree the 3ω and 4ω amplitudes, that there is a change in the regimes between Case 1 and Case 2. The 2ω harmonic force amplitude is slightly increasing from $s/D = 0.2$ until $s/D = 1.0$, which is Case 1, before decreasing towards a negligible value at around $s/D = 3.0$, which is the same spacing value where the 1ω amplitude flattened out. The 3ω amplitude is subtly decreasing from $s/D = 0.2$ to $s/D = 0.6$ before increasing to a constant value at $s/D = 2$, while the 4ω amplitude is almost constant for all spacings, but has some fluctuating values before

$s/D = 1.0$. The mean force difference curve reflects the same as the 2ω amplitude curve but with generally higher values.

These findings imply that for the cylinder spacings that are smaller than Case 1, the drag force is at its most nonlinear since it is in this first region that the higher-order harmonic force amplitudes are largest, while the linear amplitude is the smallest. For spacings between $s/D = 1.0$ and around $s/D = 3.0$, the next region is located and it is here the nonlinearity of the drag force diminishes, and where the linear harmonic force amplitudes start to converge. After $s/D = 3.0$ the drag force is almost entirely linear, with a small contribution of the 3ω amplitude, and the two cylinders are not really treated as a pair of cylinders in close proximity to each other, but rather as independent cylinders. [Havel et al. 2001] found that for two-dimensional cases the so-called close-spacing regime, which is where the two cylinders will be in the same regime, will end at a spacing value of $s/D = 1.5$, which corresponds well with the results in Figure 5.36. They also claim that there is no evidence of the existence of this regime for three-dimensional cases.

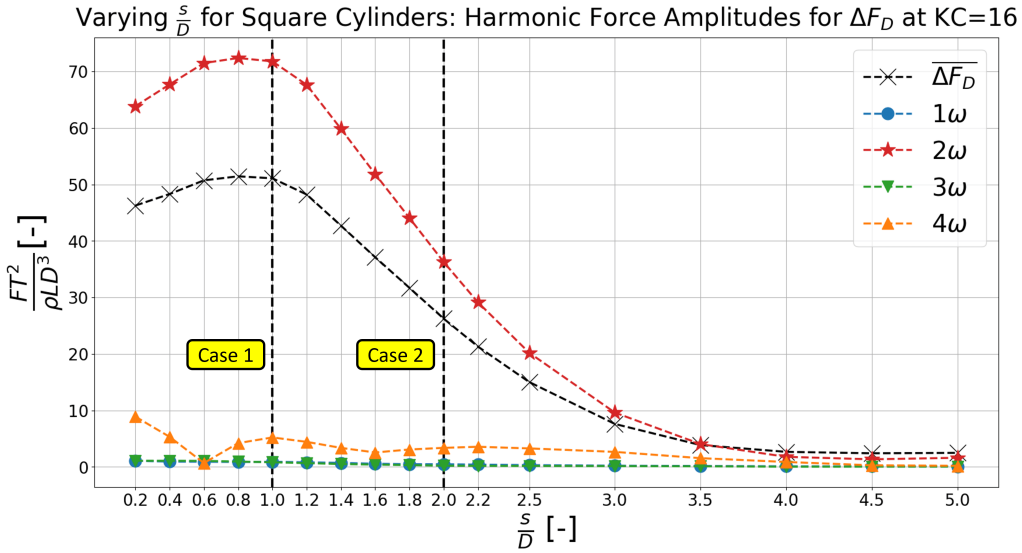

Figure 5.37: The harmonic force amplitudes of ΔF_D for the square cylinder cases with a varying s/D at KC = 16.

Figure 5.37 shows the harmonic force amplitudes of ΔF_D for the cases with varying s/D at KC=16. The same behavior of the harmonic force components is seen here as for previous models. The 1ω and 3ω are canceled out since these contributions of the two cylinders are in phase with each other, while the 2ω and 4ω amplitudes keep their shapes and double in value since they are 180° out of phase with each other, and are added together when the force difference is calculated. The same harmonic behaviors as for $F_{D,top}$ that leads to the identification of the flow regimes are also present here. Before $s/D = 0.8$ the 2ω amplitude increases quite a bit before rapidly decreasing after $s/D = 1.0$, before stabilizing at small values after $s/D = 3.5$. In the same way as before, the mean force difference has the same shape as the 2ω curve, but with different amplitude values. In Section 5.2.1 it was concluded that OpenFOAM overestimates the 2ω amplitude with regards to three-dimensional experiments while managing to correctly model the mean force difference, which explains this difference between the curves. The 4ω amplitude curve seems to increase and decrease at irregular intervals before converging towards a low value at around $s/D = 3.0$, and as previously mentioned, the 1ω and 3ω amplitudes are negligible for all spacing values. This implies many of the same ideas as the harmonic

components of $F_{D,top}$ did, which is that the nonlinearity of the drag force is nowhere near as prevalent after around $^s/_D = 3.0$ as for smaller spacing values and that for large enough spacings, the drag force is almost entirely linear.

From these results, it would seem that for spacing values larger than $^s/_D = 3.0$ ΔF_D is almost negligible, and only the odd-numbered harmonic force amplitudes have an effect on $F_{D,top}$, and thus also on $F_{D,bot}$. This implies that for single cylinders, and pairs of cylinders at sufficiently large distances, the load formulation from Morison's equation will capture the drag force almost perfectly, while for smaller spacing values there is still a need for a better load formulation to also include the even-numbered harmonic force contributions.

When creating these models an additional function was added to the `controlDict`, as explained in Section 4.2.2, that is able to extrapolate the drag coefficient directly from OpenFOAM. This means that the drag coefficient from the model created from the output forces, coefficient equations, and constructed acceleration and velocity data can be compared with the drag coefficient taken straight from the numerical solver, which can validate or invalidate the calculation model presented in Section 2.8. The coefficients will be presented in the same way as in Section 5.2.1, With individual coefficients for the top and bottom cylinders as there were some discrepancies between them. While for the other cases, the drag coefficient that was presented was the average coefficient, both the drag coefficients of the top and bottom cylinder are presented for these models. This is done so that they can be better compared to the drag coefficient from OpenFOAM, as well as to show the differences between them.

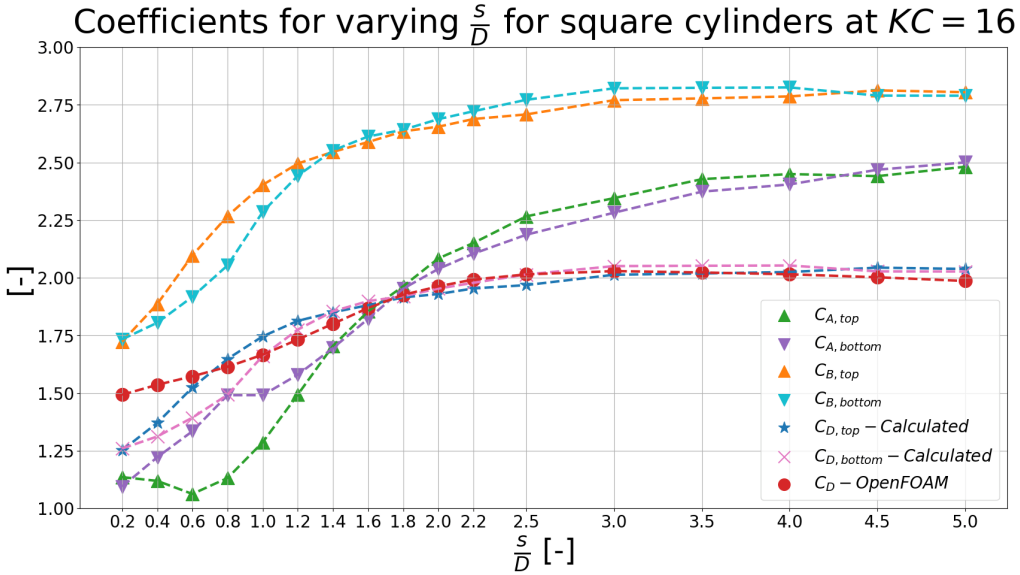

Figure 5.38: The added mass, damping, and drag coefficients for the square cylinder cases with a varying $^s/_D$ at KC = 16.

Figure 5.38 shows the added mass, damping, and drag coefficients of the top and bottom cylinders that are calculated based on the presented model, as well as the drag coefficient taken from OpenFOAM. The first takeaway from the figure is that the added mass coefficients are probably too high as for the larger spacings they should converge toward the reference added mass of a square cylinder which is 1.51, but they end up at around 2.5. This may however not be entirely wrong, but rather a consequence of the numerical models being tested in an oscillating flow, while the reference added masses presented by [Pettersen 2007] were probably found at steady flows. This is however pure speculation

and no conclusions can be drawn without extensive testing and modeling.

The drag coefficients from the top cylinder, bottom cylinder, and the one taken from OpenFOAM, which is averaged, coincide with each other closely after around $^{s}/_{D} = 1.6$. This is very promising with regards to the validation of the calculation model and shows that at least for these larger spacings at KC=16 the model will adequately calculate the drag coefficients, and thus the damping coefficients, of the system, when compared to the internal drag coefficient calculations done by the OpenFOAM solver. Before $^{s}/_{D} = 1.6$ there are a lot more differences between both the calculated drag coefficients and between them and the drag coefficient from OpenFOAM. This is possibly due to several reasons. The smaller spacing values may lead to a much more complex flow that the OpenFOAM function manages to capture, but not the calculation model, or the smearing from the RANS turbulence model may affect the force output that the calculated coefficients are based on and not the drag coefficient output.

Even though the discrepancies exist at these smaller spacings, the fact that the drag coefficients coincide as well as they do for larger spacing values and that they all converge at a value slightly higher than $C_D = 2.0$ is a very promising result. [Havel et al. 2001] found that the two-dimensional drag coefficient of a square cylinder converges at $C_{D\infty} = 2.05$ for the upstream cylinder and $C_{D\infty} = 2.08$ for the downstream cylinder when conducting experiments at $\mathrm{Re} = 22\,000$. [Hoerner 1965] also found that the drag coefficient of a two-dimensional square cylinder would be $C_D = 2.05$ for a range of Reynolds numbers between $\mathrm{Re} = 10^4$ to $\mathrm{Re} = 10^6$. The cases presented in this thesis have been modeled by the KC number, and not the Reynolds number, but by using Equation 2.57 and Equation 2.51, the Reynolds number for these model cases at $\mathrm{KC} = 16$ can be found to be $\mathrm{Re} = 40\,000$, which is the same order of magnitude as [Havel et al. 2001] and within the same range as [Hoerner 1965]. This means that the drag coefficient gathered from OpenFOAM and the calculated drag coefficients concur well with the coefficients from the existing literature.

5.3 Comparison of 2D numerical results with 2D and 3D experimental results

This section will cover a more extensive comparison between the numerical and experimental tests for Case 1 and Case 2 than what has previously been done. In Section 5.2.1 the two-dimensional numerical results from OpenFOAM were presented and compared to the three-dimensional results from the experimental test results presented in Section 5.1. These comparisons could be misleading as there are many effects that are lost when going from two to three dimensions and vice versa. Therefore, to imply that the numerical solver falsely estimates some values may only be true when comparing 2D and 3D data. To account for this the two-dimensional results will first be compared to newer three-dimensional experimental results that come from recent experiments conducted by [Mikkelsen 2023], where master student Kristian Mikkelsen replicated the tests from the specialization project and ran them again after tweaking some parameters to achieve better and less polluted results. These new experiments use a length-to-diameter ratio of $^{L}/_{D} = 3$, which means that these experimental values are probably different than the ones presented earlier in this thesis with $^{L}/_{D} = 1$. After this has been done, the numerical results will be compared with the experimental results from [Reiten 2022].

During his master's thesis in the spring of 2022, Henrik Reiten conducted experiments for Case 1 and Case 2 in a similar fashion to the ones conducted during the specialization

project for this thesis, but he did it by attaching the actuator plates on either end of the cylinders, and not in the middle. This meant that his experiments were as close to two-dimensional as possible. Comparing the 2D numerical results from this thesis with his 2D experimental results is expected to give a much closer match than when compared with the 3D experimental results.

Kristian Mikkelsen also managed to rotate Case 2 between $\theta = 90°$ and $35°$ with 5-degree increments for his thesis. The limitations of the rig made it impossible to rotate the case at lower angles. This means that the numerical data for Case 2 with a varying inflow angle from Section 5.2.2 can also be compared to experimental results, and was done as the last part of this comparison study. For both the 3D and 2D comparisons and the inflow angle comparison it is only the 1ω and 2ω harmonic force components that will be compared. All of the data sets in this section have been non-dimensionalized by their respective parameters.

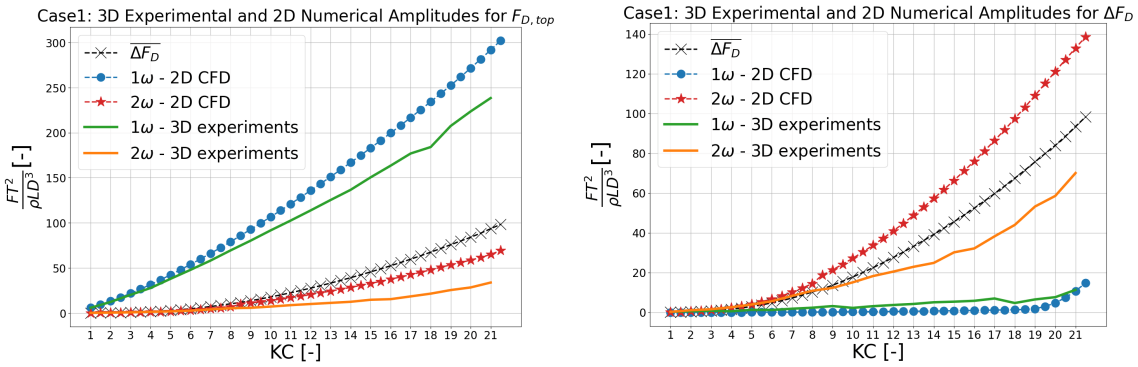

(a) A comparison of 3D experimental test results and 2D numerical test results for $F_{D,top}$ in Case 1.

(b) A comparison of 3D experimental test results and 2D numerical test results for ΔF_D in Case 1.

Figure 5.39: A comparison of 3D experimental test results and 2D numerical test results for $F_{D,top}$ and ΔF_D in Case 1. The experimental results are gathered from [Mikkelsen 2023].

First, the three-dimensional experimental results and the two-dimensional numerical results of Case 1 have been compared, and the comparisons of the harmonic force amplitudes are presented in Figure 5.39. In the first figure, both the experimental and numerical 1ω and 2ω amplitudes have similar shapes, but the numerical results are generally higher, which for the 1ω amplitude is an opposite behavior as the previous comparisons, meaning that the 3D data are heavily influenced by the length of the cylinders, which is to be expected. The 2ω amplitude in both figures shows the same tendency as before by having significantly higher amplitude values. This shows that the numerical models seem to simulate a more nonlinear drag force in two dimensions than what is captured experimentally in three dimensions.

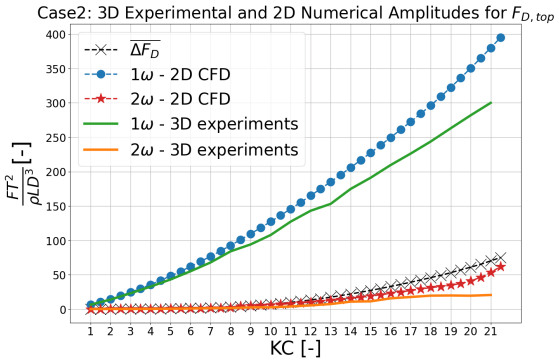

(a) A comparison of 3D experimental test results and 2D numerical test results for $F_{D,top}$ in Case 2.

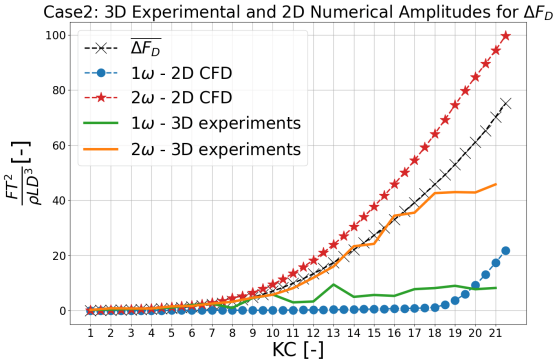

(b) A comparison of 3D experimental test results and 2D numerical test results for ΔF_D in Case 2.

Figure 5.40: A comparison of 3D experimental test results and 2D numerical test results for $F_{D,top}$ and ΔF_D in Case 2. The experimental results are gathered from [Mikkelsen 2023].

The comparison between the 3D experimental and 2D numerical results for Case 2 is shown in Figure 5.40. Here, much of the same can be said as for Case 1, but Case 2 does have 1ω and 2ω amplitudes that are much closer in value to the numerical model than in Case 1. In the first figure, the 2ω amplitudes for the 3D and 2D data are close to equal up until around KC $= 14$, while for Case 1 the similarities ended at around KC $= 9$. Also, the 2ω amplitude for ΔF_D seems to follow the numerical mean force difference closely until KC $= 18$ when it diverges from it, while the 1ω amplitudes in the same figure differ much more than they did in Case 1. It may seem that the 2D numerical model becomes better at estimating the harmonic components when the spacing between the cylinders increases, but with only two cases it is not viable to draw any conclusions.

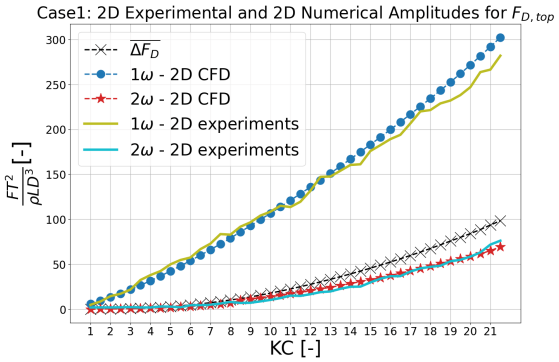

(a) A comparison of 2D experimental test results and 2D numerical test results for $F_{D,top}$ in Case 1.

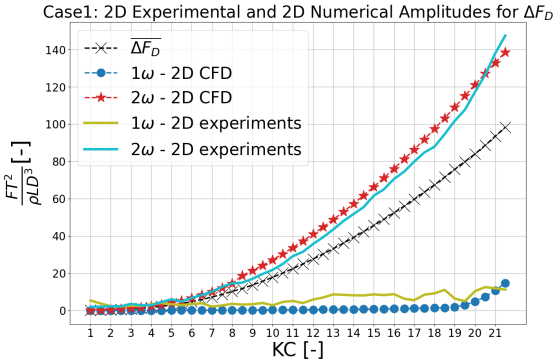

(b) A comparison of 2D experimental test results and 2D numerical test results for ΔF_D in Case 1.

Figure 5.41: A comparison of 2D experimental test results and 2D numerical test results for $F_{D,top}$ and ΔF_D in Case 1. The experimental results are gathered from [Reiten 2022].

When comparing the two-dimensional experimental results with the two-dimensional numerical results, the differences become much smaller. Figure 5.41 shows this comparison for Case 1. The 1ω amplitudes are very similar for all but the highest KC numbers, and the 2ω amplitudes are as good as equal for all KC values. This shows that there is a very

good correlation between the 2D experiments and the 2D numerical model and that the model is capable of estimating the two first harmonic components at this cylinder spacing with high precision and certainty. There are some differences in the harmonic amplitudes for ΔF_D, but nowhere near the differences when comparing the three-dimensional experiments with the model. Here, the 2ω amplitude has very similar amplitude values, but the experimental amplitude is generally slightly lower than the numerical with the exception of after KC = 20 where it overtakes the numerical amplitude. The experimental 1ω amplitude has higher values than its numerical counterpart, but since the values are low there seems to be some disturbances of the experimental curve meaning that the apparent differences may not be real.

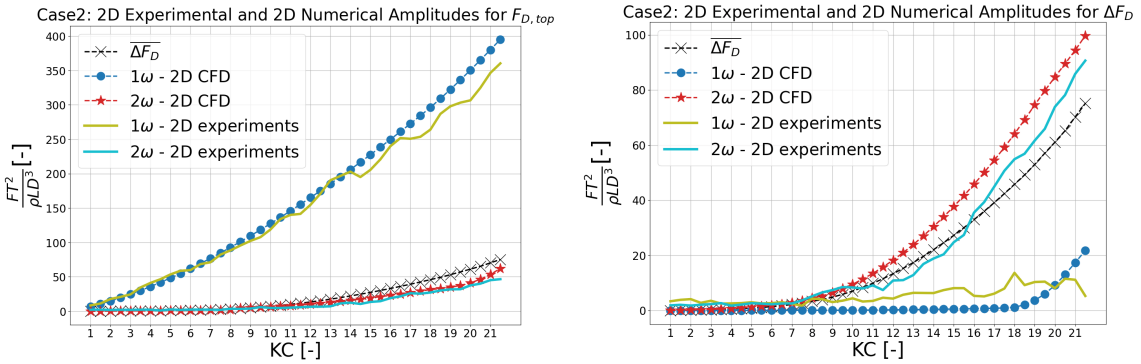

(a) A comparison of 2D experimental test results and 2D numerical test results for $F_{D,top}$ in Case 2.

(b) A comparison of 2D experimental test results and 2D numerical test results for ΔF_D in Case 2.

Figure 5.42: A comparison of 2D experimental test results and 2D numerical test results for $F_{D,top}$ and ΔF_D in Case 2. The experimental results are gathered from [Reiten 2022].

In the comparison of the two-dimensional experimental and numerical results for Case 2, there are still many similarities to Case 1, but the amplitudes seem to be slightly more different in this case. Figure 5.42 shows the comparison. In the first figure, the amplitudes behave similarly. The 1ω amplitudes are closely related until around KC = 14 where the experimental amplitude curve becomes lower, and the 2ω amplitude curves are once again very close to each other. This means that the model retains much of its precision and certainty also for this cylinder spacing. The force difference figure however shows a numerical 2ω amplitude that is much more different than the experimental curve than the same figure for Case 1, but they are still in a closer vicinity to each other than the corresponding figure in the comparison of the model and the 3D experiments. The 1ω amplitudes are also still behaving similarly as in Case 1, and the differences can probably be accounted to experimental data pollution.

This section shows that the numerical model created in OpenFOAM for this thesis can with good conscience be used as an estimation tool for two-dimensional experiments that uses the same test configurations and parameters as the numerical model, at least for a spacing of $s/D = 1$ and $s/D = 2$. The conformity of the 2D experimental and numerical results shows that even though there are probably many flaws in the model such as the imperfect RANS turbulence model, the data estimation is still good enough for these cases. When using the model as an estimation tool for three-dimensional experiments, there will be some discrepancies. So, for the best estimation results the model should be expanded into three dimensions while also replacing the turbulence model with for instance the LES model. These changes will however demand a lot more computational power and time to

achieve, and therefore, if used carefully, the two-dimensional model could still be a useful tool at least for estimations where the accuracy is less vital, and the computational speed is more important.

5.4 Sensitivity analysis

In this section, the meshes that have been used during this thesis and their characteristics will be discussed. Initially, the mesh that was used for the first tests of the numerical models was a rather coarse mesh that was chosen based on an example case that came with the `pvcFoam` solver from [Senthuran Ravinthrakumar 2023]. The example case only dealt with a single cylinder in an oscillating flow with very low motion amplitudes, meaning that the mesh could be too coarse for the numerical models in this thesis. It was therefore deemed necessary to perform a sensitivity analysis of the mesh with regard to both the cell size and the time step. Additionally, a sensitivity analysis was performed for the case-specific parameters of the inflow angle and the KC number. All the cases that have been run in this sensitivity analysis were run on the Schlichting 80-core computer.

5.4.1 Mesh size & time step sensitivity

Before the analysis, the numerical models described in Sections 4.1.1 and 4.1.2 had been run with the example mesh. It was therefore decided to run a selection of cases from Section 4.1.2 again with two finer meshes and compare the results to establish how fine the mesh should be for the rest of the cases, as well as if the already finished cases should be run again with a finer mesh. For the sensitivity analysis the example mesh was named Mesh 1, while two finer meshes called Mesh 2 and Mesh 3 were created. All of the mesh characteristics can be found in Table 5.1, and in Figure 5.43 the meshes close to the geometry of a cylinder are shown. A fourth mesh which would be twice as fine as the finest mesh in this analysis was also considered, but the number of cells needed would surpass the allowed threshold of the model, and the cases would crash. Even though this limit could be circumvented the amount of time and computational power it would take to run the cases at that mesh level would be too immense for the thesis. Moreover, as described later in this section, it was determined that there was no need for a finer mesh since the results were satisfactory enough with Mesh 2 for this stage of the project.

Table 5.1: The details of each mesh used in the convergence study. The $^{D}/_{\Delta x}$ column is only valid for the 90-degree configurations due to the geometry of the cells. The mesh level column refers to the mesh levels used in OpenFOAM, where an increase in the level equals Δx being divided by 2.

Name	Mesh Level	$\Delta x\,[m]$	$^{D}/_{\Delta x}\,[-]$	Number of cells	$\Delta t\,[s]$
Mesh 1	5	0.003333	14	10 132	0.001
Mesh 2	6	0.001667	28	32 196	0.0004
Mesh 3	7	0.000833	56	57 752	0.0002

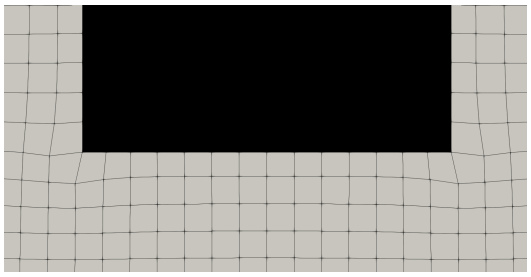

(a) Mesh 1 with the geometry of a square cylinder with 10 132 cells and $^{D}/_{\Delta x} = 14$.

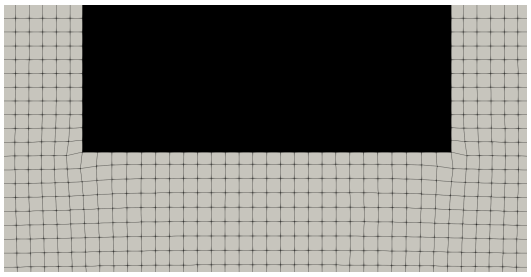

(b) Mesh 2 with the geometry of a square cylinder with 32 196 cells and $^{D}/_{\Delta x} = 28$.

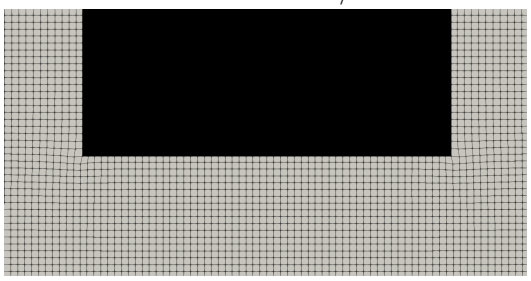

(c) Mesh 3 with the geometry of a square cylinder with 57 752 cells and $^{D}/_{\Delta x} = 56$.

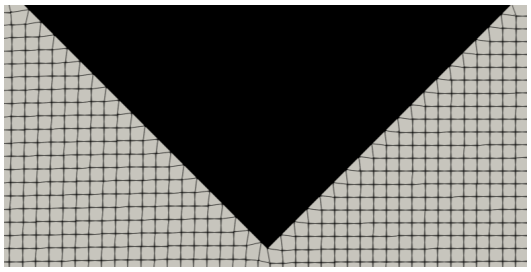

(d) Mesh 2 with the geometry of a square cylinder with an inflow angle of $\theta = 45°$.

Figure 5.43: A zoomed-in view of the meshes from Table 5.1 around the geometry of a square cylinder in a 90-degree configuration. Additionally, Mesh 2 for a 45-degree configuration is shown as a comparison of the mesh cell structure in the two configurations.

To get a clear indication of how sensitive the cases are to the mesh size and time step, cases 1 and 2 from Section 4.1.2 were run again with all three meshes and time steps. This process could also determine what type of mesh and time step that should be used for the other numerical cases. The results from this sensitivity analysis are shown in Figure 5.44, where the sensitivity of the 1ω and 2ω force components in the drag and lift directions can be studied. Each figure contains two parameters, the harmonic force output in the drag and lift directions, with three mesh iterations per parameter. This means that the sensitivity comparison can be done independently of both case and force direction.

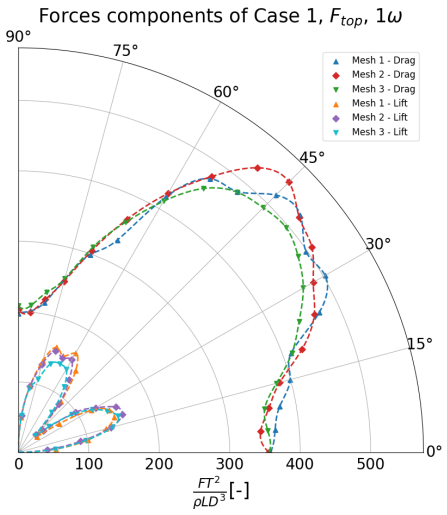

(a) The non-dimensional 1ω force outputs for the top cylinder in Case 1 for the three meshes.

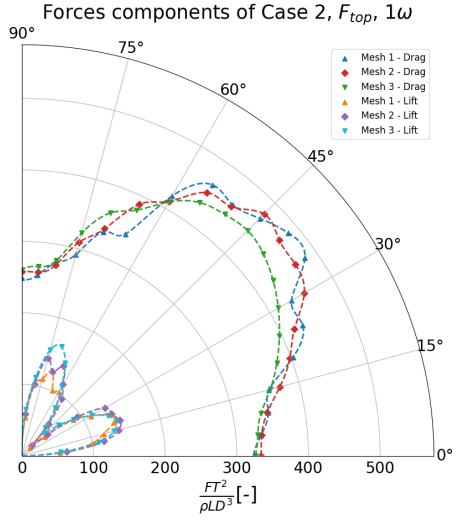

(b) The non-dimensional 1ω force outputs for the top cylinder in Case 2 for the three meshes.

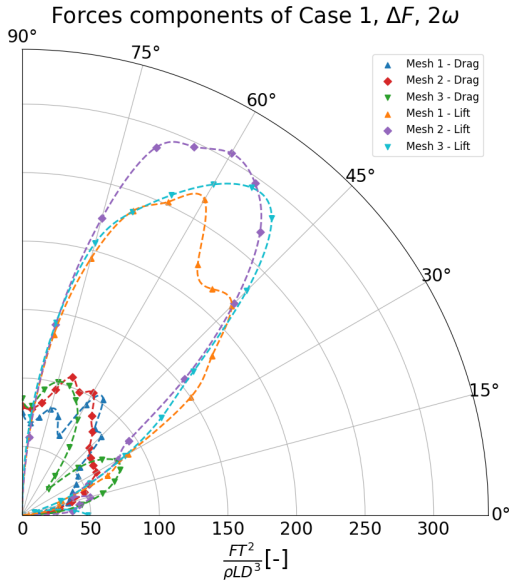

(c) The non-dimensional 2ω force outputs of the force difference of the cylinders in Case 1 for the three meshes.

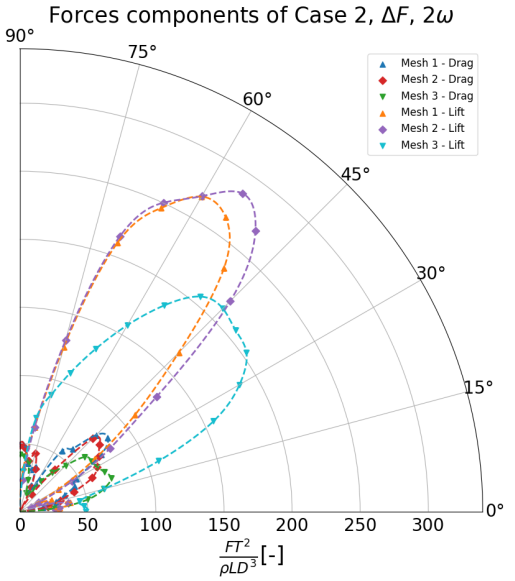

(d) The non-dimensional 2ω force outputs of the force difference of the cylinders in Case 2 for the three meshes.

Figure 5.44: The 1ω and 2ω force outputs as functions of the inflow angle for cases 1 and 2 in the drag and lift directions for Mesh 1, Mesh 2, and Mesh 3.

The drag component from Figures 5.44a and 5.44b shows that Mesh 3 is the least fluctuating mesh-iteration, but also the least conservative as its values are lower than for Mesh 1 and Mesh 2 in the region with the highest values. This could indicate that Mesh 3 is closer to reality than the other meshes, and it could also indicate numerical instability for Mesh 3, and that it should be refined before an eventual implementation. The lift components show a similar story for Case 1, but not for Case 2. In Figures 5.44c and 5.44d the drag components are quite small and messy, making it difficult to compare the meshes. The lift components are very distinct and show how Mesh 2 is the most conservative mesh for both cases and that Mesh 3 for Case 2 has a very different result than Mesh 1 and Mesh 2. This could again be due to numerical instability, and a more refined study with finer meshes should be performed to better determine the stability. Without any further studies, the recommended mesh is, therefore, Mesh 2 as it is both the most conservative mesh and results in force data with similar trends and values as Mesh 1.

5.4.2 Inflow angle and KC number sensitivity

The cases used in the sensitivity analysis of the inflow angles and KC numbers were chosen to be for an inflow angle of $\theta = 45°$, $65°$, and $90°$ and for KC numbers 0.1, 8, 16, and 21.5. These inflow angles were chosen as they represent three different mesh stages from a straightforward square mesh for $\theta = 90°$, to a more skewed mesh for $\theta = 45°$, with $\theta = 65°$ being somewhere in between the two others. The KC numbers were chosen to get a maximum spread across the KC numbers used experimentally and for the models described in Section 4.1.1. KC = 0.1 was chosen instead of KC = 1 to get the data for a case with almost no movement since this is very close to potential theory. Since the harmonic force outputs related to these parameters are widely different, they cannot be compared in the same way as the mesh size. Instead, the sensitivity can be shown through the run time, where the complexity of the flow is reflected, and the mesh creation time,

which indicates the intricateness of the mesh.

In figure Figure 5.45 the run times and mesh creation times of Mesh 1, Mesh 2, and Mesh 3 for the three inflow angles at KC = 21.5 are shown. It can be seen that the run times at an inflow angle of $\theta = 45°$ are larger than for the other inflow angles for all meshes. The relative sizes of the differences are not significant, but they do show some sensitivity with regard to the inflow angle. The mesh creation times are quite similar for inflow angles of $\theta = 45°$ and 90°, and somewhat longer for $\theta = 65°$. This is most likely due to the skewness of the mesh cells in the close vicinity of the geometries at $\theta = 65°$. At $\theta = 90°$ they are all mostly squares, and at $\theta = 45°$ they are transformed into triangular cells close to the boundary, while for $\theta = 65°$ it is a somewhat more chaotic mesh with both square-shaped and triangular mesh cells.

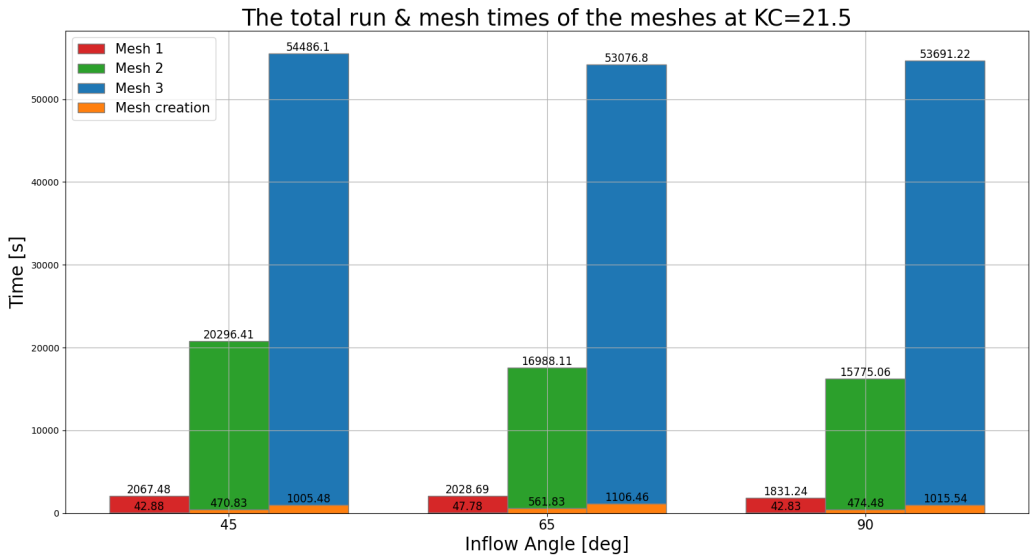

Figure 5.45: The run times and mesh creation times in seconds for the three meshes at inflow angles of $\theta = 45°$, 65°, and 90° at KC = 21.5.

Even though the effects of changing the inflow angle do not seem to be that significant, the effects of changing the mesh levels certainly are. The increases in both run times and mesh times are quite extensive with Mesh 2 taking between 8 - 12 times longer to run and mesh than Mesh 1, and Mesh 3 taking around 3 times longer than Mesh 2. This corresponds well with the data from Table 5.1 where Mesh 2 has about 3.2 times more mesh cells than Mesh 1, and Mesh 3 has 1.8 times the cells of Mesh 2.

The sensitivity of the KC number is shown in Figure 5.46. With regards to the mesh creation times the change of the KC number has no effect since it only affects the flow. The run times are however heavily affected. The trend for all three meshes is that the run times are longer for larger KC numbers, which is logical as a higher KC number will result in faster movements and more fluctuations creating a more complex flow. The run times for the lower KC numbers do seem very high, and one would think that the difference between KC = 0.1 and KC = 21.5 would be much larger, but it happens since these tests use a very low time step that is almost never modified by the solver. In reality, the lower KC numbers could have larger time steps, but for comparison sake, all KC number cases used the same base time step.

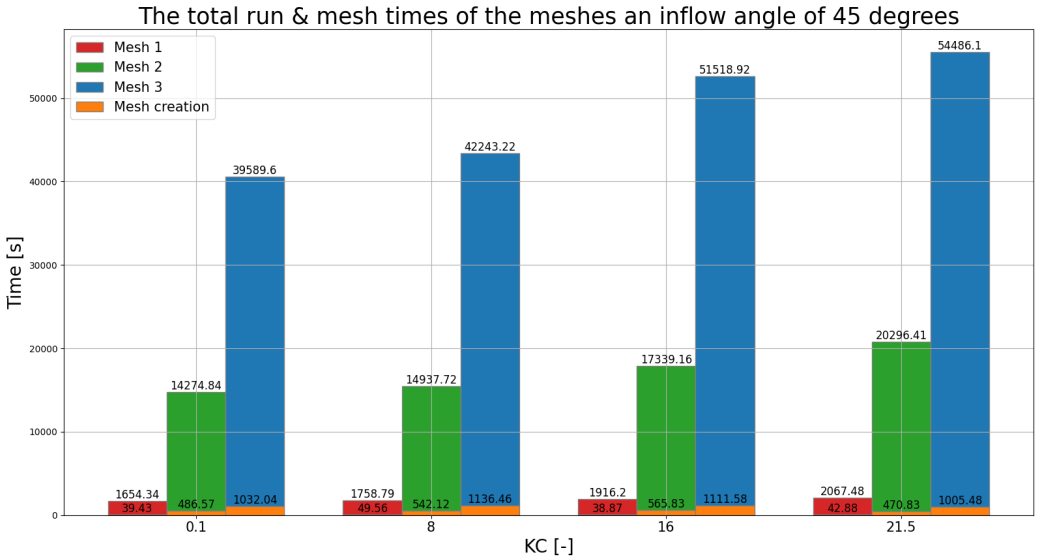

Figure 5.46: The run times and mesh creation times in seconds for a KC number of 0.1, 8, 16, and 21.5 at an inflow angle of $\theta = 45°$.

As a conclusion to both sensitivity analyses that were performed in this section, a single mesh and time step should be chosen to be used for all remaining numerical cases. Mesh 1 was very fast to use and gave decent results, but there are signs of information being lost due to the large mesh size and time step, as seen in Figure 5.44. Also, since it was originally an example mesh for a single cylinder it is probably not good enough for the more complex flow when adding a second cylinder. Mesh 2 shows better qualities than Mesh 1 with fewer fluctuations and a more conservative output estimate in most cases, but is however severely slower to use. Mesh 3 has indications of being the best mesh, but it may also be tainted by numerical instability. It is also extremely time-consuming to use for many cases, and if run in parallel it demands a lot of computational power as well, especially for the meshing. Since Mesh 2 returns output values that were deemed reasonable, while also being a lot less time-consuming than Mesh 3, it was decided to use Mesh 2 for the remainder of the numerical simulations, as well as to rerun the existing cases that had been run with Mesh 1 with Mesh 2. This was also done to have all the numerical models with the same mesh and time step so that the output data could easily be compared across cases without needing to be concerned with the mesh instability in-between cases.

5.5 Summarizing comments

In this final section, a brief summary of the results discussed in this chapter will be presented. The first takeaway from these results is that when two square-shaped cylinders are in close proximity to each other and exposed to a forced oscillatory flow, the forces experienced by the cylinders will be heavily affected by large nonlinear contributions. These contributions are present in both 2D numerical analyses and in both 2D and 3D experimental analyses. The second takeaway considers the effect the geometry and spacing of the cases have on the forces. It has been established that the diamond-shaped cylinders generally had larger experienced force amplitudes and were therefore only considered in parts of the analyses. The spacing has been found to heavily influence the nonlinearity

of the harmonic force amplitudes of the experienced forces, and also on the added mass, damping, and drag coefficients of the cylinders. The flow regimes of which the cylinders resides in the cases are also dependent on the spacing between the cylinders, and they can change if they are in the same or in different regimes based on the spacing. The final takeaway of the results is that there is a need for an improved load formulation. The existing formulation presented in Morison's equation can only account for the odd-numbered harmonic force contributions, while these results have shown that in every case there are large even-numbered harmonic force contributions present that are not accounted for, where the 2ω harmonic force amplitude has the definite highest impact on the cylinder forces. These even-numbered harmonic force contributions are also dependent on the spacing, and for spacings larger than about $^{s}/_{D} = 3$ they become negligible. This shows that the existing load formulation, while adequate for systems where there are cylinders far apart, is not capturing the complete forces for systems where there are cylinders in close proximity to each other.

A final remark on an important step of the future works regarding similar hydrodynamic theses. An improved load model should be created that accounts for all harmonic force contributions. This formulation should evaluate all harmonic force contributions separately, where each contribution has its own drag coefficient. These coefficients must be found by thorough experimental and numerical analyses. [Kristiansen 2023] explained that these new coefficients would be implemented into individual forces for each harmonic contribution, and also showed the dependencies of these coefficients. The individual drag forces are

$$F_D^{n\omega} = \rho D C_D^{n\omega}(S, C, \mathrm{KC}, \theta, \mathrm{Re})u, \tag{5.3}$$

where n signifies which harmonic contribution the force is valid for, S is the sectional shape, meaning if the cylinders are square-shaped, diamond-shaped, or have another shape, C is the configuration, meaning the number of cylinders, spacing, and other configuration specific to each case, and the rest of the parameters are known. Within the S and C parameters, there are probably many more variables that affect the drag coefficient. The same type of individual force can also be applied to the lift force. The new load formulation is complex and depends on a great number of parameters, which makes the task of developing it difficult, but necessary.

Chapter 6

Conclusions & further work

This final chapter will present the conclusions drawn from the results acquired in this thesis, as well as introduce ideas for how the findings from the thesis can be developed further.

6.1 Conclusions

The analyses that have been done in this thesis have had the purpose of studying the hydrodynamic interactions between two square-shaped cylinders in close proximity when exposed to a forced harmonically oscillating flow. A number of different parameters such as the number of cylinders, the cylinder shape, the inflow angle, the spacing between the cylinders, and different mesh configurations have all been studied to find where the hydrodynamic interaction occurs, and what it is sensitive to.

All of the numerical and experimental analyses that have been performed during this thesis have found strong indications of hydrodynamic interaction between the cylinders. The hydrodynamic interaction has been found to be especially sensitive to the KC number, the inflow angle, and the spacing between the cylinders. The focus of the thesis has been on both the forces experienced by the upstream and downstream cylinders individually, but mostly on the force difference between them which shows the hydrodynamic interaction. In most cases, the individual forces have been found to be strongly linear, with some exceptions having a larger presence of nonlinear force contributions. The force difference between the cylinders has been dominated by the nonlinear contributions in all cases, where the 2ω harmonic force amplitude has had an especially large influence. The odd-numbered harmonic force contributions of the upstream and downstream cylinders were found to be in phase with each other meaning that they would cancel out almost completely when creating the force difference, while the even-numbered contributions were 180° out of phase with each other and would therefore be added together founding the large higher-order influence of the force difference.

There is a close correlation between the 2D numerical model created in OpenFOAM and 2D experiments. This implies that the findings are backed both numerically and experimentally, which means that there is a strong validation of the presence of the hydrodynamic interaction which should be considered when designing and developing floating structures with cylinders in close proximity.

6.2 Further work

There are a great number of adjustments and improvements that can be done to the analyses that were performed in this thesis to get even better results and a wider base of knowledge regarding the hydrodynamic interaction. Below is a list of the main attributes that should be added or changed in the numerical models used in this thesis.

- The numerical solver should be expanded into three dimensions. This will give closer results to 3D experiments which give more physical results.
- If the model is three-dimensional, a new turbulence model such as LES should be implemented. If it is still in 2D, RANS may still give the best results, but one should experiment with using other model parameters than from the $k - \varepsilon$ model, for instance, the $k - \omega$ model.
- Other numerical solvers such as Ansys, Autodesk CFD, and REEF3D should be tested and implemented. OpenFOAM has many limitations and does not have the most user-friendly interface without additional proper software.
- More refined meshes should be tested. This would however demand more computational power and time.
- More configurations involving the number of cylinders, KC numbers, shapes, inflow angles, spacings, as well as other parameters.
- Testing the hydrodynamic sensitivity towards other parameters than the ones used in this thesis.
- Creating and implementing a new load formulation that captures all harmonic force contributions.

Bibliography

Atkins, Martin (2015). URL: https://pypi.org/project/stl/.

Biermann, D. and W. H. Herrnstein (1933). 'The Interference between Struts in Various Combinations'. In: *National Advisory Committee for Aeronautics, Tech. Rep.* 468.

BLUES, SFI (2022). *Floating structures for the next generation of ocean industries.* URL: https://sfiblues.no/.

Canonical, Ltd. (2018). URL: https://ubuntu.com/blog/tag/ubuntu-18-04.

Courant, R., K. Friedrichs and H. Lewy (1928). 'On the Partial Difference Equations of Mathematical Physics'. In: *Mathematische Annalen* 100, pp. 32–74.

Dadmarzi, Fatemeh et al. (2022). *Modelling of Large Modular Floating Structures, a Literature Review.* SINTEF.

DNV (2022). *ENERGY TRANSITION OUTLOOK 2022 - A global and regional forecast to 2050.*

Faltinsen, O. M. (1993). *Sea Loads on Ships and Offshore Structures.* Cambridge University Press.

Geuzaine, C. and J.-F. Remacle (2009). *Gmsh: a three-dimensional finite element mesh generator with built-in pre- and post-processing facilities.* URL: https://gmsh.info/.

Greco, Marilena (2019). *TMR 4215: Sea Loads.* Department of Marine Technology, Faculty of Engineering, NTNU.

Hals, Petter Grudt (2022). *TMR4520 - Marine Hydrodynamics: Specialization Project Multi-Modular Floating Solar Island.* NTNU.

Havel, B., H. Hangan and R. Martinuzzi (2001). 'Buffeting for 2D and 3D sharp-edged bluff bodies'. In: *Journal of Wind Engineering and Industrial Aerodynamics* 89, pp. 1369–1381.

HBM (2022). *catman Easy.* URL: https://www.hbm.com/en/2290/catman-data-acquisition-software/.

Hoerner, Sighard F. (1965). *Fluid-Dynamic Drag.* Published by the Author.

Hori, E. (1959). 'Experiments on Flow around a Pair of Parallel Circular Cylinders'. In: *Proc. 9th Japan National Congress for Applied Mech., Tokyo*, pp. 231–234.

Keulegan, G. H. and L. H. Carpenter (1958). 'Forces on Cylinders and Plates in an Oscillating Fluid'. In: *Journal of Research of the National Bureau of Standards* 60, pp. 423–440.

Kitware (2002). URL: https://www.paraview.org/.

Kristiansen, Trygve (2021). *Hydrodynamic loads on pontoon-supported modular structures*. NTNU.

Kristiansen, Trygve (2023). *Private Communication*.

Kristiansen, Trygve, Erin E. Bachynski-Polic and Dag Myrhaug (2021). *Marine Dynamics*. Department of Marine Technology, Faculty of Engineering, NTNU.

Lee, Dr. Chang-Ho and Prof. J. N. Newman (1999). URL: https://www.wamit.com/companyinfo.htm (visited on 5th Dec. 2022).

Mentzoni, Fredrik (2020). *Hydrodynamic Loads on Complex Structures in the Wave Zone*. NTNU.

Mikkelsen, Kristian (2023). *Three-dimensional experimental investigation of hydrodynamic forces and wake interaction between two or more cylinders in large-amplitude oscillatory flow*. Department of marine technology, NTNU.

Molin, Bernard (2023). *Offshore Structure Hydrodynamics*. Cambridge University Press.

Morison, J. R. et al. (1950). *The Force Exerted by Surface Waves on Piles*. Berkeley, University of California.

Onsrud, Magnus (2019). *An Experimental Study on the Wave-Induced Vertical Response of an Articulated Multi-Module Floating Solar Island*. NTNU.

OpenCFD (2004). URL: https://www.openfoam.com/.

OpenCFD (2016). URL: https://www.openfoam.com/documentation/guides/v2112/doc/guide-turbulence-les.html.

OpenCFD (2020). URL: https://www.openfoam.com/documentation/guides/latest/doc/guide-turbulence-ras-k-epsilon.html.

Pannell, J. R., E. A. Griffiths and J. D. Coales (1915). 'Experiments on the Interference between Pairs of Aeroplane Wires of Circular and Lenticular Cross Section'. In: *(British) Advisory Committee for Aeronautics, Reports and Memoranda* 208.

Pettersen, Bjørnar (2007). *TMR4247 Marin Teknikk 3 - Hydrodynamikk*. Akademika Forlag.

Reiten, Henrik (2022). *Two-dimensional Numerical and Experimental Investigation of Hydrodynamic Forces and Wake Interaction between Two or more Square Cylinders in Large-amplitude Oscillatory Flow*. NTNU.

Reynolds, O. (1883). 'An Experimental Investigation of the Circumstances which determine whether the Motion of Water shall be Direct or Sinuous, and of the Law of Resistance in Parallel Channels'. In: *The Royal Society* 35, pp. 935–982. DOI: doi/10.1098/rstl.1883.0029.

Roache, Patrick J. (1998). *Fundamentals of Computational Fluid Dynamics*. Hermosa Publishers.

Sævik, Svein (2015). *Drag Forces in Dynamic Analysis*. Department of Marine Technology, Faculty of Engineering, NTNU.

SAIPEM (2020). *SAIPEM: signed a cooperation agreement with Equinor to develop floating solar*. URL: https://www.saipem.com/en/media/news/2020-03-20/saipem-signed-cooperation-agreement-equinor-develop-floating-solar (visited on 6th Sept. 2023).

Sarpkaya, Turgut (2010). *Wave Forces on Offshore Structures*. Cambridge University Press.

Senthuran Ravinthrakumar, SINTEF (2023). *Private Communication*.

Shkoller, Steve (2009). *Notes on Lp and Sobolev Spaces*. URL: https://www.math.ucdavis.edu/~hunter/m218a_09/Lp_and_Sobolev_notes.pdf.

Zdravkovich, M. M. (1977). *Review of Flow Interference Between Two Circular Cylinders in Various Arrangements*. University of Salford, England.

Zdravkovich, M. M. and D. J. Stanhope (1972). *Flow Pattern in the Gap Between Two Cylinders in Tandem*. University of Salford, England.

Appendix

A Literature review

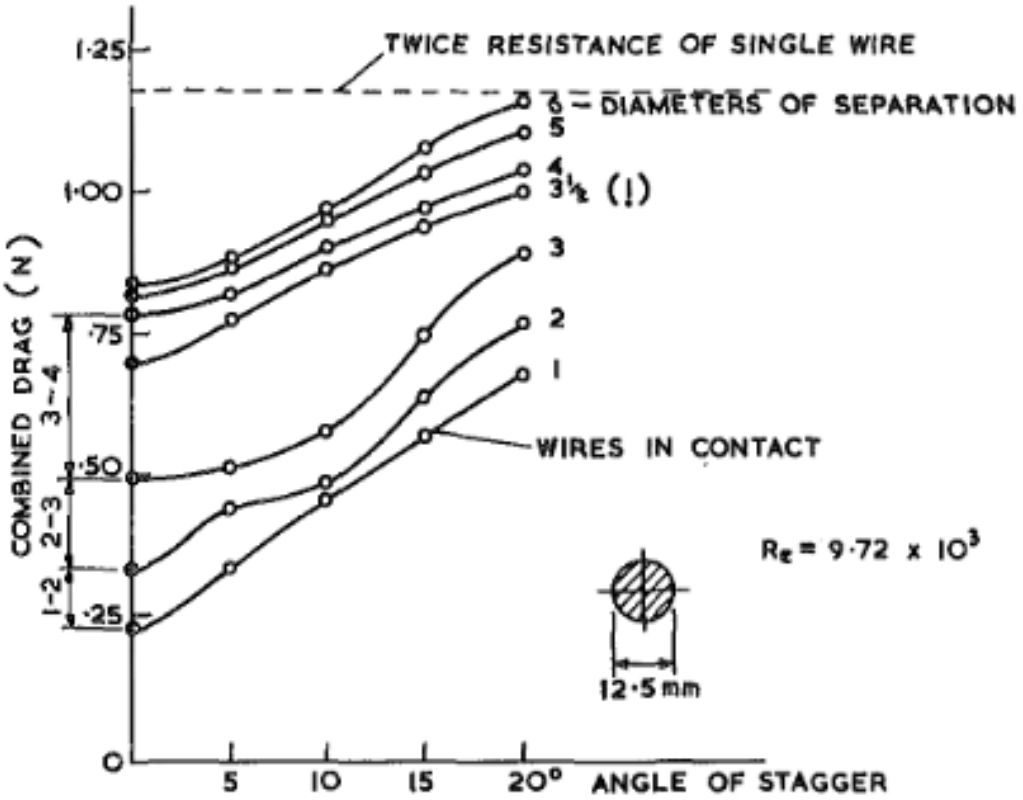

Fig. A.1: Combined drag of two wires vs. angle of stagger [Pannell et al. 1915, Zdravkovich 1977].

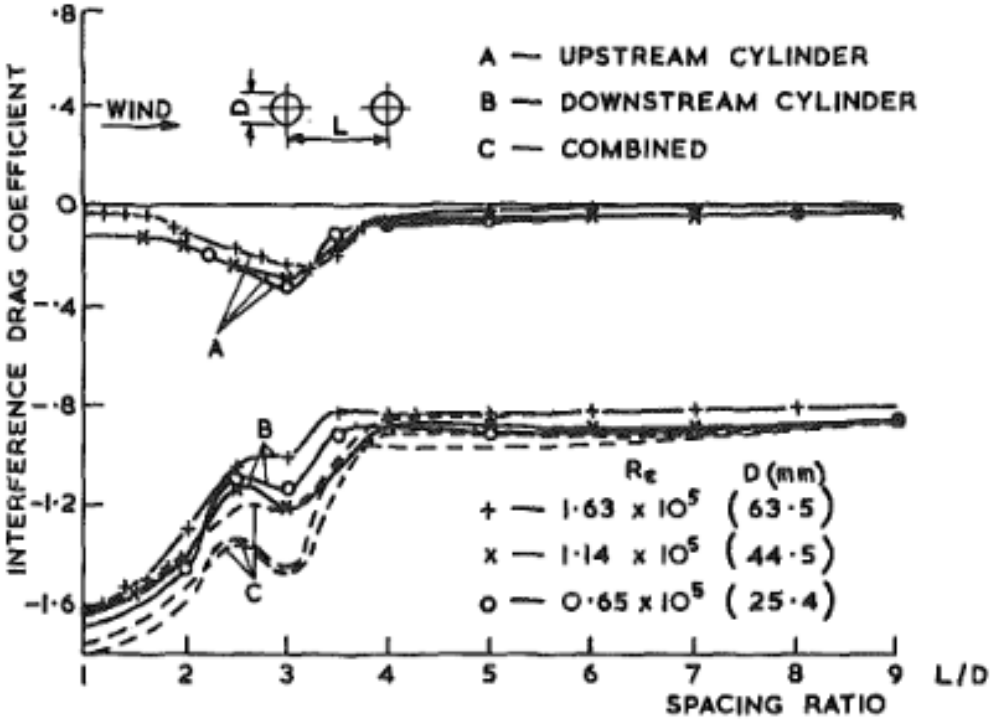

Fig. 2 Interference drag coefficient for tandem cylinders [2]

Fig. A.2: Interference drag coefficient vs. the spacing ratio [Biermann and Herrnstein 1933, Zdravkovich 1977].

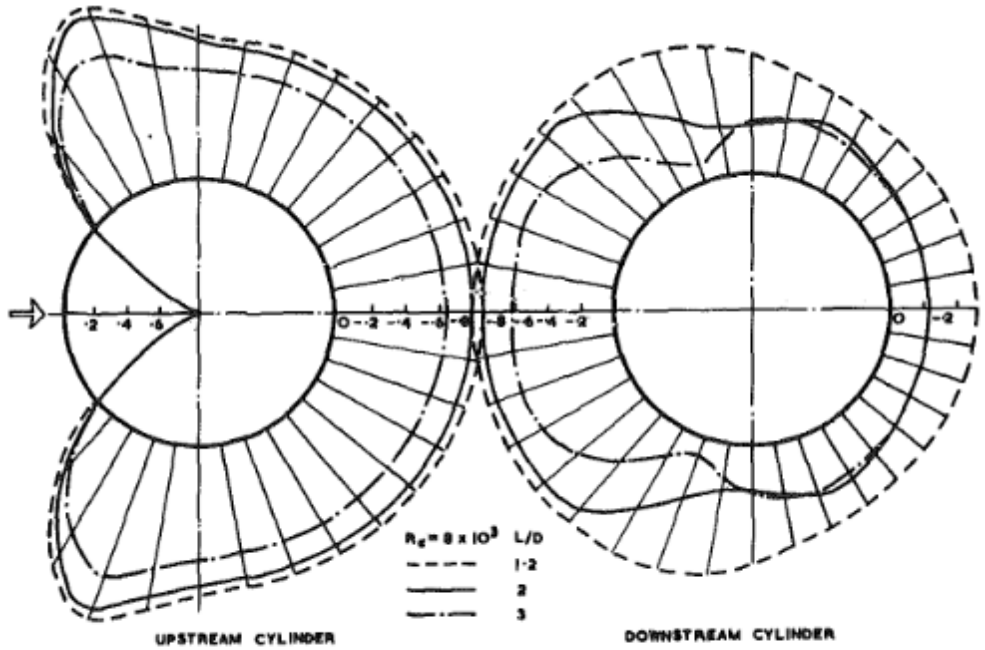

Fig. 3 Pressure distribution around two cylinders in staggered arrangement [3]

Fig. A.3: The pressure distributions around two cylinders in tandem [Hori 1959, Zdravkovich 1977].

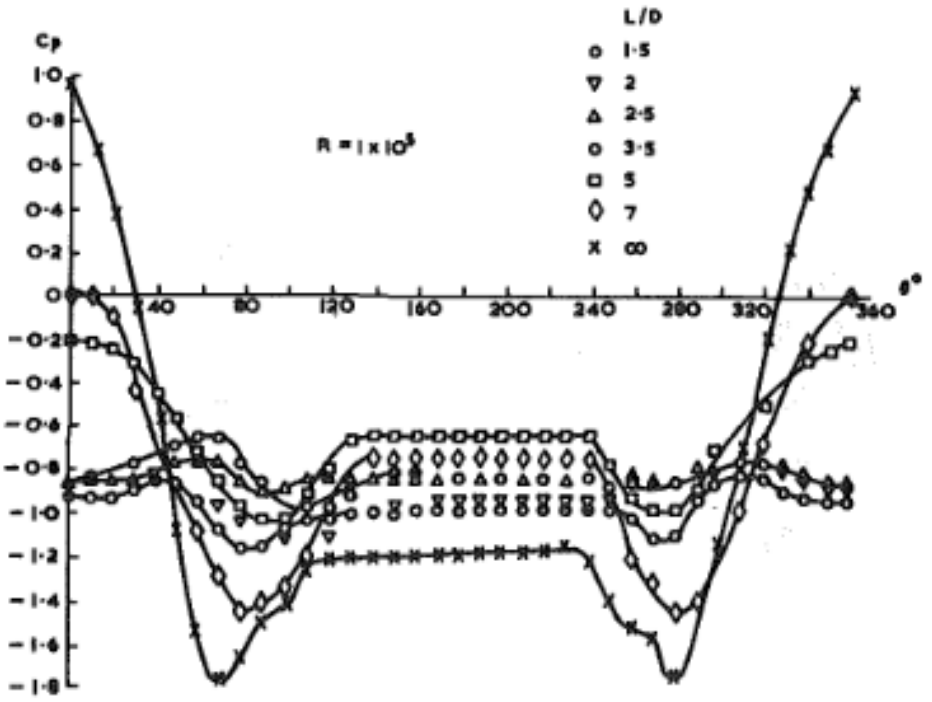

Fig. 4 Pressure distribution around downstream cylinder in various tandem arrangements [4]

Fig. A.4: Pressure distribution around downstream cylinder in various tandem arrangements [Zdravkovich and Stanhope 1972, Zdravkovich 1977].

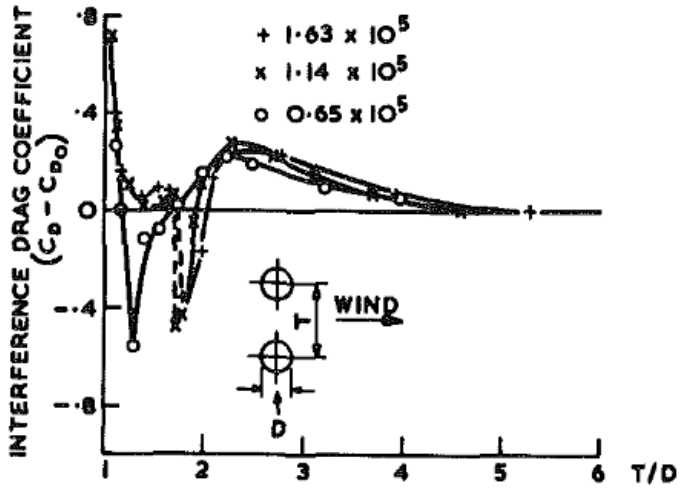

Fig. 14 Interference drag coefficient for the side by side arrangement [2]

Fig. A.5: Interference drag coefficient for side by side cylinders [Biermann and Herrnstein 1933, Zdravkovich 1977].

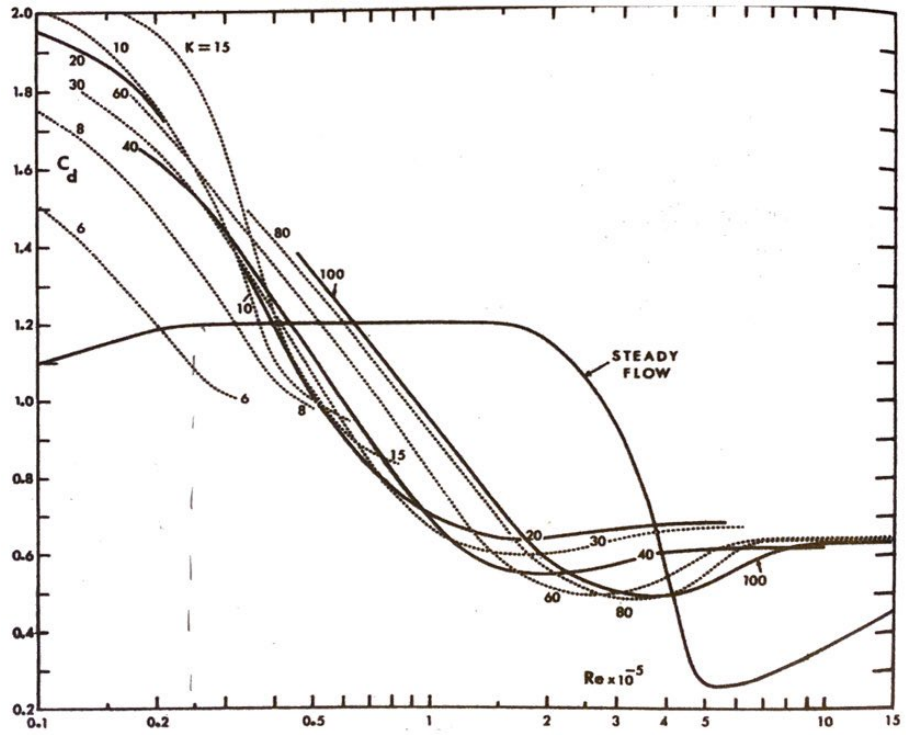

Fig. A.6: Drag coefficient vs. Reynolds number for various KC values [Sarpkaya 2010].

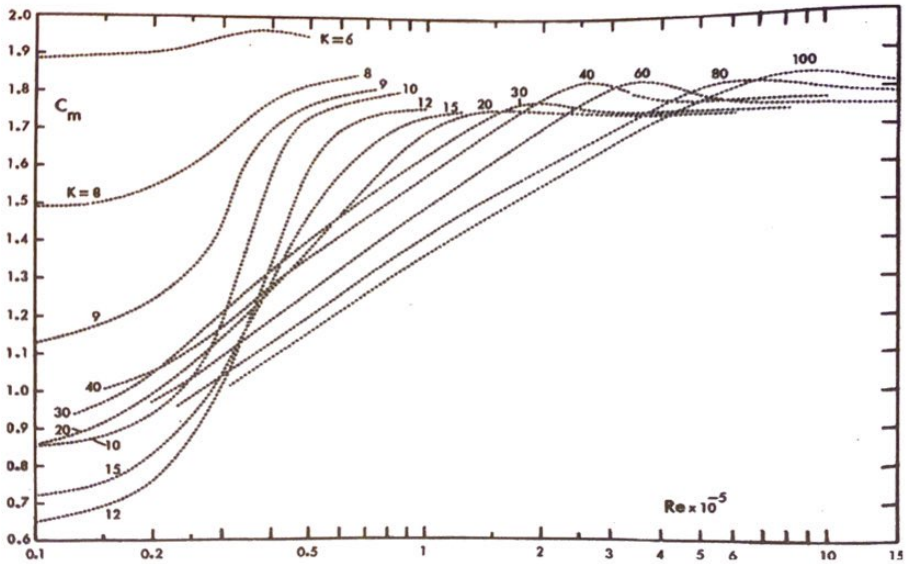

Fig. A.7: Inertia coefficient vs. Reynolds number for various KC values [Sarpkaya 2010].

B Numerical modeling

```
/*--------------------------------*- C++ -*----------------------------------*\
| =========                 |                                                 |
| \      /  F ield         | OpenFOAM: The Open Source CFD Toolbox           |
|  \    /   O peration     | Version:  2.4.0                                 |
|   \  /    A nd           | Web:      www.OpenFOAM.org                      |
|    \/     M anipulation  |                                                 |
\*---------------------------------------------------------------------------*/
FoamFile
{
     version     2.0;
     format      ascii;
     class       dictionary;
     location      "constant";
     object      movingCoordinateSystemProperties;
}
// * * * * * * * * * * * * * * * * * * * * * * * * * * * * * * * * * * * * * //

motionType oscillatory;
acc (0.0 0.0 5.0265);
period 1.0;
phase 0.0;
func "sin";
ramp
{
     type    "linear";
     startTime    0.0;
     endTime    3.0;
     startValue    (0 0 0);
}
// ************************************************************************* //
```

Fig. B.1: An example of the `movingCoordinateSystemProperties` dictionary for a case with KC = 16.

```
/*--------------------------------*- C++ -*----------------------------------*\
| =========                 |                                                 |
| \      /  F ield         | OpenFOAM: The Open Source CFD Toolbox           |
|  \    /   O peration     | Version:  2.4.0                                 |
|   \  /    A nd           | Web:      www.OpenFOAM.org                      |
|    \/     M anipulation  |                                                 |
\*---------------------------------------------------------------------------*/
FoamFile
{
     version     2.0;
     format      ascii;
     class       dictionary;
     location    "system";
     object      controlDict;
}
// * * * * * * * * * * * * * * * * * * * * * * * * * * * * * * * * * * * * * //

application     pvcFoam;

startFrom     startTime;

startTime     0.0;

stopAt     endTime;

endTime     20.0;

deltaT     0.00833333333333;

writeControl     adjustableRunTime;

writeInterval     20.0;   //0.03333333333333;

purgeWrite     0;

writeFormat     binary;

writePrecision     12;

writeCompression     uncompressed;

timeFormat     general;

timePrecision     12;

runTimeModifiable     yes;

adjustTimeStep     yes;

maxCo     1.0;

maxDeltaT     0.0005;
```

(a) The definition of the parameters in the `controlDict` dictionary.

```
functions
{
     forces
     {
          type      forces;
          libs      ("libforces.so");
          writeControl      timeStep;
          writeInterval      1;
          patches      ("hull1.*");
          rho      rhoInf;
          log      yes;
          rhoInf      1000;
          CofR      (0 0 0);
          pRef      0;
     }


     forceCoeffs
     {

          type       forceCoeffs;
          libs       ("libforces.so");
          writeControl         timeStep;
          writeInterval      1;
          patches      ("hull1.*");
          porosity      false;
          rho      rhoInf;
          log      yes;
          rhoInf      1000;
          magUInf      1.0;
          lRef        0.05;
          Aref        0.005;
          CofR        (0 0 0);
          dragDir     (0 0 -1);
          liftDir     (1 0 0);
          pitchAxis   (0 1 0);
     }
```

(b) The definition of the functions in the `controlDict` dictionary.

Fig. B.2: An example of a `controlDict` dictionary.

C Experimental results

C.1 Force plots

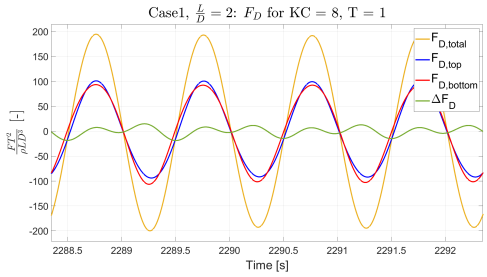

(a) The forces acting on the system for KC = 8 for cylinders with $L/D = 2$ in Case 1.

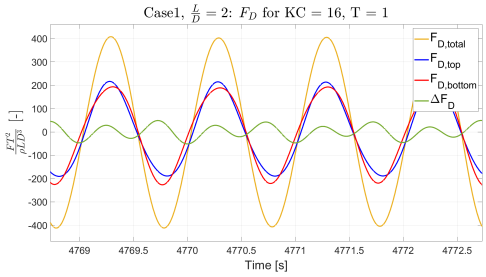

(b) The forces acting on the system for KC = 16 for cylinders with $L/D = 2$ in Case 1.

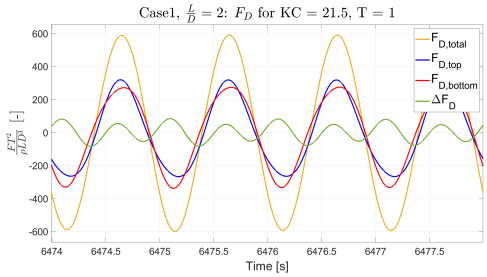

(c) The forces acting on the system for KC = 21.5 for cylinders with $L/D = 2$ in Case 1.

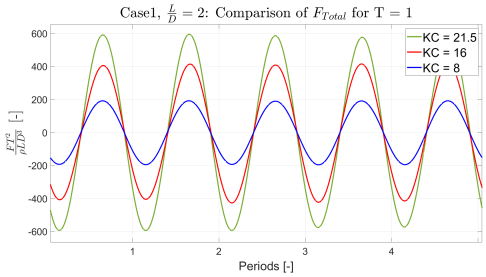

(d) A comparison of the total force for KC = 8, 16, and 21.5 in $L/D = 2$ in Case 1.

Fig. C.1: The forces acting on the system with $L/D = 2$ in Case 1, as well as a comparison of the total forces.

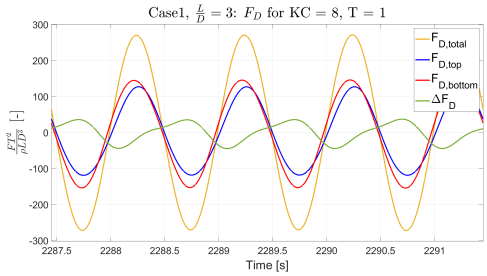

(a) The forces acting on the system for KC = 8 for cylinders with $L/D = 3$ in Case 1.

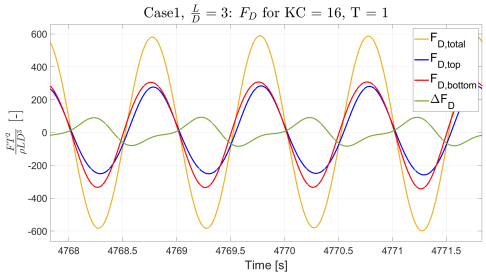

(b) The forces acting on the system for KC = 16 for cylinders with $L/D = 3$ in Case 1.

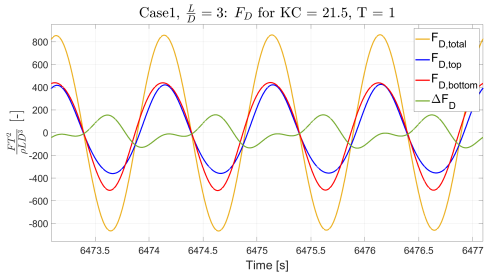

(c) The forces acting on the system for KC = 21.5 for cylinders with $L/D = 3$ in Case 1.

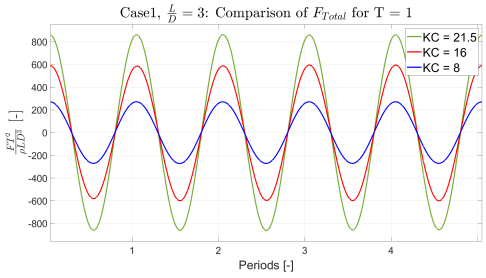

(d) A comparison of the total force for KC = 8, 16, and 21.5 in $L/D = 3$ in Case 1.

Fig. C.2: The forces acting on the system with $L/D = 3$ in Case 1, as well as a comparison of the total forces.

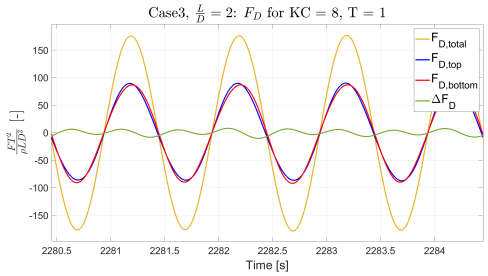

(a) The forces acting on the system for KC = 8 for cylinders with $L/D = 2$ in Case 3.

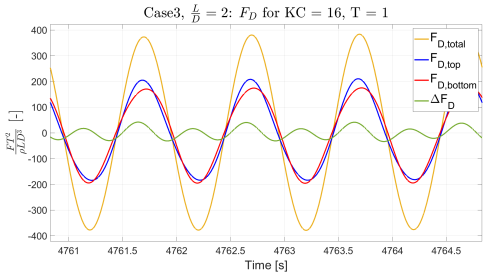

(b) The forces acting on the system for KC = 16 for cylinders with $L/D = 2$ in Case 3.

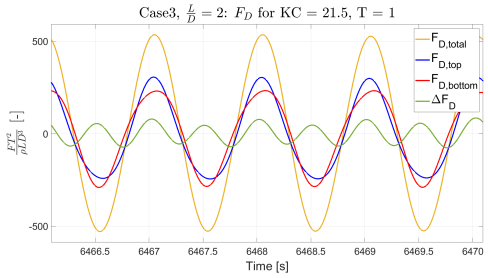

(c) The forces acting on the system for KC = 21.5 for cylinders with $L/D = 2$ in Case 3.

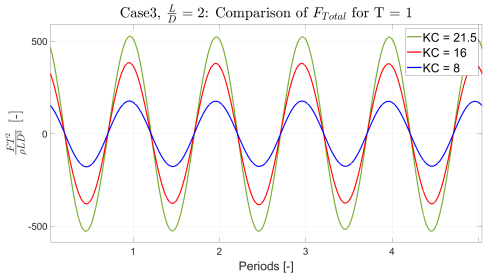

(d) A comparison of the total force for KC = 8, 16, and 21.5 in $L/D = 2$ in Case 3.

Fig. C.3: The forces acting on the system with $L/D = 2$ in Case 3, as well as a comparison of the total forces.

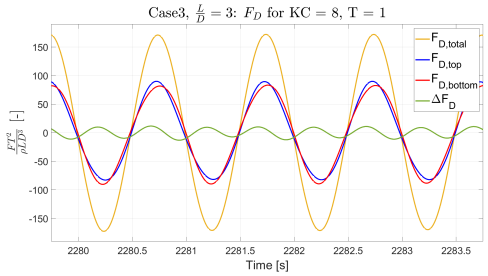

(a) The forces acting on the system for KC = 8 for cylinders with $L/D = 3$ in Case 3.

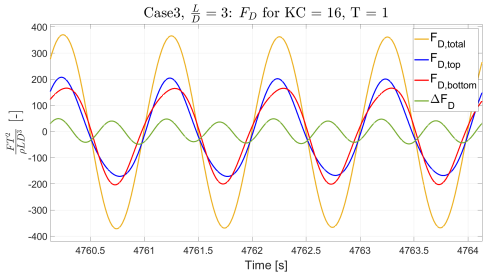

(b) The forces acting on the system for KC = 16 for cylinders with $L/D = 3$ in Case 3.

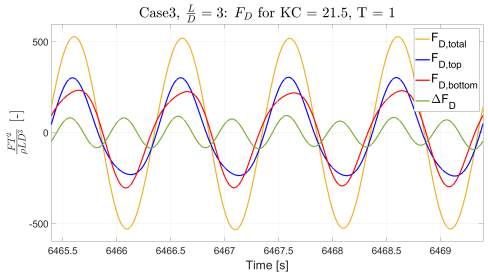

(c) The forces acting on the system for KC = 21.5 for cylinders with $L/D = 3$ in Case 3.

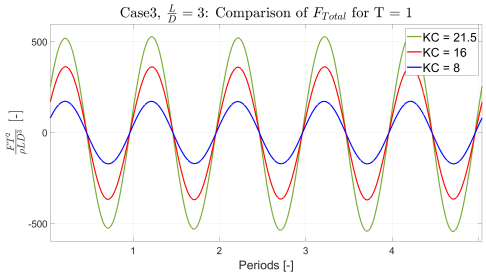

(d) A comparison of the total force for KC = 8, 16, and 21.5 in $L/D = 3$ in Case 3.

Fig. C.4: The forces acting on the system with $L/D = 3$ in Case 3, as well as a comparison of the total forces.

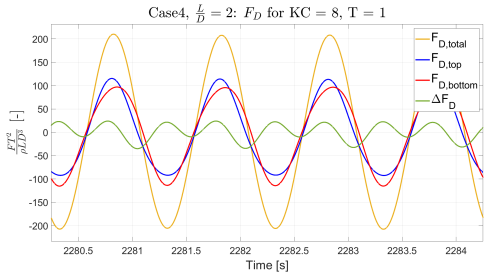

(a) The forces acting on the system for KC = 8 for cylinders with $L/D = 2$ in Case 4.

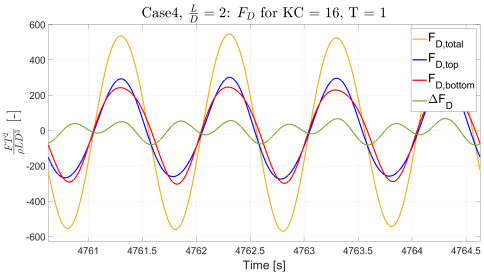

(b) The forces acting on the system for KC = 16 for cylinders with $L/D = 2$ in Case 4.

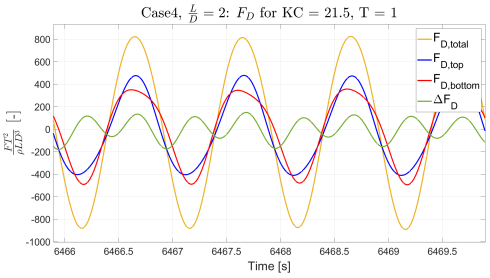

(c) The forces acting on the system for KC = 21.5 for cylinders with $L/D = 2$ in Case 4.

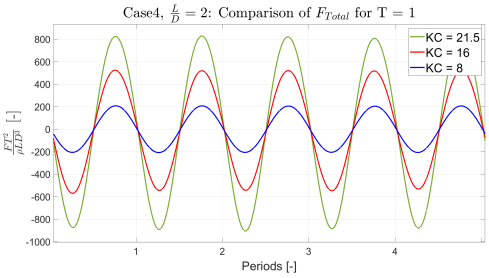

(d) A comparison of the total force for KC = 8, 16, and 21.5 in $L/D = 2$ in Case 4.

Fig. C.5: The forces acting on the system with $L/D = 2$ in Case 4, as well as a comparison of the total forces.

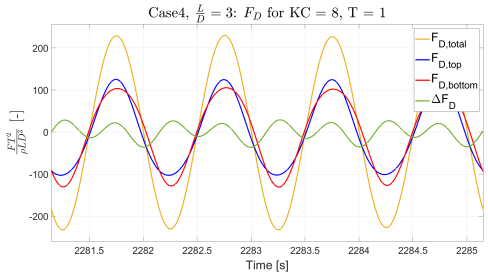

(a) The forces acting on the system for KC = 8 for cylinders with $L/D = 3$ in Case 4.

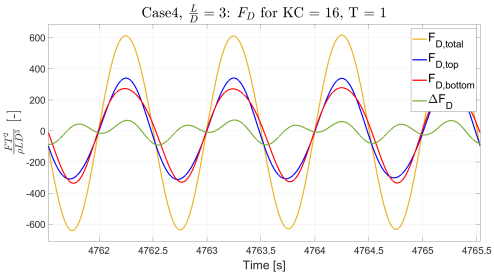

(b) The forces acting on the system for KC = 16 for cylinders with $L/D = 3$ in Case 4.

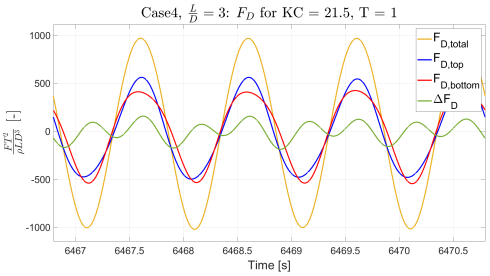

(c) The forces acting on the system for KC = 21.5 for cylinders with $L/D = 3$ in Case 4.

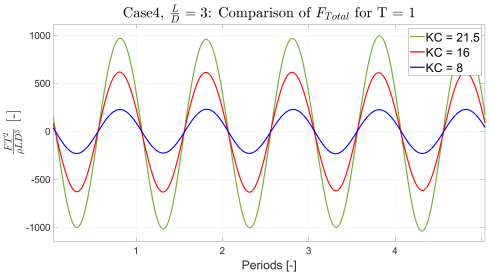

(d) A comparison of the total force for KC = 8, 16, and 21.5 in $L/D = 3$ in Case 4.

Fig. C.6: The forces acting on the system with $L/D = 3$ in Case 4, as well as a comparison of the total forces.

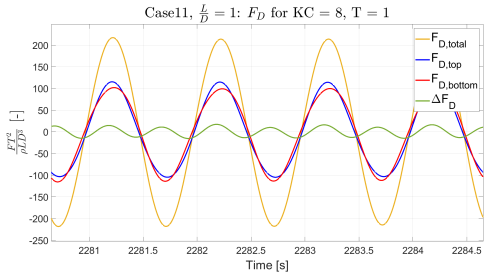

(a) The forces acting on the system for KC = 8 for cylinders with $L/D = 1$ in Case 11.

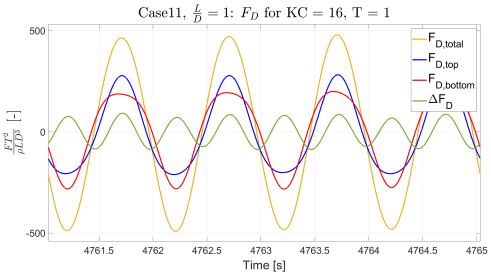

(b) The forces acting on the system for KC = 16 for cylinders with $L/D = 1$ in Case 11.

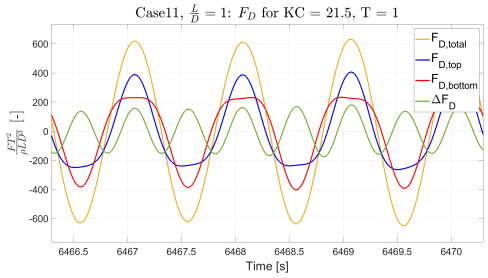

(c) The forces acting on the system for KC = 21.5 for cylinders with $L/D = 1$ in Case 11.

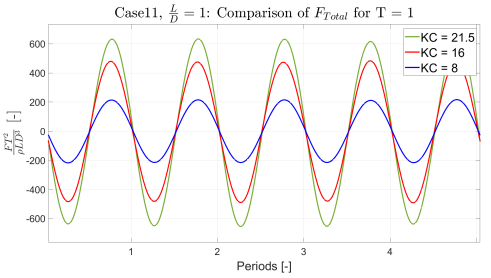

(d) A comparison of the total force for KC = 8, 16, and 21.5 in $L/D = 1$ in Case 11.

Fig. C.7: The forces acting on the system with $L/D = 1$ in Case 11, as well as a comparison of the total forces.

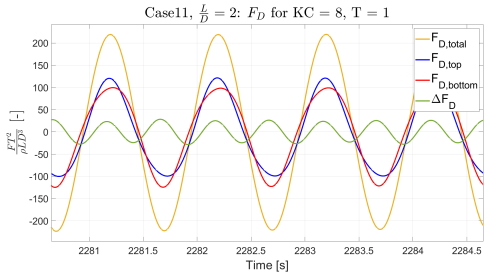

(a) The forces acting on the system for KC = 8 for cylinders with $L/D = 2$ in Case 11.

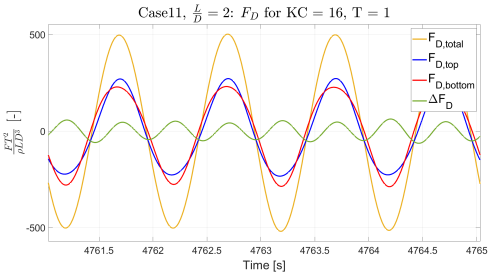

(b) The forces acting on the system for KC = 16 for cylinders with $L/D = 2$ in Case 11.

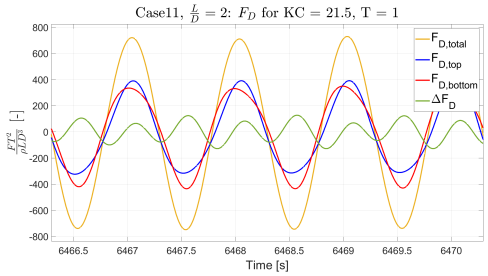

(c) The forces acting on the system for KC = 21.5 for cylinders with $L/D = 2$ in Case 11.

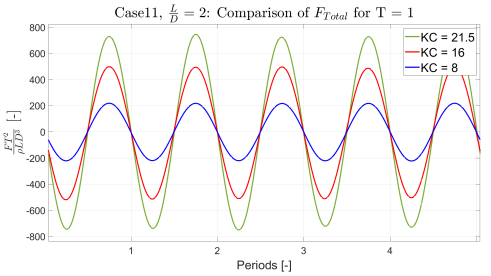

(d) A comparison of the total force for KC = 8, 16, and 21.5 in $L/D = 2$ in Case 11.

Fig. C.8: The forces acting on the system with $L/D = 2$ in Case 11, as well as a comparison of the total forces.

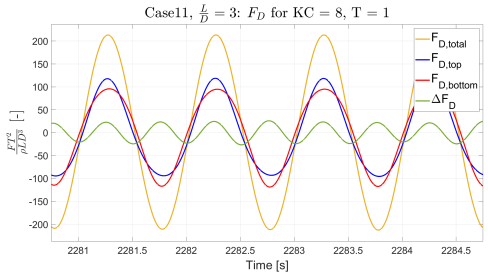

(a) The forces acting on the system for KC = 8 for cylinders with $L/D = 3$ in Case 11.

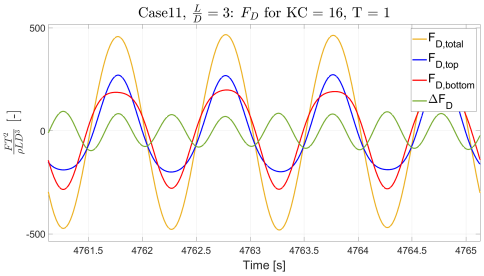

(b) The forces acting on the system for KC = 16 for cylinders with $L/D = 3$ in Case 11.

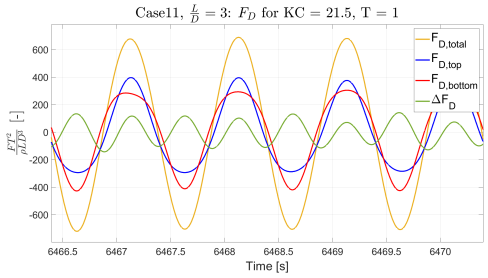

(c) The forces acting on the system for KC = 21.5 for cylinders with $L/D = 3$ in Case 11.

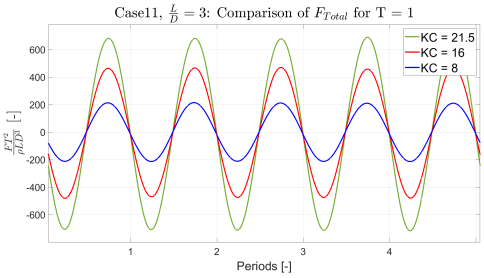

(d) A comparison of the total force for KC = 8, 16, and 21.5 in $L/D = 3$ in Case 11.

Fig. C.9: The forces acting on the system with $L/D = 3$ in Case 11, as well as a comparison of the total forces.

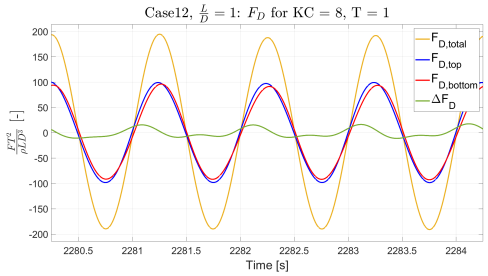

(a) The forces acting on the system for KC = 8 for cylinders with $L/D = 1$ in Case 12.

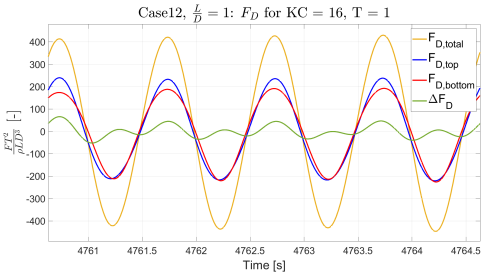

(b) The forces acting on the system for KC = 16 for cylinders with $L/D = 1$ in Case 12.

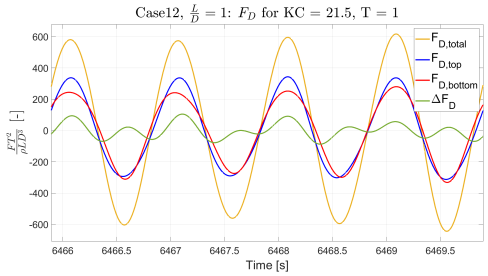

(c) The forces acting on the system for KC = 21.5 for cylinders with $L/D = 1$ in Case 12.

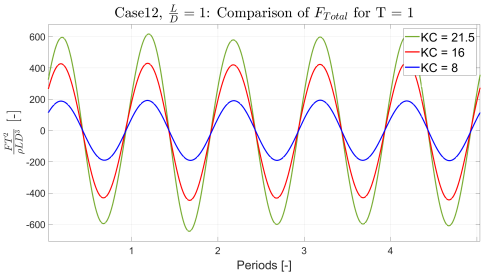

(d) A comparison of the total force for KC = 8, 16, and 21.5 in $L/D = 1$ in Case 12.

Fig. C.10: The forces acting on the system with $L/D = 1$ in Case 12, as well as a comparison of the total forces.

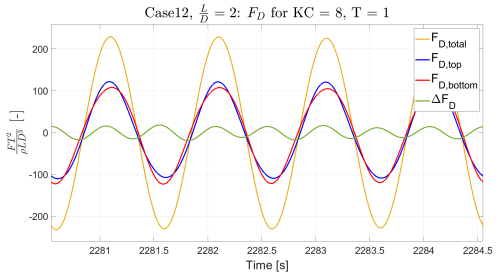

(a) The forces acting on the system for KC = 8 for cylinders with $L/D = 2$ in Case 12.

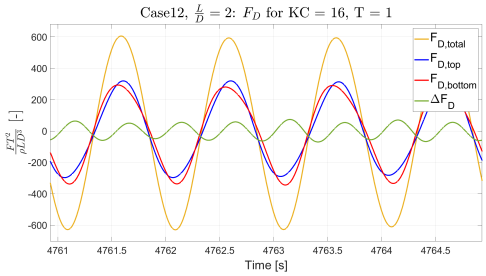

(b) The forces acting on the system for KC = 16 for cylinders with $L/D = 2$ in Case 12.

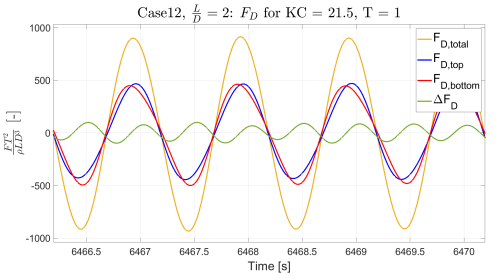

(c) The forces acting on the system for KC = 21.5 for cylinders with $L/D = 2$ in Case 12.

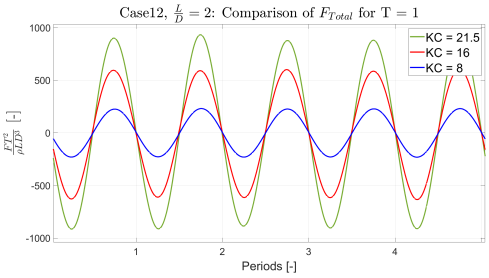

(d) A comparison of the total force for KC = 8, 16, and 21.5 in $L/D = 2$ in Case 12.

Fig. C.11: The forces acting on the system with $L/D = 2$ in Case 12, as well as a comparison of the total forces.

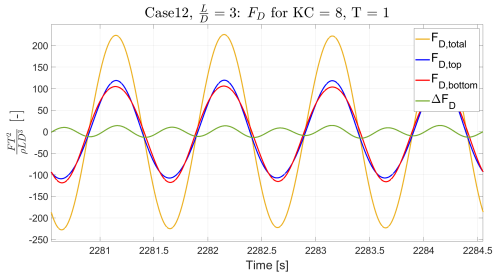

(a) The forces acting on the system for KC = 8 for cylinders with $L/D = 3$ in Case 12.

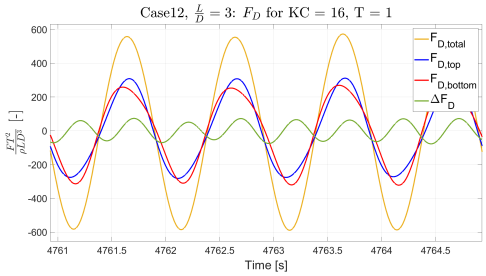

(b) The forces acting on the system for KC = 16 for cylinders with $L/D = 3$ in Case 12.

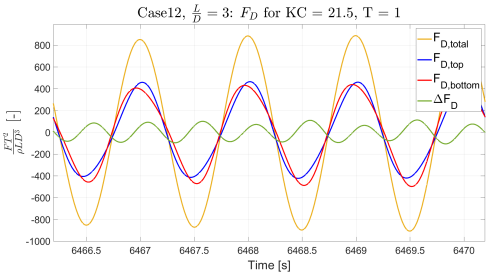

(c) The forces acting on the system for KC = 21.5 for cylinders with $L/D = 3$ in Case 12.

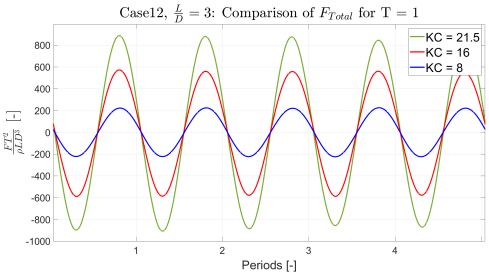

(d) A comparison of the total force for KC = 8, 16, and 21.5 in $L/D = 3$ in Case 12.

Fig. C.12: The forces acting on the system with $L/D = 3$ in Case 12, as well as a comparison of the total forces.

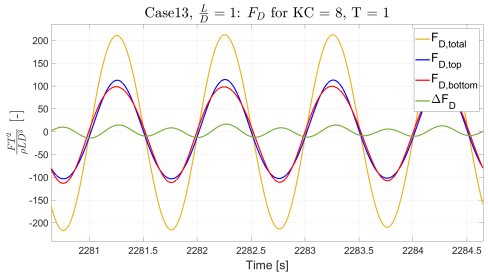

(a) The forces acting on the system for KC = 8 for cylinders with $L/D = 1$ in Case 13.

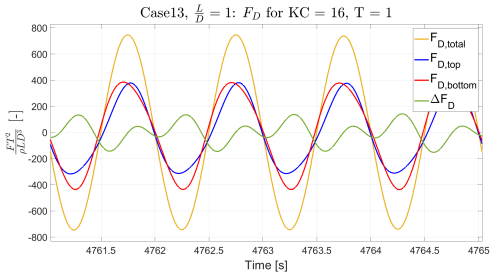

(b) The forces acting on the system for KC = 16 for cylinders with $L/D = 1$ in Case 13.

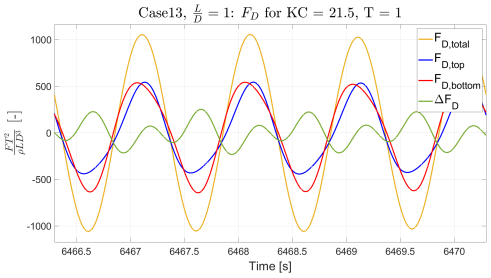

(c) The forces acting on the system for KC = 21.5 for cylinders with $L/D = 1$ in Case 13.

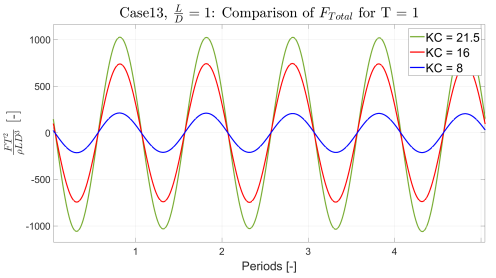

(d) A comparison of the total force for KC = 8, 16, and 21.5 in $L/D = 1$ in Case 13.

Fig. C.13: The forces acting on the system with $L/D = 1$ in Case 13, as well as a comparison of the total forces.

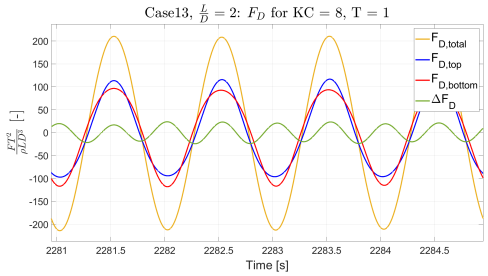

(a) The forces acting on the system for KC = 8 for cylinders with $L/D = 2$ in Case 13.

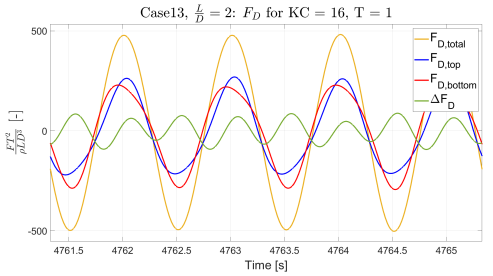

(b) The forces acting on the system for KC = 16 for cylinders with $L/D = 2$ in Case 13.

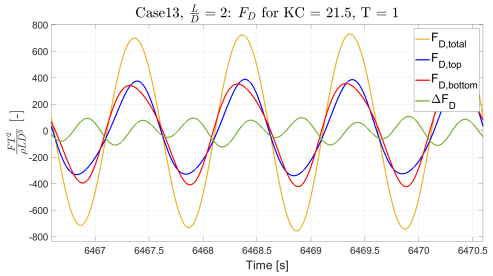

(c) The forces acting on the system for KC = 21.5 for cylinders with $L/D = 2$ in Case 13.

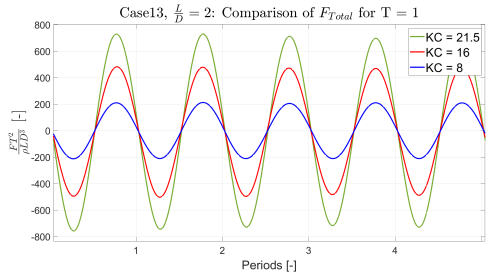

(d) A comparison of the total force for KC = 8, 16, and 21.5 in $L/D = 2$ in Case 13.

Fig. C.14: The forces acting on the system with $L/D = 2$ in Case 13, as well as a comparison of the total forces.

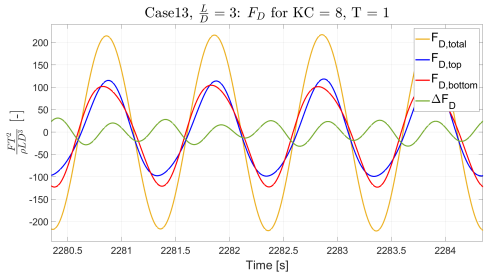

(a) The forces acting on the system for KC = 8 for cylinders with $^L/_D = 3$ in Case 13.

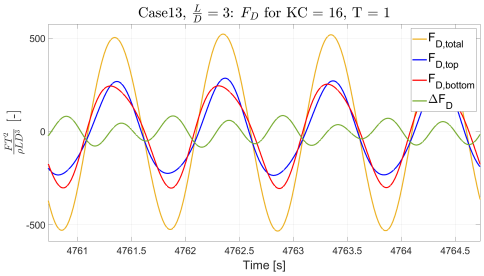

(b) The forces acting on the system for KC = 16 for cylinders with $^L/_D = 3$ in Case 13.

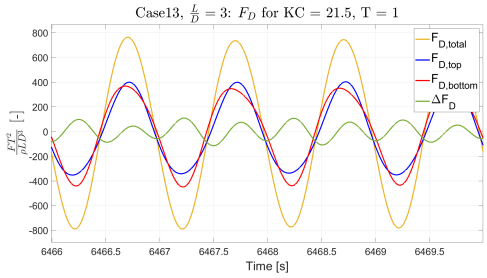

(c) The forces acting on the system for KC = 21.5 for cylinders with $^L/_D = 3$ in Case 13.

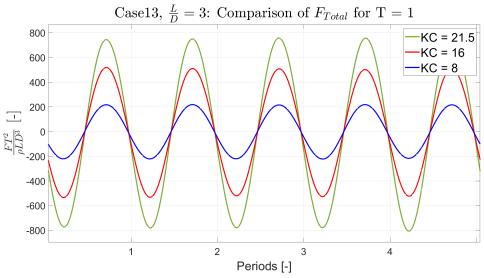

(d) A comparison of the total force for KC = 8, 16, and 21.5 in $^L/_D = 3$ in Case 13.

Fig. C.15: The forces acting on the system with $^L/_D = 3$ in Case 13, as well as a comparison of the total forces.

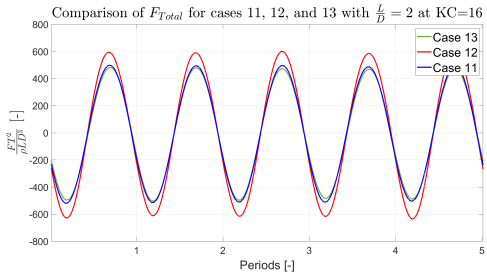

(a) A comparison of the total force for KC = 16 for cylinders with $^L/_D = 2$ in cases 11, 12, and 13.

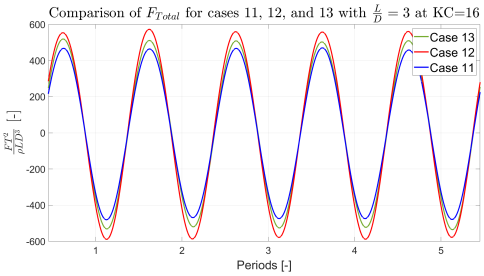

(b) A comparison of the total force for KC = 16 for cylinders with $^L/_D = 3$ in cases 11, 12, and 13.

Fig. C.16: A comparison of the total force for KC = 16 for cylinders with $^L/_D = 2$ and $^L/_D = 3$ in cases 11, 12, and 13.

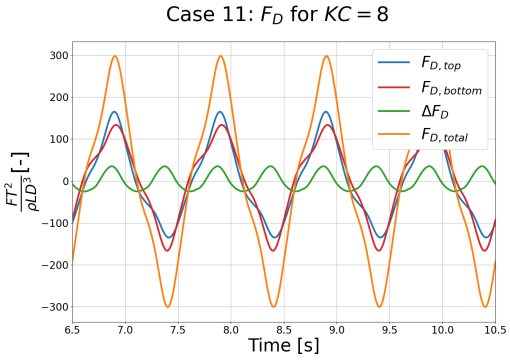

(a) The forces acting on the numerical system for KC = 8 in Case 11.

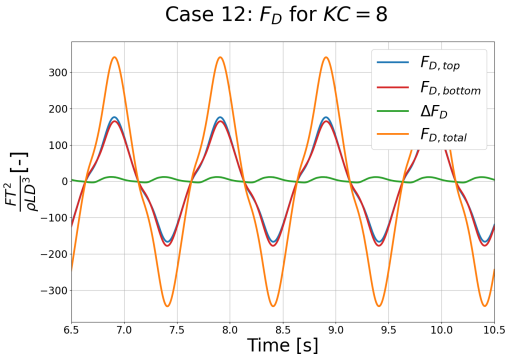

(b) The forces acting on the numerical system for KC = 8 in Case 12.

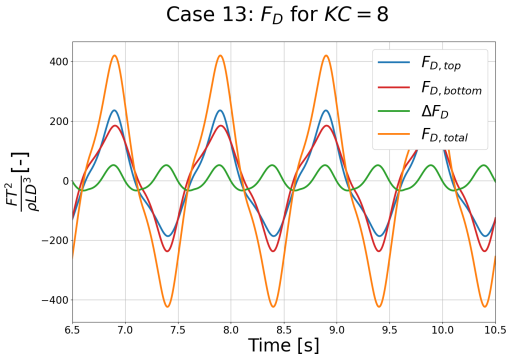

(c) The forces acting on the numerical system for KC = 8 in Case 13.

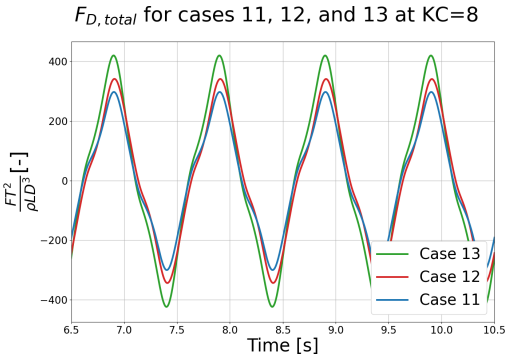

(d) A comparison of the total force for KC = 8 for cases 11, 12, and 13.

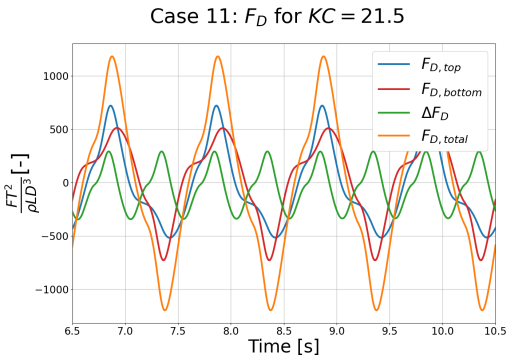

(e) The forces acting on the numerical system for KC = 21.5 in Case 11.

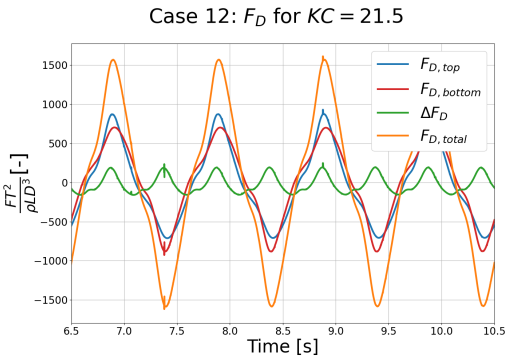

(f) The forces acting on the numerical system for KC = 21.5 in Case 12.

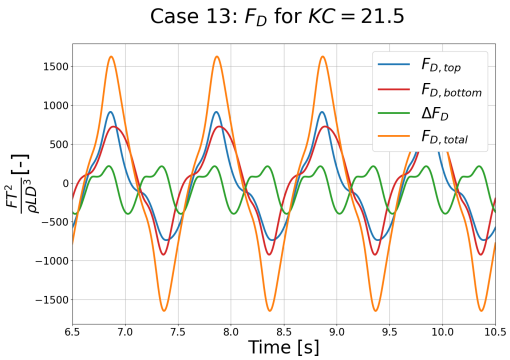

(g) The forces acting on the numerical system for KC = 21.5 in Case 13.

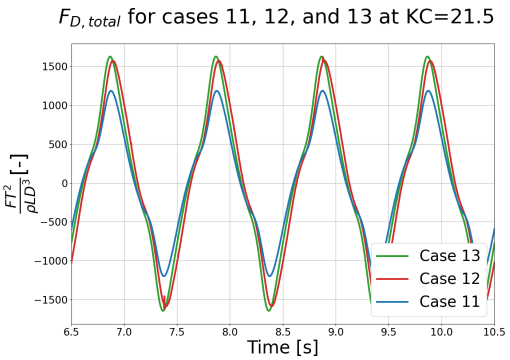

(h) A comparison of the total force for KC = 21.5 for cases 11, 12, and 13.

Fig. C.17: The numerical force amplitudes and a comparison of the total forces for KC = 8 and 21.5 in cases 11, 12, and 13.

C.2 Harmonic analysis plots

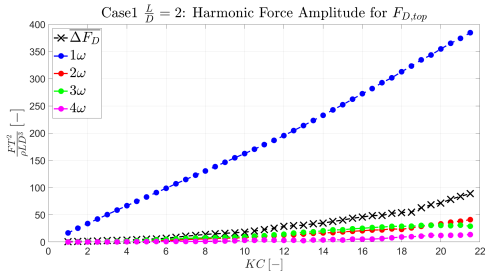

(a) The harmonic force amplitudes for $F_{D,top}$ and the mean force difference for Case 1 with $\frac{L}{D} = 2$.

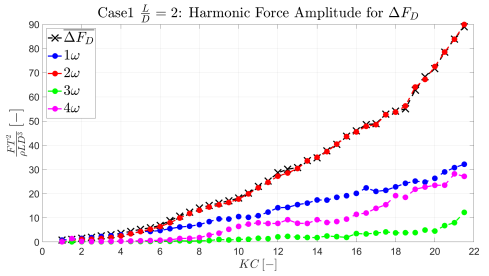

(b) The harmonic force amplitudes for ΔF_D and the mean force difference for Case 1 with $\frac{L}{D} = 2$.

Fig. C.18: The harmonic force amplitudes for $F_{D,top}$ and ΔF_D and the mean force difference for Case 1 with $\frac{L}{D} = 2$.

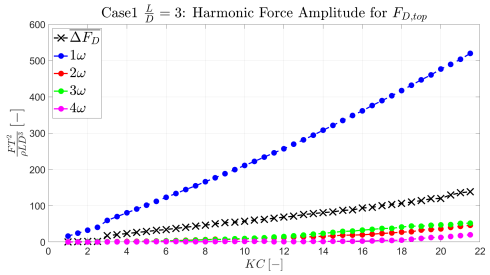

(a) The harmonic force amplitudes for $F_{D,top}$ and the mean force difference for Case 1 with $\frac{L}{D} = 3$.

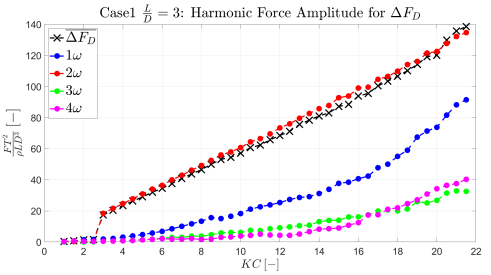

(b) The harmonic force amplitudes for ΔF_D and the mean force difference for Case 1 with $\frac{L}{D} = 3$.

Fig. C.19: The harmonic force amplitudes for $F_{D,top}$ and ΔF_D and the mean force difference for Case 1 with $\frac{L}{D} = 3$.

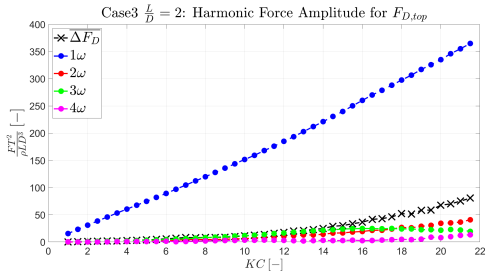

(a) The harmonic force amplitudes for $F_{D,top}$ and the mean force difference for Case 3 with $\frac{L}{D} = 2$.

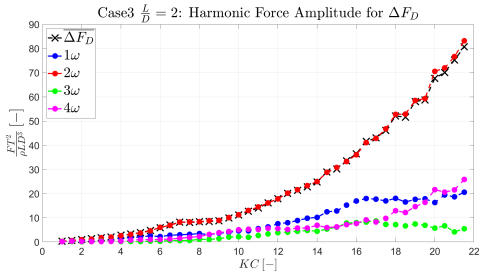

(b) The harmonic force amplitudes for ΔF_D and the mean force difference for Case 3 with $\frac{L}{D} = 2$.

Fig. C.20: The harmonic force amplitudes for $F_{D,top}$ and ΔF_D and the mean force difference for Case 3 with $\frac{L}{D} = 2$.

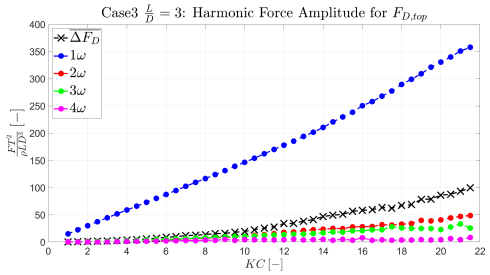

(a) The harmonic force amplitudes for $F_{D,top}$ and the mean force difference for Case 3 with $\frac{L}{D}=3$.

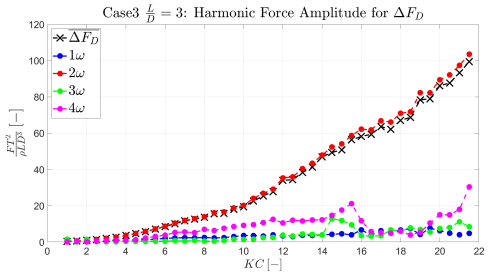

(b) The harmonic force amplitudes for ΔF_D and the mean force difference for Case 3 with $\frac{L}{D}=3$.

Fig. C.21: The harmonic force amplitudes for $F_{D,top}$ and ΔF_D and the mean force difference for Case 3 with $\frac{L}{D}=3$.

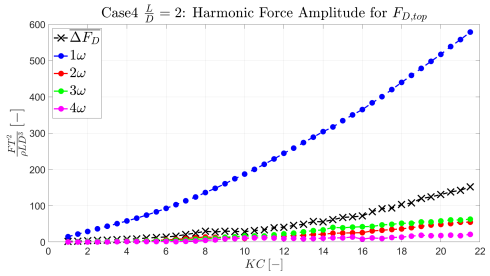

(a) The harmonic force amplitudes for $F_{D,top}$ and the mean force difference for Case 4 with $\frac{L}{D}=2$.

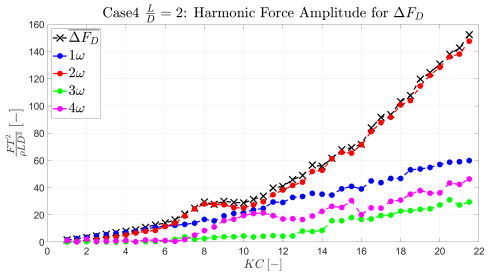

(b) The harmonic force amplitudes for ΔF_D and the mean force difference for Case 4 with $\frac{L}{D}=2$.

Fig. C.22: The harmonic force amplitudes for $F_{D,top}$ and ΔF_D and the mean force difference for Case 4 with $\frac{L}{D}=2$.

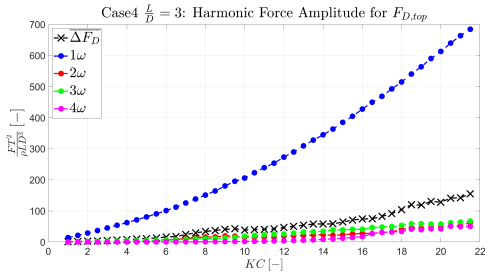

(a) The harmonic force amplitudes for $F_{D,top}$ and the mean force difference for Case 4 with $\frac{L}{D}=3$.

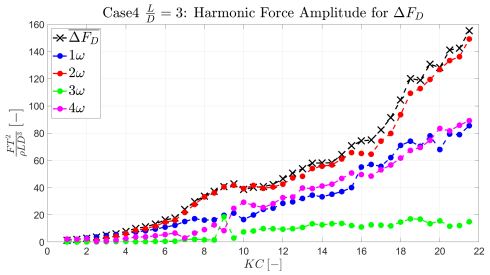

(b) The harmonic force amplitudes for ΔF_D and the mean force difference for Case 4 with $\frac{L}{D}=3$.

Fig. C.23: The harmonic force amplitudes for $F_{D,top}$ and ΔF_D and the mean force difference for Case 4 with $\frac{L}{D}=3$.

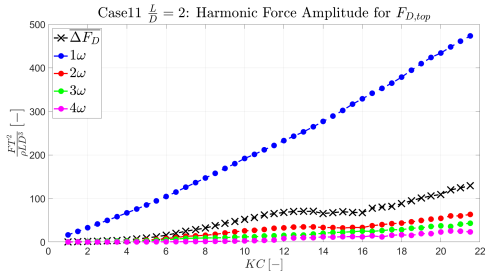

(a) The harmonic force amplitudes for $F_{D,top}$ and the mean force difference for Case 11 with $\frac{L}{D}=2$.

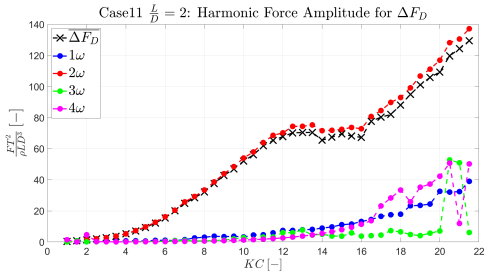

(b) The harmonic force amplitudes for ΔF_D and the mean force difference for Case 11 with $\frac{L}{D}=2$.

Fig. C.24: The harmonic force amplitudes for $F_{D,top}$ and ΔF_D and the mean force difference for Case 11 with $\frac{L}{D}=2$.

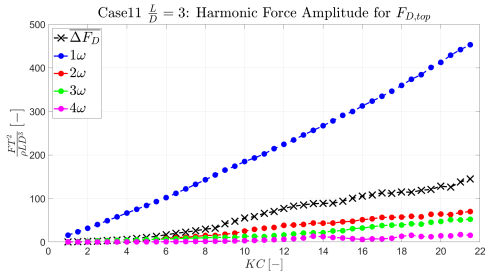

(a) The harmonic force amplitudes for $F_{D,top}$ and the mean force difference for Case 11 with $\frac{L}{D}=3$.

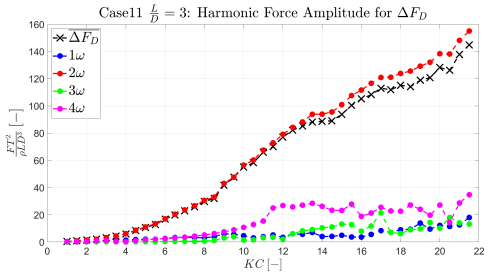

(b) The harmonic force amplitudes for ΔF_D and the mean force difference for Case 11 with $\frac{L}{D}=3$.

Fig. C.25: The harmonic force amplitudes for $F_{D,top}$ and ΔF_D and the mean force difference for Case 11 with $\frac{L}{D}=3$.

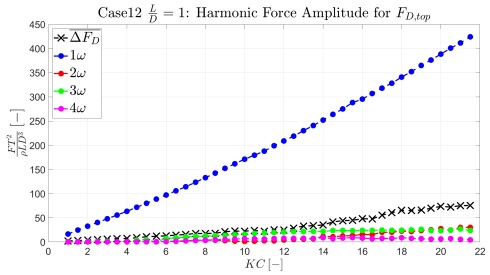

(a) The harmonic force amplitudes for $F_{D,top}$ and the mean force difference for Case 12 with $\frac{L}{D}=1$.

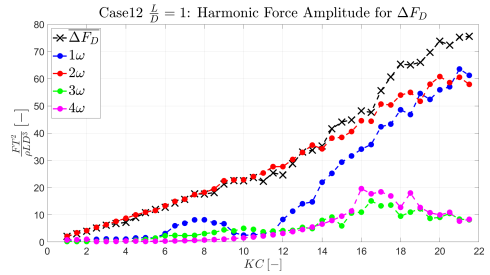

(b) The harmonic force amplitudes for ΔF_D and the mean force difference for Case 12 with $\frac{L}{D}=1$.

Fig. C.26: The harmonic force amplitudes for $F_{D,top}$ and ΔF_D and the mean force difference for Case 12 with $\frac{L}{D}=1$.

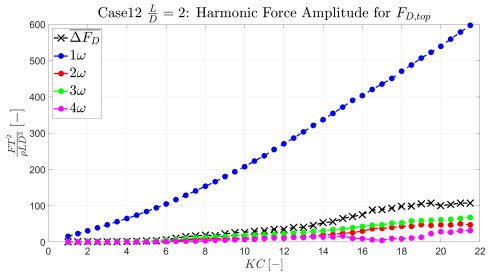

(a) The harmonic force amplitudes for $F_{D,top}$ and the mean force difference for Case 12 with $\frac{L}{D} = 2$.

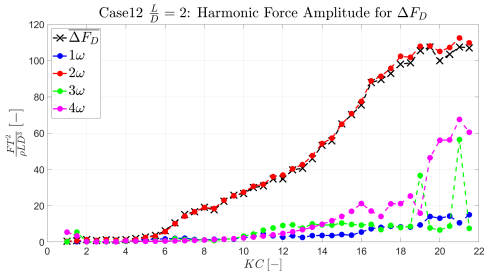

(b) The harmonic force amplitudes for ΔF_D and the mean force difference for Case 12 with $\frac{L}{D} = 2$.

Fig. C.27: The harmonic force amplitudes for $F_{D,top}$ and ΔF_D and the mean force difference for Case 12 with $\frac{L}{D} = 2$.

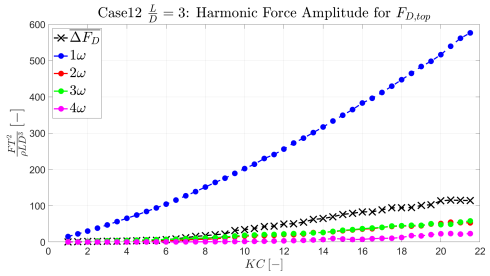

(a) The harmonic force amplitudes for $F_{D,top}$ and the mean force difference for Case 12 with $\frac{L}{D} = 3$.

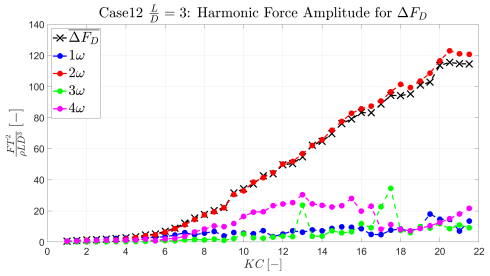

(b) The harmonic force amplitudes for ΔF_D and the mean force difference for Case 12 with $\frac{L}{D} = 3$.

Fig. C.28: The harmonic force amplitudes for $F_{D,top}$ and ΔF_D and the mean force difference for Case 12 with $\frac{L}{D} = 3$.

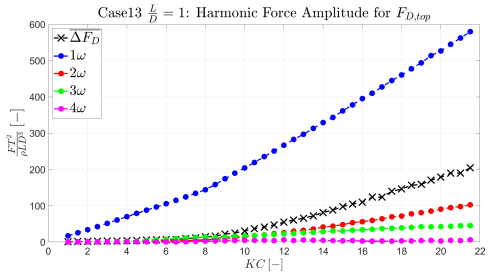

(a) The harmonic force amplitudes for $F_{D,top}$ and the mean force difference for Case 13 with $\frac{L}{D} = 1$.

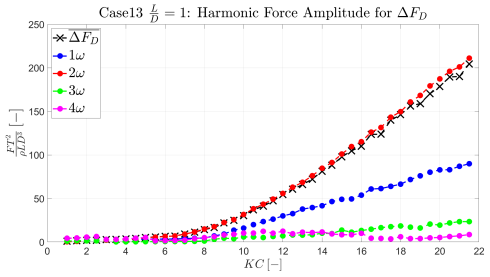

(b) The harmonic force amplitudes for ΔF_D and the mean force difference for Case 13 with $\frac{L}{D} = 1$.

Fig. C.29: The harmonic force amplitudes for $F_{D,top}$ and ΔF_D and the mean force difference for Case 13 with $\frac{L}{D} = 1$.

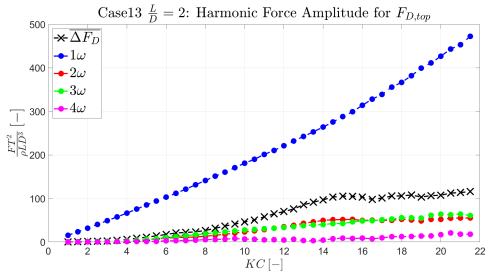

(a) The harmonic force amplitudes for $F_{D,top}$ and the mean force difference for Case 13 with $\frac{L}{D} = 2$.

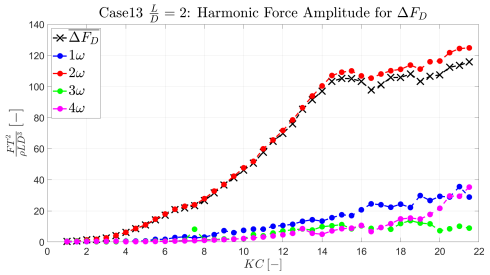

(b) The harmonic force amplitudes for ΔF_D and the mean force difference for Case 13 with $\frac{L}{D} = 2$.

Fig. C.30: The harmonic force amplitudes for $F_{D,top}$ and ΔF_D and the mean force difference for Case 13 with $\frac{L}{D} = 2$.

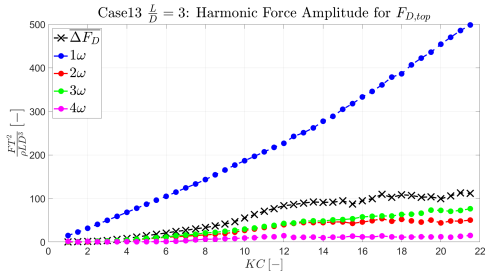

(a) The harmonic force amplitudes for $F_{D,top}$ and the mean force difference for Case 13 with $\frac{L}{D} = 3$.

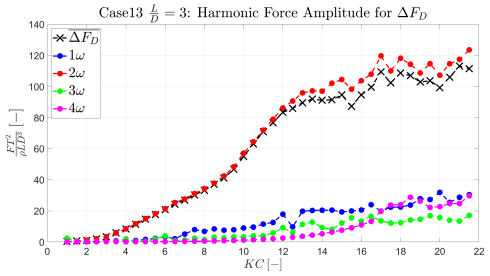

(b) The harmonic force amplitudes for ΔF_D and the mean force difference for Case 13 with $\frac{L}{D} = 3$.

Fig. C.31: The harmonic force amplitudes for $F_{D,top}$ and ΔF_D and the mean force difference for Case 13 with $\frac{L}{D} = 3$.

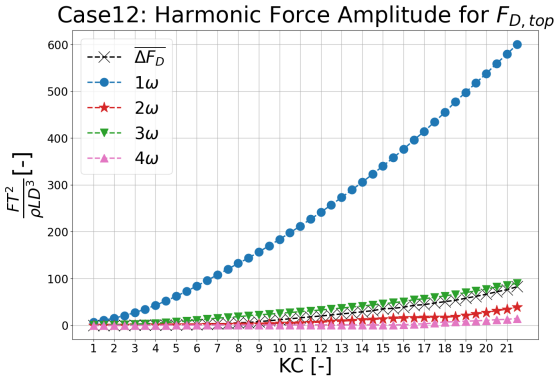

(a) The numerical harmonic force amplitudes for $F_{D,top}$ and the mean force difference in Case 12.

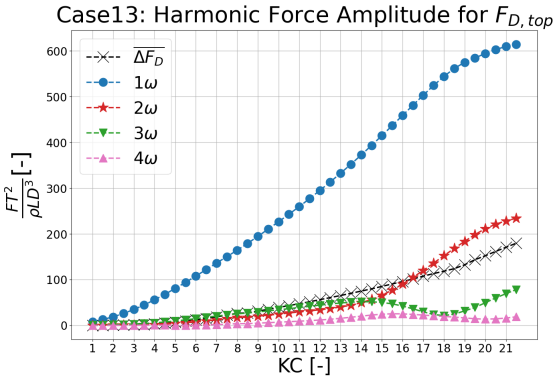

(b) The numerical harmonic force amplitudes for $F_{D,top}$ and the mean force difference in Case 13.

Fig. C.32: The numerical harmonic force amplitudes for $F_{D,top}$ and the mean force difference in cases 12 and 13.

D Streamline plots for cases 1 & 2.

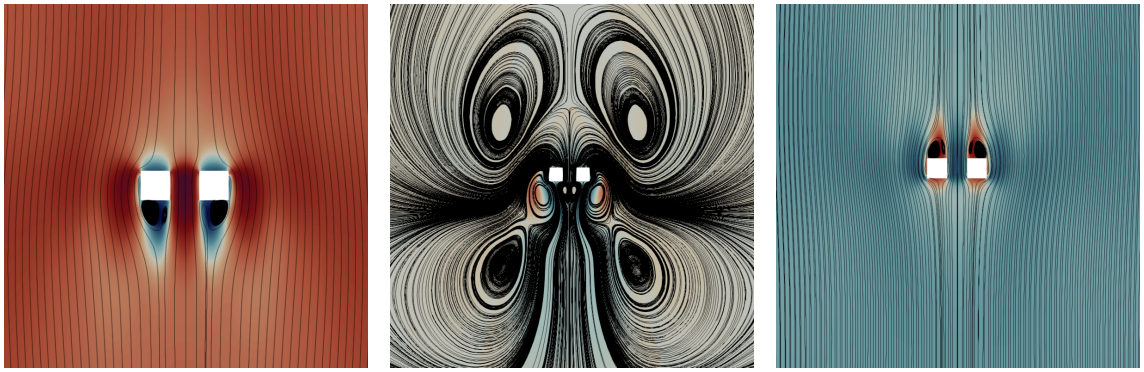

(a) The velocity streamlines of Case 1 with an inflow angle of $\theta = 0°$ at KC $= 16$ at $T = 10\,s$.

(b) The velocity streamlines of Case 1 with an inflow angle of $\theta = 0°$ at KC $= 16$ at $T = 10.25\,s$.

(c) The velocity streamlines of Case 1 with an inflow angle of $\theta = 0°$ at KC $= 16$ at $T = 10.5\,s$.

Fig. D.1: The velocity streamlines of Case 1 with an inflow angle of $\theta = 0°$ at KC $= 16$ at $T = 10$, 10.25, and 10.5 seconds.

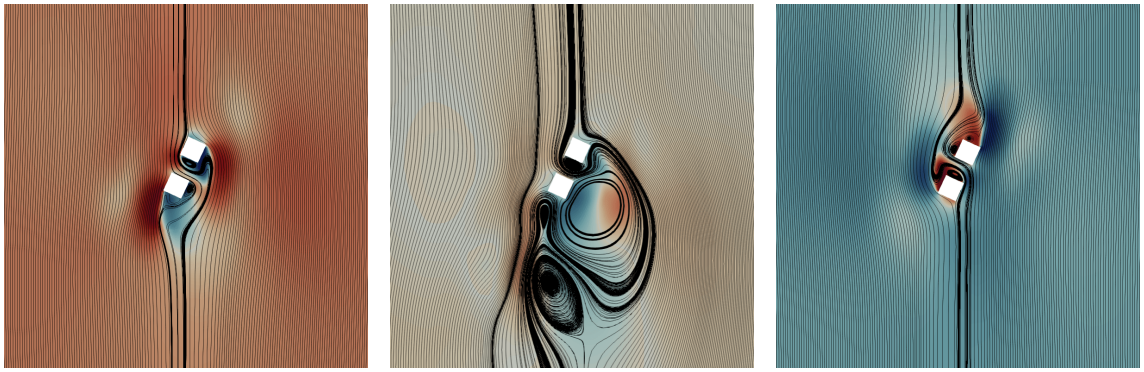

(a) The velocity streamlines of Case 1 with an inflow angle of $\theta = 65°$ at KC $= 16$ at $T = 10\,s$.

(b) The velocity streamlines of Case 1 with an inflow angle of $\theta = 65°$ at KC $= 16$ at $T = 10.25\,s$.

(c) The velocity streamlines of Case 1 with an inflow angle of $\theta = 65°$ at KC $= 16$ at $T = 10.5\,s$.

Fig. D.2: The velocity streamlines of Case 1 with an inflow angle of $\theta = 65°$ at KC $= 16$ at $T = 10$, 10.25, and 10.5 seconds.

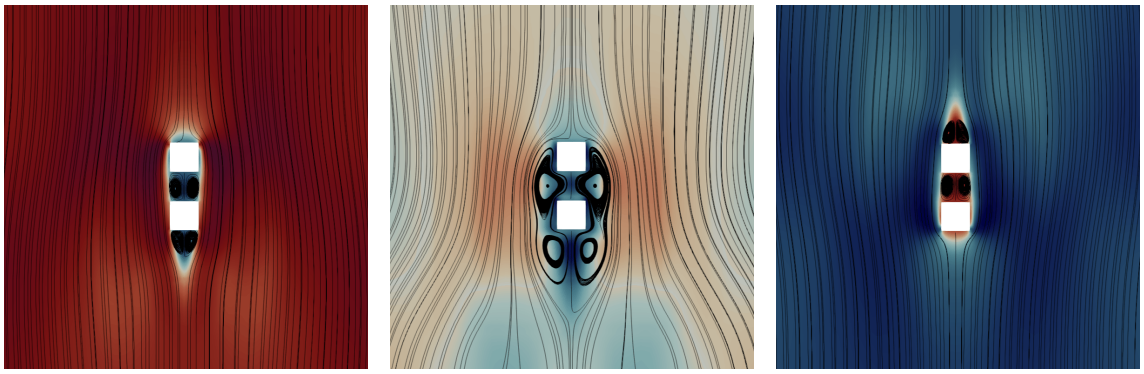

(a) The velocity streamlines of Case 1 with an inflow angle of $\theta = 90°$ at KC $= 16$ at $T = 10\,s$.

(b) The velocity streamlines of Case 1 with an inflow angle of $\theta = 90°$ at KC $= 16$ at $T = 10.25\,s$.

(c) The velocity streamlines of Case 1 with an inflow angle of $\theta = 90°$ at KC $= 16$ at $T = 10.5\,s$.

Fig. D.3: The velocity streamlines of Case 1 with an inflow angle of $\theta = 90°$ at KC $= 16$ at $T = 10$, 10.25, and 10.5 seconds.

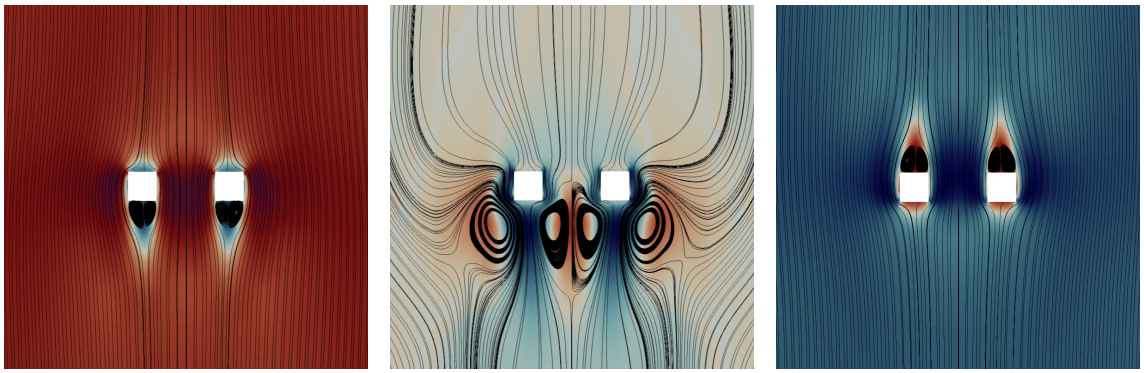

(a) The velocity streamlines of Case 2 with an inflow angle of $\theta = 0°$ at KC $= 16$ at $T = 10\,s$.

(b) The velocity streamlines of Case 2 with an inflow angle of $\theta = 0°$ at KC $= 16$ at $T = 10.25\,s$.

(c) The velocity streamlines of Case 2 with an inflow angle of $\theta = 0°$ at KC $= 16$ at $T = 10.5\,s$.

Fig. D.4: The velocity streamlines of Case 2 with an inflow angle of $\theta = 0°$ at KC $= 16$ at $T = 10$, 10.25, and 10.5 seconds.

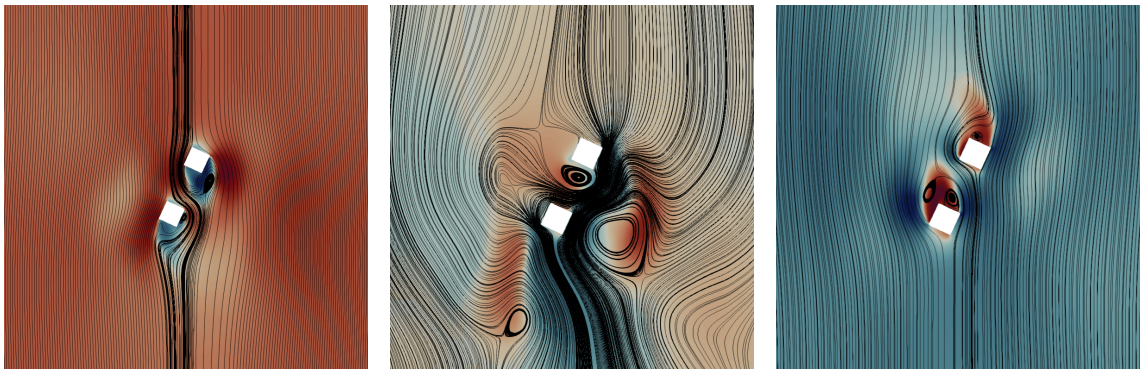

(a) The velocity streamlines of Case 2 with an inflow angle of $\theta = 65°$ at KC $= 16$ at $T = 10\,s$.

(b) The velocity streamlines of Case 2 with an inflow angle of $\theta = 65°$ at KC $= 16$ at $T = 10.25\,s$.

(c) The velocity streamlines of Case 2 with an inflow angle of $\theta = 65°$ at KC $= 16$ at $T = 10.5\,s$.

Fig. D.5: The velocity streamlines of Case 2 with an inflow angle of $\theta = 65°$ at KC $= 16$ at $T = 10$, 10.25, and 10.5 seconds.

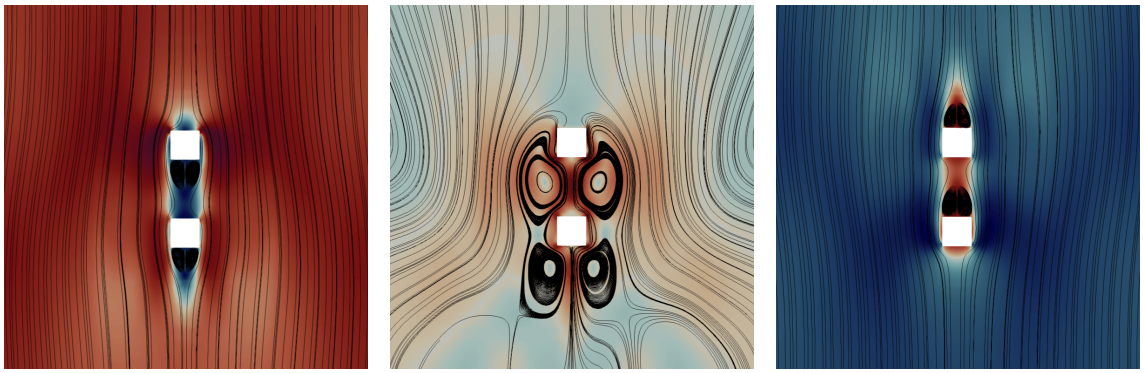

(a) The velocity streamlines of Case 2 with an inflow angle of $\theta = 90°$ at KC $= 16$ at $T = 10\,s$.

(b) The velocity streamlines of Case 2 with an inflow angle of $\theta = 90°$ at KC $= 16$ at $T = 10.25\,s$.

(c) The velocity streamlines of Case 2 with an inflow angle of $\theta = 90°$ at KC $= 16$ at $T = 10.5\,s$.

Fig. D.6: The velocity streamlines of Case 2 with an inflow angle of $\theta = 90°$ at KC $= 16$ at $T = 10$, 10.25, and 10.5 seconds.

E Polar plots comparing cases 1 & 2.

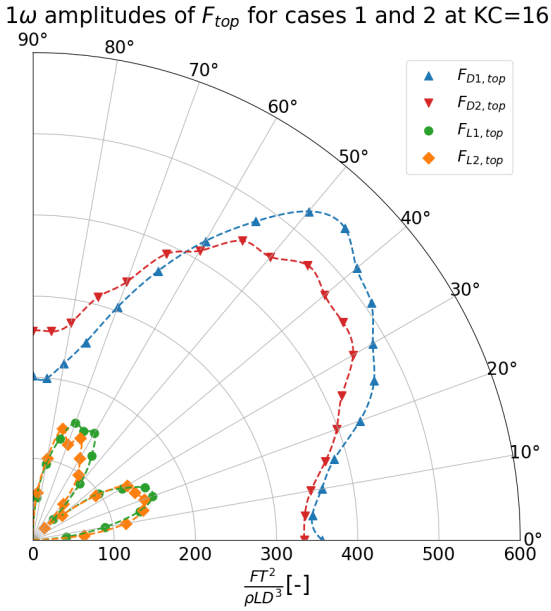

(a) The comparison of the 1ω harmonic force amplitude for F_{top} in cases 1 and 2 for $KC = 16$.

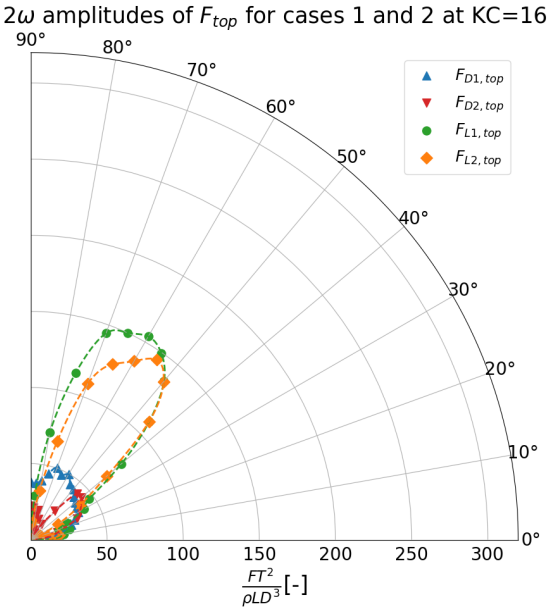

(b) The comparison of the 2ω harmonic force amplitude for F_{top} in cases 1 and 2 for $KC = 16$.

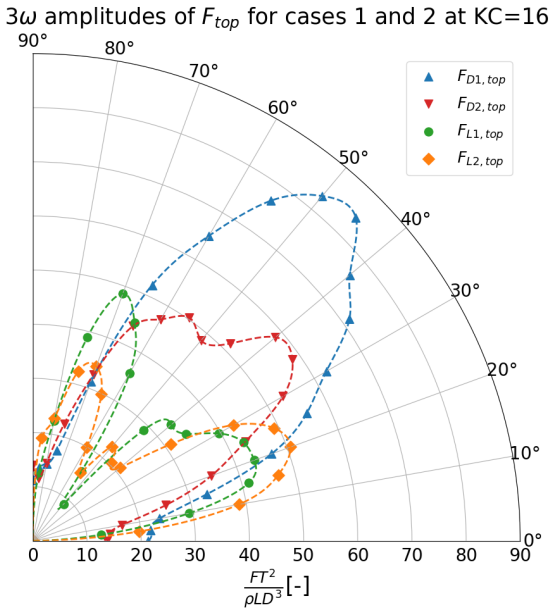

(c) The comparison of the 3ω harmonic force amplitude for F_{top} in cases 1 and 2 for $KC = 16$.

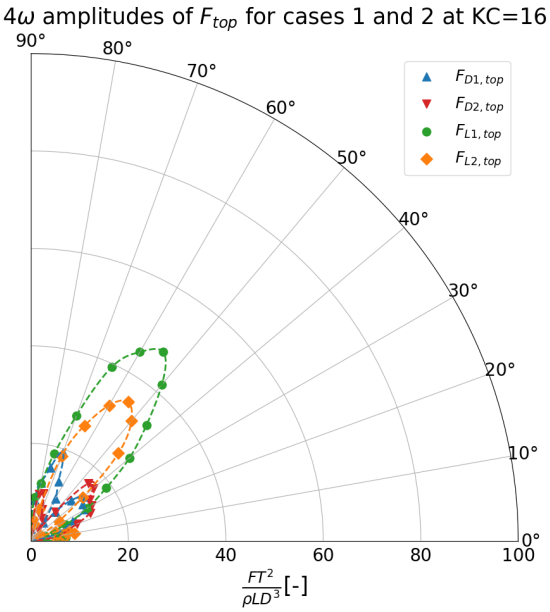

(d) The comparison of the 4ω harmonic force amplitude for F_{top} and ΔF in cases 1 and 2 for $KC = 16$.

Fig. E.1: The comparison of the harmonic force amplitudes for F_{top} in cases 1 and 2 for $KC = 16$.

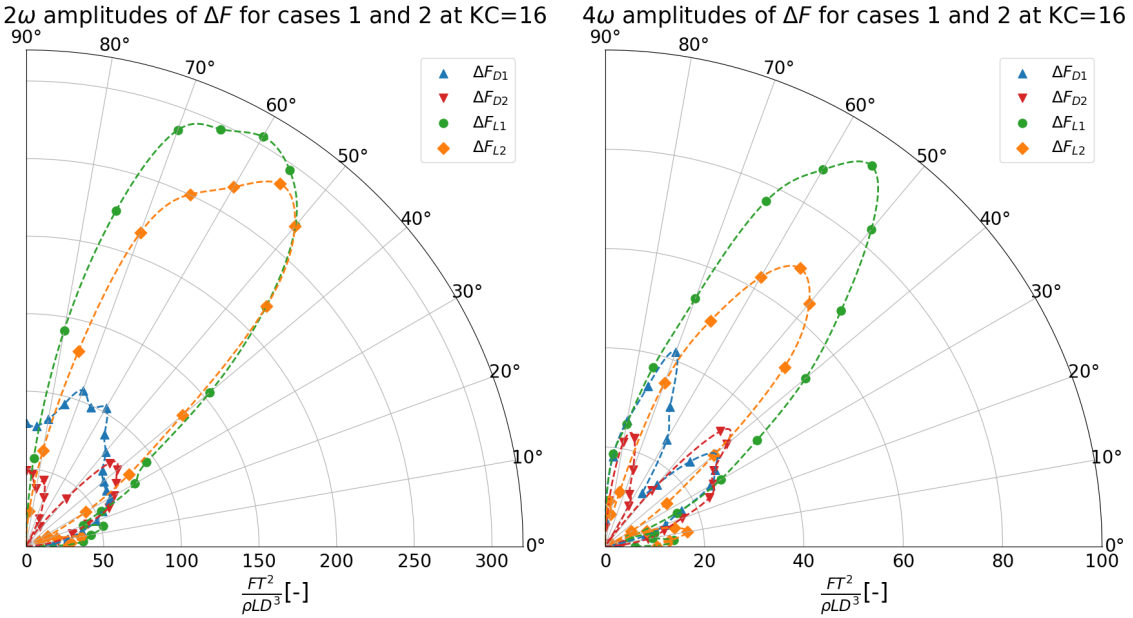

(a) The comparison of the 2ω harmonic force amplitude for ΔF in cases 1 and 2 for $KC = 16$.

(b) The comparison of the 4ω harmonic force amplitude for ΔF in cases 1 and 2 for $KC = 16$.

Fig. E.2: The comparison of the harmonic force amplitudes for ΔF in cases 1 and 2 for $KC = 16$. The 1ω and 3ω amplitudes are not presented as they were negligible.

F Script for creating the model geometries.

```
import numpy as np
import os
import stl
from stl import mesh


class Case:
    def __init__(self, case_number):
        self.shape = None
        self.dist = None
        self.cyl_number = None
        self.case_number = case_number

    def attribute(self):
        if self.case_number == 1:
            self.shape = 'square'
            self.dist = 0.1
            self.cyl_number = 2
        elif self.case_number == 2:
            self.shape = 'square'
            self.dist = 0.15
            self.cyl_number = 2
        elif self.case_number == 3:
            self.shape = 'square'
            self.dist = 0.1
            self.cyl_number = 4
        elif self.case_number == 11:
            self.shape = 'diamond'
            self.dist = 0.1
            self.cyl_number = 2
        elif self.case_number == 12:
            self.shape = 'diamond'
            self.dist = 0.15
            self.cyl_number = 2
        elif self.case_number == 13:
            self.shape = 'diamond'
            self.dist = 0.1
            self.cyl_number = 4
        else:
            print(f'Unknown case: {self.case_number}')
            exit()


def cylinder(center_x, center_z, side_length, depth, number):
    y1 = - depth / 2
    y2 = depth / 2
    z1 = center_z - side_length / 2
    z2 = center_z + side_length / 2
    vert = np.zeros((number, 8, 3))
    fac = np.zeros((number, 12, 3))
    x_sgn = -1
    z_sgn = -1
    faces = np.array([
        [0, 3, 1],
        [1, 3, 2],
        [0, 4, 7],
        [0, 7, 3],
        [4, 5, 6],
        [4, 6, 7],
        [5, 1, 2],
        [5, 2, 6],
```

```
        [2, 3, 6],
        [3, 7, 6],
        [0, 1, 5],
        [0, 5, 4]
    ])

    for idx in range(number):
        x1 = x_sgn * center_x - side_length / 2
        x2 = x_sgn * center_x + side_length / 2
        if number % 4 == 0:
            if idx <= 1:
                z1 *= z_sgn
                z2 *= z_sgn
                z_sgn *= -1
            else:
                z1, z2 = abs(z1), abs(z2)

        vertices = np.array([
            [z1, y1, x1],
            [z2, y1, x1],
            [z2, y2, x1],
            [z1, y2, x1],
            [z1, y1, x2],
            [z2, y1, x2],
            [z2, y2, x2],
            [z1, y2, x2]
        ])

        vert[idx] = vertices
        fac[idx] = faces
        x_sgn *= -1

    return vert, fac


def createSTLfile(case):
    case.attribute()
    if case.cyl_number % 4 == 0:
        z = case.dist / 2
    else:
        z = 0

    vertices, faces = cylinder(case.dist / 2, z, 0.05, 2, case.cyl_number)
    faces = faces.astype(int)
    filenames = []
    solidnames = []

    for x in range(len(vertices)):
        F = faces[x]
        print(F.shape[0])
        V = vertices[x]
        solidnames.append(f'hull{x}H')
        cube = mesh.Mesh(np.zeros(F.shape[0], dtype=mesh.Mesh.dtype))
        for i, f in enumerate(F):
            for j in range(3):
                cube.vectors[i][j] = V[f[j], :]
        cube.save(f'case_{case.case_number}_{x + 1}_BIN.stl')
        cube_text = mesh.Mesh.from_file(f'case_{case.case_number}_{x + 1}
    _BIN.stl')
        cube_text.save(f'case_{case.case_number}_{x + 1}_ASCII.stl', mode=
    stl.Mode.ASCII)
        filenames.append(f'case_{case.case_number}_{x + 1}_ASCII.stl')
        os.remove(f'case_{case.case_number}_{x + 1}_BIN.stl')
```

```
123
124     text1 = 'solid'
125     text2 = 'endsolid'
126     y = 0
127     n = []
128
129     path = "PATH"
130     name = f'{path}case_{case.case_number}.stl'
131     for nam in range(case.cyl_number):
132         n.append(f'{path}case_{case.case_number}_{nam + 1}.stl')
133
134     with open(name, 'w') as outfile:
135         for fname in filenames:
136             with open(fname) as infile:
137                 for line in infile:
138                     if text2 in line:
139                         line = f'endsolid {solidnames[y]}\n'
140                         y += 1
141                     elif text1 in line:
142                         line = f'solid {solidnames[y]}\n'
143                     outfile.write(line)
144             outfile.write('LINEBREAK!\n')
145             os.remove(fname)
146
147     with open(name) as f:
148         lines = f.read()
149     data = lines.split("LINEBREAK!\n")
150     for op in range(case.cyl_number):
151         with open(n[op], "w") as f:
152             f.write(data[op])
153     os.remove(name)
154
155     return vertices
```

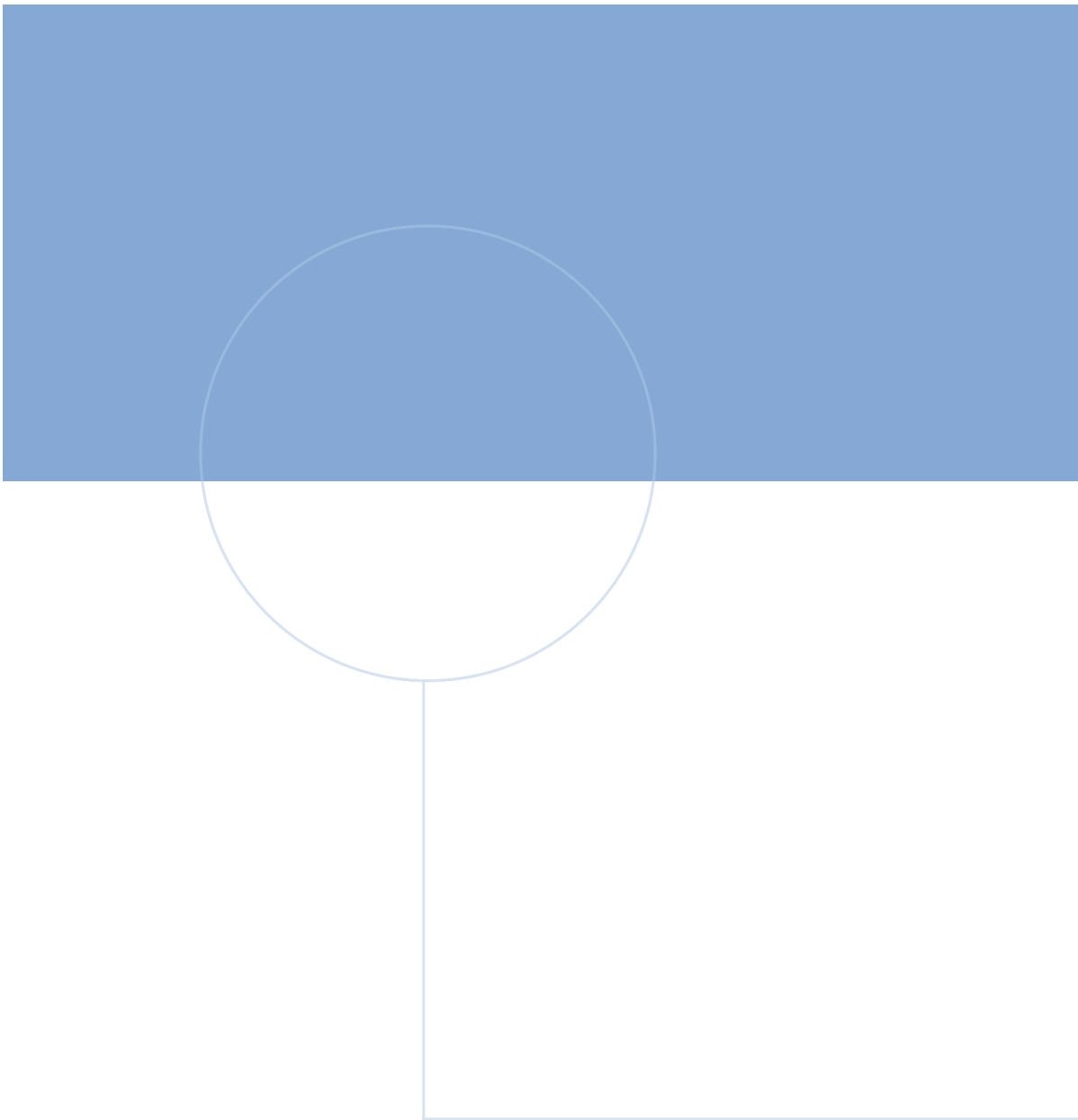

NTNU

Norwegian University of
Science and Technology